FORSCHUNGSZENTRUM JÜLICH GmbH

Code Improvements and Applications of a Two-dimensional Edge Plasma Model for Toroidal Devices

Martine Baelmans

ÉCOLE ROYALE MILITAIRE-KONINKLIJKE MILITAIRE SCHOOL

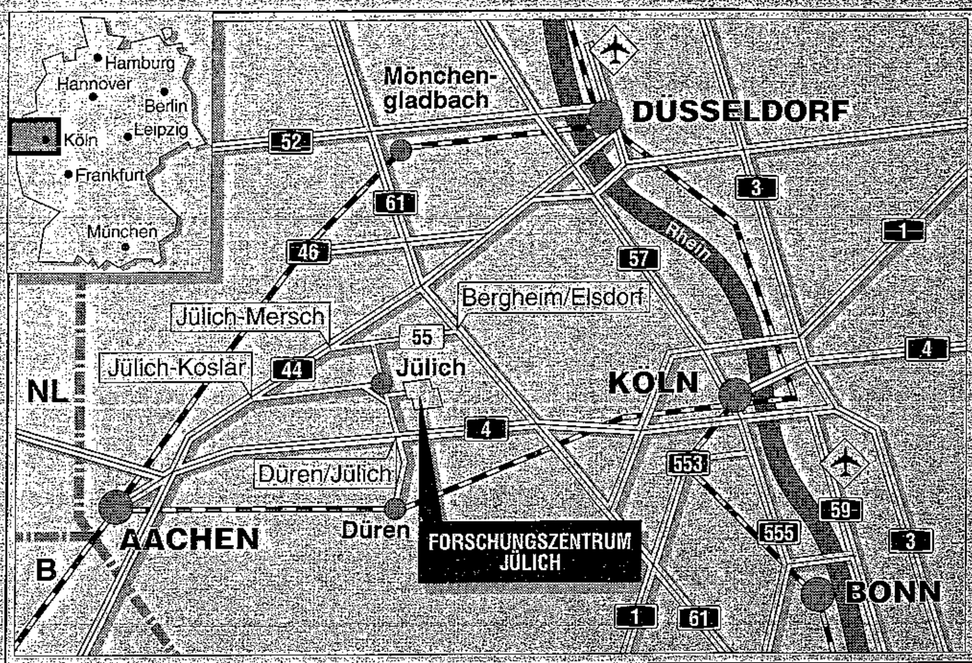

Berichte des Forschungszentrums Jülich ; 2891
ISSN 0944-2952
Institut für Plasmaphysik Jül-2891
Association EURATOM-KFA
(Diss. Universiteit Leuven)
gleichzeitig : LPP-ERM / KMS-Rep. N° 100

Zu beziehen durch : Forschungszentrum Jülich GmbH · Zentralbibliothek
D-52425 Jülich · Bundesrepublik Deutschland
Telefon : 02461 / 61 - 6102 · Telefax : 02461 / 61 - 6103 · Telex : 833 556-70 kfa d

Code Improvements and Applications of a Two-dimensional Edge Plasma Model for Toroidal Devices

Martine Baelmans

KATHOLIEKE UNIVERSITEIT LEUVEN
FAKULTEIT DER TOEGEPASTE WETENSCHAPPEN
DEPARTMENT WERKTUIGKUNDE
AFDELING TOEGEPASTE MECHANICA EN ENERGIECONVERSIE
Celestijnenlaan 300 A – B 3001 Leuven (Haverlee), Belgium

ÉCOLE ROYALE MILITAIRE – KONINKLIJKE MILITAIRE SCHOOL
LABORATOIRE DE PHYSIQUE DES PLASMAS – LABORATORIUM VOOR PLASMAFYSICA
ASSOCIATION EURATOM-BELGIAN STATE
Report N° 100

FORSCHUNGSZENTRUM JÜLICH
INSTITUT FÜR PLASMAPHYSIK
ASSOCIATION EURATOM-KFA

Contents

Nomenclature

The most important notations are summarized below. Symbols that occur only locally in one or a few sections are not mentioned here. All symbols used, including the ones below, are explained in the text.

General symbols

$\vec{B}$	: magnetic field
c_s	: isothermal ion sound speed
D	: diffusion coefficient
e	: elementary charge
$\vec{E}$	: electric field
I_p	: plasma current
$\vec{j}$	: plasma current density
$\vec{j}_c$	: compensation current density
m	: mass
n	: particle density
p	: pressure
$\vec{q}$	: conductive heat flux
$\vec{Q}$	: total heat flux
Q_{ei}	: temperature equilibration
R	: momentum transfer
R_c	: recycling coefficient
S_n	: particle source due to interaction with neutral particles
$\vec{S}_{mV}$	: momentum source due to interaction with neutral particles
S_E	: energy source due to interaction with neutral particles
t	: time
T	: temperature, expressed in energy units
$\vec{v}$	: individual particle velocity
v_{th}	: measure for the thermal speed
$\vec{V}$	: average particle velocity
Z	: ion charge state
$\vec{\Gamma}$	: particle flux
δ_i, δ_e	: sheath transmission coefficients
η	: viscosity
η_0	: parallel viscosity

κ : conductivity
λ : mean free path
μ_0 : permeability of free space
ν_s : slowing down frequency
$\overleftrightarrow{\Pi}$: visosity tensor
$\overleftrightarrow{\Pi}_0$: parallel viscosity tensor
ρ : mass density
ρ_L : Larmor radius
σ : electric conductivity
τ : basic collision time
Φ : electric potential
ω : gyrofrequency

$\Im(z)$: imaginary part of a complex number z
$\Re(z)$: real part of a complex number z

Fusion energy

D : deuterium
H : hydrogen
Li : lithium
n : neutron
P_{fus} : fusion power density
R : reaction rate
T : tritium

ϵ : energy released per reaction
σ : cross-section
$< \sigma v >$: reactivity
τ_E : energy confinement time

Tokamak geometry

a : minor radius
a_0 : minor radius of the reference circle
L_θ : poloidal length between two targets
$L_{||}$: length scale of variation of the macroscopic plasma parameters
p : pitch
q : safety factor
R : major radius
R_0 : major radius of the reference circle

Δ : displacement
$\Delta(0)$: Shafranov shift

λ	: decay length

Curvilinear co-ordinates

A_α	: covariant component of $\vec{A}$
A^α	: contravariant component of $\vec{A}$
$\tilde{A}_\alpha$	: physical component of $\vec{A}$
$\vec{b}$	: unit vector along $\vec{B}$
$\vec{e}_\alpha$	: tangent basis vector in the α-direction
$\overleftrightarrow{g}$	: metric tensor
h_α	: modulus of the tangent basis vector $\vec{e}_\alpha$
$J = \sqrt{g}$	: Jacobian of the metric matrix
$\overleftrightarrow{I}$	: unit tensor
$\Gamma^\alpha_{\beta,\gamma}$	: modified Christoffel symbol
$\left\{ \begin{array}{c} \alpha \\ \beta\gamma \end{array} \right\}$	: Christoffel symbol of the second kind

B2-notation

u	: poloidal velocity component
$u_{\parallel}$	: parallel velocity component
v	: radial velocity component
x	: poloidal co-ordinate
y	: radial co-ordinate

Indices

particles	
D	: deuterium
e	: electron
i	: ion
T	: tritium
directions	
r	: radial direction, or normal to the flux surface
θ	: poloidal direction
ϕ	: toroidal direction
$\parallel$	: direction parallel to $\vec{B}$
$\perp$	: direction perpendicular to $\vec{B}$ in the magnetic flux surface
for transport coefficients	
$\parallel$	: transport coefficient for gradients parallel to $\vec{B}$
$\perp$	: transport coefficient for gradients perpendicular to $\vec{B}$
$\wedge$	: transport coefficient for cross-terms of gradients with $\vec{B}$

position

s	: at the sheath entrance
w	: at the wall or material boundary
0	: at the "left" boundary
N	: at the "right" boundary

Nederlandse samenvatting

1. Algemene inleiding

In deze thesis wordt het gedrag van het randplasma in een "Tokamak" fusie-reactor bestudeerd. Om dit werk te situeren volgt hierna een korte uiteenzetting in verband met aspecten van het randplasma en het belang van deze randfenomenen voor het realiseren van kernfusie.

Het doel van het onderzoek naar **gecontroleerde kernfusie** is een technologie te ontwikkelen die kan bijdragen tot de wereldenergievoorziening op lange termijn. Dit onderzoek wordt gedaan in laboratoria verspreid over de geïndustrialiseerde wereld, met een grote mate van internationale samenwerking.
Bij de fusiereacties die in aanmerking komen zijn de waterstof-isotopen (waterstof (H of ${}_1^1H$), deuterium (D of ${}_1^2H$) en tritium (T of ${}_1^3H$)), de helium-isotopen (${}_2^4He$ en ${}_2^3He$) en neutronen n betrokken :

$$\begin{aligned} D+T &\longrightarrow {}_2^4He + n + 17.6 \text{ MeV} \\ D+D &\longrightarrow T + {}_1^1H + 4.0 \text{ MeV} \\ D+D &\longrightarrow {}_2^3He + n + 3.3 \text{ MeV} \\ D + {}_2^3He &\longrightarrow {}_2^4He + {}_1^1H + 18.3 \text{ MeV} \end{aligned}$$

Van deze reacties zijn de reactievoorwaarden van de $D-T$-reactie het minst veeleisend. Het huidig onderzoek spitst zich daarom in eerste instantie toe op de $D-T$-reactie, waarbij het tritium wordt aangemaakt door middel van een reactie tussen lithium (Li) en de neutronen die vrijkomen uit de fusiereactie :

$$\begin{aligned} {}_3^7Li + n &\longrightarrow {}_2^4He + T + n - 2.5\text{MeV} \\ {}_3^6Li + n &\longrightarrow {}_2^4He + T + 4.8\text{MeV} \end{aligned}$$

Om een fusiereactor economisch rendabel te maken dient de reactiviteit van de reactie voldoende hoog te zijn. Voor de eenvoudigst realiseerbare reactie, de $D-T$-reactie, wordt in een mengsel van 50 % deuterium en 50 % tritium de reactiewaarschijnlijkheid pas groot genoeg bij een temperatuur van tenminste 10 keV (ongeveer 10^8 K). Bij een dergelijke temperatuur is het $D-T$-gas volledig geïoniseerd. Men noemt dit geïoniseerde medium een plasma, en spreekt van thermonucleaire fusie.

Een tweede vereiste van economische rendabiliteit wordt bepaald door een voldoende hoge waarde voor $n\tau_E$, waarin n de plasmadichtheid is en τ_E de energie opsluitingstijd. Voor een plasma met een dichtheid van $n \approx 10^{20}\mathrm{m}^{-3}$ betekent dit dat $\tau_E \geq 1$ s moet zijn.

Eén van de bestaande ontwerpen van een fusiereactor is de **Tokamak**. Dit reactor-type is gebaseerd op het principe van magnetische opsluiting : geïoniseerde deeltjes zullen in eerste benadering magnetische veldlijnen volgen en kunnen zodoende opgesloten worden in magnetische configuratie. Om een goede opsluiting te realiseren worden torusvormige magnetische fluxoppervlakken gecreëerd waarin de magnetische veldlijnen helicoïdaal geschroefd zijn (zie figuur 0.1). De verwezenlijking van de magnetische veldlijnen gebeurt enerzijds door poloïdale spoelen die een toroïdaal magnetisch veld creëren en door een transformator die in het plasma een stroom creëert en zodoende een poloïdale component van het magnetisch veld verwezenlijkt.

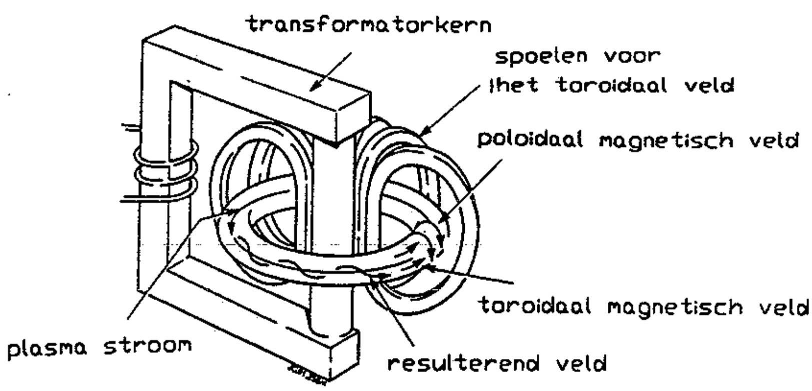

Figuur 0.1: Schematische voorstelling van een Tokamak

In de kern van de Tokamak zijn de magnetische fluxoppervlakken gesloten. Een geïoniseerd deeltje zal dan ook in eerste benadering in dit oppervlak opgesloten zijn. Ten gevolge van onderlinge botsingen en ten gevolge van fluctuaties in plasma-parameters is deze opsluiting echter niet perfect en diffunderen de plasma-deeltjes naar de rand. In deze **plasma-rand** treffen de magnetische veldlijnen de wanden van het vacuümvat waarin het plasma zich bevindt. Ionen die deze veldlijnen volgen en zodoende op de wanden terecht komen, worden geneutraliseerd en prompt weerkaatst of na een zekere residentietijd uit de wand vrijgezet. Hierdoor kunnen ze in het plasma terechtkomen, waar ze weer geïoniseerd worden. Dit proces wordt "recycling" genoemd en speelt een essentiële rol in het gedrag van het randplasma. De zone waar de "recycling" een rol speelt, noemt men de plasma-rand. In deze samenhang definieert men een "recycling"-coëfficiënt die de verhouding aangeeft tussen het aantal neutrale deeltjes dat per tijdseenheid het plasma binnenkomt en het aantal ionen dat per tijdseenheid op de wandmaterialen terechtkomt. Deze "recycling"-coëfficiënt is voor stationaire toestanden gelijk aan één, of iets lager dan één indien neutrale deeltjes worden weggepompt. Vaak kan een "recycling"-coëfficiënt merkelijk lager dan één bekomen worden doordat de wand zelf pompt. Dit kan enkel optreden zolang de wand niet gesatureerd is. In de plasma-rand onderscheidt men twee gebieden, die van elkaar gescheiden worden door het laatste gesloten fluxoppervlak ("last closed flux surface"of LCFS). Binnen dit LCFS bevindt zich het gebied waar ten gevolge van onzuiverheden een grote hoeveelheid stralingsenergie kan verloren gaan voor het plasma. Dit gebied noemt men "radiating layer" (RL) (nog verder naar binnen gelegen, bevindt zich het kernplasma waar de thermo-nucleaire reacties plaatsvinden). Buiten het LCFS worden de plasmadeeltjes voornamelijk naar de wanden, die met de magnetische veldlijnen snijden, afgevoerd. Dit gebied noemt men daarom de "scrape-off layer" (SOL).

Het gedrag van het randplasma is belangrijk omdat het de dichtheidscontrole en de afvoer van de reactieprodukten (He) en van de geproduceerde energie moet verwezenlijken. Dit dient te gebeuren zonder dat de hoge temperaturen, die nodig zijn in de kern van de reactor, worden beïnvloed. De warmteflux en de deeltjes die de wand treffen kunnen tot gevolg hebben dat verontreinigingen worden geproduceerd die mogelijk in het plasma terechtkomen. De plasmarandprofielen moeten daarom zodanig zijn dat deze onzuiverheden niet tot in de kern van de reactor kunnen doordringen.
Om de profielen van het randplasma te optimaliseren wordt in het hedendaags onderzoek met twee magnetische configuraties geëxperimenteerd. Bij een eerste methode is een materiaal ("limiter") in de rand ingebracht (zie figuur 0.2). Een tweede methode bestaat erin de magnetische veldlijnen af te buigen naar wandmateriaal dat verder van het kernplasma verwijderd is (zie figuur 0.3). Verder kunnen de plasmaprofielen in de rand beïnvloed worden door allerhande technieken, zoals onder andere door het aanleggen van potentiaalverschillen tussen verschillende wandelementen (de zogenaamde "biassing"-experimenten).
De studie van het randplasma in het algemeen is van essentieel belang voor de optimalisatie van het reactorontwerp. Hierbij wordt getracht de geometrie te optimaliseren zowel wat betreft de magnetische configuratie als wat betreft de wandgeometrie. Verder wordt er getracht de randprofielen te controleren door het aanleggen van potentiaalverschillen en het conditioneren van de wand. Met deze studies beoogt men de fenomenen die zich afspelen in het randplasma te begrijpen om zo een extrapolatie naar grotere machines zo betrouwbaar mogelijk te maken. Numerieke simulaties kunnen zeker hun bijdrage tot deze doelstellingen leveren.

2. Model voor het randplasma

De beschrijving van het randplasma gebeurt aan de hand van fluïdumvergelijkingen, zoals die voor een gemagnetiseerd plasma werden afgeleid door Braginskii [14]. Vermits de plasmadeeltjes, in eerste orde, de helicoïdaal geschroefde magnetische veldlijnen volgen, vertonen de transportcoëfficiënten een sterk anisotroop karakter. Anderzijds vereist een

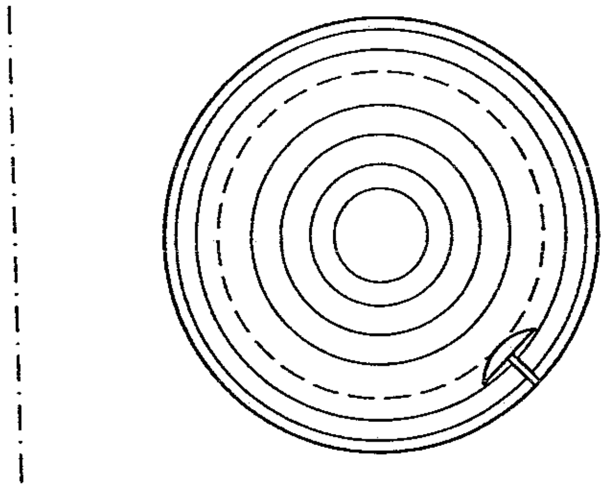

Figuur 0.2: Magnetische configuratie van een limiter-Tokamak

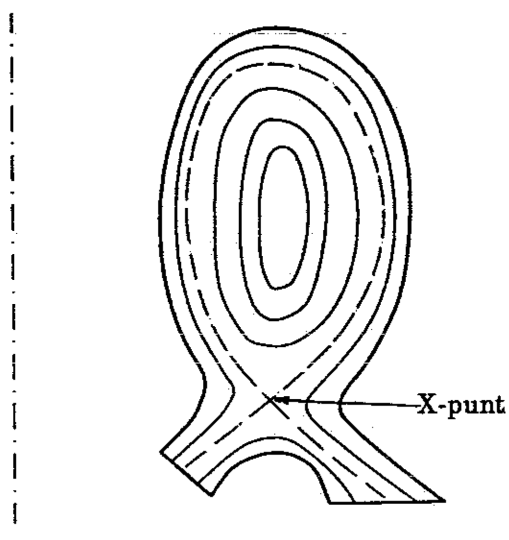

Figuur 0.3: Magnetische configuratie van een divertor-Tokamak

randplasma-model een twee-dimensionele aanpak, vermits in de rand zowel het radiale transport als het transport langsheen de magnetische veldlijnen van belang zijn. Het radiale transport is immers sterk bepalend voor het gedrag van het plasma binnen het laatste gesloten fluxoppervlak, terwijl in de "scrape-off layer" de plasmadeeltjes voornamelijk langsheen de veldlijnen naar de limiter- of divertorplaten worden afgevoerd.

De toroïdale symmetrie van een Tokamak laat hierbij toe om de fluïdumvergelijkingen neer te schrijven in een twee-dimensioneel orthogonaal curvelineair coördinaten-systeem met basisvectoren ($\vec{e}_\theta$,$\vec{e}_r$). Eén van de bijdragen van dit werk bestaat in de afleiding van een model dat rekening houdt met het anisotrope karakter volgens de parallelle richting (basisvectoren volgens de hoofdrichtingen van de anisotropie zijn ($\vec{e}_{||}$,$\vec{e}_\perp$,$\vec{e}_r$), zoals voorgesteld in figuur 0.4). Deze uitwerking in algemene coördinaten leidt tot een "neoklassiek" model dat toepasbaar is voor verschillende toroïdale geometrieën en als dusdanig de basis kan vormen voor randplasma-berekeningen.

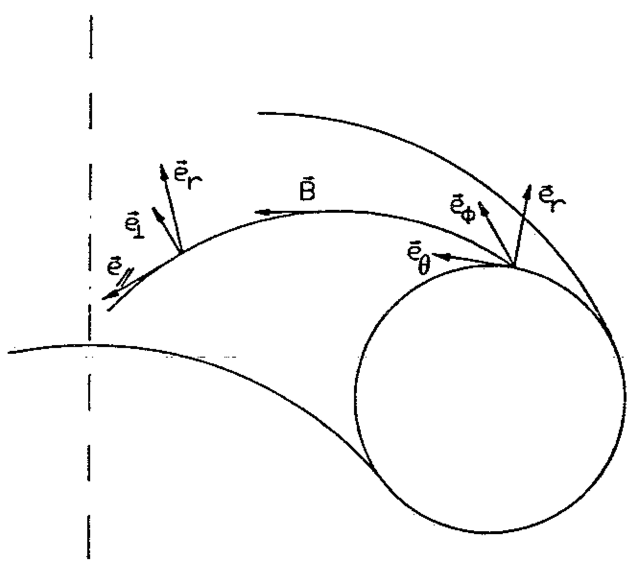

Figuur 0.4: Basisvectoren in de twee coördinatenstelsels

3. Aanpassingen en verbeteringen van een bestaande twee-dimensionele plasma-rand code (B2) voor toepassingen op TEXTOR.

Om de fenomenen die zich afspelen in het randplasma te onderzoeken, wordt gebruik gemaakt van een bestaande code. Deze code werd ontwikkeld door Braams [13] en wordt de B2-code genoemd. Vertrekkende van een gekende magnetische configuratie berekent de code "scrape-off layer"-profielen in toroïdale geometrieën. Gebaseerd op een vereenvoudigd twee-dimensioneel model kunnen de volgende plasmaparameters in de rand berekend worden : de plasmadichtheid (n), de componenten van de gemiddelde ionensnelheid in de poloïdale en radiale richting (respectievelijk V_θ en V_r) en de elektronen- en ionentemperatuur (respectievelijk T_e en T_i). Een zeer eenvoudig model beschrijft de interactie van neutrale deeltjes met het plasma. De code werd dusdanig geschreven dat implementatie van nieuwe geometrieën en specifieke randvoorwaarden relatief eenvoudig is, zodat ook een bijdrage kan geleverd worden tot de ontwerpstudie van nieuwe Tokamaks (NET, ITER). Een bijkomend voordeel van de code is dat het model voor de interactie tussen neutrale deeltjes en plasma onder de zogenoemde gebruikers-routines wordt gekatalogeerd. Een nadeel daarentegen is dat veranderingen en uitbreidingen in het randplasma-model een diepgaande verandering van de code vergen.

Met het oog op het vergelijken van de resultaten van de oorspronkelijke code met de beschikbare data van de limiter-Tokamak TEXTOR (Forschungszentrum Jülich), dienen eerst de magnetische configuratie en de correcte randvoorwaarden te worden geïmplementeerd :

1) De magnetische configuratie voor deze toepassingen wordt berekend aan de hand van een conforme transformatie die het rechthoekige rooster van de numerieke simulatie transformeert naar een orthogonaal curvelineair rooster met coördinaatlijnen langsheen de fluxoppervlakken in een poloïdale doorsnede (zie figuur 0.5). De eigenschappen van deze transformatie worden uitgewerkt in deze thesis. Hierdoor kunnen voortaan op eenvoudige wijze verschillende magnetische configuraties voor limiter-Tokamaks worden ingevoerd.

2) Het invoeren van de volledige poloïdale doorsnede van het randgebied vergt voor de transformatie vanuit het numerieke rechthoekige rooster een snede in het rooster van de poloïdale doorsnede ter hoogte van de limiter (aangeduid met ABB'A' op figuur 0.5). Hierdoor dient een voor de B2-code nieuw type van randvoorwaarde te worden ingevoerd, namelijk een periodische randvoorwaarde (aan de randen BC en B'C). Het invoeren van deze randvoorwaarde gebeurt door de periodiciteit op te leggen aan de hand van de berekende plasmaprofielen in een vorige iteratiestap en wordt daarom de expliciete methode voor de behandeling van periodieke randvoorwaarden genoemd. Met het oog op het behandelen van gelijkaardige sneden in het gesimuleerde gebied van een divertor-Tokamak (aangeduid met EFGG'F'E' op figuur 0.6), werd door Schneider et al. [42] een methode ontwikkeld die tracht om gebieden in de buurt van een snede op een een zelfde numerieke manier te behandelen als de andere gebieden. Deze methode werd ook in de code geïmplementeerd. Hierbij werd vastgesteld dat alhoewel deze laatste methode een betere evaluatie mogelijk maakt van het voldoen van de plasmaparameters aan het stelsel van vergelijkingen, ze veel trager convergeert dan de expliciete methode. Het gebruik van andere randvoorwaarden voor de randen BC en B'C van figuur 0.5 toont aan dat de convergentie van de code zeer sterk afhangt van de formulering van deze randvoorwaarden. Om snellere convergentie te verwezenlijken, kan het aangewezen zijn om eerst met een licht afwijkende formulering van de randvoorwaarde tot een convergerende oplossing te komen. Vervolgens kan men met de gewenste randvoorwaarde verder rekenen.

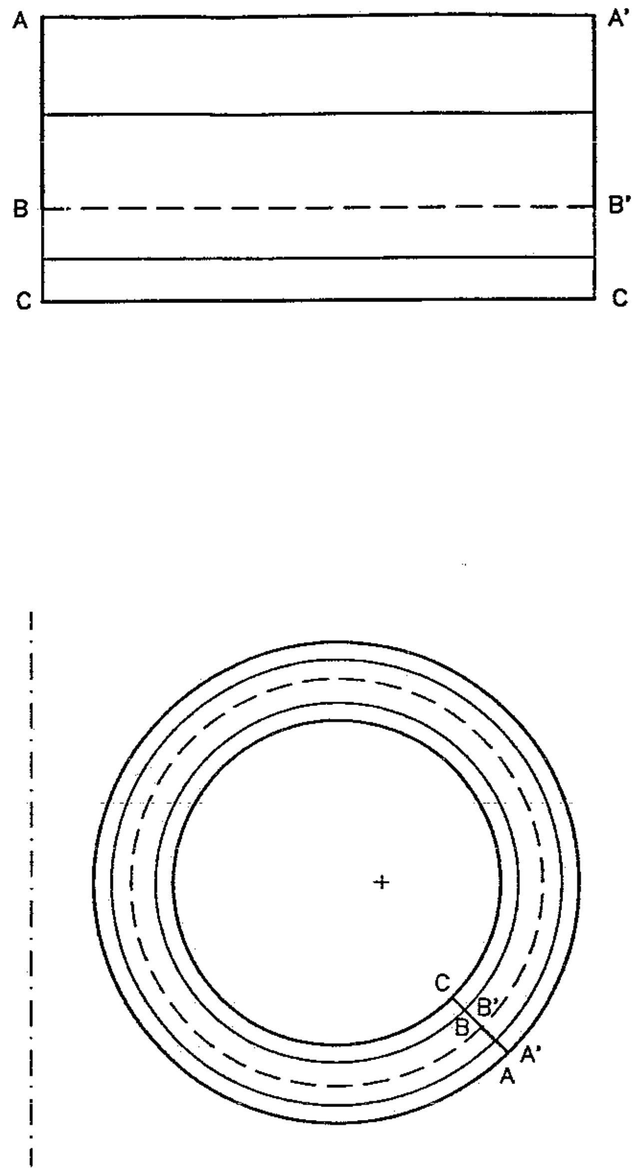

Figuur 0.5: Schematische voorstelling van het numeriek rooster en het werkelijk gesimuleerde gebied voor de limiter-Tokamak TEXTOR

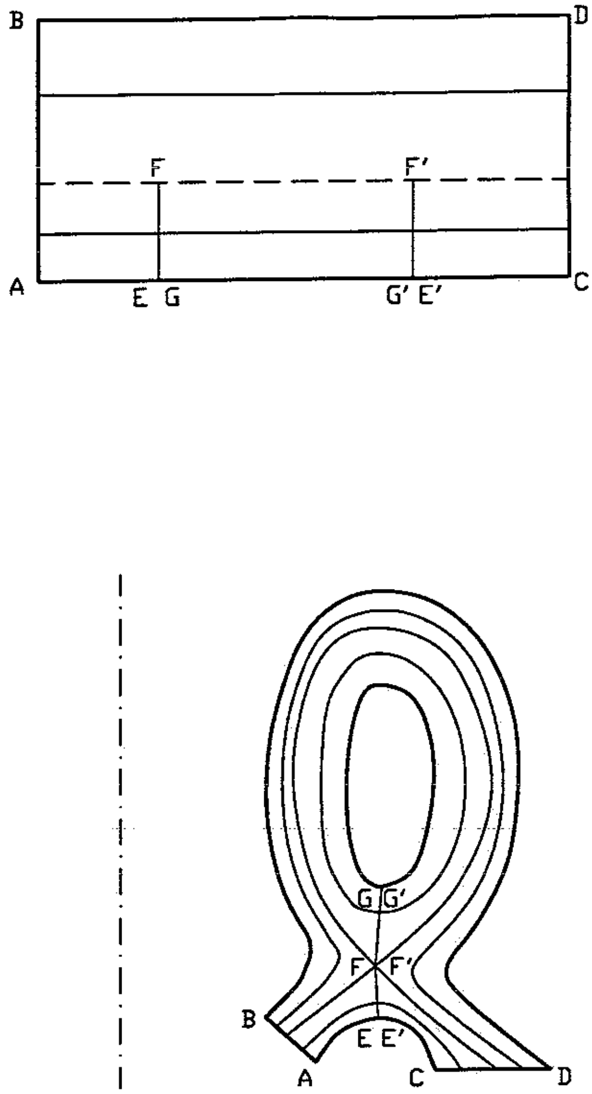

Figuur 0.6: Schematische voorstelling van het numeriek rooster en het werkelijk gesimuleerde gebied voor een divertor-Tokamak

Na de implementatie van de magnetische configuratie en de studie van het invoeren van periodieke randvoorwaarden voor TEXTOR, worden in een tweede toepassing de resultaten vergeleken met deze van een andere randplasma-code SOLXY. Deze code werd ontwikkeld door Gerhauser en Claaßen [15] en is specifiek voor de TEXTOR-geometrie geschreven. Resultaten van deze code werden reeds vergeleken met de resultaten van experimentele data in Ref. [19]. Een voordeel van deze code is dat ze gebaseerd is op een meer uitgebreid model, dat de berekening toelaat van de elektrische stroomdichtheid $\vec{j}$, de elektrische potentiaal Φ en de gemiddelde ionensnelheid in de diamagnetische richting $V_\perp$. De vergelijking van deze twee codes heeft tot doel de invloed van het invoeren van deze bijkomende plasmaparameters na te gaan. Deze studie geeft aanleiding tot volgende aanpassingen en opmerkingen :

1) Uit een eerste vergelijking met de resultaten van de SOLXY code blijkt dat het oorspronkelijke model voor neutrale deeltjes in de B2 code slechte resultaten geeft. Daarom wordt het model voor neutrale deeltjes aangepast. Alhoewel na deze aanpassing de profielen voor de dichtheid van de neutralen overeenstemmen, zijn er nog beduidende verschillen voor de elektronentemperatuur, maar vooral voor de ionentemperatuur (zie figuren 0.7 en 0.8).

2) Een vergelijking van de termen in de energievergelijkingen, brengt het belang van één specifieke term aan het licht ($V_r \frac{\partial p}{h_r \partial u^r}$) ; de zogenaamde vdp-term. Na inbreng van deze vdp-term, wat aanleiding geeft tot een variante van de code B2-vdp, stemmen de plasmaprofielen zeer goed overeen. Figuur 0.9 toont het profiel voor de ionentemperatuur bekomen met de B2-vdp code. Kwantitatief verschillen de resultaten van de SOLXY code en de B2-vdp code nog slechts 6 %.

3) Het feit dat het inbrengen van deze vdp-term tot betere overeenstemming leidt met de resultaten van de SOLXY-code, kan evenwel geen definitief uitsluitsel geven betreffende de noodzaak van het al dan niet invoeren van deze term. Dit komt doordat in de meeste codes, de gemiddelde radiale ionensnelheid wordt vervangen door een veel grotere anomale waarde voor V_r.

4) Uit deze eerste toepassing blijkt dat het model voor de neutrale deeltjes niet voldoet voor om het even welke magnetische configuratie en voor het hele gamma van plasmaparameters. Om toch een goed en betrouwbaar model voor de neutrale deeltjes beschikbaar te hebben, wordt, als onderdeel van dit doctoraatswerk en in samenwerking met Reiter (Forschungszentrum Jülich, Duitsland), de code gekoppeld met de Monte Carlo code EIRENE [20]. Deze code is in staat om het gedrag van neutrale deeltjes in verschillende geometrieën te bestuderen. Alhoewel een simulatie met de gekoppelde codes (B2-EIRENE) meer rekenintensief wordt (een verdubbeling in rekentijd voor toepassingen op TEXTOR), biedt dit pakket van codes een goed hulpmiddel bij het ontwerpen van nieuwe Tokamaks. De gekoppelde versies van de codes worden B2-EIRENE en B2-vdp-EIRENE genoemd, naargelang de vdp-term al dan niet wordt ingevoerd.

In een derde toepassing worden de resultaten van de gewijzigde B2 code vergeleken met gemeten poloïdale asymmetrieën. Het optreden van deze poloïdale asymmetrieën

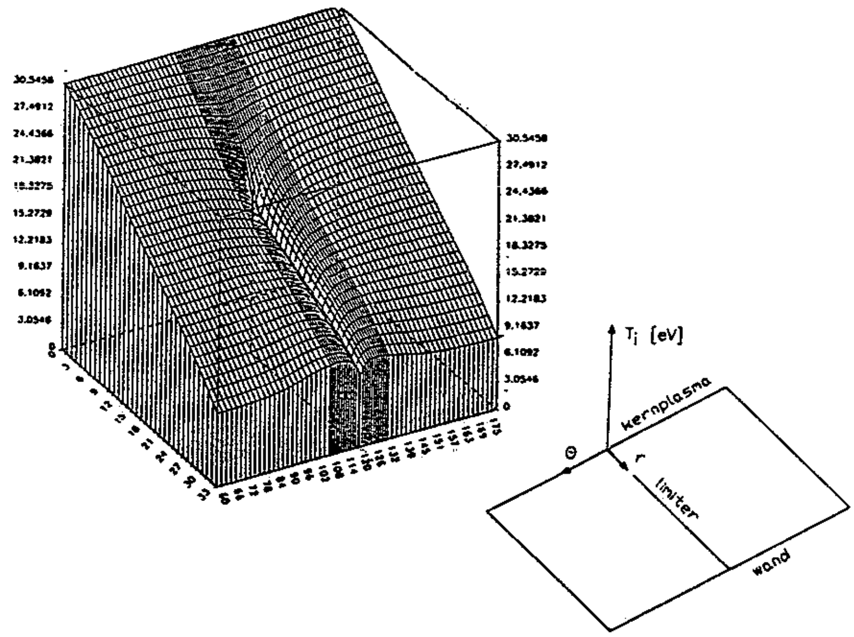

Figuur 0.7: Profiel voor de ionentemperatuur bekomen met SOLXY

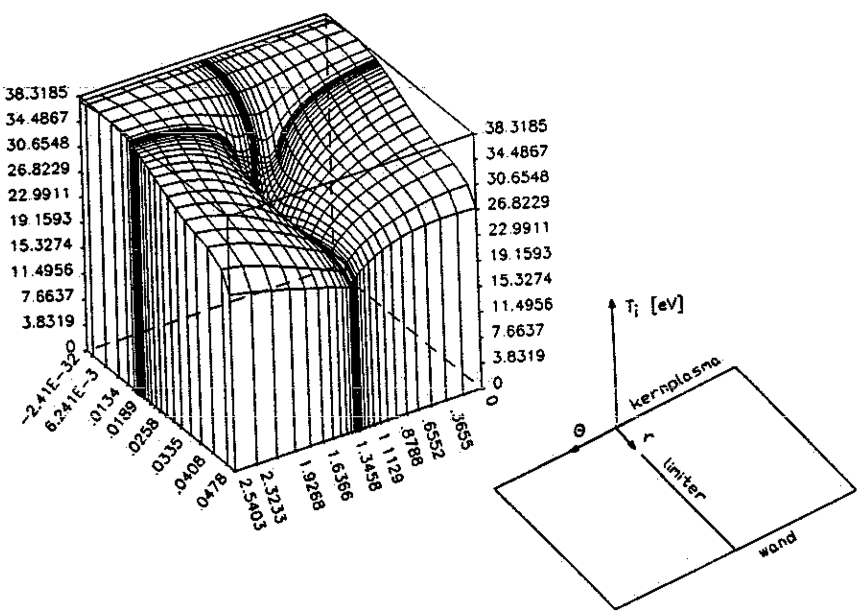

Figuur 0.8: Profiel voor de ionentemperatuur bekomen met B2

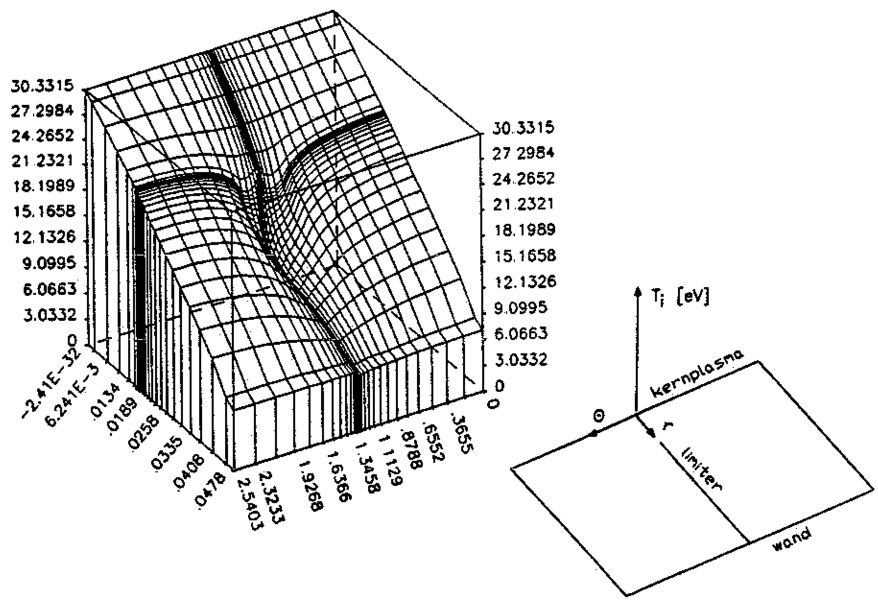

Figuur 0.9: Profiel voor de ionentemperatuur bekomen met B2-vdp

in de randprofielen is van belang voor het bepalen van de optimale plaats voor het wegpompen van neutrale deeltjes, alsook voor het bepalen van de thermische belasting op de verschillende wandmaterialen.

Uit experimentele gegevens voor TEXTOR blijkt dat sommige asymmetrieën niet veranderen bij het ompolen van het toroïdaal magneetveld, terwijl andere asymmetrieën wel beïnvloed worden door de richting van het toroïdaal magneetveld. Hierdoor kan men besluiten dat een poloïdale asymmetrie in plasmaparameters verschillende oorzaken kan hebben. In de eerste plaats kan de positie van de limiter reeds voor bepaalde asymmetrieën zorgen. Verder kan de poloïdale plasmarotatie, ten gevolge van de radiale druk- en potentiaalgradiënten (zie vergelijking (2.97)), een invloed hebben. Voor deze plasmarotatie speelt de richting van het magneetveld een rol. Vermits het model van de oorspronkelijke B2 code deze poloïdale rotatie niet beschrijft, is het duidelijk dat deze laatste asymmetrieën niet kunnen worden gesimuleerd. Voor wat betreft de eerste soort asymmetrieën kan de B2-vdp-EIRENE code de experimentele resultaten voorspellen.

4. Uitbreiding van het fysisch model van de B2-code

Uit de vergelijking van resultaten van de B2-code met SOLXY, blijkt dat het invoeren van elektrische stromen voornamelijk effect heeft op de profielen van de ionen- en elektronentemperatuur. Hoewel invoeren van de vdp-term hierbij aanleiding geeft tot goede overeenstemming met de resultaten van SOLXY, is het meer consistent wanneer deze elektrische stromen en ook de plasmapotentiaal volledig mee bepaald worden.

Het invoeren van stromen en elektrische velden is verder ook interessant om de huidige

"biassing"-experimenten te simuleren. Met deze techniek tracht men een methode te ontwikkelen om de plasmaprofielen in de rand te controleren. Dit gebeurt met het oog op het beïnvloeden van de opsluiting van het kernplasma in het algemeen, en met de controle van de afvoer van deeltjes uit de reactor en van de warmtedepositie op de limiter- en divertorplaten in het bijzonder.
Het model van de B2-code wordt daarom uitgebreid met vijf vergelijkingen ter bepaling van de drie componenten van de elektrische stroomdichtheid $\vec{j}$, de elektrische potentiaal Φ en de component van de gemiddelde ionensnelheid in de diamagnetische richting $V_\perp$. Twee redenen bemoeilijken het numeriek oplossen van het stelsel vergelijkingen voor deze uitbreiding : ten eerste bevatten de bijkomende vergelijkingen kruisafgeleiden en ten tweede moet de potentiaalvergelijking (vergelijking (5.4)) worden opgelost met sterk niet-lineaire randvoorwaarden. Voor het oplossen van de potentiaalvergelijking wordt in dit werk een specifieke methode ontwikkeld die garandeert dat de berekende elektrische potentiaal en vooral de elektrische stroomdichtheid in de parallelle richting, fysisch zinvolle resultaten levert. Naar deze versie van de B2-code wordt gerefereerd onder de naam "extended B2".

De structuur van de vergelijkingen laat toe dat het inbrengen van deze bijkomende plasmaparameters stapsgewijze kan gebeuren :

1) De berekening van $j_\parallel$ en E_θ kan worden ingevoerd zonder de kennis van de andere bijkomende plasma-variabelen. Vermits E_θ gegeven wordt door $-\frac{1}{h_\theta}\frac{\partial\Phi}{\partial u^\theta}$, moet in deze stap de potentiaalvergelijking worden opgelost.

2) De elektrische stroomdichtheid in de diamagnetische richting $j_\perp$ kan berekend worden uit de drukprofielen. Vermits de stroom die hieruit voortkomt niet noodzakelijk divergentievrij is, moeten via de berekening van $j_\parallel$ en E_θ een divergentievrije stroom bekomen worden. Dit houdt een correctie in van stap 1). Vermits deze stroomdichtheid ontstaat ten gevolge van radiale drukgradiënten die ionen en elektronen in tegengestelde richtingen drijven, is het ook wenselijk de component van de gemiddelde ionensnelheid in de diamagnetische richting te implementeren.

3) Voor de berekening van de component van de gemiddelde ionensnelheid in de diamagnetische richting, dient ment het radiaal elektrisch veld te kennen. Dit radiaal elektrisch veld kan eenvoudig berekend worden buiten het laatste gesloten fluxoppervlak. In dit gebied is immers de elektrische potentiaal gekend via de randvoorwaarden aan de limiter- of divertorplaten. Binnen het laatste gesloten fluxoppervlak biedt de oplossing van de potentiaalvergelijking enkel een waarde voor het poloïdaal elektrisch veld E_θ. Ten gevolge van de periodieke randvoorwaarden is de elektrische potentiaal slechts bepaald op een constante na. Daardoor is het radiaal elektrisch veld niet zonder meer gekend, en moet dit worden berekend via de relatie tussen de radiale stroomdichtheid en het radiaal elektrisch veld. Deze relatie is in de neo-klassieke theorie slecht indirect gegeven via twee vergelijkingen ($j_r = f(V_\perp)$ en $V_\perp = g(E_r)$).

Een eerste uitbreiding van de B2 code bestaat dus in de implementatie van de parallelle elektrische stroomdichtheid $j_\parallel$ en het poloïdaal elektrisch veld E_θ. Toepassing van dit

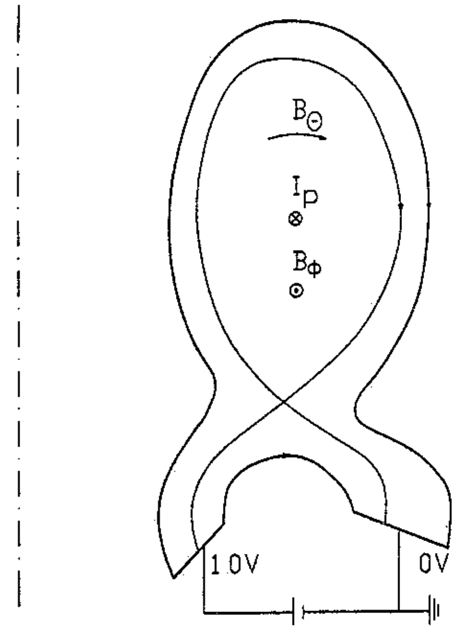

Figuur 0.10· Schematische voorstelling van het gesimuleerde "biassing"-experiment

model voor de divertor-Tokamak ASDEX-Upgrade (Max Planck Institut, Garching bei München, Duitsland), levert volgende resultaten :

1) Kwalitatief stemmen de berekende profielen voor de elektrische stroomdichtheid en de elektrische potentiaal in de "scrape-off layer" overeen met de meetresultaten.

2) De simulatie van een "biassing"-experiment, waarbij een potentiaalverschil van 10 V wordt aangelegd tussen de twee divertorplaten (zie figuur 0.10), toont hoe men de stroom in de "scrape-off layer" van richting kan veranderen. De berekende poloïdale elektrische stroom blijkt echter hoog te zijn in vergelijking met experimentele gegevens. In overeenstemming met de experimentele resultaten, wordt aangetoond dat door "biassing" de thermische belasting van de kathode naar de anode wordt verschoven.

In een volgende stap wordt de code verder uitgebreid met de parameters $j_\perp$, $V_\perp$, j_r en E_r :

1) Deze implementatie geeft evenwel aanleiding tot beduidend lagere convergentiesnelheden. Voor toepassingen op de limiter-Tokamak TEXTOR, wordt de nodige computertijd zelfs onaanvaardbaar lang. Daarom wordt een schatting van de verhouding tussen de gemiddelde ionensnelheid in de diamagnetische richting en de gemiddelde ionensnelheid in de poloïdale richting aan een limiter- of divertorplaat numeriek uitgewerkt voor TEXTOR en ASDEX-Upgrade. Een eenvoudig één-dimensionaal model kan de verschillen tussen deze twee configuraties verklaren. Uit dit model blijkt verder dat de invloed van het inbrengen van de gemiddelde ionensnelheid in de diamagnetische richting verkleint naarmate de lokale "recycling"-coëfficiënt verhoogt. Dit betekent dat in dit opzicht divertor-Tokamaks eenvoudiger te simuleren zijn dan limiter-Tokamaks.

2) Toepassing van de "extended B2" voor de configuratie van ASDEX-Upgrade, levert tijdsafhankelijke oscillaties in plasmadichtheid, plasmapotentiaal en gemiddelde ionensnelheid in de diamagnetische richting in de buurt van het X-punt (zie figuur 0.6). Omdat deze oscillaties zeer lokaal zijn, kan men geloof hechten aan de bekomen resultaten op andere plaatsen van het gesimuleerde gebied.

3) Met de implementatie en toepassing van de "extended B2" komen we in dit werk tot het nieuwe inzicht dat de radiale profielen voor de elektrische potentiaal binnen het laatste gesloten fluxoppervlak berekend kunnen worden in overeenstemming met experimentele gegevens, voor zover rekening wordt gehouden met de viscositeit.

4) Ten gevolge van het inbrengen van plasmastromen in de diamagnetische richting wordt de elektrische stroom zoals berekend in de eerste uitbreiding van de code verder verhoogd. Dit kan verklaard worden aan de hand van de veranderingen in plasmaparameters in de buurt van de divertorplaten. Verder voorspelt de "extended B2", in overeenstemming met metingen, een verhoging van de elektronendruk aan de binnenste divertorplaat.

5. Besluit

In dit werk wordt een bestaande code, "B2", voor het berekenen van het randplasma in een fusiereactor geconfronteerd met data van een experimentele fusiereactor, TEXTOR. Vertrekkende van een neo-klassiek model, dat in deze thesis wordt uitgewerkt voor een algemene geometrie met toroïdale symmetrie, wordt aangetoond dat de veronderstellingen die gemaakt werden in deze code, de verwaarlozing van een belangrijke term in de energievergelijkingen impliceren. Verder wordt ook het eenvoudig model voor de interactie met neutralen verbeterd door de code te koppelen aan een Monte Carlo-code voor het transport van neutrale deeltjes.
Onder impuls van de resultaten van een eerste evaluatie van de code en ten gevolge van de aandacht die in het hedendaags onderzoek uitgaat naar "biassing"-experimenten wordt in dit werk het model van de code uitgebreid. Hierdoor kunnen reeds heel wat fenomenen in verband met elektrische stromen en elektrische velden voor een divertor-Tokamak worden besproken en vergeleken met experimentele gegevens. Omdat voor de limiter-Tokamak de convergentie van de code nog te traag is, zijn simulaties voor deze geometrieën met de uitgebreide code vooralsnog niet haalbaar.
Dit onderzoek leidde reeds tot verschillende publicaties ([42], [52], [66], [112], [113], [114], [115]).

Chapter 1

General introduction

Nuclear fusion is potentially a resource which can provide long-term supply of energy. In order to realize controlled fusion, it is necessary to design a reactor in which the fusion reaction can take place at a rate that guarantees economical operation. The fuel is known to be in the plasma state under such conditions. Ultimately, a practical fusion reactor would operate in an ignited or sub-ignited condition. In the case of an ignited operation, the plasma would be heated by the fusion reactions occurring within it and, once ignited by the initial application of additional heating, no further external heating of the plasma would be required. A sub-ignited condition would require some amount of additional heating throughout operation. This would allow to control reactor conditions with the applied external heating. Research towards the goal of an ignited or sub-ignited operating condition is being carried out in laboratories all over the industrialized world, mainly on devices of the Tokamak type.

This thesis focuses mainly on plasma behaviour in boundary layers of magnetically confined plasmas. Increasing emphasis has been put on edge studies during the last decade, as it became evident that some aspects of Tokamak operations are largely controlled, or even dominated, by edge processes. Therefore, the motivation for this research is to improve understanding of plasma behaviour in general, and edge plasma behaviour in particular, firstly in present experiments, and also to predict edge plasma conditions in future nuclear fusion devices.

In a first section some fundamental concepts and principles of controlled fusion are described. Two different types of plasma confinement concepts which have promising features with regard to the above mentioned goal are outlined in a next section, 1.2. In section 1.3 an introduction to plasma edge phenomena is given. In a last section, 1.4, the outline of the thesis is described.

1.1 Basic principles of controlled fusion

This subsection reviews certain fundamentals of controlled fusion research appearing in much of the introductory fusion literature, e.g. in refs. [1], [2] and [3].

1.1.1 Fusion as a source of energy

The aim of fusion technology is to provide, on earth, a nuclear energy source based on the same physical processes as those which power the sun and the stars. Nuclear energy can be described by Einstein's famous equation $E = mc^2$, which expresses the basic principle that mass m may be converted into an amount of energy E. In this equation $c = 3 \cdot 10^8 m \cdot s^{-1}$ is the speed of light in vacuum. Since the mass of an atom is less than the sum of masses of its components (i.e. protons and neutrons) a so-called mass defect occurs when an atom is build up. This mass defect corresponds with the release of an amount of energy, which is called the binding energy. Figure 1.1 represents the binding energy per nucleon as a function of atomic mass number. The decrease of this function for elements with a mass number greater than ≈ 54 shows that fission of heavy atoms, like uranium, in two similar parts leads to the release of energy. On the other hand, a fusion reaction which combines two light atoms to form a single nucleus, can also produce a certain amount of energy. In this case this is caused by the increase of binding energy per nucleon with increasing mass number.

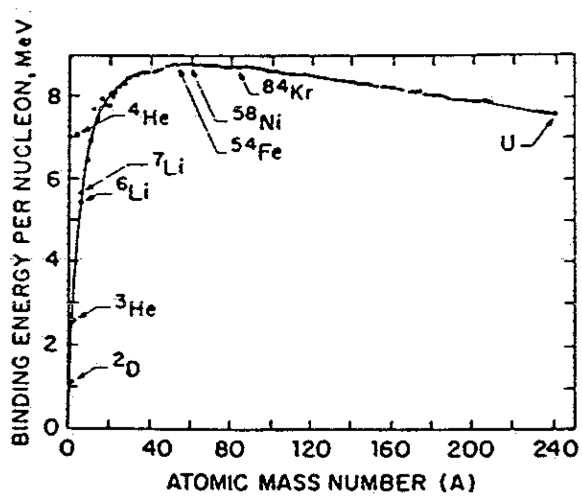

Figure 1.1: Binding energy per nucleon as a function of mass taken from [1]

The reactions of practical use involve the hydrogenic isotopes hydrogen (H or ${}^1_1H$), deuterium (D or ${}^2_1H$) and tritium (T or ${}^3_1H$) as well as the helium isotopes ${}^4_2He$ and ${}^3_2He$ and neutrons n :

$$D + T \longrightarrow {}^4_2He + n + 17.6 \text{ MeV} \tag{1.1}$$
$$D + D \longrightarrow T + {}^1_1H + 4.0 \text{ MeV} \tag{1.2}$$
$$D + D \longrightarrow {}^3_2He + n + 3.3 \text{ MeV} \tag{1.3}$$
$$D + {}^3_2He \longrightarrow {}^4_2He + {}^1_1H + 18.3 \text{ MeV} \tag{1.4}$$

fuel	requirements in tonnes
Coal	2100,000
Oil	1500,000
Fission	150
Fusion	0.6

Table 1.1: Comparison of annual fuel requirements for a 1000 MW electric power plant

The energy is released as kinetic energy of the reaction products. For the first reaction, one fifth of the energy is carried by He and four fifths is carried by the neutrons. This reaction produces an energy amount of 337 MJ per mg fuel.
The annual fuel requirement of a power plant of 1000 MW electric are compared for different types of energy conversion systems in table 1.1.
The table shows that only small amounts of nuclear fuels are needed, relative to traditional fuels like coal and oil. Moreover, deuterium can easily and cheaply be extracted from water, and therefore the available supply of deuterium should suffice for thousands of years. Tritium undergoes a radioactive decay with a half-life of 12.3 years and is therefore not available in nature, while ^3He is stable but extremely scarce. Although the fuel for the $D-D$ reaction is almost inexhaustible, the requirements for the $D-T$ reaction are much less stringent than those for the others. Therefore, this reaction is expected to be utilized in first generation fusion reactors. To this end, tritium can be provided from lithium by the breeding process from fusion neutrons :

$$^7_3Li + n \longrightarrow {}^4_2He + T + n - 2.5\text{MeV} \tag{1.5}$$
$$^6_3Li + n \longrightarrow {}^4_2He + T + 4.8\text{MeV} \tag{1.6}$$

using neutrons from the $D-T$ reactions themselves.
According to Ref. [1] there is enough retrievable lithium to support globalscale fusion energy for several hundred years at least.

1.1.2 Safety and environmental aspects

Since nuclear fusion is based on nuclear reactions, an evaluation of aspects concerning radioactivity is desirable. Although the $D -^3_2 He$ reaction (1.4) does not induce any radioactivity, reactor conditions for this fusion reaction are that stringent that at least for first generation reactors the use of the $D-T$ reaction (1.1) seems to be inevitable. Therefore, safety and environmental aspects of fusion energy are often investigated and compared with those of fission. Whereas fission results in radioactive reaction products, the fusion reaction mainly activates the surrounding material. Therefore, for fusion, the radioactivity problem can be controlled by an optimized choice of reactor materials. In Ref. [4] fusion reactors are compared with fission reactors with identical power and life-time. From this report one can conclude that the nuclear inventory (i.e. the total number of disintegration reactions per second) is much lower in fusion reactors. Especially for volatile elements, which are most important in case of accident, the difference amounts to a factor of seventy five. Therefore, fusion has an important safety advantage in comparison with fission energy production. It should be mentioned that because of the existence of radioactive materials, maintenance operations have to be performed with remote handling. From the point of view of environmental aspects, the production of radioactive structure material leads to nuclear waste. Throughout its life-time, a fusion reactor will produce four times more radioactive volume than a fission reactor with comparable power and life-time [4]. Nevertheless, for a fusion reactor with optimized choice of structure materials, the radioactive inventory reduces with a factor of 10^{-7} in thirty years. In contrast for a fission reactor, the radioactive inventory reduces in the same time only with a factor of 10^{-3}.

1.1.3 Reaction rates and physics requirements for fusion energy production

As the reactants of a fusion reaction are bare nuclei, they must have enough energy to overcome their mutual electric repulsion. Therefore minimum temperatures for nuclear fusion reactions to take place at a sufficiently high reaction rate in a hydrogenic gas are several orders of magnitude higher than those characteristic for atomic processes. The reaction rate of a reaction $A + B \longrightarrow C + D$ can be expressed as :

$$R = -\frac{dn_A}{dt} = -\frac{dn_B}{dt} = \frac{n_A n_B < \sigma v >}{1 + \delta_{AB}} \quad , \tag{1.7}$$

with n_A and n_B the density of species A and B, δ the Kronecker symbol and $< \sigma v >$ the reactivity. This reactivity $< \sigma v >$ in a gas at thermal equilibrium is obtained from the product of the cross-section σ and the relative velocity of the reactants, averaged over a Maxwellian velocity distribution. Figure 1.2 shows the reactivity for three possible fusion reactions. Data for $< \sigma v >$ is obtained from Ref. [5] For the $D - T$ reaction a maximum is obtained at an ion temperature of 10 keV, or about 100 million degrees K (in fusion research, temperatures are generally expressed in energy units; 1 eV corresponds to 1.16×10^4 K approximately). This temperature is high enough for the reactants to be in their fourth state of aggregation, namely in the state of a "fully-ionized plasma".
The fusion power density P_{fus} is :

$$P_{fus} = R\varepsilon \quad , \tag{1.8}$$

with ε the energy released per reaction, e.g. $\varepsilon_{DT} = 17.6$ MeV.
In case of a magnetically confined plasma, the energy carried by neutrons immediately leaves the reactor chamber. The fusion power density deposited in the plasma can therefore be defined as :

$$P'_{fus} = R\varepsilon' \quad , \tag{1.9}$$

with ε' the energy carried by the charged (and thus magnetically confined) reaction products, e.g. $\varepsilon'_{DT} = 3.5$ MeV.
Based on these definitions, some requirements for sustained fusion energy production can be deduced. It is customary to consider these requirements as levels of achievement in fusion energy research.
A first requirement comes from the condition that more energy should be produced by fusion as defined in Eq.(1.8) than is lost by radiation. An inevitable energy loss comes

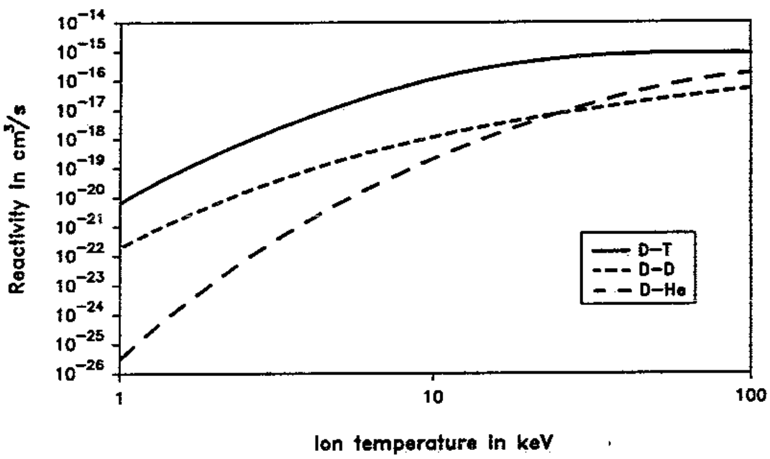

Figure 1.2: $<\sigma v>$for $D-T$, $D-D$ (total) and $D-^3He$ reactions

from the bremsstrahlung, which occurs due to collisions between electrons (e) and ions (i). Assuming that electrons and ions have the same temperature ($T \approx T_i \approx T_e$), the power density of this radiation is given by :

$$P_{rad}\,[\mathrm{W}\cdot\mathrm{m}^{-3}] = 1.6910^{-38}\,Z_i\,(T_e[\mathrm{eV}])^{\frac{1}{2}}\,n_e n_i[\mathrm{m}^{-6}] \tag{1.10}$$

with n_e and n_i respectively the electron and ion density and $n_i = n_A + n_B$. For a $D-T$ reaction this leads to a minimum temperature for ignition of 4.5 keV.
One limiting parameter in a magnetically confined plasma is the plasma pressure $p = nT$. Therefore, the maximum achievable density will tend to scale as T^{-1}. Thus :

$$P_{fus} = \frac{<\sigma v> n_A n_B}{1+\delta_{AB}}\varepsilon \sim \frac{<\sigma v>}{T^2} \quad . \tag{1.11}$$

An optimum temperature for the D-T reaction is typically about 12 keV. Furthermore, for a certain ion density $n_i = n_A + n_B$, maximum power is obtained when $n_A = n_B$.
More stringent conditions follow from some considerations concerning stages of reactor-relevant operation. In this context the concepts of scientific breakeven and ignition are employed.
Scientific breakeven is achieved when the produced fusion power exceeds the power losses in the reactor. With τ_E in a stationary regime defined as the ratio of energy density E to power input, this condition can be written as :

$$P_{fus} \geq \frac{E}{\tau_E} \quad , \tag{1.12}$$

or with the assumptions that $n_D = n_T = n/2$, $n = n_i = n_e$ and $T = T_i = T_e$:

$$\frac{n^2}{4} < \sigma v > \varepsilon_{DT} \geq \frac{3nT[\mathrm{eV}]}{\tau_E} \quad . \tag{1.13}$$

We therefore obtain a condition for $n\tau_E$:

$$n\tau_E \geq \frac{12T[\text{eV}]}{<\sigma v> \varepsilon_{DT}} \quad . \tag{1.14}$$

Ignition is achieved if the fusion power directly captured in the plasma (P'_{fus}) is sufficient to sustain the fusion reaction. This condition is obtained for a $D-T$ reaction, where one fifth of the power is carried by $\alpha-$particles if :

$$n\tau_E \geq \frac{12T[\text{eV}]}{<\sigma v> \varepsilon'_{DT}} = \frac{60T[\text{eV}]}{<\sigma v> \varepsilon_{DT}} \quad . \tag{1.15}$$

These two conditions are represented as a function of the temperature in Fig. 1.3. From this it can be seen that an optimum temperature amounts again about 12 keV.

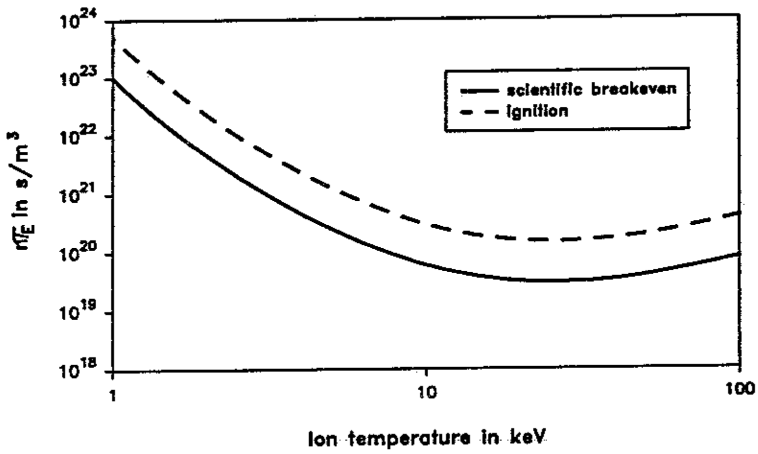

Figure 1.3: Two conditions for reactor-relevant operation.

At the present status of fusion research, the minimum required temperature for nuclear fusion has been attained in JET (the Joint European Torus), which produced with a mixture of $D-T$ an average power of 1MW during about 2 seconds, with a peak of 1.7 MW. Although from expression (1.11) it is clear that a maximum fusion power is obtained when $n_D = n_T = n/2$, in these experiments only 14% tritium was used. Furthermore, conditions close to scientific breakeven for a $D-T$ reaction are obtained in $D-D$ plasmas on the same experimental device. Experiments with full $D-T$ mixtures are planned for 1996. The progress of fusion experiments towards ignition is shown in figure 1.4. Although extrapolation of the data would lead to a reactor working under ignited conditions in about 10 years, realization of such an experimental reactor (ITER, International Thermonuclear Experimental Reactor) is planned to start in 1998.

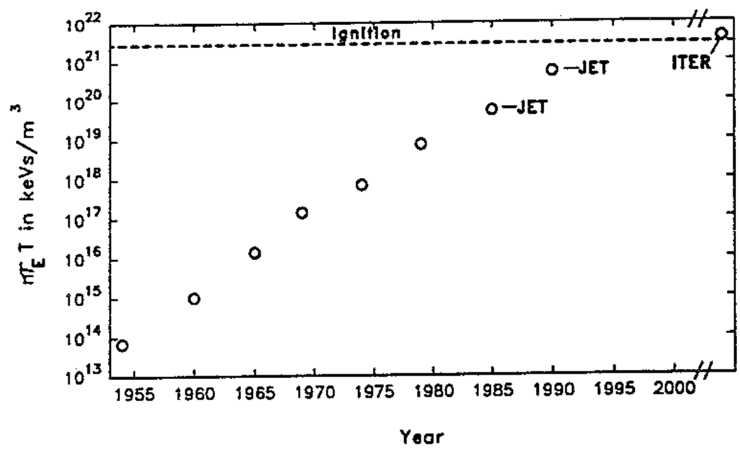

Figure 1.4: Progress in fusion research taken from [6]

1.2 The concept of a Tokamak device

1.2.1 Different approaches to reactor design

The sun fulfils the requirements for fusion reactions by confining itself due to gravitational forces. A similar concept on earth is impossible. One alternative attempt to achieve these conditions makes use of inertial confinement. The fuel injected as small frozen pellets is rapidly heated and compressed using laser or particle beams. Ignition in this case could be fulfilled with high particle densities of $n \approx 10^{32}\mathrm{m}^{-3}$ (10^3 to 10^4 times higher than the normal solid state density of hydrogen), and an energy confinement time between 10 and 100 ps. Thus, the fusion reactor would be driven by a fast sequence of "minute H-bomb explosions". The military aspects and the need for application of the high power laser technology are characteristic for this concept. Most of the research in this field is classified and will not be discussed further in this present work.
An alternative approach is to confine a low-density plasma during a relatively long time with the use of strong magnetic fields. Typical values for $D-T$ plasmas are $T_i \geq 10$ keV, $n \geq 10^{20}\mathrm{m}^{-3}$ and $\tau_E \geq 1$ s. As the Lorentz force $\vec{F} = q\vec{v} \times \vec{B}$ acts on electrically charged particles with charge q and velocity $\vec{v}$, it forces the electrons and ions to gyrate about magnetic field lines. Therefore, a favourable approach in magnetically-confined-fusion reactors is the choice of a toroidal design. It does not suffer from the problem of end losses, which would exist and dominate physics in open magnetic configurations. For these toroidal devices helically-twisted field lines are necessary in order to establish stable plasma configurations.
One particular concept, the "Tokamak device" has so far proved to be the most promising candidate. In this design, the helically-twisted magnetic field lines are obtained by poloidal coils inducing the toroidal component of the field, and a toroidal plasma current, induced by a transformer coil, which produces the poloidal component. The Tokamak up to now has achieved the best plasma conditions, but has the disadvantage of a pulsed

operation mode (in future Tokamaks with periods of about 1 hour), which is necessary to unload the magnetic flux in the transformer. This could be avoided in the so called "Stellarator", where the magnetic field is produced by external coils exclusively. Since no internal currents are induced, the Stellarator has the potential of being less vulnerable to MHD instabilities, i.e. instabilities of magnetic configurations. The concept, however, is not yet developed as far as the Tokamak, due to complex geometrical aspects (e.g. lack of toroidal symmetry).

1.2.2 The Tokamak reactor

The Tokamak is a concept devised and first built in Russia in the late 1950s. From around 1970 the Tokamak was used worldwide in experimental reactor research and has come closest to the requirements for temperature and $n\tau_E$. As in other magnetic fusion devices, confinement of the plasma depends on the fact that electrically charged particles spiral around the magnetic field lines. For stable plasma behaviour the field lines are twisted helically on magnetic flux surfaces. The toroidal component of the magnetic field is induced by poloidal coils, designated as "toroidal field coils", as is shown in figure 1.5. The poloidal component is provided by a toroidal current in the plasma itself, which acts as the secondary winding of a transformer. Besides creating the poloidal component of the magnetic field, this current serves to heat the plasma by ohmic dissipation. Nevertheless, the efficiency of heating the plasma decreases with increasing temperature. Hence the plasma can be heated ohmically to a maximum temperature of about 4 keV only and additional heating is required to achieve higher values. Auxiliary heating can be provided e.g. by the injection of very high energetic particle beams of neutral hydrogen or deuterium atoms, or by electromagnetic waves.

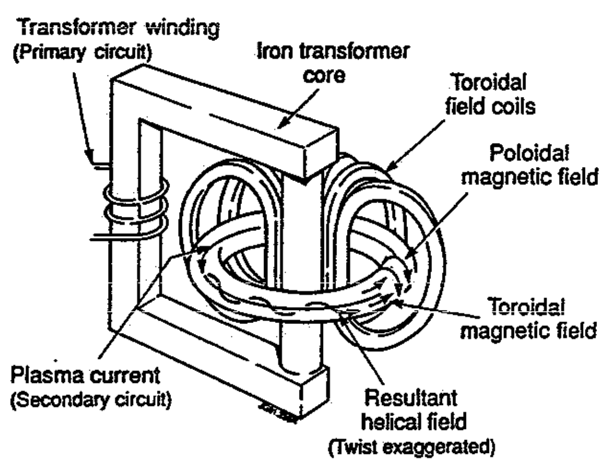

Figure 1.5: Schematic view of a Tokamak

A basic property of the magnetic configuration in a Tokamak is that the field lines lie on magnetic flux surfaces, forming a set of nested toroidal flux surfaces. In the core region, where the nuclear reactions take place, magnetic field lines are either wound infinitely many times in this surface, or close after a finite number of toroidal and poloidal turns.

Due to the very rapid transport of particles, momentum and energy along magnetic field lines in comparison to the radial transport, plasma properties over a magnetic surface will quickly become uniform, in this region. The radial transport is caused by collisions and turbulence phenomena. The latter seem to dominate the radial transport, but are not yet well understood. Outside the last closed flux surface (LCFS), magnetic field lines still lie on magnetic flux surfaces, but now intersect with material boundaries. Physics aspects in this region are totally different, and an introductory discussion will be the subject of section 1.3.

A second property of the magnetic configuration of a Tokamak is based on the safety factor q, which is defined as the number of toroidal turns of a magnetic field line for one poloidal turn. The flux surfaces containing field lines with a rational value of q are called rational flux surfaces. The safety factor at the boundary should be greater than 2 to obtain macroscopic stability. Therefore, the magnetic field pitch p at the edge, which is defined as the ratio of poloidal to toroidal magnetic field $\frac{B_\theta}{B_\phi} \approx \frac{a}{Rq_b}$ (with R the major and a the minor radius and q_b the safety factor at the boundary) is always much less than one.

1.3 The plasma edge

Turning in more detail to the physics aspects of the plasma edge, the region and its specific nomenclature is given in a first subsection. The important role of the plasma edge region in attaining nuclear fusion power is discussed in subsection 1.3.2. Subsequently some methods for influencing and even controlling the edge are described. A recent review on plasma boundary phenomena is given in Ref. [7].

1.3.1 Definition of the plasma edge

In the core region of the plasma, magnetic field surfaces close on themselves. Charged particles move mainly along the magnetic field lines, due to the Lorentz force, and thus are confined on magnetic flux surfaces. This confinement, however, is not perfect, and plasma particles can diffuse by collisions and anomalous transport processes towards the plasma edge. Outside the last closed flux surface (LCFS) or separatrix, the plasma particles principally move along "open" magnetic field lines and will mainly hit intersecting material boundaries (often referred to as "targets" or "target plates"), such as limiters and divertor plates (see section 1.3.3). Ions which reach these boundaries are neutralized and then either absorbed into the material boundary or returned into the plasma. Neutral particles move into the plasma until they are reionized. This process between plasma and neutral particles is called "recycling" and plays a crucial role in edge plasma behaviour. Therefore, the region where this recycling takes place is defined as the plasma edge or boundary plasma (BP). In this context, a recycling coefficient is defined as the ratio between neutral particle flow entering the plasma and ion particle flow reaching the surrounding materials. It should be mentioned that in steady state operation this recycling coefficient equals unity, except when additional pumping ducts are foreseen. However, in edge modelling the recycling coefficient is sometimes redefined as the ratio between neutral particles ionized per second in the described edge region and ion particle flow to the boundary material. This can lead to recycling coefficients significantly less than unity.

The boundary plasma is divided in two zones by the last closed flux surface : the radiating layer (RL) and the scrape-off layer (SOL). The SOL, refers to the region outside of the last closed flux surface, where plasma particles are "scraped" from the core plasma and directed towards the targets. Ion particle flow in this region is determined by two competing processes : a diffusive flow radially outward and a convective flow along the magnetic field lines. The average distance the plasma particles must travel along $\vec{B}$ within the scrape-off layer to reach the material boundary strongly influences the radial plasma profiles and is called the connection length.

Beside the phenomenon of recycling, the ion particle flux towards the material boundaries also induces atoms and molecules of the surrounding material in the plasma. Since they can reach a higher ion charge state, they will radiate more strongly. This phenomenon of radiation often occurs just inside the last closed flux surface. Therefore this region is referred to as the radiating layer. Already a low concentration of these impurities can influence the plasma edge.

1.3.2 Importance of the plasma edge behaviour

Since the plasma edge forms the boundary of the core plasma, it is clear that it will influence the conditions in the core. However, even more important, is its role in particle and energy exhaust. Indeed, both the produced α-particles and the energy they carry, have to be conveyed through the scrape-off layer. One of the most critical problems in developing fusion power reactors for practical operations is to design a system with a plasma-surface interface which can handle the intense, hot plasma exhaust, without interfering with the high temperature conditions needed in the plasma core region to sustain the fusion reactions. Furthermore, the plasma-wall interaction will induce impurities in the plasma. Therefore, it is desirable that scrape-off layer profiles are such that they can prevent that impurities go too far inside the last closed flux surface.

As the magnetic configuration and geometrical details of the plasma chamber strongly affect the edge plasma profiles, their design should directly depend on features of the edge plasma :

1) The power density on the targets must stay below technological limits. Therefore, it is desirable that the power load is spread out radially over the target. The power density profile, however, is determined by the plasma edge profiles which rapidly decrease outside the last closed flux surface (see section 1.3.3).

2) The heat load is not necessary equal on all targets (e.g. on inner and outer target of a divertor, see section 1.3.3), due to poloidal asymmetries in edge plasma profiles.

3) The pressure at the pump entrance determines the pumping efficiency and therefore controls the particle exhaust.

4) Scrape-off layer profiles control the screening efficiency of wall released particles. This means that the purity of the core plasma directly depends on edge plasma physics.

From this one can conclude that, in order to optimize plasma core conditions and to control heat and particle exhaust, it is necessary to understand and even control the plasma edge.

1.3.3 Controlling the plasma edge

In a first subsection the present chamber configurations in the plasma edge region are discussed. Subsequently, wall conditioning and edge biassing as means for controlling the edge plasma, are described.

Different magnetic configurations

The importance of the separatrix or last closed flux surface becomes clear by looking at consequences of open magnetic field surfaces as they occur outside the separatrix. In this region the plasma can flow at high speed to the material boundary, which thus acts as a strong particle and energy sink for the plasma. Therefore, radial density and temperature profiles decrease rapidly outside the LCFS, with decay lengths typically of the order of centimeters. In order to control the edge plasma profiles, the shapes of the magnetic flux surfaces outside the separatrix and of the intersecting material objects have to be optimized.
Basically, two methods are distinguished in Tokamaks in order to minimize damaging effects of plasma-wall interactions. A first method involves a material "limiter", which is introduced in the edge (see figure 1.6). In this case the last closed flux surface (dashed line in figure 1.6) is defined by the position of the limiter tip. These limiters are used successfully in experiments with modest heating power, where the plasma-wall interaction is not a severe problem. It is still an open question whether a limiter configuration will be adequate for future fusion reactors. At present more confidence seems to rest on the "magnetic divertor" concept, although this concept too still has to prove its compatibility with reactor conditions. This method consists of an arrangement of coils such that the magnetic field lines are diverted to special plates or wall areas relatively far from the core plasma (see figure 1.7).

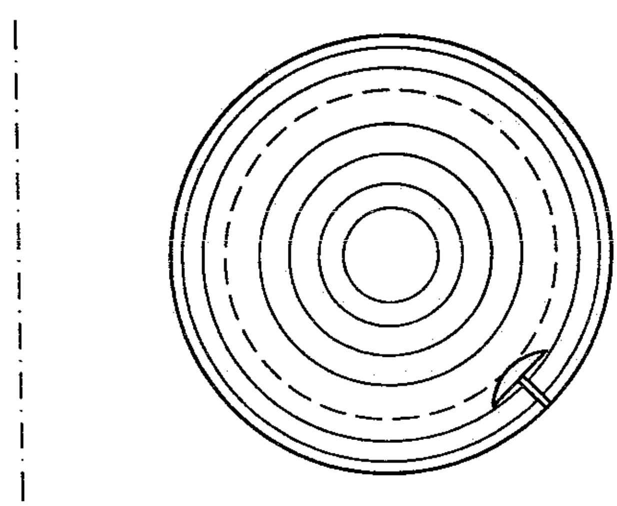

Figure 1.6: Schematic view of the limiter magnetic configuration

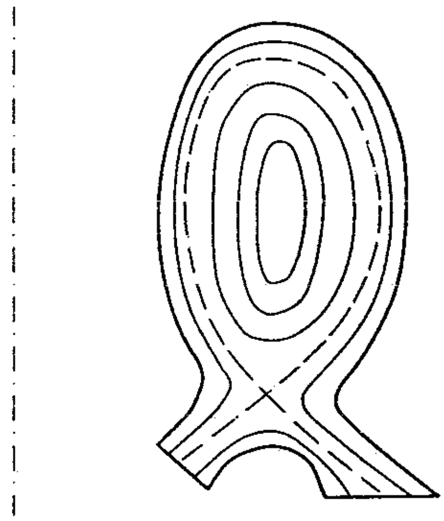

Figure 1.7: Schematic view of the divertor magnetic configuration

Limiter configurations Three configurations of limiters can be distinguished :

1) toroidal limiter : the contact zone in between plasma and limiter is symmetric in the toroidal co-ordinate, i.e. the limiter extends the long way around the torus. This configuration retains the toroidal symmetry of the device.

2) poloidal limiter : one or more rings are introduced in poloidal cross-sections of the Tokamak (i.e. the short way around).

3) local limiters : the plasma is limited by a localized material boundary. In this case there is neither toroidal nor poloidal symmetry.

The strength of a limiter sink is inversely dependent on the connection length. For toroidal and poloidal limiters this distance is well determined and depends on the magnetic field pitch angle, the minor and the major radii of the Tokamak. For a local limiter the connection length will change over the limiter surface.
Limiters are usually constructed so that the magnetic field lines intersect with grazing angle, in order to spread out the particle and energy heat fluxes over a larger area than with normal incidence of the field lines (see figure 1.8). A disadvantage of the shape is that such a limiter will produce impurities which are released in the direction of the main plasma. This, therefore, can lead to a loss of purity and energy content by radiation from inside the last closed flux surface.
Some experimental devices, such as e.g. TEXTOR, have a pumped limiter, which is designed to control the plasma density by pumping out neutralized particles, as will be necessary for helium-ash removal in future Tokamaks. A schematic view of a pumped limiter is given in figure 1.8.
Since the pumping of neutral particles takes place on the outer part of the limiter behind the plasma facing blades, where the density and temperature are already decreased, the

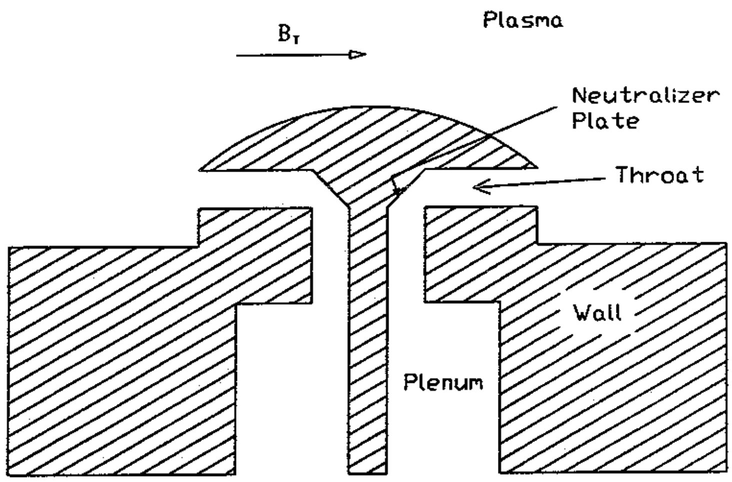

Figure 1.8: Schematic view of a pumped limiter

pumping efficiency of these pumped limiters is very sensitive to the shape of the radial scrape-off layer profiles.

Magnetic divertor configuration As an alternative to the limiter configurations, divertor Tokamaks have become a widely used tool in Tokamak physics. To obtain a poloidal divertor configuration, a coil in the toroidal direction is added with a divertor current I_d parallel to the plasma current I_p (see figure 1.9), which produces a contribution to the poloidal magnetic field. In this way a poloidal magnetic null, which is called the X-point, can be obtained. The magnetic flux surface which goes through the X-point is the last closed flux surface or separatrix. The region beneath the X-point is called the private flux region (PF). The diverted magnetic field lines can be conveyed some distance away from the core plasma, for example into a separate divertor chamber (see figure 1.9). Because of the remoteness of the plasma-wall interactions the main plasma can potentially be cleaner. Another advantage of the divertor configuration is that due to the recycling inside the divertor chamber, higher neutral densities can be obtained, which enhance pumping efficiency. If this high recycling occurs in front of the targets also the ion density increases and the temperature decreases along the magnetic fields towards the plate. This gives rise to the very promising effect of a low plasma temperature at the plate and a high plasma temperature at the separatrix. This high recycling condition in front of the target plate is assumed to be all important for future devices as NET and ITER and will strongly affect their divertor design.

It should be noted that besides the closed divertor configurations (see figure 1.9) with separated divertor chambers, also the open divertor configurations (see figure 1.10) has been investigated (e.g. DIII-D, JET).

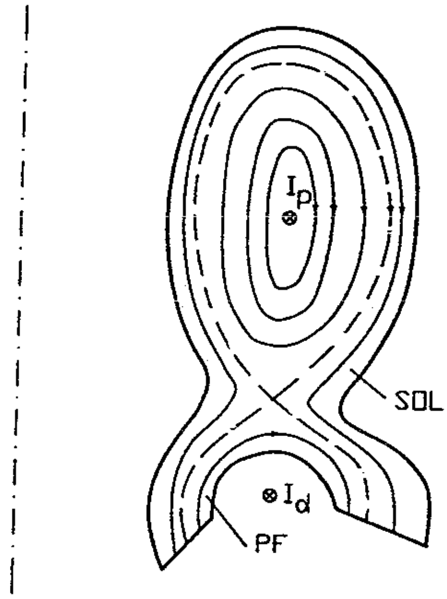

Figure 1.9: A closed divertor configuration

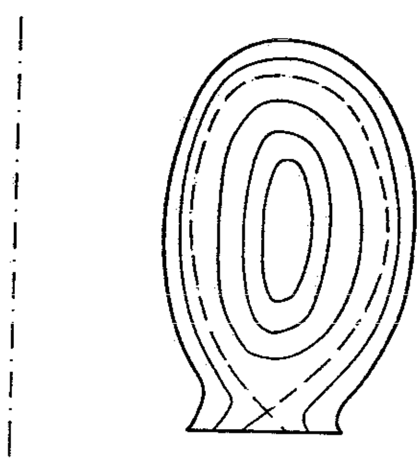

Figure 1.10: An open divertor configuration

Additional methods for controlling the edge

Wall conditioning Wall conditioning methods such as cleaning, carbonization [8], boronization [9], siliconization [10] and gettering, are effective for reducing impurities and controlling recycling. Their effectiveness, however, is transitory and therefore the application of these techniques in long pulse high power conditions still requires further intensive research. However, these methods have already frequently been used in present experiments. Experimental performance of Tokamak behaviour can strongly be influenced by the frequency of wall conditioning.

Biassing and polarization experiments Presently, many experiments are concentrated on the influence of electric fields both in limiter and in divertor Tokamaks. The aim is to find active means to influence edge plasma profiles in order to improve particle and energy exhaust, to control impurity behaviour and to enforce transition into regimes of improved plasma confinement (e.g. the so-called H-mode). This is done by biassing limiters relative to the vacuum vessel, by setting divertor targets at different electric potentials, or by inserting electric probes into the plasma, the so-called polarization experiments [11]. The influence of an induced electric field on plasma confinement is currently an active research topic, and was motivation for a significant fraction of the research concerning edge modelling as presented in this work. A recent review has been given by Weynants and Van Oost [12].

1.4 Outline of the thesis

This thesis is concerned with two-dimensional modelling of the plasma edge. These computational studies cover, in general, the following physical aspects : fluid equations for the plasma (electrons and ions) describing conservation of particles, momentum and electron and ion energy. This information must be supplemented with data concerning neutral particle interactions with the plasma, and the considered magnetic configuration.
Edge modelling in this work is based on a two-dimensional edge plasma code "B2", which is written by Braams [13]. This code starts from an edge model described with a simplified set of the Braginskii equations and has the advantage that it can be applied to different magnetic configurations. Although all 2-d plasma edge codes are currently based on fluid equations with transport coefficients as derived by Braginskii [14], general expressions for these equations written in a curvilinear co-ordinate system assuming toroidal symmetry are not readily available in the literature. One of the contributions of this thesis, is therefore the derivation of such a plasma edge model in toroidal geometry. This will permit us to extend the physics content of the available edge code. In chapter 2, after a short elaboration of the fluid approximation for the boundary plasma of fusion devices, the equations are written in an orthogonal curvilinear co-ordinate system, assuming toroidal symmetry and taking into account the anisotropic behaviour of a plasma confined in a strong magnetic field. Furthermore, standard modifications to the neoclassical theory used in edge modelling are described and a survey of existing codes is given. A description of the B2 code, as available at the beginning of this work, is given in chapter 3.
As part of the thesis, the B2 code is confronted in broad sense with data of the experimental limiter Tokamak device TEXTOR, situated at the Kernforschungsanlage, Jülich

(Germany). In order to perform calculations on the TEXTOR geometry, some adaptations in B2 were needed. The specific limiter geometry (i.e. the specific position of the ALT-limiter) has lead to the investigation and application of periodic boundary conditions. A condition which was thus far never applied in B2.
A comparison with TEXTOR data is partly done by comparing results of B2 with those of a TEXTOR-specific 2-d edge code "SOLXY", which is written by Gerhauser and Claaßen [15]. Results of this code have already been checked against experimental results in Refs. [16]-[18],[19]. The model of this "SOLXY" code is more complete concerning the number of terms kept in the equations, but applications are restricted to TEXTOR-like configurations. From this comparison it can be seen that the assumption of a currentless plasma, mainly affects the temperature profiles. However, only partly implementing the physics of electric currents by introducing just one term in the energy equations of the B2 code can already provide similar results as those of the SOLXY code.
From this first application of B2 to the TEXTOR geometry, it can be seen that the "minimal" model for neutral particle behaviour, as originally incorporated in the code, does not adequately describe neutral particle behaviour for this specific geometry and plasma conditions. Therefore, as a contribution of this thesis, the B2-code was coupled to a Monte Carlo code EIRENE [20] in collaboration with D. Reiter (Forschungszentrum Jülich, Germany). The coupled B2-EIRENE code now permit us to describe both plasma and neutral particle behaviour in a consistent way, for an arbitrary magnetic configuration and chamber geometry with toroidal symmetry. Finally, the code is also confronted with some recent experimental data.
As a consequence of this evaluation and due to the impetus of recent attention paid to biassing and polarization experiments, the code is extended to include drift terms and electric currents. The implementation in B2 of the additional equations, which now have mixed derivatives and which should accommodate non-linear boundary conditions, is described in chapter 5; a survey of the development of 2-d codes including these terms is given.
In chapter 6, the extension of the code is implemented stepwise with different degrees of sophistication. As a first application of this extended code, the influence of parallel electric currents on the divertor configuration of ASDEX-Upgrade (Max-Planck-Institut für Plasmaphysik, Garching bei München, Germany) with grounded and biassed plates is qualitatively compared with experimental data.
Increasing the complexity of the model by implementing flows in the diamagnetic direction, gives rise to very slow convergence. In particular, for the limiter configuration of TEXTOR a converged solution is not yet possible within a realistic computing time. An estimate of the impact of perpendicular flow on the target conditions of the limiter configuration of TEXTOR and of the divertor configuration of ASDEX-Upgrade brings out some differences between these two configurations. Application of the extended B2 code on the divertor configuration is more successful and reveals various physics aspects with respect to drift flows.
In a last chapter the conclusions of this thesis are summarized and suggestions for further research are presented.

Chapter 2

2-D plasma edge model in toroidal geometry

2.1 Introduction

As a description for the plasma edge has to include both transport perpendicular to the magnetic surfaces, which dominates plasma properties inside the last closed flux surface, and parallel transport to the material boundaries in the scrape-off layer, at least a two-dimensional description for edge plasma modelling is required. Although plasma particles -to lowest order- move along the twisted magnetic field lines, a two-dimensional model is based on the toroidal axisymmetrical geometry of Tokamaks. This should result in a two-dimensional edge model which describe the plasma parameters in a poloidal cross-section of the torus. Since such a model is not available in literature, in this work a fluid description for the plasma particles in an orthogonal curvilinear co-ordinate system for a toroidal geometry is derived, starting from the Braginskii equations in vector notation. As the derivation of an edge plasma fluid model in toroidal geometry is essential for interpretation of the physics content of edge codes, and since it provides possibilities for future improvements, this chapter contains theoretical fundamentals for research in plasma edge physics. In a first section, 2.2, the approximation embedded in a fluid description is elucidated and the three typical approaches to describe transport in magnetically confined plasmas are touched upon. The neoclassical equations for the collisional regime are employed in this work and are derived in section 2.3. In a next section the changes to neoclassical transport for edge modelling necessary both to match experimental observations and to render the problem computationally feasible are described. Subsequently, a survey of existing two-dimensional codes is given.

2.2 Use of fluid equations in edge modelling

Without exception, two-dimensional plasma edge models follow the approach of Braginskii [14]. Although the validity of a fluid approach in the boundary layer may be questionable at first sight, a two-dimensional kinetic treatment for charged particles is not yet a reachable alternative. The currently used kinetic codes are usually restricted to a rather simple geometry and developed for specific problems like the electrostatic sheath

and presheath. A survey has been given by Chodura [21]. Therefore, it is necessary to determine the parameters which characterize the validity of the fluid approximation.
For the fluid approach to be valid, the collisionality of a particle should be large, meaning that its mean free path λ should be small in comparison with a typical characteristic length of the device $L_{||}$. The ions and electrons are treated separately, because the electron gas and the ion gas reach separate equilibria in a time scale much shorter than required for the two gases to equilibrate among themselves. Therefore

$$L_{||} \gg v_{th,i}\tau_i \tag{2.1}$$

and

$$L_{||} \gg v_{th,e}\tau_e \tag{2.2}$$

with $L_{||}$ the scale length of variation of the macroscopic plasma parameters (e.g. density n, and temperature T) and the magnitude of the magnetic field B and

$$v_{th,\alpha} = \sqrt{\frac{T_\alpha}{m_\alpha}} \tag{2.3}$$

a measure for the thermal speed of fluid species α with mass m_α. The temperature is -as usual in fusion research- expressed in energy units.
Since τ_e and τ_i are defined as $\tau_e = \frac{1}{<\nu_s^{e,i}>}$ and $\tau_i = \frac{1}{<\nu_s^{i,i}>}$, where $\nu_s^{\alpha,\beta}$ is the slowing down frequency for a test particle α on a Maxwellian background of β-particles as defined in the NRL plasma formulary [22] and where the angular brackets represent averaging over a Maxwellian test particle distribution, the expression for the basic collision times τ_e and τ_i [22] read :

$$\tau_i = 2.09 \cdot 10^{13} \frac{T_i^{3/2}}{n\lambda} \mu^{\frac{1}{2}} \text{ s} \tag{2.4}$$

$$\tau_e = 3.44 \cdot 10^{11} \frac{T_e^{3/2}}{n\lambda} \text{ s.} \tag{2.5}$$

In expressions (2.4) and (2.5) all variables are expressed in S.I. units, except for the temperature which is expressed in eV. Furthermore, μ is the ion mass expressed in units of the proton mass, $\mu = m_i/m_p$ and λ is the Coulomb logarithm.
In order to define $L_{||}$ attention will be paid now to the validity of the fluid equations with respect to the scale length for the magnitude of the magnetic field B. Subsequently, the scale lengths for plasma properties are considered.
The scale length for the magnetic field is defined as $L_{||} = \left|\frac{\nabla_{||}B}{B}\right|^{-1}$ which approximately equals the connection length in the scrape-off layer defined as :

$$L_{||} = \frac{\pi a}{B_\theta / B_\phi} \tag{2.6}$$

with a the minor radius and B_θ and B_ϕ respectively the poloidal and toroidal component of the magnetic field.

For example, in TEXTOR applications, with a minor radius $a \approx 0.5$ m, typical edge plasma values are $n = 10^{18}\mathrm{m}^{-3}$, $T = 10$ eV, $B_\theta/B_\phi = 0.1$ and $\lambda = 13$. For this parameters we obtain for a Deuterium plasma :

$$
\begin{aligned}
L_{\|} &\approx 16 \ \mathrm{m} \quad , \\
v_{th,i} &\approx 20{,}000 \ \mathrm{m/s} \quad , \\
\tau_i &\approx 7.2 \times 10^{-5} \ \mathrm{s} \quad .
\end{aligned}
$$

Hence $v_{th,i}\tau_i \ll 16$ m.
For the electrons, transport is dominated by the tail of the Maxwellian distribution. Therefore, it is more appropriate to use $v_{th,e} = \sqrt{\gamma T_e/m_e}$ with $\gamma \approx 3$ as a measure for the thermal speed :

$$
\begin{aligned}
v_{th,e} &\approx 2.3 \times 10^{6} \ \mathrm{m/s}, \\
\tau_e &\approx 8.4 \times 10^{-7} \ \mathrm{s}
\end{aligned}
$$

Hence $v_{th,e}\tau_e \ll 16$ m.
From this, one can conclude that the plasma in the boundary layer of TEXTOR is likely to be collisional enough for fluid equations to be valid.
However, a related, but quite specific "limitation" of the fluid equations for edge plasma modelling should be mentioned. Whereas the charged particle mean-free-path is usually smaller than the characteristic length for the magnetic field making a fluid description in the edge plasma feasible, the same condition with respect to scale lengths for plasma properties has to be fulfilled. Since, the plasma-metal interface, the sheath, is a collisionless region where steep gradients of density and temperature exists [23], the fluid equations are not expected to describe properly the physics in this region (although fluid treatments do give the proper order of magnitude [23]). In fluid codes, it is customary to take the sheath entrance as the boundary to the computational domain and to impose appropriate boundary conditions (e.g. setting the mach number equal to unity and prescribing energy transfer coefficients). To make sure that the steep gradients to be expected near the sheath entrance do not lead to unphysical results, special measures such as heat flux limiters [24] or a kinetic transition layer [25] are introduced. The determination of the exact boundary conditions at the plate is still an active area of research, reflecting the "tension" between purely theoretical considerations and pragmatic computational approaches [26]. Encouraged by the fact that full fluid treatments in the edge give better results than expected from purely theoretical considerations [27], in this work the pragmatic approach is adapted and "the usual" boundary conditions at the sheath entrance are imposed.

2.3 Braginskii equations in toroidal geometry

2.3.1 Introduction

The moment equations as written down by e.g Braginskii [14] or Hinton [28] have general validity, as they are obtained by integrating the kinetic transport equations. However, when the constitutive relations for the heat flux ($\vec{q} \propto -\vec{\nabla} T$) and the viscosity tensor ($\overleftrightarrow{\Pi} \propto \vec{\nabla}\vec{V}$) are established and hence the transport coefficients are obtained, the above mentioned restriction $\lambda \ll L_{||}$ is invoked, limiting the resulting fluid equations to the high collisionality regime. In their general form, the "Braginskii" equations are applicable to general magnetic geometries. Braginskii himself [14] only wrote the viscosity components in a local Cartesian system; his tensorial expressions were written in terms of arbitrary curvilinear coordinates by Mikhailovskii and Tsypin [29] and in orthogonal curvilinear co-ordinates by Stacey and Sigmar [30]. In principle then, the Braginskii equations contain all necessary information to describe collisionally dominated magnetically confined toroidal plasmas, which result in neoclassical collisionally dominated theory. To describe the low collisionality neoclassical regimes such as the banana and plateau regimes, the equations need to be generalized; this has been done by Hirshman and Sigmar [32]. A review is given by Hinton and Hazeltine [31]. To date, most numerical codes that describe the edge physics phenomena, including the B2 code, which will form the framework for this work, ignore typical neoclassical effects such as drift flows and curvilinear contributions. It is one of the goals of this thesis to extend the validity of the B2 code to include those effects. In this section the 2-D component form of the fluid equations for the scrape-off-layer is derived starting from the classical tensor formulation as given in subsection 2.3.2. In the process of specifying a co-ordinate system to formulate the equations, a choice has to be made between a toroidal-poloidal-radial co-ordinate system (henceforth referred to as "poloidal" system) and a parallel-diamagnetic-radial co-ordinate system (shortened to "parallel" system). Toroidal symmetry is easily imposed in the "poloidal" system, but it is less obvious in parallel co-ordinates aligned with the magnetic field lines. Conversely, the transport equations are closed by defining an anisotropic fluid viscosity and thermal conductivity which are easier specified in a "parallel" co-ordinate system. Historically, "parallel" co-ordinates have been predominant, however, the proper inclusion of diamagnetic motion is likely to force models to adapt to "poloidal" co-ordinates in order to incorporate macroscopic features of the Tokamak physics and boundary conditions. Therefore further attention is devoted to the vector algebra and calculus in curvilinear co-ordinate systems in section 2.3.3. In section 2.3.4, the transformation from a co-ordinate system parallel to the magnetic field to a more computationally convenient poloidal-toroidal co-ordinate system is investigated. Finally the 2-D fluid equations in toroidal geometry are derived in section 2.3.5.

2.3.2 General formulation of the Braginskii equations

As indicated above, the B2 code starts from the Braginskii equations. For further derivations in a toroidal geometry the equations will be written for a simple case in which the plasma consists of electrons and a single ion species with ion charge state Z_i and mass m_i. Furthermore, interactions with neutral particles are incorporated by means of neutral source terms. In order to determine macroscopic plasma properties as density n_α, average

particle velocity $\vec{V}_\alpha$, temperature T_α and electric field $\vec{E}$, a plasma edge model is based on a subset of the following equations, assuming local quasineutrality $n_e = Z_i n_i$:
a) continuity equations for ions

$$\frac{\partial}{\partial t} n_i + \vec{\nabla} \cdot (n_i \vec{V}_i) = S_{n_i} \tag{2.7}$$

and electrons

$$\frac{\partial}{\partial t} n_e + \vec{\nabla} \cdot (n_e \vec{V}_e) = S_{n_e} \tag{2.8}$$

b) momentum equations for ions

$$\begin{aligned} \frac{\partial}{\partial t}\left(m_i n_i \vec{V}_i\right) + \vec{\nabla} \cdot (m_i n_i \vec{V}_i \vec{V}_i) &= -\vec{\nabla} p_i - \vec{\nabla} \cdot \overleftrightarrow{\Pi}_i \\ &\quad + Z_i e n_i (\vec{E} + \vec{V}_i \times \vec{B}) + \vec{R}_i + \vec{S}_{m_i \vec{V}_i} \end{aligned} \tag{2.9}$$

and a simplified momentum equation for electrons

$$-\vec{\nabla} p_e - e n_e (\vec{E} + \vec{V}_e \times \vec{B}) + \vec{R}_e = 0 \tag{2.10}$$

where

$$\vec{R} \equiv \vec{R}_e = -\vec{R}_i = e n_e \left(\frac{\vec{j}_{\|}}{\sigma_{\|}} + \frac{\vec{j}_{\perp}}{\sigma_{\perp}} \right) - 0.71 n_e \vec{\nabla}_{\|} T_e - \frac{3}{2} \frac{e n_e^2}{\sigma_{\perp} B^2} \vec{B} \times \vec{\nabla} T_e \tag{2.11}$$

for single ion fluid species with $Z_i = 1$ [14] .
Equation (2.10) is obtained by neglecting those terms which become small (because $m_e/m_i \ll 1$) in the electron momentum equation. Because this equation bears some similarity to the generalized Ohm's law in plasmas, it is also often quoted under that name.
Sometimes it is more convenient to use the total momentum equation, obtained via summation over all species present :

$$\begin{aligned} &\frac{\partial}{\partial t}\left(m_i n_i \vec{V}_i\right) + \vec{\nabla} \cdot (m_i n_i \vec{V}_i \vec{V}_i) = \\ &\qquad -\vec{\nabla} p - \vec{\nabla} \cdot \overleftrightarrow{\Pi}_i + \vec{j} \times \vec{B} + \vec{S}_{m_i \vec{V}_i} \end{aligned} \tag{2.12}$$

c) energy equations for ions

$$\begin{aligned} \frac{\partial}{\partial t}\left(\frac{3}{2} n_i T_i + \frac{m_i n_i}{2} \vec{V}_i^2\right) + \vec{\nabla} \cdot \left[\left(\frac{5}{2} n_i T_i + \frac{m_i n_i}{2} \vec{V}_i^2\right) \vec{V}_i + \overleftrightarrow{\Pi}_i \cdot \vec{V}_i + \vec{q}_i\right] &= \\ \left(e n_i Z_i \vec{E} - \vec{R}\right) \cdot \vec{V}_i - Q_{ei} + S_E^i & \end{aligned} \tag{2.13}$$

and again a simplified form for electrons

$$\frac{\partial}{\partial t}\left(\frac{3}{2} n_e T_e\right) + \vec{\nabla} \cdot \left(\frac{5}{2} n_e T_e \vec{V}_e + \vec{q}_e\right) = -e n_e \vec{E} . \vec{V}_e + \vec{R} \cdot \vec{V}_i + Q_{ei} + S_E^e \tag{2.14}$$

with

$$\vec{q}_i = -\kappa^i_{\parallel}\nabla_{\parallel}T_i - \kappa^i_{\perp}\nabla_{\perp}T_i + \kappa^i_{\wedge}\frac{\vec{B}}{B}\times\vec{\nabla}_{\perp}T_i \tag{2.15}$$

and if $Z_i = 1$

$$\vec{q}_e = -\kappa^e_{\parallel}\nabla_{\parallel}T_e - \kappa^e_{\perp}\nabla_{\perp}T_e - \kappa^e_{\wedge}\frac{\vec{B}}{B}\times\vec{\nabla}_{\perp}T_e - 0.71\frac{T_e}{e}\vec{j}_{\parallel} - \frac{3}{2}\frac{T_e}{e\omega_e\tau_e B}\vec{B}\times\vec{j}_{\perp} \tag{2.16}$$

and

$$Q_{ei} = \frac{3m_e}{m_i}\frac{n_e}{\tau_e}(T_i - T_e) \tag{2.17}$$

where

$$\begin{aligned}
S_{n_\alpha}, S_{m_\alpha\vec{V}_\alpha}, S_E^\alpha &= \textit{volume sources of particles, momentum and} \\
&\quad\ \textit{energy for particle species } \alpha \\
\overleftrightarrow{\Pi} &= \textit{viscosity tensor} \\
\sigma_{\parallel}, \sigma_{\perp} &= \textit{classical electrical conductivities} \\
\kappa^\alpha_{\parallel}, \kappa^\alpha_{\perp}, \kappa^\alpha_{\wedge} &= \textit{classical thermal conductivities} \\
&\quad\ \textit{for particle species } \alpha \\
\omega_e &= \textit{electron gyrofrequency} \\
\tau_e &= \textit{basic collisional time for electrons.}
\end{aligned}$$

Auxiliary physical quantities are the electron and ion pressures,

$$p_e = n_e T_e, p_i = n_i T_i \quad ; \tag{2.18}$$

the total pressure,

$$p = p_e + p_i \quad ; \tag{2.19}$$

and the electric current density,

$$\vec{j} = e(Z_i n_i \vec{V}_i - n_e \vec{V}_e) \quad . \tag{2.20}$$

2.3.3 Use of physical components in a curvilinear co-ordinate system

The fundamental treatment concerning vector algebra and calculus in curvilinear co-ordinates makes use of the mathematical formalism of covariant A_α and contravariant A^α components of a vector $\vec{A}$ (as described e.g. by D'haeseleer et al. [33]). For physical applications in orthogonal systems, one rather is interested in the use of **physical** components, which are determined as the real length of the orthogonal projection of a vector in the direction along the co-ordinate curves. In this chapter the physical components are designated with the symbol $\tilde{}$, and relate to the co- and contravariant components as $\tilde{A}_\alpha = h_\alpha A^\alpha = A_\alpha / h_\alpha$, with h_α the modulus of the corresponding tangent-basis vector.

It is then convenient to define some sort of modified Christoffel symbols [30], so as to keep a form-similarity of the expressions. To clarify this potentially confusing issue, firstly the expressions for the tensorial components for the gradient of a vector and the vector components for the divergence of a tensor are considered, employing the proper Christoffel symbols [33] and the "modified Christoffel symbols" [30]. Details of the derivation of these formulae can be found in appendix A.

The gradient of a vector or the dyad $\vec{\nabla}\vec{A}$

As shown in appendix A, the dyad $\vec{\nabla}\vec{A}$, or the gradient of a vector $\vec{A}$, has the following contravariant components in a general curvilinear co-ordinate system (u^1, u^2, u^3) :

$$\left(\vec{\nabla}\vec{A}\right)^{\alpha\beta} = g^{\alpha j}\left(\frac{\partial}{\partial u^j}A^\beta + A^i \left\{ \begin{array}{c} \beta \\ ij \end{array} \right\}\right) \tag{2.21}$$

in which the $g^{\alpha j}$ are the contravariant components of the metric tensor [33]. The symbol with curly brackets is the Christoffel symbol of the second kind :

$$\left\{ \begin{array}{c} \beta \\ ij \end{array} \right\} = \frac{1}{2}g^{\beta k}\left(\frac{\partial g_{kj}}{\partial u^i} + \frac{\partial g_{ki}}{\partial u^j} - \frac{\partial g_{ij}}{\partial u^k}\right) \quad . \tag{2.22}$$

In these expressions summation over repeated symbols i, j, k is understood.
In orthogonal systems the cross metric coefficients g^{ij} and g_{ij} vanish for $i \neq j$, and the Christoffel symbols acquire simple values. It is shown in appendix A that for orthogonal systems, the physical component for $\vec{\nabla}\vec{A}$ in terms of the physical components of the vector $\vec{A}$, defined as $\tilde{A}_\alpha \equiv h_\alpha A^\alpha \equiv A_\alpha / h_\alpha$, can be expressed as

$$\begin{aligned} \left(\widetilde{\vec{\nabla}\vec{A}}\right)_{\alpha\beta} &= h_\alpha h_\beta \left(\vec{\nabla}\vec{A}\right)^{\alpha\beta} \\ &= \frac{\partial \tilde{A}_\beta}{h_\alpha \partial u^\alpha} + \sum_k \tilde{A}_k \Gamma^\alpha_{\beta k} \quad . \end{aligned} \tag{2.23}$$

Here, the symbols $\Gamma^\alpha_{\beta\gamma}$ are given by the expression

$$\Gamma^\alpha_{\beta\gamma} = \delta^\alpha_\beta \frac{\partial \ln h_\alpha}{h_\gamma \partial u^\gamma} - \delta^\alpha_\gamma \frac{\partial \ln h_\alpha}{h_\beta \partial u^\beta} \quad . \tag{2.24}$$

Because of the similarity of Eq.(2.23) with Eq.(2.21), the $\Gamma^\alpha_{\beta\gamma}$ symbols could also be referred to as "modified Christoffel symbols". However, the proper Christoffel symbols $\left\{ \begin{array}{c} \beta \\ ij \end{array} \right\}$ and the $\Gamma^\alpha_{\beta\gamma}$ symbols have quite different properties.

$\left[\widetilde{div(\vec{A}\vec{B})}\right]_l$ for physical components

As derived in appendix A, the divergence of a dyad $\vec{A}\vec{B}$ in physical components can be written as :

$$\begin{aligned}
\left[\vec{\nabla}\cdot\widetilde{\left(\vec{A}\vec{B}\right)}\right]_l &= \sum_i \frac{1}{\sqrt{g}}\frac{\partial}{\partial u^i}\left(\frac{\sqrt{g}}{h_i}\tilde{A}_i\tilde{B}_l\right) + \sum_i\sum_k \tilde{A}_i\tilde{B}_k\Gamma^i_{lk} \\
&= \sum_i \frac{1}{\sqrt{g}}\frac{\partial}{\partial u^i}\left(\frac{\sqrt{g}}{h_i}\tilde{A}_i\tilde{B}_l\right) \\
&\quad +\tilde{B}_\beta\left(\tilde{A}_\alpha\frac{\partial \ln h_\alpha}{h_\beta \partial u^\beta} - \tilde{A}_\beta\frac{\partial \ln h_\beta}{h_\alpha \partial u^\alpha}\right) \\
&\quad +\tilde{B}_\gamma\left(\tilde{A}_\alpha\frac{\partial \ln h_\alpha}{h_\gamma \partial u^\gamma} - \tilde{A}_\gamma\frac{\partial \ln h_\gamma}{h_\alpha \partial u^\alpha}\right) \quad .
\end{aligned} \tag{2.25}$$

The components of the vector product

Given that the expression for the vector product in contravariant components is [33]

$$(A\times B)^k = \frac{1}{J}\left(A_iB_j - A_jB_i\right) \tag{2.26}$$

with $J \equiv \sqrt{g} = \sqrt{g_{\alpha\alpha}g_{\beta\beta}g_{\gamma\gamma}} = h_\alpha h_\beta h_\gamma$ the Jacobian of the metric matrix, one can easily obtain that

$$\left(\widetilde{A\times B}\right)_k = \frac{h_k}{\sqrt{g}}\left(\tilde{A}_i\tilde{B}_jh_ih_j - \tilde{A}_j\tilde{B}_ih_ih_j\right) = \tilde{A}_i\tilde{B}_j - \tilde{A}_j\tilde{B}_i \quad . \tag{2.27}$$

2.3.4 Consequences of a co-ordinate transformation from the basic transport directions to a poloidal co-ordinate system

As the three characteristic directions of the plasma motion are directed parallel to the magnetic field $\vec{B}$ ($\|$), perpendicular to $\vec{B}$ in the magnetic flux surface ($\perp$), henceforth referred to as the diamagnetic direction, and "radial" or normal to the flux surface (r), the components of the velocity are best resolved in this orthogonal co-ordinate system. On the other hand, the toroidal symmetry of a Tokamak allows one to describe the plasma with a two- dimensional model using an orthogonal poloidal-radial co-ordinate system (θ, r), with the toroidal co-ordinate ϕ ignorable (this co-ordinate system will henceforth be referred to as "poloidal" co-ordinate system). Therefore a non-linear co-ordinate transformation is required, as will be described in a first subsection. In a next subsection we examine the implications for the vector notations. Finally, the use of derivatives is discussed.

The two sets of tangent-basis vectors

The poloidal co-ordinate system (u^θ, u^r, u^ϕ) is determined by a family of co-ordinate curves on the magnetic flux surface in the poloidal plane, a second family of curves normal to the flux surfaces, and a family of toroidal co-ordinate curves (see figure 2.1). The parallel-diamagnetic-radial system or shortened to "parallel" system $(u^{\|}, u^{\perp}, u^r)$, on the other hand, is defined by the requirement that the first co-ordinate is along the magnetic field, the second is located on the flux surfaces but perpendicular to the first one and the third family of co-ordinate curves is normal to the flux surfaces (see figure 2.1). By use of these definitions the tangent-basis vectors of a parallel co-ordinate system can be written as functions of those of a poloidal system.

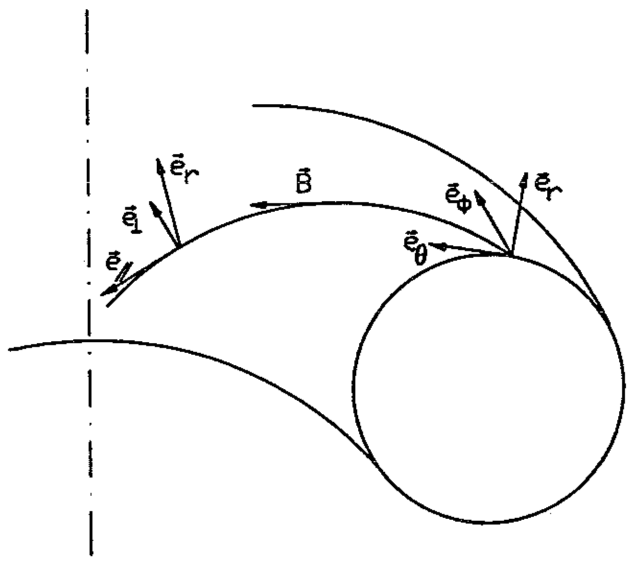

Figure 2.1: Two basic co-ordinate systems for Tokamak applications

For the parallel tangent basis vector this leads to

$$\vec{B} \equiv B^{\parallel}\vec{e}_{\parallel} = B^{\theta}\vec{e}_{\theta} + B^{\phi}\vec{e}_{\phi} \tag{2.28}$$

or with physical components for $\vec{B}$

$$\frac{\tilde{B}}{h_{\parallel}}\vec{e}_{\parallel} = \frac{\tilde{B}_{\theta}}{h_{\theta}}\vec{e}_{\theta} + \frac{\tilde{B}_{\phi}}{h_{\phi}}\vec{e}_{\phi} \quad . \tag{2.29}$$

The diamagnetic tangent basis vector is perpendicular to the parallel basis vector and directed tangent to the flux surface, which means that it can be expressed as a linear combination of the poloidal and toroidal tangent-basis vectors of the poloidal system :

$$\vec{e}_{\perp} = X\vec{e}_{\theta} + Y\vec{e}_{\phi} \tag{2.30}$$

and

$$\vec{e}_{\parallel} \cdot \vec{e}_{\perp} = 0 \quad . \tag{2.31}$$

This leads to

$$h_{\perp}^{2} = (Xh_{\theta})^{2} + (Yh_{\phi})^{2} \tag{2.32}$$

and

$$\frac{\tilde{B}_\theta}{h_\theta} X h_\theta^2 + \frac{\tilde{B}_\phi}{h_\phi} Y h_\phi^2 = 0 \quad . \tag{2.33}$$

And after a choice for the direction of $\vec{e}_\perp$ we find

$$\vec{e}_\perp = \frac{h_\perp \tilde{B}_\phi}{h_\theta \tilde{B}} \vec{e}_\theta - \frac{h_\perp \tilde{B}_\theta}{h_\phi \tilde{B}} \vec{e}_\phi \quad . \tag{2.34}$$

The third tangent basis vector is directed normal to the magnetic flux surface and is taken equal to the second tangent basis vector of the poloidal co-ordinate system.

Vector relations

A vector $\vec{A}$ can be written in both co-ordinate systems

$$A^\theta \vec{e}_\theta + A^\phi \vec{e}_\phi + A^r \vec{e}_r = A^{||} \vec{e}_{||} + A^\perp \vec{e}_\perp + A^r \vec{e}_r \quad . \tag{2.35}$$

With the use of the co-ordinate transformation as defined by Eqs. (2.29) and (2.34) this results in

$$A^\theta = \frac{\tilde{B}_\theta h_{||}}{\tilde{B} h_\theta} A^{||} + \frac{\tilde{B}_\phi h_\perp}{\tilde{B} h_\theta} A^\perp \quad ; \tag{2.36}$$

$$A^\phi = \frac{\tilde{B}_\phi h_{||}}{\tilde{B} h_\phi} A^{||} - \frac{\tilde{B}_\theta h_\perp}{\tilde{B} h_\phi} A_\perp \tag{2.37}$$

or in physical co-ordinates

$$\tilde{A}_\theta = \frac{\tilde{B}_\theta}{\tilde{B}} \tilde{A}_{||} + \frac{\tilde{B}_\phi}{\tilde{B}} \tilde{A}_\perp \quad ; \tag{2.38}$$

$$\tilde{A}_\phi = \frac{\tilde{B}_\phi}{\tilde{B}} \tilde{A}_{||} - \frac{\tilde{B}_\theta}{\tilde{B}} \tilde{A}_\perp \tag{2.39}$$

and, conversely,

$$\tilde{A}_{||} = \frac{\tilde{B}_\theta}{\tilde{B}} \tilde{A}_\theta + \frac{\tilde{B}_\phi}{\tilde{B}} \tilde{A}_\phi \quad ; \tag{2.40}$$

$$\tilde{A}_\perp = \frac{\tilde{B}_\phi}{\tilde{B}} \tilde{A}_\theta - \frac{\tilde{B}_\theta}{\tilde{B}} \tilde{A}_\phi \quad . \tag{2.41}$$

Differentiation concepts

In this section we consider the differentiation of scalar functions, vectors and tensors [33] in order to transform them from one curvilinear co-ordinate system to another. Therefore we will start again from the formalism of curvilinear co-ordinates, using co- and contra-variant components of a vector, and then specialise to orthogonal systems with physical components.

Gradient of a scalar function Let $\Phi\left(u^\theta, u^r, u^\phi\right) = \Phi\left(u^{\|}, u^{\perp}, u^r\right)$ be a scalar function and $\vec{A} = \vec{\nabla}\Phi$ the gradient of this function. Then one can write according to the definition of the gradient operator that the covariant component of vector $\vec{A}$ equals

$$A_i = \frac{\partial \Phi}{\partial u^i} \quad . \tag{2.42}$$

With the use of Eqs. (2.40) and (2.41), $\tilde{A}_i = \frac{A_i}{h_i}$ and assuming toroidal symmetry this results in

$$\frac{\partial \Phi}{h_{\|}\partial u^{\|}} = \frac{\tilde{B}_\theta}{\tilde{B}} \frac{\partial \Phi}{h_\theta \partial u^\theta} \quad , \tag{2.43}$$

$$\frac{\partial \Phi}{h_{\perp}\partial u^{\perp}} = \frac{\tilde{B}_\phi}{\tilde{B}} \frac{\partial \Phi}{h_\theta \partial u^\theta} \quad . \tag{2.44}$$

Divergence of a vector For the divergence of a vector and for derivatives of vectors in general it is important to take into account the differentiation of the basis vectors. The divergence of a vector can be derived in a general curvilinear co-ordinate system as

$$\vec{\nabla} \cdot \vec{A} = \frac{\partial A^k}{\partial u^k} + \left(\vec{\nabla} \cdot \vec{e}_i\right) A^i \quad . \tag{2.45}$$

Here the Einstein convention is used and

$$\vec{\nabla} \cdot \vec{e}_i = \frac{1}{\sqrt{g}} \frac{\partial}{\partial u^i} \sqrt{g} \quad . \tag{2.46}$$

This results in

$$\vec{\nabla} \cdot \vec{A} = \frac{1}{\sqrt{g}} \frac{\partial}{\partial u^i} \sqrt{g} A^i \tag{2.47}$$

or in physical co-ordinates

$$\vec{\nabla} \cdot \vec{A} = \frac{1}{\sqrt{g}} \frac{\partial}{\partial u^i} \frac{\sqrt{g}}{h_i} \tilde{A}_i \quad . \tag{2.48}$$

Gradient of a vector and divergence of a tensor Similar to the derivation of a divergence of a vector, there are no general rules to transform a derivative from one co-ordinate system into another. Therefore whenever a differentiation of a vector or a tensor is necessary, one first has to consider the specific co-ordinate system for differentiation. Vector components can then be transformed readily from one system to the other using the vector relations as described in section 2.3.2. and similar relations can be obtained for tensor components.

2.3.5 Tokamak edge model : Braginskii equations along the basic transport directions in toroidal geometry

Recalling the general formulation of the neoclassical equations as they are given in section 2.3.2, the fluid equations will now be derived in a poloidal co-ordinate system. For the computational description of transport in the edge plasma on orthogonal grids, we are interested in the physical components of the velocity rather than the co- or contravariant components; therefore we will use the expressions as derived in section 2.3.3. As the momentum equations are projected on the directions of the tangent-basis vectors of the parallel co-ordinate system, the derivation of these equations is somewhat more extensive, using the concepts of a co-ordinate transformation as described in section 2.3.4. The ion velocity $\vec{V}_i$ and the electric current density $\vec{j}$ will be described with notations for physical components $(\tilde{V}_\theta, \tilde{V}_r, \tilde{V}_\phi)$ and $(\tilde{j}_\theta, \tilde{j}_r, \tilde{j}_\phi)$ respectively in the poloidal co-ordinate system and with notations $(\tilde{V}_{||}, \tilde{V}_\perp, \tilde{V}_r)$ and $(\tilde{j}_{||}, \tilde{j}_\perp, \tilde{j}_r)$ respectively in the parallel co-ordinate system.

a) Continuity equations

a.1) Continuity equation for the ions Recalling the general formulation, Eq. (2.7), and using Eq. (2.47), the continuity equation becomes

$$\begin{aligned}\frac{\partial n_i}{\partial t} + \frac{1}{\sqrt{g}}\frac{\partial}{\partial u^\theta}\left(\frac{\sqrt{g}}{h_\theta} n_i \tilde{V}_{i,\theta}\right) &+ \frac{1}{\sqrt{g}}\frac{\partial}{\partial u^r}\left(\frac{\sqrt{g}}{h_r} n_i \tilde{V}_{i,r}\right) \\ &+ \frac{1}{\sqrt{g}}\frac{\partial}{\partial u^\phi}\left(\frac{\sqrt{g}}{h_\phi} n_i \tilde{V}_{i,\phi}\right) = S_{n_i} \quad .\end{aligned} \tag{2.49}$$

Assuming toroidal symmetry this leads to

$$\frac{\partial n_i}{\partial t} + \frac{1}{\sqrt{g}}\frac{\partial}{\partial u^\theta}\left(\frac{\sqrt{g}}{h_\theta} n_i \tilde{V}_{i,\theta}\right) + \frac{1}{\sqrt{g}}\frac{\partial}{\partial u^r}\left(\frac{\sqrt{g}}{h_r} n_i \tilde{V}_{i,r}\right) = S_{n_i} \quad . \tag{2.50}$$

a.2) Total continuity equation The particle sources induced by interactions with neutrals are equal for ions and electrons. Therefore subtracting the electron continuity equation from the ion continuity equation, assuming local charge neutrality $n_e = Z_i n_i$, results in the current continuity equation

$$\frac{1}{\sqrt{g}}\frac{\partial}{\partial u^\theta}\left(\frac{\sqrt{g}}{h_\theta}\tilde{j}_\theta\right) + \frac{1}{\sqrt{g}}\frac{\partial}{\partial u^r}\left(\frac{\sqrt{g}}{h_r}\tilde{j}_r\right) = 0 \tag{2.51}$$

where $\vec{j} = e\left(Z_i n_i \vec{V}_i - n_e \vec{V}_e\right)$.
When charge neutrality is not assumed the total continuity equation results in

$$\frac{\partial \rho}{\partial t} + \frac{1}{\sqrt{g}}\frac{\partial}{\partial u^\theta}\left(\frac{\sqrt{g}}{h_\theta}\tilde{j}_\theta\right) + \frac{1}{\sqrt{g}}\frac{\partial}{\partial u^r}\left(\frac{\sqrt{g}}{h_r}\tilde{j}_r\right) = 0 \tag{2.52}$$

with

$$\rho = e(Z_i n_i - n_e) \tag{2.53}$$

and the charge distribution can be obtained using the electrostatic equation

$$\nabla^2 \Phi = -\frac{\rho}{\epsilon_0} \quad . \tag{2.54}$$

where Φ is the electric potential and ϵ_0 is the permittivity of free space.

b) Momentum equations

The derivation of momentum equations is somewhat more involved. Therefore the evaluation of the tensors $\nabla \cdot mn\vec{V}\vec{V}$ and $\nabla \cdot \overleftrightarrow{\Pi}$ will be given in the first sections. The momentum equations in the main transport directions are derived in sections 3 to 8.

b.1) The components of $\nabla \cdot mn\vec{V}\vec{V}$ Recalling the expression for $\nabla \cdot \vec{A}\vec{B}$, the components of $\nabla \cdot mn\vec{V}\vec{V}$ in the poloidal co-ordinate system are

$$\begin{aligned} \left[\vec{\nabla} \cdot (\widetilde{mn\vec{V}\vec{V}})\right]_\theta &= \frac{1}{\sqrt{g}} \frac{\partial}{\partial u^i} \left(\frac{\sqrt{g}}{h_i} mn\tilde{V}_i \tilde{V}_\theta \right) \\ &+ mn\tilde{V}_r \left(\tilde{V}_\theta \frac{\partial \ln h_\theta}{h_r \partial u^r} - \tilde{V}_r \frac{\partial \ln h_r}{h_\theta \partial u^\theta} \right) \\ &+ mn\tilde{V}_\phi \left(\tilde{V}_\theta \frac{\partial \ln h_\theta}{h_\phi \partial u^\phi} - \tilde{V}_\phi \frac{\partial \ln h_\phi}{h_\theta \partial u^\theta} \right) \quad , \end{aligned} \tag{2.55}$$

$$\begin{aligned} \left[\vec{\nabla} \cdot (\widetilde{mn\vec{V}\vec{V}})\right]_\phi &= \frac{1}{\sqrt{g}} \frac{\partial}{\partial u^i} \left(\frac{\sqrt{g}}{h_i} mn\tilde{V}_i \tilde{V}_\phi \right) \\ &+ mn\tilde{V}_r \left(\tilde{V}_\phi \frac{\partial \ln h_\phi}{h_r \partial u^r} - \tilde{V}_r \frac{\partial \ln h_r}{h_\phi \partial u^\phi} \right) \\ &+ mn\tilde{V}_\theta \left(\tilde{V}_\phi \frac{\partial \ln h_\phi}{h_\theta \partial u^\theta} - \tilde{V}_\theta \frac{\partial \ln h_\theta}{h_\phi \partial u^\phi} \right) \end{aligned} \tag{2.56}$$

and

$$\begin{aligned} \left[\vec{\nabla} \cdot (\widetilde{mn\vec{V}\vec{V}})\right]_r &= \frac{1}{\sqrt{g}} \frac{\partial}{\partial u^i} \left(\frac{\sqrt{g}}{h_i} mn\tilde{V}_i \tilde{V}_r \right) \\ &+ mn\tilde{V}_\theta \left(\tilde{V}_r \frac{\partial \ln h_r}{h_\theta \partial u^\theta} - \tilde{V}_\theta \frac{\partial \ln h_\theta}{h_r \partial u^r} \right) \\ &+ mn\tilde{V}_\phi \left(\tilde{V}_r \frac{\partial \ln h_r}{h_\phi \partial u^\phi} - \tilde{V}_\phi \frac{\partial \ln h_\phi}{h_r \partial u^r} \right) \quad . \end{aligned} \tag{2.57}$$

We employ the relations of Eqs. (2.40) and (2.41) to get the parallel and diamagnetic components

$$\begin{aligned} \left[\vec{\nabla} \cdot \left(\widetilde{mn\vec{V}\vec{V}}\right)\right]_{\|} &= \frac{\tilde{B}_\theta}{\tilde{B}} \left(\vec{\nabla} \cdot \left(\widetilde{mn\vec{V}\vec{V}}\right) \right)_\theta \\ &+ \frac{\tilde{B}_\phi}{\tilde{B}} \left(\nabla \cdot \left(\widetilde{mn\vec{V}\vec{V}}\right) \right)_\phi \quad ; \end{aligned} \tag{2.58}$$

$$\left[\vec{\nabla}\cdot\left(\widetilde{mn\vec{V}\vec{V}}\right)\right]_{\perp} = \frac{\tilde{B}_{\phi}}{\tilde{B}}\left(\vec{\nabla}\cdot\left(\widetilde{mn\vec{V}\vec{V}}\right)\right)_{\theta} - \frac{\tilde{B}_{\theta}}{\tilde{B}}\left(\nabla\cdot\left(\widetilde{mn\vec{V}\vec{V}}\right)\right)_{\phi} \tag{2.59}$$

The expressions can be simplified assuming toroidal symmetry and using the relation

$$\frac{\tilde{B}_{\theta}^{2}+\tilde{B}_{\phi}^{2}}{\tilde{B}^{2}} = 1 \tag{2.60}$$

which we can differentiate with respect to the poloidal co-ordinate to get

$$\frac{\partial}{h_{\theta}\partial u^{\theta}}\left(\frac{\tilde{B}_{\phi}}{\tilde{B}}\right) = -\frac{\tilde{B}_{\theta}}{\tilde{B}_{\phi}}\frac{\partial}{h_{\theta}\partial u^{\theta}}\left(\frac{\tilde{B}_{\theta}}{\tilde{B}}\right) \quad . \tag{2.61}$$

Hence $\left[\vec{\nabla}\cdot\left(\widetilde{mn\vec{V}\vec{V}}\right)\right]_{\parallel}$ can finally be written as

$$\left[\vec{\nabla}\cdot\left(\widetilde{mn\vec{V}\vec{V}}\right)\right]_{\parallel} = \frac{1}{\sqrt{g}}\frac{\partial}{\partial u^{i}}\left(\frac{\sqrt{g}}{h_{i}}mn\tilde{V}_{i}\tilde{V}_{\parallel}\right) + \beta_{div,\parallel} + \chi_{div,\parallel} \tag{2.62}$$

with

$$\beta_{div,\parallel} = -mn\left(\frac{\tilde{B}}{\tilde{B}_{\phi}}\tilde{V}_{\perp}\right)\frac{\tilde{V}_{i}}{h_{i}}\frac{\partial}{\partial u^{i}}\left(\frac{\tilde{B}_{\theta}}{\tilde{B}}\right) \tag{2.63}$$

and

$$\begin{aligned}\chi_{div,\parallel} = {} & \frac{\tilde{B}_{\theta}}{\tilde{B}}mn\tilde{V}_{r}\tilde{V}_{\theta}\frac{\partial \ln h_{\theta}}{h_{r}\partial u^{r}} - \frac{\tilde{B}_{\theta}}{\tilde{B}}mn\tilde{V}_{r}^{2}\frac{\partial \ln h_{r}}{h_{\theta}\partial u^{\theta}} \\ & + \frac{\tilde{B}_{\phi}}{\tilde{B}}mn\tilde{V}_{r}\tilde{V}_{\phi}\frac{\partial \ln h_{\phi}}{h_{\theta}\partial u^{\theta}} + mn\tilde{V}_{\perp}\tilde{V}_{\phi}\frac{\partial \ln h_{\phi}}{h_{\theta}\partial u^{\theta}} \quad .\end{aligned} \tag{2.64}$$

And also for $\left[\vec{\nabla}\cdot\left(\widetilde{mn\vec{V}\vec{V}}\right)\right]_{\perp}$:

$$\left[\vec{\nabla}\cdot\left(\widetilde{mn\vec{V}\vec{V}}\right)\right]_{\perp} = \frac{1}{\sqrt{g}}\frac{\partial}{\partial u^{i}}\left(\frac{\sqrt{g}}{h_{i}}mn\tilde{V}_{i}\right)\tilde{V}_{\perp} + \beta_{div,\perp} + \chi_{div,\perp} \tag{2.65}$$

with

$$\beta_{div,\perp} = mn\frac{\tilde{B}}{\tilde{B}_{\phi}}\tilde{V}_{\parallel}\frac{\tilde{V}_{i}}{h_{i}}\frac{\partial}{\partial u^{i}}\left(\frac{\tilde{B}_{\theta}}{\tilde{B}}\right) \tag{2.66}$$

and

$$\begin{aligned}\chi_{div,\perp} = {} & mn\tilde{V}_{r}\left[\frac{\tilde{B}_{\phi}}{\tilde{B}}\tilde{V}_{\theta}\frac{\partial \ln h_{\theta}}{h_{r}\partial u^{r}} - \frac{\tilde{B}_{\phi}}{\tilde{B}}\tilde{V}_{r}\frac{\partial \ln h_{r}}{h_{\theta}\partial u^{\theta}} - \frac{\tilde{B}_{\theta}}{\tilde{B}}\tilde{V}_{\phi}\frac{\partial \ln h_{\phi}}{h_{r}\partial u^{r}}\right] \\ & - mn\tilde{V}_{\phi}\tilde{V}_{\parallel}\frac{\partial \ln h_{\phi}}{h_{\theta}\partial u^{\theta}}\end{aligned} \tag{2.67}$$

b.2) The components of $\nabla\cdot\overleftrightarrow{\Pi}$ We start from the expression for the parallel viscosity tensor $\overleftrightarrow{\Pi}_0$, which is the first order term of the viscosity tensor $\overleftrightarrow{\Pi}$ for a magnetized plasma as it was given by Braginskii [14] :

$$\begin{aligned}
\overleftrightarrow{\Pi} &= -\eta_0 \overleftrightarrow{W}_0 \\
\overleftrightarrow{W}_0 &= 3\left(\vec{b}\vec{b}-\frac{1}{3}\vec{I}\right)\left(\vec{b}\cdot\overleftrightarrow{W}\cdot\vec{b}\right) \\
\overleftrightarrow{W} &= \frac{1}{2}\vec{\nabla}\vec{V}+\frac{1}{2}\left(\vec{\nabla}\vec{V}\right)^T-\frac{1}{3}\overleftrightarrow{I}\left(\vec{\nabla}\cdot\vec{V}\right) \quad .
\end{aligned} \tag{2.68}$$

Here $\vec{b}$ is the unit vector along $\vec{B}$, $\vec{b}\equiv\frac{\vec{B}}{|\vec{B}|}\equiv\frac{\vec{e}_\parallel}{|\vec{e}_\parallel|}=\frac{\vec{e}_\parallel}{h_\parallel}$, T stands for transpose and $\overleftrightarrow{I}$ is the unit tensor.
Recalling the formulae of section 2.3.3, we can easily derive the expression for $\left(\widetilde{\overleftrightarrow{W}}\right)_{\alpha\beta}$:

$$\begin{aligned}
\left(\widetilde{\overleftrightarrow{W}}\right)_{\alpha\beta} &= \frac{1}{2}\left[\frac{\partial\tilde{V}_\beta}{h_\alpha\partial u^\alpha}+\sum_k\tilde{V}_k\Gamma^\alpha_{\beta k}+\frac{\partial\tilde{V}_\alpha}{h_\beta\partial u^\beta}+\sum_k\tilde{V}_k\Gamma^\beta_{\alpha k}\right] \\
&\quad -\frac{1}{3}\delta^\beta_\alpha\sum_i\frac{1}{\sqrt{g}}\frac{\partial}{\partial u^i}\left(\frac{\sqrt{g}}{h_i}\tilde{V}_i\right)
\end{aligned} \tag{2.69}$$

with

$$\Gamma^\alpha_{\beta k}=\delta^\alpha_\beta\frac{\partial\ln h_\beta}{h_k\partial u^k}-\delta^\alpha_k\frac{\partial\ln h_k}{h_\beta\partial u^\beta} \quad , \tag{2.70}$$

which results in

$$\begin{aligned}
\left(\tilde{W}\right)_{\alpha\beta} &= \frac{1}{2}\left(\frac{\partial\tilde{V}_\beta}{h_\alpha\partial u^\alpha}+\frac{\partial\tilde{V}_\alpha}{h_\beta\partial u^\beta}\right)-\frac{1}{3}\delta^\beta_\alpha\sum_k\frac{\partial\tilde{V}_k}{h_k\partial u^k} \\
&\quad +\sum_k\tilde{V}_k\left[\delta^\alpha_\beta\frac{\partial\ln h_\beta}{h_k\partial u^k}-\frac{1}{2}\delta^\alpha_k\frac{\partial\ln h_k}{h_\beta\partial u^\beta}\right. \\
&\quad \left.-\frac{1}{2}\delta^\beta_k\frac{\partial\ln h_k}{h_\alpha\partial u^\alpha}-\frac{1}{3}\delta^\beta_\alpha\frac{1}{\sqrt{g}}\frac{\partial}{\partial u^k}\left(\frac{\sqrt{g}}{h_k}\right)\right] \quad .
\end{aligned} \tag{2.71}$$

Subsequently, $\vec{b}\cdot\overleftrightarrow{W}\cdot\vec{b}$ can be found using the poloidal co-ordinate system once again with $\tilde{b}_\theta\equiv\frac{\tilde{B}_\theta}{\tilde{B}}$ and $\tilde{b}_\phi\equiv\frac{\tilde{B}_\phi}{\tilde{B}}$, viz.

$$\vec{b}\cdot\overleftrightarrow{W}\cdot\vec{b}=\frac{2}{3}\frac{\tilde{B}_\theta}{\tilde{B}}\frac{1}{h_\theta}\frac{\partial\tilde{V}_\parallel}{\partial u^\theta}-\frac{1}{3}\frac{\tilde{B}_\phi}{\tilde{B}}\frac{1}{h_\theta}\frac{\partial\tilde{V}_\perp}{\partial u^\theta}-\frac{1}{3h_r}\frac{\partial\tilde{V}_r}{\partial u^r}+\beta^*+\chi^*\equiv\tilde{W}_{\parallel\parallel} \tag{2.72}$$

where

$$\beta^* = -\frac{\tilde{B}_\theta}{\tilde{B}}\frac{\tilde{V}_\theta}{h_\theta}\frac{\partial \tilde{B}_\theta/\tilde{B}}{\partial u^\theta} - \frac{\tilde{B}_\phi}{\tilde{B}}\frac{\tilde{V}_\phi}{h_\theta}\frac{\partial \tilde{B}_\phi/\tilde{B}}{\partial u^\theta}$$
$$-\frac{1}{3}\tilde{V}_\| \frac{\partial \tilde{B}_\theta/\tilde{B}}{h_\theta \partial u^\theta} - \frac{1}{3}\tilde{V}_\perp \frac{\partial \tilde{B}_\phi/\tilde{B}}{h_\theta \partial u^\theta} \tag{2.73}$$

and

$$\chi^* = -\frac{1}{3}\tilde{V}_\theta \frac{1}{\sqrt{g}}\frac{\partial}{\partial u^\theta}\left(\frac{\sqrt{g}}{h_\theta}\right) - \frac{1}{3}\tilde{V}_r \frac{1}{\sqrt{g}}\frac{\partial}{\partial u^r}\left(\frac{\sqrt{g}}{h_r}\right) \tag{2.74}$$
$$+\tilde{V}_r\left(\frac{\tilde{B}_\theta^2}{\tilde{B}^2}\frac{1}{h_r}\frac{\partial \ln h_\theta}{\partial u^r} + \frac{\tilde{B}_\phi^2}{\tilde{B}^2}\frac{1}{h_r}\frac{\partial \ln h_\phi}{\partial u^r}\right) - \tilde{V}_\phi \frac{\tilde{B}_\theta \tilde{B}_\phi}{\tilde{B}^2}\frac{1}{h_\theta}\frac{\partial \ln h_\phi}{\partial u^\theta} \quad .$$

Using the relation (2.61) the expression for β^* reduces now to :

$$\beta^* = -\tilde{V}_\| + \tilde{V}_\phi\left(3\frac{\tilde{B}_\phi}{\tilde{B}} + 3\frac{\tilde{B}_\theta}{\tilde{B}} - \frac{\tilde{B}}{3\tilde{B}_\phi}\right)\frac{\partial \tilde{B}_\theta/\tilde{B}}{h_\theta \partial u^\theta} \quad . \tag{2.75}$$

Recalling the definitions for $\overleftrightarrow{W}_0$ and $\overleftrightarrow{\Pi}$ (Eqs. (2.68)) we write :

$$\left(\widetilde{\overleftrightarrow{\Pi}}\right)_{\alpha\beta} = -3\eta_0\left(\tilde{b}_\alpha \tilde{b}_\beta - \frac{1}{3}\tilde{\delta}_\alpha^\beta\right)\left(\vec{b}\cdot \overleftrightarrow{W} \cdot \vec{b}\right) \quad . \tag{2.76}$$

So that with $\tilde{b}_\theta = \frac{\tilde{B}_\theta}{\tilde{B}}$, $\tilde{b}_\phi = \frac{\tilde{B}_\phi}{\tilde{B}}$ and $\tilde{b}_r = 0$, this leads to

$$\tilde{\Pi}_{\theta\theta} = -3\eta_0\left(\frac{\tilde{B}_\theta^2}{\tilde{B}^2} - \frac{1}{3}\right)\tilde{W}_{\|\|}$$
$$\tilde{\Pi}_{\phi\phi} = -3\eta_0\left(\frac{\tilde{B}_\phi^2}{\tilde{B}^2} - \frac{1}{3}\right)\tilde{W}_{\|\|}$$
$$\tilde{\Pi}_{\phi\theta} = \tilde{\Pi}_{\theta\phi} = -3\eta_0\left(\frac{\tilde{B}_\theta \tilde{B}_\phi}{\tilde{B}^2} - \frac{1}{3}\right)\tilde{W}_{\|\|}$$
$$\tilde{\Pi}_{rr} = \eta_0 \tilde{W}_{\|\|}$$
$$\tilde{\Pi}_{r\theta} = \tilde{\Pi}_{r\phi} = \tilde{\Pi}_{\theta r} = \tilde{\Pi}_{\phi r} = 0 \quad . \tag{2.77}$$

For the components of $\nabla\cdot \overleftrightarrow{\Pi}$ in the poloidal system, we have,

$$\left(\widetilde{\vec{\nabla}\cdot \overleftrightarrow{\Pi}}\right)_\theta = \frac{1}{\sqrt{g}}\frac{\partial}{\partial u^\theta}\left(\frac{\sqrt{g}}{h_\theta}\tilde{\Pi}_{\theta\theta}\right) + \tilde{A}_\theta \tag{2.78}$$

with

$$\tilde{A}_\theta = \eta_0 \tilde{W}_{\|\|}\left[\left(\frac{3\tilde{B}_\phi^2}{\tilde{B}^2} - 1\right)\frac{\partial \ln h_\phi}{h_\theta \partial u^\theta} - \frac{\partial \ln h_r}{h_\theta \partial u^\theta}\right] \tag{2.79}$$

for the poloidal component ;

$$\left(\widetilde{\vec{\nabla}\cdot\overleftrightarrow{\Pi}}\right)_\phi = \frac{1}{\sqrt{g}}\frac{\partial}{\partial u^\theta}\left(\frac{\sqrt{g}}{h_\theta}\tilde{\Pi}_{\theta\phi}\right) + \tilde{A}_\phi \tag{2.80}$$

with

$$\tilde{A}_\phi = -3\eta_0\tilde{W}_{\|\|}\frac{\tilde{B}_\theta\tilde{B}_\phi}{\tilde{B}^2}\frac{\partial\ln h_\phi}{h_\theta\partial u^\theta} \tag{2.81}$$

for the toroidal component;

$$\left(\widetilde{\vec{\nabla}\cdot\overleftrightarrow{\Pi}}\right)_r = \frac{1}{\sqrt{g}}\frac{\partial}{\partial u^r}\left(\frac{\sqrt{g}}{h_r}\tilde{\Pi}_{rr}\right) + \tilde{A}_r \tag{2.82}$$

with

$$\begin{aligned}\tilde{A}_r \;=\; & \eta_0\tilde{W}_{\|\|}\left[\left(\frac{3\tilde{B}_\theta^2}{\tilde{B}^2}-1\right)\frac{\partial\ln h_\theta}{h_r\partial u^r}+\right.\\ & \left.\left(\frac{3\tilde{B}_\phi^2}{\tilde{B}^2}-1\right)\frac{\partial\ln h_\phi}{h_r\partial u^r}\right]\end{aligned} \tag{2.83}$$

for the radial component.
On the other hand, the components in the parallel system can be found, upon using the vector relations as discussed above,

$$\begin{aligned}\left(\widetilde{\vec{\nabla}\cdot\overleftrightarrow{\Pi}}\right)_\| \;=\; & -\frac{1}{\sqrt{g}}\frac{\partial}{\partial u^\theta}\left[\frac{\sqrt{g}}{h_\theta}2\eta_0\frac{\tilde{B}_\theta}{\tilde{B}}\left(\frac{2}{3}\frac{\tilde{B}_\theta}{\tilde{B}}\frac{1}{h_\theta}\frac{\partial\tilde{V}_\|}{\partial u^\theta}\right.\right.\\ & \left.\left.-\frac{1}{3}\frac{\tilde{B}_\phi}{\tilde{B}}\frac{1}{h_\theta}\frac{\partial\tilde{V}_\perp}{\partial u^\theta}-\frac{1}{3h_r}\frac{\partial\tilde{V}_r}{\partial u^r}\right)\right]+\beta_{\Pi,\|}+\chi_{\Pi,\|}\end{aligned} \tag{2.84}$$

in which

$$\begin{aligned}\beta_{\Pi,\|} = & \\ & \frac{1}{\sqrt{g}}\frac{\partial}{\partial u^\theta}\left\{\frac{\sqrt{g}}{h_\theta}2\eta_0\frac{\tilde{B}_\theta}{\tilde{B}}\left[\tilde{V}_\|+\tilde{V}_\phi\left(-\frac{\tilde{B}_\phi}{\tilde{B}}-\frac{\tilde{B}_\theta}{\tilde{B}}+\frac{\tilde{B}}{3\tilde{B}_\phi}\right)\right]\frac{\partial\tilde{B}_\theta/\tilde{B}}{h_\theta\partial u^\theta}\right\}\\ & +\eta_0\tilde{W}_{\|\|}\left[\left(4\frac{\tilde{B}_\theta^2}{\tilde{B}^2}-1\right)\frac{1}{h_\theta}\frac{\partial}{\partial u^\theta}\left(\frac{\tilde{B}_\theta}{\tilde{B}}\right)\right]\end{aligned} \tag{2.85}$$

and

$$\chi_{\Pi,\|} =$$
$$\frac{1}{\sqrt{g}}\frac{\partial}{\partial u^\theta}\left\{\frac{\sqrt{g}}{h_\theta}2\eta_0\frac{\tilde{B}_\theta}{\tilde{B}}\left[\frac{1}{3}\tilde{V}_\theta\frac{1}{\sqrt{g}}\frac{\partial}{\partial u^\theta}\frac{\sqrt{g}}{h_\theta}+\frac{1}{3}\tilde{V}_r\frac{1}{\sqrt{g}}\frac{\partial}{\partial u^r}\frac{\sqrt{g}}{h_r}\right.\right.$$
$$\left.\left.-\tilde{V}_r\left(\frac{\tilde{B}_\theta^2}{\tilde{B}^2}\frac{1}{h_r}\frac{\partial\ln h_\theta}{\partial u^r}+\frac{\tilde{B}_\phi^2}{\tilde{B}^2}\frac{1}{h_r}\frac{\partial\ln h_\phi}{\partial u^r}\right)+\tilde{V}_\phi\frac{\tilde{B}_\theta\tilde{B}_\phi}{\tilde{B}^2}\frac{1}{h_\theta}\frac{\partial\ln h_\theta}{\partial u^\theta}\right]\right\}$$
$$-\eta_0\tilde{W}_{\|\|\|}\frac{\tilde{B}_\theta}{\tilde{B}}\frac{1}{\sqrt{g}}\frac{\partial}{\partial u^\theta}\frac{\sqrt{g}}{h_\theta} \tag{2.86}$$

for the parallel component ;

$$\left(\widetilde{\nabla\cdot\overleftrightarrow{\Pi}}\right)_\perp = \frac{1}{\sqrt{g}}\frac{\partial}{\partial u^\theta}\left[\frac{\sqrt{g}}{h_\theta}\eta_0\frac{\tilde{B}_\phi}{\tilde{B}}\left(\frac{2}{3}\frac{\tilde{B}_\theta}{\tilde{B}}\frac{1}{h_\theta}\frac{\partial\tilde{V}_\|}{\partial u^\theta}\right.\right.$$
$$\left.\left.-\frac{1}{3}\frac{\tilde{B}_\phi}{\tilde{B}}\frac{1}{h_\theta}\frac{\partial\tilde{V}_\perp}{\partial u^\theta}-\frac{1}{3h_r}\frac{\partial\tilde{V}_r}{\partial u^r}\right)\right]+\beta_{\Pi,\perp}+\chi_{\Pi,\perp} \tag{2.87}$$

where

$$\beta_{\Pi,\perp} =$$
$$\frac{1}{\sqrt{g}}\frac{\partial}{\partial u^\theta}\left\{\frac{\sqrt{g}}{h_\theta}\eta_0\frac{\tilde{B}_\phi}{\tilde{B}}\left[-\tilde{V}_\|+\tilde{V}_\phi\left(\frac{\tilde{B}_\phi}{\tilde{B}}+\frac{\tilde{B}_\theta}{\tilde{B}}-\frac{\tilde{B}}{3\tilde{B}_\phi}\right)\right]\frac{1}{h_\theta}\frac{\partial\tilde{B}_\theta/\tilde{B}}{\partial u^\theta}\right\}$$
$$+\eta_0\tilde{W}_{\|\|\|\|}\cdot 2\frac{\tilde{B}_\theta}{\tilde{B}}\left(-\frac{\tilde{B}}{\tilde{B}_\phi}+3\frac{\tilde{B}_\phi}{\tilde{B}}\right)\frac{1}{h_\theta}\frac{\partial\tilde{B}_\theta/\tilde{B}}{\partial u^\theta} \tag{2.88}$$

and

$$\chi_{\Pi,\perp} =$$
$$-\frac{1}{\sqrt{g}}\frac{\partial}{\partial u^\theta}\left[\frac{\sqrt{g}}{h_\theta}\eta_0\frac{\tilde{B}_\phi}{\tilde{B}}\left(\frac{1}{3}\tilde{V}_\theta\frac{1}{\sqrt{g}}\frac{\partial}{\partial u^\theta}\frac{\sqrt{g}}{h_\theta}-\frac{1}{3}\tilde{V}_r\frac{1}{\sqrt{g}}\frac{\partial}{\partial u^r}\frac{\sqrt{g}}{h_r}\right)\right.$$
$$\left.+\tilde{V}_r\left(\frac{\tilde{B}_\theta^2}{\tilde{B}^2}\frac{1}{h_r}\frac{\partial\ln h_\theta}{\partial u^r}+\frac{\tilde{B}_\phi^2}{\tilde{B}^2}\frac{1}{h_r}\frac{\partial\ln h_\phi}{\partial u^r}\right)-\tilde{V}_\phi\frac{\tilde{B}_\theta\tilde{B}_\phi}{\tilde{B}^2}\frac{1}{h_\theta}\frac{\partial\ln h_\phi}{\partial u^\theta}\right]$$
$$+\eta_0\tilde{W}_{\|\|\|\|}\frac{\tilde{B}_\phi}{\tilde{B}}\frac{1}{h_\phi^2/h_r}\frac{\partial h_\phi^2/h_r}{\partial u^\theta} \tag{2.89}$$

for the diamagnetic component, and finally,

$$\left(\widetilde{\vec{\nabla}\cdot\overleftrightarrow{\Pi}}\right)_r = \frac{1}{\sqrt{g}}\frac{\partial}{\partial u^r}\left[\frac{\sqrt{g}}{h_r}\eta_0\left(\frac{2}{3}\frac{\tilde{B}_\theta}{\tilde{B}}\frac{1}{h_\theta}\frac{\partial\tilde{V}_\|}{\partial u^\theta}\right.\right.$$
$$\left.\left.-\frac{1}{3}\frac{\tilde{B}_\phi}{\tilde{B}}\frac{1}{h_\theta}\frac{\partial\tilde{V}_\perp}{\partial u^\theta}-\frac{1}{3h_r}\frac{\partial\tilde{V}_r}{\partial u^r}\right)\right]+\beta_{\Pi,r}+\chi_{\Pi,r} \tag{2.90}$$

in which

$$\beta_{\Pi,r} = \frac{1}{\sqrt{g}}\frac{\partial}{\partial u^r}\left\{\frac{\sqrt{g}}{h_r}\eta_0\left[-\tilde{V}_{\|} + \tilde{V}_\phi\left(\frac{\tilde{B}_\phi}{\tilde{B}} + \frac{\tilde{B}_\theta}{\tilde{B}} - \frac{\tilde{B}}{3\tilde{B}_\phi}\right)\right]\frac{1}{h_\theta}\frac{\partial \tilde{B}_\theta/\tilde{B}}{\partial u^\theta}\right\} \tag{2.91}$$

and

$$\begin{aligned}\chi_{\Pi,r} \;=\;& \frac{1}{\sqrt{g}}\frac{\partial}{\partial u^r}\left\{\frac{\sqrt{g}}{h_r}\eta_0\left[-\frac{1}{3}\tilde{V}_\theta\frac{1}{\sqrt{g}}\frac{\partial}{\partial u^\theta}\frac{\sqrt{g}}{h_\theta} - \frac{1}{3}\tilde{V}_r\frac{1}{\sqrt{g}}\frac{\partial}{\partial u^r}\frac{\sqrt{g}}{h_r}\right]\right.\\ &\left.+\tilde{V}_r\left(\frac{\tilde{B}_\theta^2}{\tilde{B}^2}\frac{1}{h_r}\frac{\partial \ln h_\theta}{\partial u^r} + \frac{\tilde{B}_\phi^2}{\tilde{B}^2}\frac{1}{h_r}\frac{\partial \ln h_\phi}{\partial u^r}\right) - \tilde{V}_\phi\frac{\tilde{B}_\theta\tilde{B}_\phi}{\tilde{B}^2}\frac{1}{h_\theta}\frac{\partial \ln h_\phi}{\partial u^\theta}\right\}\\ &+\eta_0\tilde{W}_{\|\|}\left[\left(\frac{3\tilde{B}_\theta^2}{\tilde{B}^2} - 1\right)\frac{\partial \ln h_\theta}{h_r\partial u^r} + \left(\frac{3\tilde{B}_\phi^2}{\tilde{B}^2} - 1\right)\frac{\partial \ln h_\phi}{h_r\partial u^r}\right]\end{aligned} \tag{2.92}$$

for the radial component.

b.3 Total momentum equation in the parallel direction Using the vector equation for the total momentum equation, Eq.(2.12), we can derive the parallel component for a single ion fluid species

$$\begin{aligned}&\frac{\partial}{\partial t}\left(m_i n_i \tilde{V}_{i,\|}\right) + \frac{1}{\sqrt{g}}\frac{\partial}{\partial u^\theta}\left(\frac{\sqrt{g}}{h_\theta}m_i n_i \tilde{V}_{i,\theta}\tilde{V}_{i,\|}\right) +\\ &\frac{1}{\sqrt{g}}\frac{\partial}{\partial u^r}\left(\frac{\sqrt{g}}{h_r}m_i n_i \tilde{V}_{i,r}\tilde{V}_{i,\|}\right) + \beta_{div,\|} + \chi_{div,\|} -\\ &\frac{1}{\sqrt{g}}\frac{\partial}{\partial u^\theta}\left[\frac{\sqrt{g}}{h_\theta}2\eta_0\frac{\tilde{B}_\theta}{\tilde{B}}\left(\frac{2}{3}\frac{\tilde{B}_\theta}{\tilde{B}}\frac{1}{h_\theta}\frac{\partial \tilde{V}_{i,\|}}{\partial u^\theta} -\right.\right.\\ &\left.\left.\frac{1}{3}\frac{\tilde{B}_\phi}{\tilde{B}}\frac{1}{h_\theta}\frac{\partial \tilde{V}_{i,\perp}}{\partial u^\theta} - \frac{1}{3}\frac{1}{h_r}\frac{\partial \tilde{V}_{i,r}}{\partial u^r}\right)\right] + \beta_{\Pi,\|} + \chi_{\Pi,\|} =\\ &\qquad -\frac{\tilde{B}_\theta}{\tilde{B}h_\theta}\frac{\partial p}{\partial u^\theta} + \tilde{S}_{m_i\tilde{V}_{i,\|}} \quad .\end{aligned} \tag{2.93}$$

This equation is often employed in a reduced formulation to determine the parallel ion velocity in the edge.

b.4) Electron momentum equation in the parallel direction For the parallel component of the electron momentum equation, Eq. (2.10), we obtain

$$0 = -\frac{1}{h_\theta}\frac{\tilde{B}_\theta}{\tilde{B}}\frac{\partial p_e}{\partial u^\theta} + en\frac{\tilde{B}_\theta}{\tilde{B}}\frac{1}{h_\theta}\frac{\partial \phi}{\partial u^\theta} + \tilde{R}_{e,\|} \tag{2.94}$$

with

$$\tilde{R}_{e,\|} = \frac{en_e}{\sigma_{\|}}\tilde{j}_{\|} - 0.71 n_e\frac{\tilde{B}_\theta}{\tilde{B}}\frac{1}{h_\theta}\frac{\partial T_e}{\partial u^\theta} \quad . \tag{2.95}$$

Alternatively,

$$\tilde{j}_{\|} = \frac{\sigma_{\|}}{en_e}\frac{\tilde{B}_\theta}{\tilde{B}}\left(\frac{1}{h_\theta}\frac{\partial p_e}{\partial u^\theta} - en_e\frac{1}{h_\theta}\frac{\partial \phi}{\partial u^\theta} + 0.71n_e\frac{1}{h_\theta}\frac{\partial T_e}{\partial u^\theta}\right) \tag{2.96}$$

gives the parallel component of the plasma current.

b.5) Ion momentum equation in the radial direction The ion momentum equation in the radial direction may be written as

$$\begin{aligned}
&\frac{\partial}{\partial t}\left(m_i n_i \tilde{V}_{i,r}\right) + \frac{1}{\sqrt{g}}\frac{\partial}{\partial u^\theta}\left(\frac{\sqrt{g}}{h_\theta}m_i n_i \tilde{V}_{i,\theta}\tilde{V}_{i,r}\right) + \frac{1}{\sqrt{g}}\frac{\partial}{\partial u^r}\left(\frac{\sqrt{g}}{h_r}m_i n_i \tilde{V}_{i,r}\tilde{V}_{i,r}\right) + \\
&\chi_{div,r} + \frac{1}{\sqrt{g}}\frac{\partial}{\partial u^r}\left[\frac{\sqrt{g}}{h_r}\eta_0\left(\frac{2}{3}\frac{\tilde{B}_\theta}{\tilde{B}}\frac{1}{h_\theta}\frac{\partial \tilde{V}_{i,\|}}{\partial u^\theta} - \right.\right. \\
&\left.\left.\frac{1}{3}\frac{\tilde{B}_\phi}{\tilde{B}}\frac{1}{h_\theta}\frac{\partial \tilde{V}_{i,\perp}}{\partial u^\theta} - \frac{1}{3h_r}\frac{\partial \tilde{V}_{i,r}}{\partial u^r}\right)\right] + \beta_{\Pi,r} + \chi_{\Pi,r} = \\
&\qquad -\frac{1}{h_r}\frac{\partial}{\partial u^r}p_i - Z_i e n_i \frac{1}{h_r}\frac{\partial \phi}{\partial u^r} - Z_i e n_i \tilde{V}_{i,\perp}\tilde{B} + \tilde{R}_{i,r} + \tilde{S}_{m_i\tilde{V},r}
\end{aligned} \tag{2.97}$$

with

$$\tilde{R}_{i,r} = +en_e\frac{\tilde{j}_r}{\sigma_\perp} + \frac{2}{3}\frac{en_e^2\tilde{B}_\phi}{\sigma_\perp \tilde{B}^2}\frac{1}{h_\theta}\frac{\partial T_e}{\partial u^\theta} \quad . \tag{2.98}$$

This equation can be used to obtain ion velocities in the perpendicular direction, because the cross-term will be one of the dominant terms.

b.6) Total momentum equation in the radial direction For the total momentum equation in the radial direction we find

$$\begin{aligned}
&\frac{\partial}{\partial t}\left(m_i n_i \tilde{V}_{i,r}\right) + \frac{1}{\sqrt{g}}\frac{\partial}{\partial u^\theta}\left(\frac{\sqrt{g}}{h_\theta}m_i n_i \tilde{V}_{i,\theta}\tilde{V}_{i,r}\right) + \frac{1}{\sqrt{g}}\frac{\partial}{\partial u^r}\left(\frac{\sqrt{g}}{h_r}m_i n_i \tilde{V}_{i,r}\tilde{V}_{i,r}\right) + \\
&\chi_{div,r} + \frac{1}{\sqrt{g}}\frac{\partial}{\partial u^r}\left[\frac{\sqrt{g}}{h_r}\eta_0\left(\frac{2}{3}\frac{\tilde{B}_\theta}{\tilde{B}}\frac{1}{h_\theta}\frac{\partial \tilde{V}_{i,\|}}{\partial u^\theta} - \right.\right. \\
&\qquad\left.\left.\frac{1}{3}\frac{\tilde{B}_\phi}{\tilde{B}}\frac{1}{h_\theta}\frac{\partial \tilde{V}_{i,\perp}}{\partial u^\theta} - \frac{1}{3h_r}\frac{\partial \tilde{V}_{i,r}}{\partial u^r}\right\}\right] + \beta_{\Pi,r} + \chi_{\Pi,r} = \\
&\qquad\qquad -\frac{1}{h_r}\frac{\partial}{\partial u^r}p - \tilde{B}\tilde{j}_\perp + \tilde{S}_{m_i\tilde{V}_{i,r}} \quad .
\end{aligned} \tag{2.99}$$

This equation is often reduced to the equilibrium equation $-\frac{1}{h_r}\frac{\partial}{\partial u^r}p = \tilde{j}_\perp \tilde{B}$, which is a first order estimate. We certainly can consider those two terms as the dominant ones, and use this equation to determine the diamagnetic plasma current.

b.7) Ion momentum equation in the diamagnetic direction This equation becomes

$$
\begin{aligned}
&\frac{\partial}{\partial t}\left(m_i n_i \tilde{V}_{i,\perp}\right) + \frac{1}{\sqrt{g}}\frac{\partial}{\partial u^\theta}\left(\frac{\sqrt{g}}{h_\theta} m_i n_i \tilde{V}_{i,\theta}\tilde{V}_{i,\perp}\right) + \\
&\frac{1}{\sqrt{g}}\frac{\partial}{\partial u^r}\left(\frac{\sqrt{g}}{h_r} m_i n_i \tilde{V}_{i,r}\tilde{V}_{i,\perp}\right) + \beta_{div,\perp} + \chi_{div,\perp} + \\
&\frac{1}{\sqrt{g}}\frac{\partial}{\partial u^\theta}\left[\frac{\sqrt{g}}{h_\theta}\eta_0 \frac{\tilde{B}_\phi}{\tilde{B}}\left(\frac{2}{3}\frac{\tilde{B}_\theta}{\tilde{B}}\frac{1}{h_\theta}\frac{\partial \tilde{V}_{i,\|}}{\partial u_\theta} - \right.\right. \\
&\left.\left.\frac{1}{3}\frac{\tilde{B}_\phi}{\tilde{B}}\frac{1}{h_\theta}\frac{\partial \tilde{V}_{i,\perp}}{\partial u^\theta} - \frac{1}{3}h_r\frac{\partial \tilde{V}_{i,r}}{\partial u^r}\right)\right] + \beta_{\Pi,\perp} + \chi_{\Pi,\perp} = \\
&\qquad\qquad -\frac{\tilde{B}_\phi}{\tilde{B}}\frac{1}{h_\theta}\frac{\partial p_i}{\partial u^\theta} - Z_i e n_i \frac{\tilde{B}_\phi}{\tilde{B}}\frac{1}{h_\theta}\frac{\partial \phi}{\partial u^\theta} \\
&\qquad\qquad + Z_i e n_i \tilde{V}_r \tilde{B} + \tilde{R}_{i,\perp} + \tilde{S}_{m_i \tilde{V}_{i,\perp}}
\end{aligned}
\tag{2.100}
$$

where

$$
\tilde{R}_{i,\perp} = +en_e \frac{\tilde{j}_\perp}{\sigma_\perp} + \frac{2}{3}\frac{en_e^2}{\sigma_\perp \tilde{B}}\frac{1}{h_r}\frac{\partial T_e}{\partial u^r} \quad . \tag{2.101}
$$

In principle the ion momentum equation in the diamagnetic direction could be used to obtain the neoclassical radial ion velocity. This velocity, however, deviates from observed "anomalous" experimental values. Therefore the neoclassical radial velocity is replaced by an anomalous expression, which is written according to experimental data as a diffusive Fick relation

$$
\tilde{V}_{i,r} = -\frac{D}{h_r}\frac{\partial}{\partial r}\ln(n_i) \quad . \tag{2.102}
$$

This equation should be used with care, however, as will be explained in section 2.4.1.

b.8) Total momentum equation in the diamagnetic direction The sum of ion and electron momentum equations in the diamagnetic direction will be used to calculate the radial current $\tilde{j}_r$.

$$
\begin{aligned}
&\frac{\partial}{\partial t} m_i n_i \tilde{V}_{i,\perp} + \frac{1}{\sqrt{g}}\frac{\partial}{\partial u^\theta}\left(\frac{\sqrt{g}}{h_\theta} m_i n_i \tilde{V}_{i,\theta}\tilde{V}_{i,\perp}\right) + \\
&\frac{1}{\sqrt{g}}\frac{\partial}{\partial u^r}\left(\frac{\sqrt{g}}{h_r} m_i n_i \tilde{V}_{i,r}\tilde{V}_{i,\perp}\right) + \beta_{div,\perp} + \chi_{div,\perp} + \\
&\frac{1}{\sqrt{g}}\frac{\partial}{\partial u^\theta}\left[\frac{\sqrt{g}}{h_\theta}\eta_0 \frac{\tilde{B}_\phi}{\tilde{B}}\left(\frac{2}{3}\frac{\tilde{B}_\theta}{\tilde{B}}\frac{1}{h_\theta}\frac{\partial \tilde{V}_{i,\|}}{\partial u_\theta} - \right.\right. \\
&\left.\left.\frac{1}{3}\frac{\tilde{B}_\phi}{\tilde{B}}\frac{1}{h_\theta}\frac{\partial \tilde{V}_{i,\perp}}{\partial u^\theta} - \frac{1}{3}h_r\frac{\partial \tilde{V}_{i,r}}{\partial u^r}\right)\right] + \beta_{\Pi,\perp} + \chi_{\Pi,\perp} =
\end{aligned}
$$

$$-\frac{\tilde{B}_\phi}{\tilde{B}}\frac{1}{h_\theta}\frac{\partial p}{\partial u^\theta}+\tilde{j}_r\tilde{B}+\tilde{S}_{m_i\vec{V}_i,\perp} \quad . \tag{2.103}$$

c) Energy equations

In order to eliminate certain terms involving electric fields and currents in the energy equations, the electron momentum equation, Eq. (2.10), has been incorporated in both the ion and the electron energy equation.

c.1) Ion energy equation Substitution of the electron momentum equation in the ion energy equation results in :

$$\frac{\partial}{\partial t}\left(\frac{3}{2}n_iT_i+\frac{m_in_i}{2}\vec{V}_i^2\right)+\vec{\nabla}\cdot\left[\left(\frac{5}{2}n_iT_i+\frac{m_in_i}{2}\vec{V}_i^2\right)\vec{V}_i+\overleftrightarrow{\Pi}_i\cdot\vec{V}_i+\vec{q}_i\right]=$$
$$-\vec{V}_i\cdot\left(\vec{\nabla}p_e-\vec{j}\times\vec{B}\right)-Q_{ei}+S_E^i \tag{2.104}$$

or more explicitly, in terms of the physical components

$$\frac{\partial}{\partial t}\left(\frac{3}{2}n_iT_i+\frac{m_in_i}{2}\vec{V}_i^2\right)+\frac{1}{\sqrt{g}}\frac{\partial}{\partial u^\theta}\left\{\frac{\sqrt{g}}{h_\theta}\left[\frac{5}{2}n_iT_i+\frac{m_in_i}{2}\vec{V}_i^2\right)\tilde{V}_{i,\theta}-\right.$$
$$\frac{\sqrt{g}}{h_\theta}\left(3\eta_0\left(\frac{\tilde{B}_\theta}{\tilde{B}}\tilde{V}_{i,\|}-\frac{1}{3}\tilde{V}_{i,\theta}-\frac{1}{3}\tilde{V}_{i,\phi}\right)\left(\frac{2}{3}\frac{\tilde{B}_\theta}{\tilde{B}}\frac{1}{h_\theta}\frac{\partial\tilde{V}_{i,\|}}{\partial u^\theta}-\right.\right.$$
$$\left.\frac{1}{3}\frac{\tilde{B}_\phi}{\tilde{B}}\frac{1}{h_\theta}\frac{\partial\tilde{V}_{i\perp}}{\partial u^\theta}-\frac{1}{3h_r}\frac{\partial\tilde{V}_{i,r}}{\partial u^r}+\beta^*+\chi^*\right)+$$
$$\left.\left.\left(\frac{\tilde{B}_\theta^2}{\tilde{B}^2}\kappa_\|^i+\frac{\tilde{B}_\phi^2}{\tilde{B}^2}\kappa_\perp^i\right)\frac{1}{h_\theta}\frac{\partial T_i}{\partial u^\theta}+\frac{\tilde{B}_\phi}{\tilde{B}}\kappa_\wedge^i\frac{1}{h_r}\frac{\partial T_i}{\partial u^r}\right]\right\}+$$
$$\frac{1}{\sqrt{g}}\frac{\partial}{\partial u^r}\left\{\frac{\sqrt{g}}{h_r}\left(\frac{5}{2}n_iT_i+\frac{m_in_i}{2}\vec{V}_i^2\right)\tilde{V}_{i,r}+\right.$$
$$\frac{\sqrt{g}}{h_r}\left(\eta_0\tilde{V}_{i,r}\left[\frac{2}{3}\frac{\tilde{B}_\theta}{\tilde{B}}\frac{1}{h_\theta}\frac{\partial\tilde{V}_{i,\|}}{\partial u^\theta}-\frac{1}{3}\frac{\tilde{B}_\phi}{\tilde{B}}\frac{1}{h_\theta}\frac{\partial\tilde{V}_{i,\perp}}{\partial u^\theta}-\frac{1}{3h_r}\frac{\partial\tilde{V}_{i,r}}{\partial u^r}+\right.\right.$$
$$\left.\left.\left.\beta^*+\chi^*\right)-\kappa_\perp^i\frac{1}{h_r}\frac{\partial T_i}{\partial u^r}+\frac{\tilde{B}_\phi}{\tilde{B}}\kappa_\wedge^i\frac{1}{h_\theta}\frac{\partial T_i}{\partial u^\theta}\right]\right\}=$$
$$-\left(\tilde{V}_{i,\theta}\frac{1}{h_\theta}\frac{\partial p_e}{\partial u^\theta}+\tilde{V}_{i,r}\frac{1}{h_r}\frac{\partial p_e}{\partial u^r}\right)$$
$$-\tilde{j}_\perp\tilde{V}_{i,r}\tilde{B}+\tilde{j}_r\tilde{V}_{i,\perp}\tilde{B}-Q_{ei}+S_E^i \quad . \tag{2.105}$$

c.2) Electron energy equation A combination of the electron energy equation (Eq.(2.14)) and the electron momentum equation, Eq. (2.10), results in

$$\frac{\partial}{\partial t}\left(\frac{3}{2}n_eT_e\right)+\vec{\nabla}.\left(\frac{5}{2}n_eT_e\vec{V}_e+\vec{q}_e\right)= \tag{2.106}$$

$$\vec{V}_i \cdot \vec{\nabla} p_e - \vec{j} \cdot \vec{\nabla}\Phi + \vec{j} \cdot \left(\vec{V}_i \times \vec{B}\right) + Q_{ei} + S_E^e \quad .$$

With the definition of $\vec{q}_e$ as given in Eq. (2.16) we obtain in a poloidal co-ordinate system

$$\begin{aligned}
&\frac{\partial}{\partial t}\left(\frac{3}{2}n_e T_e\right) + \frac{1}{\sqrt{g}}\frac{\partial}{\partial u^\theta}\left\{\frac{\sqrt{g}}{h_\theta}\frac{5}{2}T_e\left(n_e\tilde{V}_{i,\theta} - \frac{\tilde{j}_\theta}{e}\right) - \right.\\
&\frac{\sqrt{g}}{h_\theta}\left[\left(\frac{\tilde{B}_\theta^2}{\tilde{B}^2}\kappa_\parallel^e + \frac{\tilde{B}_\phi^2}{\tilde{B}^2}\kappa_\perp^e\right)\frac{1}{h_\theta}\frac{\partial T_e}{\partial u^\theta} - \frac{\tilde{B}_\phi}{\tilde{B}}\kappa_\wedge^e\frac{1}{h_r}\frac{\partial T_e}{\partial u^r} + \right.\\
&\left.\left.0.71\frac{\tilde{B}_\theta}{\tilde{B}}\frac{T_e}{e}\tilde{j}_\parallel + \frac{3}{2}\frac{\tilde{B}_\phi}{\tilde{B}}\frac{T_e}{e\omega_e\tau_e}\tilde{j}_r\right]\right\} + \frac{1}{\sqrt{g}}\frac{\partial}{\partial u^r}\left[\frac{\sqrt{g}}{h_r}\frac{5}{2}T_e\left(n_e\tilde{V}_{i,r} - \frac{\tilde{j}_r}{e}\right) - \right.\\
&\left.\frac{\sqrt{g}}{h_r}\left(\kappa_\perp^e\frac{1}{h_r}\frac{\partial T_e}{\partial u^r} + \frac{B_\phi}{B}\kappa_\wedge^e\frac{1}{h_\theta}\frac{\partial T_e}{\partial u^\theta} - \frac{3}{2}\frac{T_e}{e\omega_e\tau_e}j_\perp\right)\right] = \\
&\qquad\left(\tilde{V}_{i,\theta}\frac{1}{h_\theta}\frac{\partial p_e}{\partial u^\theta} + \tilde{V}_{i,r}\frac{1}{h_r}\frac{\partial p_e}{\partial u^r}\right) - \tilde{j}_\theta\frac{1}{h_\theta}\frac{\partial\Phi}{\partial u^\theta} - \tilde{j}_r\frac{1}{h_r}\frac{\partial\Phi}{\partial u^r}\\
&\qquad-\tilde{j}_\perp\tilde{V}_{i,r}\tilde{B} + \tilde{j}_r\tilde{V}_{i,\perp}\tilde{B} + Q_{ei} + S_E^e \quad .
\end{aligned} \tag{2.107}$$

This brings us to the end of the display of all relevant fluid equations, expressed in a poloidal co-ordinate system assuming toroidal symmetry. From now on we will use physical components of a vector only. This permit us to simplify the notations by omitting the tilde $\tilde{()}$. In the following we shall discuss simplifications with the aim of reaching a set of equations that describe the edge-physics phenomena with sufficient accuracy but that remains computationally solvable.

2.4 2-D edge plasma modelling

As the importance of plasma edge physics for fusion research became evident in the past few years, a lot of effort was spent to develop predictive computer codes in order to investigate both present experiments and next generation devices. A recent review concerning physical models is given by Vold et al. [34]; recent development issues are summarized by Reiter [35] and Vold [36].

In this section attention will be paid to features in present steady state 2-dimensional fluid edge plasma models in order to compare with those of the "B2" code used in this thesis. In a first subsection simplifications to the fluid equations are elucidated. A next section summarizes the different approaches to model neutral particle behaviour in these codes. In a third subsection the geometrical issues in relation to the numerical implementation approaches are discussed. In a last subsection, characteristics of different codes are reviewed.

2.4.1 Modifications to the neoclassical fluid equations for edge plasma purposes

Simplifications

The various models diverge because of extra simplifications introduced to reduce the transport coefficients and moment equations to simpler forms.

1) In the viscous stress term many mixed derivatives and velocity gradients are typically neglected in order to reduce its contribution to terms of a conductive type.

2) Gradients in magnetic field and metric coefficients are usually neglected.

3) Transport in the flux surface is often assumed to be dominated by parallel flow. Perpendicular flows have been neglected in all but the most recent work. Introduction of these flows results in mixed derivatives in the continuity and energy equations.

4) A usual approximation made is that of ambipolar flows, i.e. electric currents are neglected. Eliminating electric currents removes many terms from expressions for the tensor fluxes and from the inhomogeneous factors. In addition it is not necessary to solve Ohm's law in conjunction with the transport set.

Items 3) and 4) are the subjects of considerable recent development efforts and will be the subjects of chapter 5 and 6 of this thesis. Therefore more detailed code comparison concerning those issues will be presented in chapter 5.

Flux-limited electron conductivity

In some codes the parallel electron thermal conductivity is "flux-limited" in order to take into account kinetic "effects" at the sheath, where large gradients exist. This ensures that heat conduction as calculated from the neoclassical formulation is maintained below the maximum physically-possible value. This upper limit for the parallel electron heat conductivity is given by the corresponding maximum convection provided by electrons, if they all had a directed velocity equal to their thermal speed. The concept of a flux-limiter has been used extensively in laser fusion studies. The use of the flux-limiting factor has been compared with Fokker-Planck simulations by Luciani and Mora [24]. Both Igitkhanov et al. [37] and Luciani et al. [24] proposed a non-local expression for the heat flux.
For the B2 code the corrected parallel electron heat flux $\vec{q}_e$ is given by

$$\vec{q}_e = \frac{\vec{\nabla} T_e}{|\vec{\nabla} T_e|} \frac{1}{\left|\kappa^e_{\|,cl} \nabla T_e\right|^{-1} + q_{lim}^{-1}} \tag{2.108}$$

with

$$q_{lim} = F.nv_{th,e}T_e \quad . \tag{2.109}$$

This means that the parallel electron heat conductivity reads :

$$\kappa^e_{\|} = \kappa^e_{\|,cl} \cdot \left(1 + \left|\frac{\kappa^e_{\|,cl} \frac{\partial T_e}{\partial u_\|}}{F.nv_{th,e}T_e}\right|\right)^{-1} \tag{2.110}$$

with F the flux-limiting factor, $v_{th,e} = \sqrt{T_e/m_e}$ a measure for the electron thermal speed, and $\kappa^e_{\|,cl}$ the classical Spitzer-Härm electron heat conduction coefficient.

Anomalous radial transport

As was already mentioned in section 2.3.5, the neoclassical value of the radial ion velocity as obtained with the ion momentum equation in the diamagnetic direction, Eq. (2.100), is replaced by a simple Fick expression (Eq.(2.102)). Furthermore, conventionally, anomalous expressions are taken for "radial" diffusive coefficients in order to fit experimental data. In some codes [38] the radial velocity is determined by a summation of an anomalous and a neoclassical expression. Choices of diffusion coefficients vary from dimensional constants to Bohm-like (T_e/B) representations.
Although this assumption is based on experimental data, blind implementation of it in a model suffers from consistency as is shown in appendix B. From this discussion one can conclude that by introducing anomalous transport, ambiguity exists whenever the radial velocity occurs in the neoclassical equations. Furthermore, edge models can strongly differ from each other depending whether the energy equations are based on the total or on the internal energy. On the other hand, for the phenomenon of anomalous transport a theory is being developed based on electrostatic and magnetic fluctuations, not included in the Braginskii equations. This theory can reveal the magnitude of the observed radial fluxes. For the time being, anomalous transport is introduced in edge modelling as a **phenomenological description**. The implementation of a full theory of anomalous transport will require some more attention in the next years.

2.4.2 Neutral modelling

Recycling of neutrals in the edge strongly influences the plasma properties near the target. Furthermore, it serves as a primary fueling source for the plasma and thus can influence the global particle confinement. Neutral particle behaviour is either described by simple analytic approximations or is treated by iterations with a Monte Carlo code. The first approach is strongly dependent on the geometrical features of the modelled area. The second approach requires a lot of computer time. Recently neutral diffusion models have been developed with varying success in an atttempt to find a good compromise. Furthermore, this last model has been improved by treating the first flight neutrals, originating at the boundary, separatly and exactly, and using the diffusion approach for neutrals suffering one or more charge exchange interactions. Whereas neutral diffusion models are certainly transporting neutrals in a physically realistic manner, they are not as acccurate as Monte Carlo calculations. Therefore, they have to be considered as complementary tools rather than real alternatives.

2.4.3 Geometrical aspects

The domain of calculation for plasma edge codes usually consists of some part of the SOL, some private flux region and the radiating layer interior to the separatrix. In two-dimensional modelling most of the codes use a **finite difference** or a **finite volume technique** [39]. With respect to the geometrical implementation there are three possibilities used :

1) The use of a simple rectangular grid where the x and y co-ordinate correspond respectively to the parallel and the radial direction.

2) The equations are written in a toroidal geometry. The poloidal projection of the magnetic flux surfaces is then assumed to consist of a set of concentric circles.

3) A third approach makes use of an orthogonal curvilinear co-ordinate system with one co-ordinate along the poloidal projection of a magnetic flux surface.

General curvilinear co-ordinates are not yet used for codes numerically based on finite differencing or finite volume techniques.
Two problems arise in relation to the geometry. First, in modelling, magnetic flux surfaces are mostly assumed to intersect orthogonal to the target. Calculations for divertors with non-orthogonal targets are approximately solved by Vold for the EPIC code [40], by Ueda [41] and by Schneider et al. for the B2 code [42]. Secondly, numerical grids for finite difference techniques include discontinuities for divertor calculations. This means that neighbouring cells in the numerical grid may physically be far apart and vice versa. In B2, the problem of linking physically neighbouring cells over discontinuities in the numerical grid for a geometrical universal approach, is recently resolved by Schneider et al. [42].
The use of **finite element methods** (F.E.M.) for plasma edge modelling is expected to be adequate in solving these problems. Recently, development efforts in this direction were initialised by Zanino et al. [43],[44] and by Pütz [45]. For these computations the convective-conductive form of the equations makes straight-forward use of F.E.M. difficult. Despite recent progress in this area, it will certainly require some more years before they achieve the same degree of physics content as the other codes.

2.4.4 Survey of existing codes

A survey of features of existing codes is presented in table 2.1. The first four columns elucidate the contents of the fluid equations. In column four to six the available neutral models incorporated in or coupled with the codes are summarized. In the next columns the present geometrical aspects as described in section 2.4.3 are indicated.
Concerning physical aspects, Gerhauser and Claaßen [15] were the first to introduce drift flows and electric currents and even to date their description remains the most complete. The code is, however, geometry specific and therefore not available for divertor simulations. Recent efforts have been made to introduce similar effects in other codes, which will be compared in chapter 5.
Three groups (B2 code [13], EPIC [40] and UEDA [41]) did formulate the set of equations in general orthogonal co-ordinate systems and are therefore of interest for both code validation in comparison with experimental data and design simulation for future Tokamaks. From these three codes the B2 code is certainly the most widespread, with use at Courant Institute-New York (B.J. Braams), Culham Laboratories, U.K. (G.P. Maddison and formerly M.F. Harrison, E.S. Hotston), K.F.A.-Jüelich, Germany (M. Baelmans, P. Börner, D. Reiter, M.W. Wuttke), IPP-Garching, Germany (J. Neuhauser, R.F. Schneider, H.-S. Bosch, H. Kastelewicz, R. Wunderlich), the NET-team (W.D. D'haeseleer, G.W. Pacher, H.D. Pacher), PPL-Princeton (D.P. Coster, D.P. Stotler), CCFM, Canada (R. Marchand, X. Bonnin).
Due to its flexibility concerning the implementation of different toroidal devices, and its frequent use, the B2 code is a useful tool for Tokamak design. In order to evaluate the B2 code, we have been specifically asked to compare the code with available data from the

limiter Tokamak TEXTOR. In this work the B2 code is confronted with TEXTOR data in broad sense. This is done by a comparison with the more complete, but TEXTOR specific, two-dimensional edge plasma code SOLXY, and with experimental data. The results of this investigation are discussed in chapter 4. As a consequence of this evaluation the physics content of the code is extended including drift flows in the diamagnetic direction and electric currents. In chapter 5 and 6 is dealt with the so-called "extended B2".

Recent developments in numerical techniques are obtained by Knoll et al. [46], Rognlien et al. [47] with F.D. techniques and by Zanino et al. [43],[44] and Pütz [45] with F.E.M. techniques. However, these new codes are not yet that far elaborated concerning physics contents, neutral models or geometrical aspects.

CODE Author	Equations: Variables solved	Equations: Diamagnetic component	Equations: Electric current	Equations: Heat-flux limit	Neutral modelling: Analytic	Neutral modelling: Diffusive	Neutral modelling: Monte Carlo	Geometry: Rectilinear	Geometry: Specific geometry	Geometry: Curvilinear orthog.	Geometry: Non ortho.appl.	Geometry: Finite element	Applications	References
B2 B.J.Braams	$n_i, V_\parallel, V_r, T_e, T_i$	-	-	x	x	-	x (1)	-	-	x	x (2)	-	ASDEX, TEXTOR, ITER, TFTR, JET, ...	[13], [42], [77], [48]-[51], [76], [113], [114], [115]
EXTENDED B2 M.Baelmans	$n_i, V_\parallel, V_\perp, V_r, j_\parallel, j_\perp, j_r, T_e, T_i, \phi$	x	x	x	x	-	x (1)	-	-	x	-	-	ASDEX, TEXTOR,	[52]
SOLXY H.Gerhauser	$n_i, V_\parallel, V_\perp, V_r, j_\parallel, j_\perp, j_r, T_e, T_i, \phi$	x	x	-	x	-	x (3)	-	x	-	-	-	TEXTOR : poloidal and torodial limiter	[15]-[19], [53]
EDGE-2D R.Simonini	$n_i, V_\parallel, V_r, j_\parallel, E_\parallel, T_e, T_i$	-	x (6)	-	-	-	x (5)	-	x	-	x	-	JET, torodial limiter, divertor	[38], [54], [55]
EPIC E.L.Vold	$n_i, V_\parallel, V_\perp, V_r, T_e, T_i, \phi$	x (4)	-	x	-	x	-	-	-	x	x	-	ASDEX,ALCATORC, MOD, TEXTOR,CCT	[34], [36], [40]
ODIC-90 Yu.L.Igitkhanov	$n_i, V_\parallel, V_r, T_e, T_i$	-	-	?	x	x	x	x	-	-	-	-	ASDEX, ITER	[22], [56], [57]
UEDA N.Ueda	$n_i, V_\parallel, V_r, T_e, T_i$	-	-	-	-	-	x	-	-	x	x	-	DOUBLET III	[41]
NEWEDGE D.A.Knoll	$n_i, V_\parallel, V_\perp, V_r, T_e, T_i$	-	-	-	-	x	-	-	x	-	-	-	divertor	[46], [59]
D.A.Knoll	$n_i, V_\parallel, V_\perp, V_r, T, \phi$	x	-	?	x	x?	-	x	-	-	-	-	-	[58]
PLANET M.Petravic	$n_i, V_\parallel, V_r, T_e, T_i$	-	-	?	-	x	x	-	-	x	-	-	ITER, INTOR	[60], [61]
LEDGE T.D.Rognlien	$n_i, V_\parallel, V_\perp, V_r, j_\parallel, j_\perp, j_r, T_e, T_i, \phi$	x	x	x	-	x	-	-	-	-	x	-	DOUBLET III-D	[47], [62]
R.Zanino	$n, V_\parallel, T_e, T_i$	-	-	?	x	-	-	-	-	x	-	x	ITER?	[43], [44], [63]
Th. Putz	$n_i, V_\parallel, T_i$	-	-	x	-	-	x	-	-	-	x	x	TEXTOR	[45]

Table 2.1: Survey of existing codes

comments on table 2.1

(1) extension of B2 calculations with Monte Carlo treatment for neutrals (EIRENE code) implemented at KFA by D.Reiter et al.

(2) non-orthogonal target calculations with different implementation by Maddison et al. [48] and Schneider et al. [42]

(3) Monte Carlo calculations used for comparison in poloidal limiter calculations

(4) additional variables ($V_\perp$ and Φ) calculated afterwards without coupling to the basic equations

(5) coupled with Monte Carlo code NIMBUS

(6) only $j_{||}$ and therefore only $E_{||}$ is included

Chapter 3

Standard B2 code anno 1988

3.1 Introduction

As the importance of edge physics and especially its influence on particle and energy confinement in fusion Tokamaks became more evident during the past ten years in fusion research, a big demand on plasma edge codes arose in the eighties. In addition more information about power and particle exhaust is required in order to design next generation fusion devices.

A numerical fluid code for the edge must combine the processes which are dominant inside the separatrix (i.e. the radial transport) with the flow and thermal conduction along open field lines onto a material boundary. Therefore it must be two-dimensional. Such a code must also incorporate recycling of neutral particles and energy loss by radiation.

The two-dimensional Braams code (B2) [13], [51] fulfils these requirements, and is set up to handle scrape-off layers of different Tokamak types and dimensions, as is explained in section 3.2. Starting from theoretical models as described by Petravic [64] or Singer [65] which are based on the Braginskii equations [14], the B2 code solves a reduced set of fluid equations simplified for improved numerical convergence. The B2 model is compared with the derived fluid edge model of chapter 2. This leads to a list of assumptions for the B2 equations in section 3.3. The next section, 3.4, gives typical boundary conditions used to solve the partial differential equations. The standard treatment of neutral particles is outlined in section 3.5. Finally, the numerical method is described in a last section, 3.6.

3.2 Description of magnetic configuration

The B2 two-dimensional plasma edge transport code is set up to describe the dominant edge plasma effects. It is appropriate for toroidally symmetric configurations such as toroidal-limiter and poloidal-divertor Tokamaks under conditions of sufficiently high collisionality. Finite-difference calculations are performed on a topologically rectangular mesh, which is related to the physical geometry by specifying for each cell the discrete metric functions characterizing the transformation. By means of these metric functions, geometrical effects of both the toroidal geometry and the magnetic configuration can be taken into account.

The physical region of interest for edge plasma modelling consists of the outer section of a

poloidal cross-section, i.e. the scrape-off layer and an annulus of closed flux surfaces inside the separatrix. This physical region is mapped onto the x-y plane (see e.g. figures 3.1 and 3.2), with the poloidal projection of the magnetic field lines along the x co-ordinate, and the radial direction along the y co-ordinate. The particular choice of this orthogonal co-ordinate system is necessary in order to treat the strong anisotropic transport numerically appropriately. Another advantage of the orthogonality of the co-ordinate system is that it ensures that all fluxes out of a volume element can be specified between the cell itself and those neighbouring its faces, rather than involving other cells adjoining just its edges as well (see figure 3.3). Orthogonality therefore simplifies the discretized equations and reduces computing time.
The metric functions of the transformation can be obtained either by conformal mappings or by numerical treatment of output data from a magnetostatic equilibrium code. Analytic transformations have been used for both limiter and divertor Tokamaks, describing a restricted region of the boundary plasma, e.g. TFCX and ASDEX in Ref. [51] (see figures 3.1 and 3.2 respectively) and some other applications in Refs. [49] and [50].
The magnetic geometry linear interpolator, LINDA [66], provides the geometrical information in a discretized form, e.g. for a double-null divertor [48] (see Fig. 3.4). In the case of Ref.[48], the full poloidal cross section was considered, but the inner and outer divertor plates were physically isolated by a barrier ("cut") A-B.

3.3 Fluid equations for the standard B2 code

In this section we will discuss the set of equations as they are used in the B2 code. As mentioned above, the code solves a reduced set of fluid equations on a two-dimensional grid in the poloidal cross-section of a Tokamak. The basic model consists of the ion continuity equations and the parallel ion momentum balance equations for all ion species. Only two energy balance equations are considered : one for the averaged ion energy and one for the electron energy. Momentum and heat transport parallel to the magnetic field are determined by neoclassical theory with the possibility of flux-limited conduction for the electrons. In contrast, the transport normal to the magnetic flux surfaces is represented by anomalous transport coefficients. For the complete derivation of the Braginskii equations in toroidal curvilinear geometry in chapter 2, attention was restricted to a plasma with one ion fluid only. However, the B2 code has been set up to handle multispecies cases as well. The additional terms for multi-fluid edge modelling are given in Refs. [67] and [51]. It should be noted that although the model contains time-dependent terms, it is designed primarily for steady-state solutions.

3.3.1 Assumptions

The B2 code is based on certain simplifying assumptions to reduce the number and complexity of the equations :

1) The plasma is quasineutral ($n \equiv n_i = n_e/Z_i$) and the flow is ambipolar ($\vec{j} = 0$). Therefore no separate electron momentum equation is considered.

2) The ion velocity in the diamagnetic direction $u_\perp$ or $V_\perp$ is neglected. Thus, one component of the ion momentum equation is eliminated.

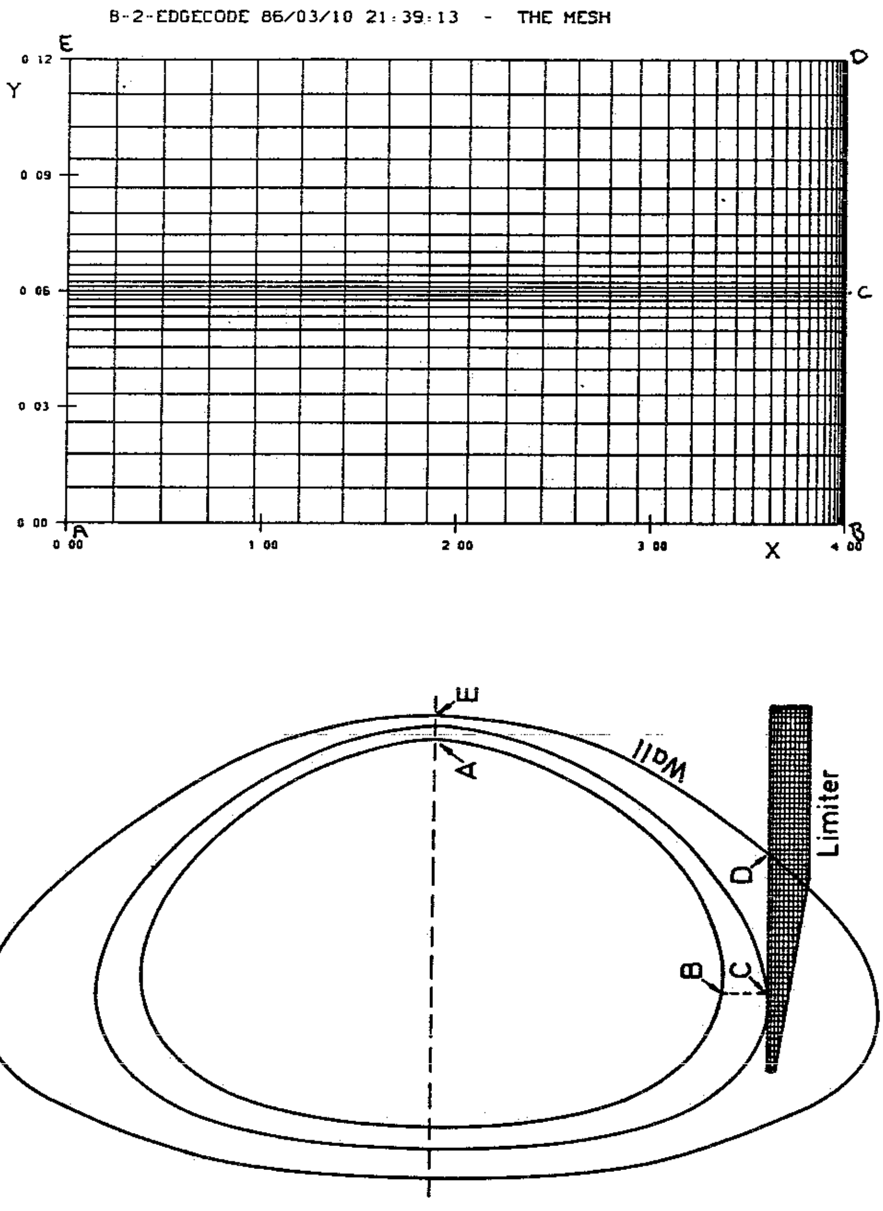

Figure 3.1: The computational and physical meshes for TFCX, taken from Ref. [49]

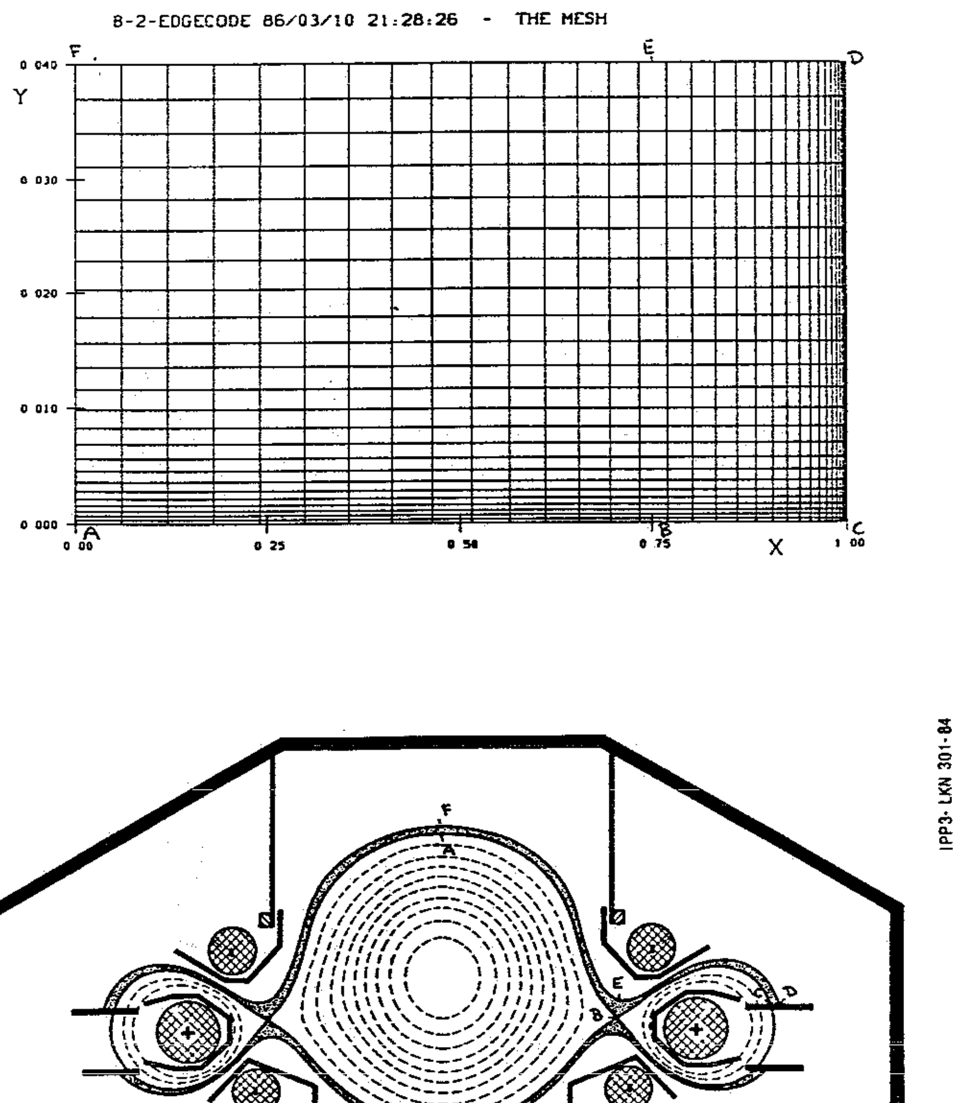

Figure 3.2: The computational and physical meshes for ASDEX, taken from Ref. [49]

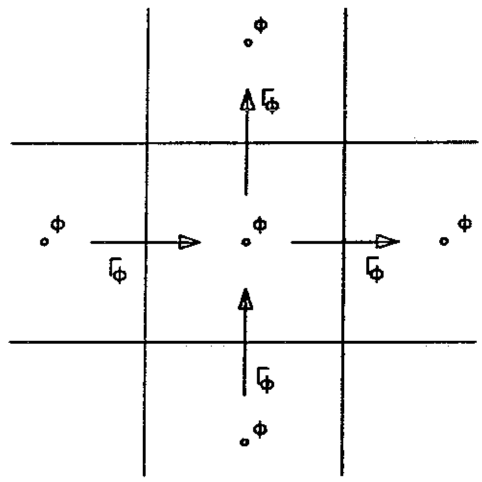

Figure 3.3: Fluxes in an orthogonal discretized grid

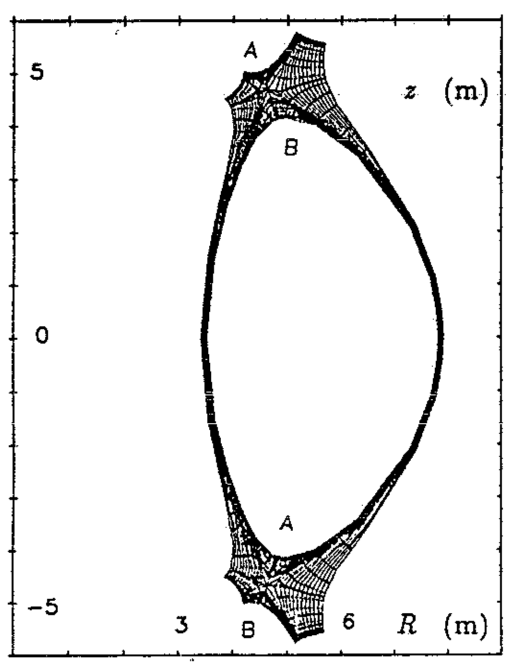

Figure 3.4: The physical mesh for ITER, taken from Ref. [48]

3) The classical cross-field transport terms are complemented by anomalous transport in the radial direction. The radial momentum equation is replaced by a diffusive equation of Fick's form with constant particle diffusion coefficient D_n. Radial transport coefficients $\eta_y = \eta_r$ and $\kappa_y = \kappa_r$ are introduced to model anomalous effects in viscosity stress and heat conductivity. These coefficients are related to constant diffusion coefficients for the viscosity D_η and the heat conductivity D_κ : $\eta_y = \eta_r = mnD_\eta$ and $\kappa_y = \kappa_r = nD_\kappa$.

4) The viscosity tensor is simplified ; cross-field derivative terms are neglected.

5) Terms due to curvature of $\vec{B}$ and gradients of $\vec{B}$ are only partially accommodated.

3.3.2 Basic equations

In order to avoid confusion about the notations, the expressions will first be given with the notation as used by Braams [13] (the so-called B2 notation). Then, the equations will be written with the notation as used in this thesis.
In B2 notation the co-ordinates x and y correspond to the "poloidal" and "radial" directions respectively, as defined in chapter 2. Physical components of the fluid velocity in these two directions are, respectively, u and v. The parallel component is denoted $u_\parallel$ with $u_\parallel = \frac{B}{B_\theta}u$. With the assumptions spelled out in subsection 3.3.1 one obtains for a pure hydrogenic plasma ($Z_i = 1$; $n \equiv n_i = n_e$) the five equations governing the evolution of ion density n, the parallel and radial flow velocity components $u_\parallel$ and v, and electron and ion temperatures T_e and T_i , which are used in the B2 code single ion fluid applications, viz.

$$\frac{\partial}{\partial t}(n) + \frac{1}{\sqrt{g}}\frac{\partial}{\partial x}\left(\frac{\sqrt{g}}{h_x}nu\right) + \frac{1}{\sqrt{g}}\frac{\partial}{\partial y}\left(\frac{\sqrt{g}}{h_y}nv\right) = S_n \tag{3.1}$$

$$\begin{aligned}\frac{\partial}{\partial t}\left(\rho u_\parallel\right) &+ \frac{1}{\sqrt{g}}\frac{\partial}{\partial x}\left(\frac{\sqrt{g}}{h_x}\rho u u_\parallel - \frac{\sqrt{g}}{h_x^2}\eta_x^i\frac{\partial u_\parallel}{\partial x}\right)\\ &+\frac{1}{\sqrt{g}}\frac{\partial}{\partial y}\left(\frac{\sqrt{g}}{h_y}\rho v u_\parallel - \frac{\sqrt{g}}{h_y^2}\eta_y^i\frac{\partial u_\parallel}{\partial y}\right) =\\ &\qquad S_{mu_\parallel} - \frac{B_x}{B}\frac{1}{h_x}\frac{\partial p}{\partial x}\end{aligned} \tag{3.2}$$

$$v = -\frac{D_n}{h_y}\frac{\partial}{\partial y}ln\,(n) \tag{3.3}$$

$$\begin{aligned}\frac{\partial}{\partial t}\left(\frac{3}{2}nT_e\right) &+ \frac{1}{\sqrt{g}}\frac{\partial}{\partial x}\left(\frac{\sqrt{g}}{h_x}\frac{5}{2}nuT_e - \frac{\sqrt{g}}{h_x^2}\kappa_x^e\frac{\partial T_e}{\partial x}\right)\\ &+\frac{1}{\sqrt{g}}\frac{\partial}{\partial y}\left(\frac{\sqrt{g}}{h_y}\frac{5}{2}nvT_e - \frac{\sqrt{g}}{h_y^2}\kappa_y^e\frac{\partial T_e}{\partial y}\right) =\\ &\qquad S_E^e - k\left(T_e - T_i\right) + \frac{u}{h_x}\frac{\partial p_e}{\partial x} + \frac{v}{h_y}\frac{\partial p_e}{\partial y}\end{aligned} \tag{3.4}$$

$$\frac{\partial}{\partial t}\left(\frac{3}{2}nT_i+\frac{1}{2}\rho u_{\|}^2\right)+$$
$$\frac{1}{\sqrt{g}}\frac{\partial}{\partial x}\left[\frac{\sqrt{g}}{h_x}\left(\frac{5}{2}nuT_i+\frac{1}{2}\rho u u_{\|}^2\right)-\frac{\sqrt{g}}{h_x^2}\left(\kappa_x^i\frac{\partial T_i}{\partial x}+\frac{1}{2}\eta_x^i\frac{\partial u_{\|}^2}{\partial x}\right)\right]+$$
$$\frac{1}{\sqrt{g}}\frac{\partial}{\partial y}\left[\frac{\sqrt{g}}{h_y}\left(\frac{5}{2}nvT_i+\frac{1}{2}\rho v u_{\|}^2\right)-\frac{\sqrt{g}}{h_y^2}\left(\kappa_y^i\frac{\partial T_i}{\partial y}+\frac{1}{2}\eta_y^i\frac{\partial u_{\|}^2}{\partial y}\right)\right]=$$
$$S_E^i+k\left(T_e-T_i\right)-\frac{u}{h_x}\frac{\partial p_e}{\partial x}-\frac{v}{h_y}\frac{\partial p_e}{\partial y} \tag{3.5}$$

where

$$\begin{aligned}
S_n, S_{mu_{\|}}, S_E^e, S_E^i &= \textit{volume sources of ions, parallel momentum,}\\
&\quad \textit{electron and ion energy, respectively,}\\
\eta_x^i, \eta_y^i &= \textit{poloidal and radial ion viscosity coefficients,}\\
\kappa_x^{e,i}, \kappa_y^{e,i} &= \textit{thermal conductivities.}
\end{aligned}$$

Auxiliary physical quantities are the mass density, $\rho = m_i n$; the electron and ion pressures, $p_e = nT_e, p_i = nT_i$; the total pressure, $p = p_e + p_i$. Further, $k(T_e - T_i)$ is the rate of energy transfer from electrons to ions, where $k = \frac{3m_e}{m_i}\frac{n}{\tau_e}$.
The poloidal coefficients are related to classical parallel coefficients according to $\eta_x^i = \left(B_\theta^2/B^2\right)\eta_{\|}^i$, and similarly for $\kappa_x^{e,i}$. For κ_x^e, there exists a possibility to incorporate a flux limitation (cfr. Eq.(2.108)).
Extensions to a multifluid model is described in Ref. [13], in which data for ionization and recombination rates are taken from Ref. [68].
The equations are now converted to be consistent with the notation as used in this work. Table 3.1 gives the corresponding symbols for the two notations :

B2	thesis	
x	u^θ	poloidal co-ordinate
y	u^r	radial co-ordinate
u	V_θ	poloidal ion velocity
v	V_r	radial ion velocity
$u_{\|}$	$V_{\|}$	parallel ion velocity

Table 3.1: Different notations

This results in the following set of equations :

$$\frac{\partial}{\partial t}(n)+\frac{1}{\sqrt{g}}\frac{\partial}{\partial u^\theta}\left(\frac{\sqrt{g}}{h_\theta}nV_\theta\right)+\frac{1}{\sqrt{g}}\frac{\partial}{\partial u^r}\left(\frac{\sqrt{g}}{h_r}nV_r\right)=S_n \tag{3.6}$$

$$\frac{\partial}{\partial t}\left(\rho V_{\|}\right)+\frac{1}{\sqrt{g}}\frac{\partial}{\partial u^\theta}\left(\frac{\sqrt{g}}{h_\theta}\rho V_\theta V_{\|}-\frac{\sqrt{g}}{h_\theta^2}\eta_\theta^i\frac{\partial V_{\|}}{\partial u^\theta}\right)$$

$$+\frac{1}{\sqrt{g}}\frac{\partial}{\partial u^r}\left(\frac{\sqrt{g}}{h_r}\rho V_r V_{\parallel}-\frac{\sqrt{g}}{h_r^2}\eta_r^i\frac{\partial V_{\parallel}}{\partial u^r}\right)=$$
$$S_{mV_{\parallel}}-\frac{B_\theta}{B}\frac{1}{h_\theta}\frac{\partial p}{\partial u^\theta} \tag{3.7}$$

$$V_r=-\frac{D_n}{h_r}\frac{\partial}{\partial u^r}ln\left(n\right) \tag{3.8}$$

$$\frac{\partial}{\partial t}\left(\frac{3}{2}nT_e\right)+\frac{1}{\sqrt{g}}\frac{\partial}{\partial u^\theta}\left(\frac{\sqrt{g}}{h_\theta}\frac{5}{2}nV_\theta T_e-\frac{\sqrt{g}}{h_\theta^2}\kappa_\theta^e\frac{\partial T_e}{\partial u^\theta}\right)$$
$$+\frac{1}{\sqrt{g}}\frac{\partial}{\partial u^r}\left(\frac{\sqrt{g}}{h_r}\frac{5}{2}nV_rT_e-\frac{\sqrt{g}}{h_r^2}\kappa_r^e\frac{\partial T_e}{\partial u^r}\right)=$$
$$S_E^e-k\left(T_e-T_i\right)+\frac{V_\theta}{h_\theta}\frac{\partial p_e}{\partial u^\theta}+\frac{V_r}{h_r}\frac{\partial p_e}{\partial u^r} \tag{3.9}$$

$$\frac{\partial}{\partial t}\left(\frac{3}{2}nT_i+\frac{1}{2}\rho V_{\parallel}^2\right)+$$
$$\frac{1}{\sqrt{g}}\frac{\partial}{\partial u^\theta}\left[\frac{\sqrt{g}}{h_\theta}\left(\frac{5}{2}nV_\theta T_i+\frac{1}{2}\rho V_\theta V_{\parallel}^2\right)-\frac{\sqrt{g}}{h_\theta^2}\left(\kappa_\theta^i\frac{\partial T_i}{\partial u^\theta}+\frac{1}{2}\eta_\theta^i\frac{\partial V_{\parallel}^2}{\partial u^\theta}\right)\right]+$$
$$\frac{1}{\sqrt{g}}\frac{\partial}{\partial u^r}\left[\frac{\sqrt{g}}{h_r}\left(\frac{5}{2}nV_rT_i+\frac{1}{2}\rho V_rV_{\parallel}^2\right)-\frac{\sqrt{g}}{h_r^2}\left(\kappa_r^i\frac{\partial T_i}{\partial u^r}+\frac{1}{2}\eta_r^i\frac{\partial V_{\parallel}^2}{\partial u^r}\right)\right]=$$
$$S_E^i+k\left(T_e-T_i\right)-\frac{V_\theta}{h_\theta}\frac{\partial p_e}{\partial u^\theta}-\frac{V_r}{h_r}\frac{\partial p_e}{\partial u^r} \tag{3.10}$$

where

$$\begin{aligned} S_{mV_{\parallel}} &= volume\ sources\ of\ parallel\ momentum, \\ \eta_\theta^i,\eta_r^i &= poloidal\ and\ radial\ ion\ viscosity\ coefficients, \\ \kappa_\theta^{e,i},\kappa_r^{e,i} &= thermal\ conductivities. \end{aligned}$$

3.4 Boundary conditions

3.4.1 Flexibility and constraints

The numerical implementations of boundary conditions are obtained by introducing "infinitesimally" additional small volume elements along the boundaries, which are for all practical purposes isolated from each other, due to the small areas in between (see Fig. 3.5). A flux Γ_Φ, through an area A, towards such an additional volume element can be enforced by putting a sink $-S$ in this otherwise isolated cell. The solution of the set of equations on the numerical grid including these additional cells will result in $\Gamma_\Phi A=-S$ at the boundary. As these sinks $-S$ can be given as a function of the local plasma parameter

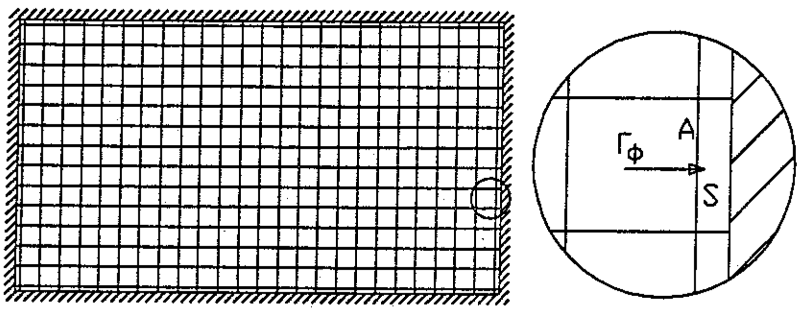

Figure 3.5: Isolated additional volume elements

Φ and all other plasma parameters (i.e. $S = S_v + S_c = S_v^{coeff} \cdot \Phi + S_c$), this concept is very flexible. In particular, not only fluxes, but also plasma parameters or mixed conditions can readily be prescribed (see below). However, one restriction is introduced by this method, i.e. only one condition can be prescribed on each side. This means that whenever physically two boundary conditions need to be imposed on one side, this should be implemented iteratively.
On the other hand, this flexible implementation of boundary conditions leads to a straightforward application of following conditions :

1) A constant flux Γ_Φ towards the boundary, a Neumann condition, is imposed by putting a constant sink $S = -\Gamma_\Phi A$ in the additional volume element.

2) A mixed condition $\Gamma(\Phi) = h\,(\Phi - \Phi_\infty)$ can be obtained by a so-called weak boundary condition, i.e. a combination of a finite variable sink $-S_v$ (proportional to the plasma parameter) and a constant source S_c. This means that the source S is set to $S = S_v + S_c$, with $S_v = -h\Phi$ and $S_c = h\Phi_\infty$.

3) The plasma parameter itself, a Dirichlet condition, can be preset by using a very high coefficient h, so that a sink $S = -h\,(\Phi - \Phi_b)$ leads to $\Phi \approx \Phi_b$. This can be implemented by a combination of a large (infinite) variable sink $S_v = -h\Phi$ and a large (infinite) constant source $S_c = h\Phi_b$. This implementation is often referred to as a strongly conditioned method.

4) A gradient can be defined at a boundary, by using the method as described in 3), putting a constant source as a function of the neighbouring plasma parameter. For a condition of the form $\frac{\partial \Phi}{\partial x} = C$, which leads in the discretized form to $\frac{\Phi_E - \Phi_b}{\Delta x} = C$ (see figure 3.6) or $\Phi_b = \Phi_E - C\Delta x$. In terms of variable and constant sources in

the additional cell this means $S_v = -h\Phi$ and $S_c = h(\Phi_E - C\Delta x)$ with h a large number.

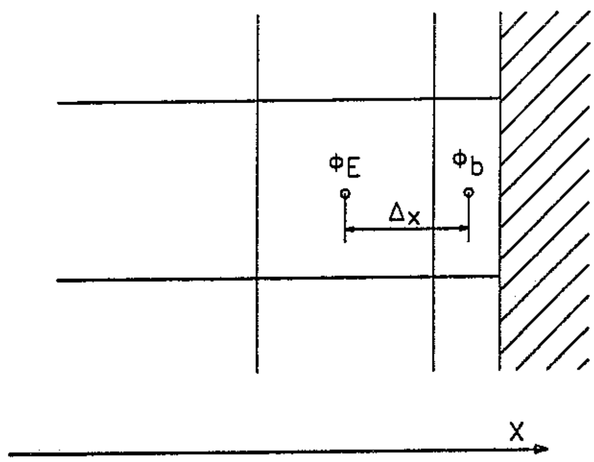

Figure 3.6: Prescribing a gradient at a boundary

Number of boundary conditions It should be noted that the additional cells are involved for each equation which should be solved. This means that for each equation in each co-ordinate direction, two appropriate boundary conditions have to be imposed. Counting derivatives of the five equations governing the edge model, one sees that seven conditions are required for boundaries normal to the x or u^θ co-ordinate and eight conditions for boundaries normal to the y or u^r co-ordinate. For the parallel momentum equation and the energy equations two conditions are required in each direction. For the continuity equation together with the radial diffusion equation only one condition is required in the poloidal direction and two conditions in the radial direction. Therefore, the above described method to impose boundary conditions, poses a problem for the continuity equation in the poloidal direction, where only one condition is required. This is solved intrinsically by using an up-wind differencing scheme for the particle flux, which means that the particle flux at an outflow boundary will not depend on the density in the additional cells. Therefore, the condition at this boundary will only influence the solution indirectly by the calculation of transport coefficients, but will not be taken as an effective boundary condition for the continuity equation.

3.4.2 Typical boundary conditions

At the **main plasma boundary**, a prescribed particle and energy flux or prescribed density and temperature are used, in combination with a zero parallel velocity.

At the **wall** some pedestal temperature or some temperature gradient is usually imposed, together with a zero gradient for density (i.e. no radial flux) and for parallel velocity (i.e. no shear). In some cases a low particle flux towards the wall is prescribed instead.

In the $x-$ or poloidal direction one of the boundaries is often a **symmetry plane**, which means that at this boundary a zero gradient in poloidal direction is prescribed for all plasma variables (n, $V_{\|}$, T_i and T_e).

At the other side the magnetic field lines usually intercept a material boundary. At a **floating limiter or divertor target plate**, a plasma or electrostatic sheath forms to retard the electron flow so that the electron and ion currents to the plate are equal. This requirement leads to boundary conditions for the particle and heat fluxes. The behaviour of the sheath has been investigated extensively for one-dimensional plasma models. A review concerning kinetic edge modelling was given by Chodura [21]. A fluid approach was described by Stangeby [23], and a kinetic approach which takes into account the oblique incidence of the magnetic field was given by Chodura [69]. A review of models for collisionless one-dimensional plasma flow and its application to edge modelling was given by Bissell et al. [70].

Stangeby's calculations [23] show that the plasma fluid equations become singular near the material boundary when the parallel velocity $V_{\|}$ reaches the sound speed. However, looking at the problem from the sheath side, it follows that the ion speed must exceed the sound speed to make a monotonic potential drop possible. This leads to the conclusion that the plasma ceases to exists right in front of the boundary and that a "singular region", called the sheath exists. The criterion $V_{\|} \geq c_s$ with c_s the sound speed, has been confirmed by Chodura [69] for cases where magnetic field lines make an oblique angle with the material boundary. Since it is not immediately obvious how much $V_{\|}$ is to exceed c_s at the sheath entrance, and since the plasma fluid theory breaks down at $V_{\|} = c_s$ anyway, it is generally assumed that the computational domain in plasma computations should be limited by the boundary condition $V_{\|} = c_s$.

Therefore the condition of

$$\Gamma = nV_\theta = n\frac{B_\theta}{B}c_s = n\frac{B_\theta}{B}\sqrt{\frac{(T_i + T_e)}{m_i}} \tag{3.11}$$

is generally adopted for edge modelling. This expression is only for isothermal perturbations of an ideal gas plasma with $Z_i = 1$. Generalizations exists e.g. Igitkhanov et al. [25] favour instead an adiabatic form.

For the heat fluxes all sheath models prescribe mixed conditions of the form

$$\begin{aligned} Q_i &= \delta_i T_i \Gamma \\ Q_e &= \delta_e T_e \Gamma \end{aligned} \tag{3.12}$$

where Γ is the particle flux to the plate.

Following Stangeby [23] (assuming collisional ions in an isothermal model), the transmission coefficients δ_i and δ_e are given by

$$\delta_i = 2.5 + 0.5 \cdot \left(1 + \frac{T_e}{T_i}\right)$$

$$\delta_e = \frac{2}{1-\gamma_e} - \ln\left(\sqrt{2\pi\frac{m_e}{m_i}\left(1+\frac{T_i}{T_e}\right)}\cdot\frac{1}{1-\gamma_e}\right) \tag{3.13}$$

where γ_e is the secondary electron yield per incident ion-electron pair.
For Deuterium with $T_i \approx T_e$ and $\gamma_e = 0$ this leads to

$$\begin{aligned}\delta_i &\approx 3.5\\ \delta_e &\approx 4.8 \quad .\end{aligned} \tag{3.14}$$

Note that for a collisionless plasma the Stangeby formulae (Eq.(3.13)) result in $\delta_i = 2$.
The numerical results obtained by Chodura's treatment [69], for a magnetic field at normal incidence ($\Psi = 0°$ in his notation) and for Deuterium with $T_i \approx T_e$ and $\gamma_e = 0$, are

$$\begin{aligned}\delta_i &= 2.5 + 0.5\cdot\left(1+\frac{T_e}{T_i}\right) \approx 3.5\\ \delta_e &= \frac{2}{1-\gamma_e} - \frac{e\,(\Phi_w - \Phi_s)}{T_e} \approx 4.3\end{aligned} \tag{3.15}$$

where

$$\frac{e\,(\Phi_w - \Phi_s)}{T_e} \approx -2.3 \quad . \tag{3.16}$$

In these formulae Φ_w and Φ_s are respectively the electric potential at the wall or material boundary and at the sheath entrance.
For oblique incidence of the magnetic field line (e.g. $\Psi = 80°$), which is usually the case for fusion Tokamaks, these values are changed to

$$\begin{aligned}\frac{e\,(\Phi_w - \Phi_s)}{kT_e} &\approx -2.8\\ \delta_e &\approx 4.8 \quad .\end{aligned} \tag{3.17}$$

In the work of Bissell et al. [70] several approaches have been reviewed. The range of values for δ_i and δ_e are :

$$\begin{aligned}\delta_i &= 1.5 \rightarrow 2.93\\ \delta_e &= 4.83 \rightarrow 5.12 \quad .\end{aligned} \tag{3.18}$$

The low value for δ_i is due to collisionless modelling of the ions. This range is in accordance with Stangeby's derivations [23], who obtained in this case a value of $\delta_i = 2$.
It should be noted that although a plasma sheath is created at a plasma wall interface regardless of the angle of incidence of the magnetic field, in edge modelling the sheath is only taken into account at material target boundaries which are normal or slightly inclined to the magnetic field lines. Cross-field transport to the wall, as was already indicated above, is prescribed without sheath theory being considered.

3.5 Neutral particle model

Whereas all transport coefficients are determined as analytic functions of local parameters, interactions between recycled neutral particles and the plasma do not only depend on the local parameters. Therefore, more information is required to obtain the source terms $S_n, S_{mV\|}, S_E^e, S_E^i$. A wide range of models can be implemented in the code, ranging from very simple models to sophisticated Monte Carlo calculations.

The default neutral particle model, which is implemented in the B2 code gives a highly simplified description. This model assumes that a prescribed fraction of the ion particle flow impinging on the limiter and the wall is recycled as neutral atoms with a fixed energy of 5 eV. These neutrals are moving essentially along the poloidal co-ordinate away from the target with a velocity $V_{n,\theta} = \sqrt{10\text{eV}/m_i}$, although some artificially introduced radial "dispersion" is possible. The neutral atoms interact with the plasma only via ionization, defined by the rate coefficient :

$$S_{ion} = <\sigma_{ion} v> = 3.10^{-14} \frac{\left(\frac{T_e}{10\text{eV}}\right)^2}{3 + \left(\frac{T_e}{10\text{eV}}\right)^2} \text{m}^3/\text{s} \quad . \tag{3.19}$$

Therefore, particle sources are determined by the expression

$$S_n = n_0 n_e S_{ion} \quad . \tag{3.20}$$

The neutral density n_0 is computed as :

$$n_0 = \frac{\Gamma_0 \tau_0}{\mathcal{V}} \tag{3.21}$$

where Γ_0 is the integrated neutral particle flux through the surface of a grid cell, and τ_0 is the average time a particle is expected to stay in the grid volume $\mathcal{V}$.

With each ionization event an electron energy loss of 25 eV and an ion energy gain of 5 eV is associated. The value for the electron energy sink for ionization of 13.6 eV is enhanced by accounting for the radiation from the excited states of neutral hydrogen throughout its trajectory [71], the ion energy source is determined by the neutral particles originated at the plate with an energy of 5 eV. The parallel momentum sources from ionization processes are ignored in view of the small pitch angle of the field lines. This leads to expressions for momentum, ion and electron energy sources, respectively :

$$S_{mu_\|} = 0 \tag{3.22}$$

$$S_E^i = 5\text{eV} S_n \tag{3.23}$$

$$S_E^e = -25\text{eV} S_n \tag{3.24}$$

It should be stressed that this "minimal" model does not include charge-exchange processes between neutral particles and ions, although they can be dominant for some combinations of configurations and plasma conditions. Also molecular processes are not considered.

In some calculations, as in Ref. [72], a different analytic neutral model is compared with the results of a Monte Carlo calculation for the atoms. In this analytic model some further molecular and atomic physics is implemented. These changes however were not incorporated in the "standard" B2 code. Since the recycling model is part of the "user-supplied routines", it can be changed if so desired.

3.6 Numerical Aspects

3.6.1 Introduction

Numerical implementation of the set of equations as given in section 3.3 is made difficult by certain physics aspects. Firstly, the transport coefficients have strong non-linear dependences on the local variables. Secondly, the source terms due to neutral particles are non-local functions of plasma parameters. Finally, the relative contributions of convective and conductive terms are difficult to predict and vary by orders of magnitude over the grid. For example, the parallel ion velocity is mostly subsonic and increases to sonic conditions at the outflow boundary. However, the parallel electron energy conduction can generally be regarded as the dominant term in the total energy equation.
The procedure to solve the equations is based primarily on the method described by Patankar [39], which consists of a finite-volume spatial discretization on a non-uniform staggered mesh, and a fully implicit discretization in time. This method employs separate relaxation of the differential equations in cyclic order, with the continuity equation replaced by a pressure correction equation of the standard convection-conduction form [39]. Although the method can be used for time-dependent problems, the B2 code is mainly explored for steady-state solutions.

3.6.2 Solution procedure

In B2, the fluid equations, $\mathcal{D}(\Phi) = 0$, which describe the evolution of plasma variables Φ such as n, $V_{||}$, T_e or T_i, are solved iteratively (see subsection 3.6.3) over a two-dimensional mesh. $\mathcal{D}$ represents the generally non-linear differential operator. Each equation is used to improve the initial "guess" of a corresponding plasma variable : the parallel velocity is determined by the parallel momentum equation and the plasma temperatures are obtained by an evaluation of the energy equations. The continuity equation, which contains information for the plasma density n, is converted to a so-called pressure-correction equation , as described in subsection 3.6.4. Starting from the "guess" $\overline{\Phi}$ for the plasma parameter Φ, the residuals are evaluated as $\mathcal{D}(\overline{\Phi}) = -R$, as discussed in 3.6.5. Subsequently, a linearized differential correction equation $\mathcal{D}'(\Delta\Phi) = R$ with $\Delta\Phi = \Phi - \overline{\Phi}$ is discretized (see subsection 3.6.6). This leads to a set of equations $[D][\Delta\Phi] = [R]$, where $[D]$ is a matrix with plasma-state-dependent coefficients. The matrix $[D]$ is inverted approximately by the Strongly Implicit Procedure of Stone [73].

3.6.3 Relaxation method

In order to obtain a steady-state solution, a relaxation method is used which solves the five equations in a cyclic order until convergence is achieved. The time-dependent term is included to permit some under-relaxation. The discretization of each equation is fully implicit in time, but some relaxation can be introduced to accommodate convergence. The continuity equation is solved taking into account the simultaneous changes of n, V_θ, V_r and p, as described before. The possibility of strong coupling between the two energy equations

is dealt with by solving the electron and ion energy equations separately, and by relaxing in addition the total energy balance by an equal correction of the two temperatures.
The equations are solved in the following sequence :

1) The sources, i.e. the inhomogeneous terms in the equations are computed.

2) The poloidal velocity V_θ is corrected in order to relax the parallel momentum equation.

3) The radial diffusion velocity V_r is calculated according the density profile.

4) The continuity equation is relaxed through simultaneous changes of n, V_θ, V_r and p in the pressure-correction equation (see subsection 3.6.4).

5) The electron and ion energy equations are relaxed separately by changes in T_e and T_i.

6) A coupled correction for T_e and T_i is obtained by evaluating the total energy equation.

7) The continuity equation is relaxed once again.

3.6.4 Pressure correction equation

Since the energy equations determine the electron and ion temperatures, and the parallel velocity is corrected in order to fulfil the parallel momentum equation, the continuity equation should provide some information about the density. However, through the equation of state the density is proportional to the pressure, which in turn has a considerable impact on the parallel momentum flow. Therefore, starting from the continuity equation, a pressure correction equation is derived which takes into account simultaneous changes of n,V_θ,V_r and p. The basic idea is that a change ξ in pressure leads to changes in the other variables. For the density this change can be determined according to the equation of state $p = n(T_i + T_e)$, which results in a corrected density

$$n + \left(\frac{\partial n}{\partial p}\right)_T \xi = n + \frac{\xi}{T_i + T_e} \quad . \tag{3.25}$$

Starting from the momentum equation a corrected parallel velocity $V_\| - c_\theta \frac{B_\theta}{B} \frac{\partial \xi}{h_\theta \partial u^\theta}$ is implemented to cancel out the change in p. The prescription of Patankar [39] is to set $c_\theta = 1/a_p$, with a_p the diagonal coefficient of the discretization matrix. In order for the adjustments in the radial velocity $V_r - c_r \frac{\partial \xi}{h_r \partial u^r}$ to approximately cancel the change in p in the diffusion equation, the assignment $c_r = \frac{\kappa D}{n}$ is indicated with $\kappa = \frac{1}{T_i + T_e}$.
Substituting these changes in the continuity equation results in the pressure correction equation of a standard convection-conduction form

$$\frac{\partial}{\partial u^\theta}\left[\frac{\sqrt{g}}{h_\theta}\left(\kappa V_\theta \xi - n c_\theta \frac{B_\theta^2}{B^2}\frac{\partial \xi}{h_\theta \partial u^\theta}\right)\right] + \frac{\partial}{\partial u^r}\left[\frac{\sqrt{g}}{h_r}\left(\kappa V_r \xi - n c_r \frac{\partial \xi}{h_r \partial u^r}\right)\right] = R \tag{3.26}$$

where R is the residual before the parameter n is partially adapted to the new solution of Eq. (3.26), i.e. before relaxation

$$R = \sqrt{g} S_n - \frac{\partial}{\partial u^\theta}\left(\frac{\sqrt{g}}{h_\theta} n V_\theta\right) - \frac{\partial}{\partial u^r}\left(\frac{\sqrt{g}}{h_r} n V_r\right) \quad . \tag{3.27}$$

3.6.5 Detailed evaluation of the approximate solution

Since a finite-volume method is used, the interpolation functions of the variables in between the grid points, which are implicitly assumed for discretization of the differential equations, are not necessarily used for the computation of other terms in each equation. Turning in detail to the code, it can be seen that the differential equation $\mathcal{D}(\Phi) = 0$ itself is not solved, but the corresponding correction equation. This means that starting from an approximate solution $\overline{\Phi}$ which results in $\mathcal{D}(\overline{\Phi}) = -R$, a differential correction equation $\mathcal{D}'(\Delta\Phi) = R$ is solved (see section 3.6.6), with $\Delta\Phi = \Phi - \overline{\Phi}$. Therefore, the residual R is first computed. This is achieved by evaluating the finite-volume formulation of $\mathcal{D}(\overline{\Phi}) = -R$, which is obtained by integrating the differential equation over each control volume.
Consider a convection-conduction equation in conservation form

$$\mathcal{D}(\Phi) = \vec{\nabla} \cdot \left(\rho\vec{V}\Phi - \kappa\vec{\nabla}\Phi\right) - S = 0 \quad . \tag{3.28}$$

With the assumption that κ is diagonal when $\mathcal{D}$ is expanded on co-ordinates we obtain

$$\frac{1}{\sqrt{g}}\sum_{\alpha}\frac{\partial}{\partial u^\alpha}\left[\frac{\sqrt{g}}{h_\alpha}\left(\rho V_\alpha\Phi - \frac{\kappa_\alpha}{h_\alpha}\frac{\partial\Phi}{\partial u^\alpha}\right)\right] - S = 0 \tag{3.29}$$

for deriving the finite-volume expression.
We concentrate now on the two-dimensional case. The numerical mesh is divided into topologically rectangular cells, each having a length in the third ignorable co-ordinate direction. Consider one particular control volume with values at its centre denoted by index P. The centres of the neighbouring cells are denoted by the indices E, W, N, S (east, west, north, south), and the cell faces adjacent to P by e, w, n, s (see figure 3.7). The volume integral of equation (3.29) over the particle cell can then be written as

$$J_e - J_w + J_n - J_s - \int\int\int S d\mathcal{V} = 0 \tag{3.30}$$

with J denoting the flux across a surface and $\mathcal{V}$ the volume of the cell.
For example, for the flux at the east face we obtain

$$J_e = \int\int\left(\rho V_x\Phi - \frac{\kappa_x}{h_x}\frac{\partial\Phi}{\partial u^x}\right) h_y h_z du^y du^z \quad . \tag{3.31}$$

In order to obtain a five-point discretization scheme this flux may be written as

$$J_e = \beta\Phi_E - \alpha\Phi_P \tag{3.32}$$

where α and β depend on the approximation F_e of the flow through the surface and the conductance D_e between the grid points, viz.

$$\begin{aligned} F_e &\approx \int\int \rho V_x h_y h_z du^y du^z = \rho V_x A_e \\ D_e &\approx \frac{1}{d_e}\int\int \kappa_x h_y h_z du^y du^z = \frac{\kappa_x A_e}{d_e} \quad . \end{aligned} \tag{3.33}$$

Here d_e is the distance between the points P and E, and A_e the area of the cell east face.

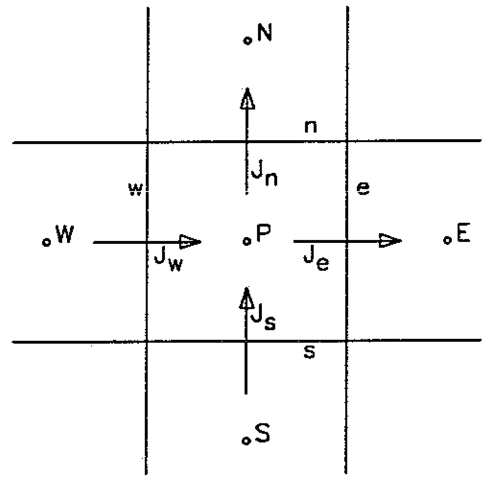

Figure 3.7: Situation in the neighbourhood of a control volume

A choice of a profile between these two points then provides the relation between α, β and D_e and F_e.
In the B2 code the following discretization schemes or ansatz functions are available ([39] and [49]) :

1) central difference scheme for pure conduction equations

2) up-wind difference scheme for pure convection equations

3) regular central difference scheme, including a contribution of the convective term

4) regular up-wind difference scheme, including a contribution of the conductive term

5) simple hybrid scheme

6) fifth power scheme

7) modified hybrid scheme for positive fields

The first four discretization schemes are most often used. The fifth and sixth methods were described by Patankar [39], and correspond approximately to the analytic expression of a one-dimensional convection-conduction equation with constant parameters.The last discretization scheme, a modification of the piecewise linear or hybrid scheme, has been introduced by Braams [49], and is more robust in cases where strong gradients are present.
In the B2 code the standard methods for transport calculations are

1) for the particle flux : regular up-wind difference scheme

2) for the parallel momentum flux : fifth power scheme

3) for the energy fluxes : modified hybrid scheme for positive fields

3.6.6 Discretization and solution of the correction equation

After an evaluation of the approximate solution $\overline{\Phi}$ of the differential equation $\mathcal{D}(\Phi) = 0$ by means of the residuals in each control volume, a linearized correction equation $\mathcal{D}'(\Delta\Phi) = \mathcal{D}'(\Phi - \overline{\Phi}) = \mathcal{D}(\Phi) - \mathcal{D}(\overline{\Phi}) = R$ can be solved. Again according to the finite-volume method [39], [49], a profile in between grid points must be chosen in order to obtain a discretized differential equation. The choice for discretization is restricted to the first six schemes as listed above. The B2 code default setting uses the up-wind scheme for all correction equations.

After the discretization has been computed, the correlation in between neighbouring cells is known. For calculations, the variables may be stored in an array which contains them row after row. Therefore the matrix of correlation coefficients has on each row five non-zero elements : three of the five non-zero elements are located on the principal diagonal and the two adjacent diagonals, the other two elements are located on diagonals situated further away on each side of the principal diagonal. The set of equations is therefore approximately solved by the iterative "Strongly Implicit Method" of Stone. This method is based on an incomplete L*U decomposition [73].

Chapter 4

Adaptations and improvements of the B2 code for TEXTOR applications

4.1 Introduction

In this chapter a confrontation of the B2 code with TEXTOR data in a broad sense is performed. This is partly done by comparing results of B2 with numerical results of a TEXTOR-specific code "SOLXY". This code itself has been confronted with TEXTOR data before in Refs. [16] - [18], [19]. Furthermore, results are compared with new experimental data.

Application of the B2-code on the specific ALT-limiter configuration of TEXTOR, required some adaptation in mesh-generation and boundary conditions. Since the ALT-limiter is located 45° downward, measured from the outward part of the equatorial plane, it destroys any symmetry in the poloidal plane. Therefore, the full poloidal cross-section of the scrape-off layer is modelled. In a first section, 4.2 the geometry is constructed using a conformal mapping procedure. Although parameters of the conformal mapping in this work are calculated for TEXTOR experiments, the analytic mesh generation can easily be extended to other limiter configurations. It therefore permits parametric studies of geometrical effects. For the description of the TEXTOR boundary plasma, one cannot make use of a symmetry plane as a boundary. Therefore, the code is adapted to perform calculations with periodic boundaries, as described in section 4.3. In a next section, 4.4, results of the B2 code are compared with those of a TEXTOR-specific code, SOLXY of Gerhauser and Claaßen [15]. These comparisons reveal the importance of incorporating electric currents in an edge plasma description and result in an adapted version of the code, the so-called B2-vdp version. In section 4.5, the impact of rather detailed neutral particle modelling on limiter configurations is demonstrated by use of a Monte Carlo code, EIRENE [74], for the description of neutral particles. In order to obtain a fully coupled calculation the B2 and EIRENE codes are called alternately, accompanied by an upgrading of the neutral partical sources at each internal iteration of the B2 code. As these B2-EIRENE calculations provide realistic information concerning neutral particle interaction with the plasma a major unknown in the B2 code is eliminated. Therefore, such a coupled

B2-EIRENE calculation should be recommended, whenever a new geometry is set up or large changes in boundary plasma parameters are involved. In a last section, 4.6, poloidal asymmetries in computed radial density profiles are compared with recent experimental results. This permits to discriminate those features that are caused purely by geometrical aspects, such as limiter position, from others which are induced by changing the direction of the magnetic field and therefore can be explained by drift terms only.

4.2 Computational area and analytic mesh generation

4.2.1 Analytic mesh generation

The free parameters for the conformal transformation described here are chosen with the scrape-off layer of the TEXTOR tokamak, determined by the toroidal ALT-II belt limiter, in mind. As the toroidal limiter is located 45° below the equatorial plane (on the outboard side), it does not permit any straight-forward symmetry condition to be imposed. Therefore, the full poloidal cross-section has been modelled. The B2 edge model simulates the radial area between an inner circular flux surface at a minor radius of a_{in} cm and an outer, again circular, but non-concentric flux surface with a minor radius of a_{out} cm.

In order to generate an orthogonal curvilinear co-ordinate mesh for such plasma edge configurations, with the x co-ordinate tangential to the circular magnetic flux surfaces in the poloidal plane and the y co-ordinate normal to the flux surfaces, we use a conformal transformation from a rectilinear (ξ, η)-grid onto that physical mesh. Since boundary conditions have to be imposed at the limiter, the η co-ordinate at $\xi = 0$ and at $\xi = 1$ is chosen to correspond to the position of the limiter (lower and upper limiter sides, respectively). The ξ co-ordinate line at $\eta = 0$ corresponds to the magnetic flux surface at a minor radius of a_{in} cm. Two other ξ co-ordinate lines, at $\eta = 0.25$ and $\eta = 1$ respectively, correspond to the last closed flux surface or separatrix, with minor radius a_0, and to the outermost flux surface at a_{out}, respectively.

Furthermore, the need for high spatial resolution was anticipated in the poloidal zone near the limiter, as well as near the separatrix radially. Therefore, a non-equidistant rectangular mesh was used with 32 and 24 cells in the ξ-(poloidal) and η-(radial) directions, respectively. A flexible resolution is obtained by introducing two scale functions f and g (Fig. 4.2) arising in the conformal mapping function.

The general conformal mapping function $z(\xi, \eta)$ is given by :

$$z = x + iy = R_0 + a_0 \frac{e^{-i\zeta} + \delta}{\delta e^{-i\zeta} + 1} \tag{4.1}$$

where $\zeta = 2\pi f(\xi) + \alpha_0 + ig(\eta)\frac{W}{a_0}$ and

R_0 : the major radius of the reference circle

a_0 : the limiter minor radius of the reference circle

δ : parameter to characterize the Shafranov shift

W : parameter to define the radial width of the grid

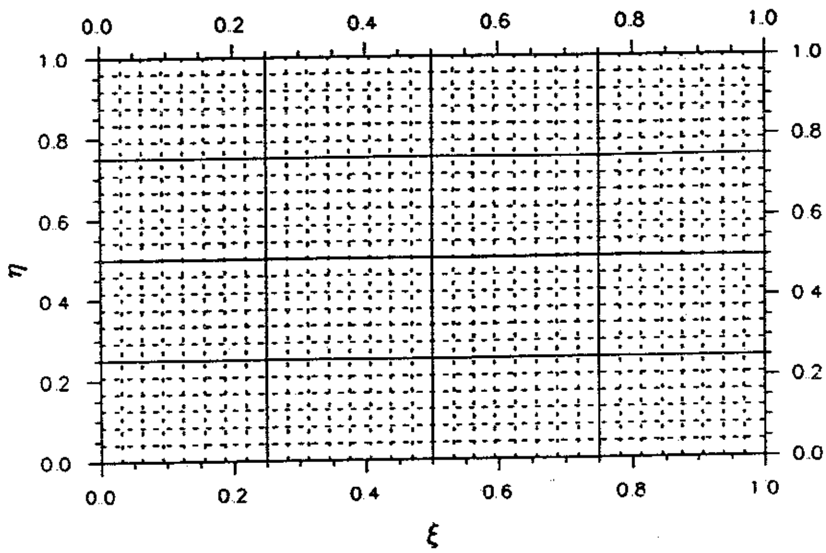

Figure 4.1: The computational mesh

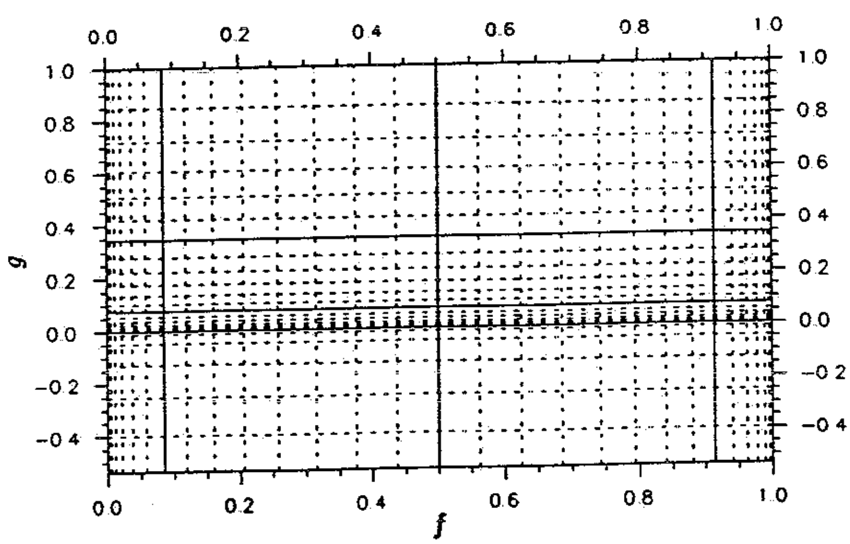

Figure 4.2: The mesh as obtained with scale functions f and g

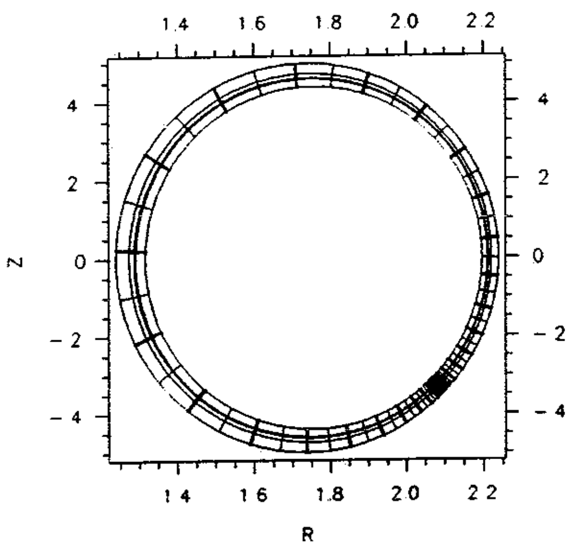

Figure 4.3: The modelled poloidal cross-section

α_0 : parameter to define the poloidal angle of the limiter position.

In appendix C it is shown that this transformation generates an orthogonal mesh of non-concentric circles (Fig. 4.3) with the following properties :

at $g(\eta) = 0$, the centre of the circle is located at R_0 and its radius is a_0

at $g(\eta) =$ constant, the centre of the circle is located at $R_0 + a_0 \frac{(\rho^2-1)\delta}{\delta^2\rho^2-1}$ and its radius equals $a_0\rho\frac{\delta^2-1}{\delta^2\rho^2-1}$, with $\rho = e^{Wg(\eta)/a_0}$.

The Shafranov shift $\Delta(0)$, which is defined as the displacement between the centre of the reference circle with minor radius a_0 and the magnetic axis, turns out to be given by δa_0. Different choices of the parameters R_0, a_0, δ, W, α_0 and of the scale functions f and g allow a wide range of limiter configurations to be modelled, and in particular, for code comparison, also the one used by the SOLXY code. The computational mesh in the SOLXY-code [18] consists of a hard wired set of non-concentric circles with radii from 44 to 50 cm. In these calculations the shift was determined by the metric coefficient $h_y = R_0/R$, with $R = R_0 + r\cos\theta$. In order to use a similar boundary region in the B2 code as in SOLXY the Shafranov shift in the SOLXY geometry has to be calculated. Moreover, the displacement functions $\Delta(r)$ of the two grids will be compared in the next subsection.

4.2.2 Comparison with the displacement function in SOLXY geometry

The transformation for mesh generation in B2, as defined in section 4.2.1, leads to a set of non-concentric circles labeled with ρ, with a nearly parabolic relation ($\delta \ll 1$) between shift $\Delta(\rho)$ and radius $r(\rho)$. The shift $\Delta(\rho)$ is defined as the displacement between the centres of the reference circle and a circle with label ρ. For B2, the displacement function $\Delta(r)$ is determined by a set of parametric equations :

$$\Delta(\rho) = a_0 \frac{(\rho^2 - 1)\delta}{\delta^2 \rho^2 - 1} \tag{4.2}$$

and

$$r(\rho) = a_0 \rho \frac{\delta^2 - 1}{\delta^2 \rho^2 - 1} \tag{4.3}$$

with $\rho = e^{W g(\eta)/a_0}$.

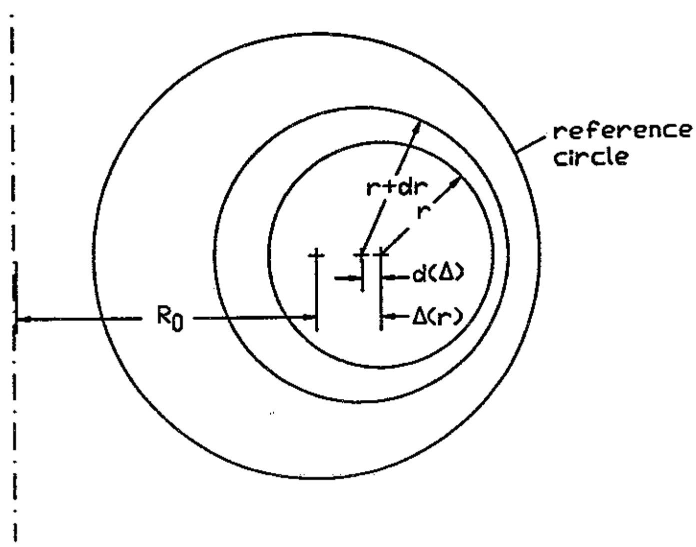

Figure 4.4: The displacement between two circles

For the SOLXY code the displacement function $\Delta(r)$ can be derived starting from the knowledge of the metric coefficient $h_y = R_0/R$, with $R = R_0 + r\cos\theta$, which means that $dy = \frac{R_0}{R} dr$.
Therefore, the variation of the displacement $d(\Delta(r))$ between two circles with minor radius r and $r + dr$ equals (see Fig. 4.4) :

$$d(\Delta(r)) = \frac{1}{2}\left[\frac{R_0}{R_0 - r + \Delta(r)} - \frac{R_0}{R_0 + r + \Delta(r)}\right] dr \tag{4.4}$$

or

$$\frac{d\Delta}{dr} = -\frac{r R_0}{(R_0 + \Delta(r))^2 - r^2} \quad . \tag{4.5}$$

The solution of this differential equation is :

$$r^2 = C_0 e^{2\frac{R_0+\Delta}{R_0}} + (R_0 + \Delta)^2 + R_0 (R_0 + \Delta) + \frac{R_0^2}{2} \quad . \tag{4.6}$$

We take as reference circle the last closed flux surface with minor radius a_0, to eliminate the integration constant C_0 :

$$r^2 = \left(a_0^2 - \frac{5}{2}R_0^2\right) e^{\frac{2\Delta}{R_0}} + \frac{5}{2}R_0^2 + 3R_0\Delta + \Delta^2 \quad . \tag{4.7}$$

With the assumption $\Delta \ll R_0$ we also end up with an approximately parabolic solution for $\Delta(r)$:

$$r^2 = a_0^2 + \left(\frac{2a_0^2}{R_0} - 2R_0\right)\Delta + \left[2\left(\frac{a_0}{R_0}\right)^2 - 4\right]\Delta^2 \quad . \tag{4.8}$$

If we wish to model a comparable geometry for both the B2 and the SOLXY codes, the total Shafranov shift is determined such that the last closed flux surface and the outermost flux surface both coincide in the two models. This means $\Delta\left(a_{out}\right)_{SOLXY} = \Delta\left(a_{out}\right)_{B2}$. Here $\Delta\left(a_{out}\right)_{SOLXY}$ can be calculated with expression Eq. (4.8) for $r = a_{out}$.
$\Delta(0)$ for B2 can then be calculated iteratively with equations (4.2) and (4.3). Fig. 4.5 shows the displacement function $\Delta(r)$ for SOLXY and B2 for TEXTOR geometry with $R_0 = 1.75$ m and $a_0 = 46$ cm. It can be seen that there is good agreement at least for the region of interest, i.e. from $a_{in} = 44$ cm to $a_{out} = 50$ cm.

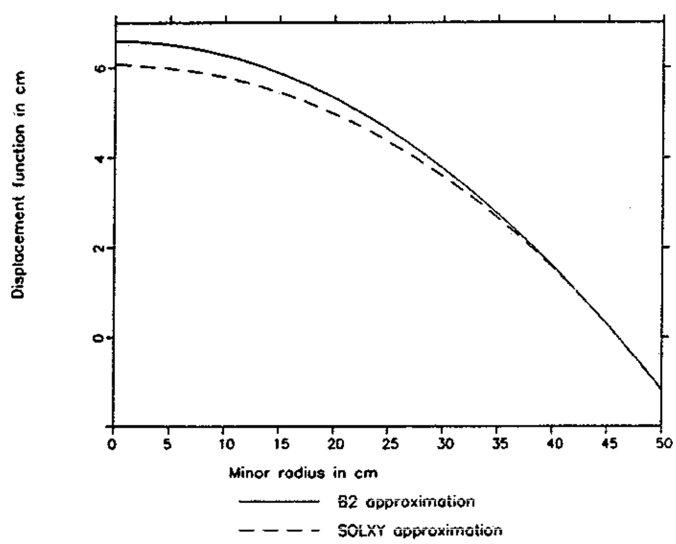

Figure 4.5: Displacement functions

4.2.3 Determination of transformation parameters for TEXTOR

In order to set up a mesh for the B2 code, information about geometrical aspects and the magnetic equilibrium is required. More specifically, for the conformal mapping as described in subsection 4.2.1, values are needed for the major radius R_0, minor radius a_0, Shafranov shift $\Delta(0)$, minor radii of inner and outer circles of the described region, a_{in} and a_{out} respectively, and the limiter position. With this information the transformation

parameters δ, W, α_0 and $g(0)$ can be computed using the expressions which are derived in appendix C and summarized in this subsection.
For a limiter tokamak the major radius R_0 (where the plasma is centred) and the minor radius of the limiter position are given by an experimental feedback procedure.
The Shafranov shift can either be extracted from experimental data, or computed according to the SOLXY geometry as explained in section 4.2.2. This provides the value for $\delta = \frac{\Delta(0)}{a_0}$.
At $g(1) = 1$ the radius of the corresponding circle in the physical mesh should equal a_{out}. This means :

$$W = a_0 \ln \rho \tag{4.9}$$

with

$$\rho = \frac{a_0\left(\delta^2 - 1\right) + \sqrt{a_0^2\left(\delta^2 - 1\right)^2 + 4a_{out}^2\delta^2}}{2a_{out}\delta^2} \quad . \tag{4.10}$$

The inner boundary is provided by the choice of $g(0)$ for which the radius of the corresponding circle in the physical mesh equals a_{in} :

$$g(0) = \frac{a_0}{W} \ln \rho \tag{4.11}$$

with

$$\rho = \frac{a_0\left(\delta^2 - 1\right) + \sqrt{a_0^2\left(\delta^2 - 1\right)^2 + 4a_{in}^2\delta^2}}{2a_{in}\delta^2} \quad . \tag{4.12}$$

The limiter can easily be positioned at 45 $^\circ$ beneath the outer midplane by imposing :

$$\Re(z) - R_0 = -\Im(z)$$

for $f(0) = 0$, where $\Re(z)$ is the real part and $\Im(z)$ is the imaginary part of a complex number z.
This results in :

$$\alpha_0 = -\arcsin\left(\frac{-2\delta}{\sqrt{(1+\delta^2)^2 + (\delta^2 - 1)^2}}\right) - \arctan\left(\frac{\delta^2 + 1}{\delta^2 - 1}\right) \quad . \tag{4.13}$$

To map the rectangular grid onto the specific TEXTOR geometry corresponding to the SOLXY geometry with $a_0 = 1.75$ m, $a_0 = 46$ cm, $a_{out} = 50$ cm and $a_{in} = 44$ cm the following parameters are specified :

$R_0 = 1.75$ m

$a_0 = 46$ cm

$\Delta(0) = \delta a_0 = 6.59$ cm

$W = 3.67$ cm

$\alpha_0 = 1.01$ (radians)

This value for the Shafranov shift is a typical value for TEXTOR given the experimental values for β_p (poloidal β) en l_i (the internal inductance).

Magnetic field

The vacuum toroidal induction is $B_\phi = B_0 R_0/R$, and the poloidal field B_θ is prescribed at the poloidal position of the limiter. Inside the separatrix the poloidal magnetic field depends on the current profile. It can easily be shown that this current profile is approximately given by :

$$j(r) = j_o(1 - (\frac{r}{a_0})^2)^{q_a} \tag{4.14}$$

with

$$q_a = \frac{2\pi}{\mu_0}\frac{a_0^2}{R_0}\frac{B_0}{I_p} = 5.0\frac{a_0^2}{R_0}\frac{B_0\,(\mathrm{T})}{I_p\,(\mathrm{MA})} \tag{4.15}$$

and j_o is determined by the total plasma current I_p :

$$I_p \;=\; \int_0^{a_0} j(r) 2\pi r dr \quad . \tag{4.16}$$

Making use of $I_p = \displaystyle\int \frac{\vec{B}}{\mu_0} \cdot \vec{dl}$ and assuming an almost poloidally constant value for B_θ, this leads to :

$$B_\theta \approx \frac{B_\phi a_0^2}{R_0 q_a r}\left(1 - \left(1 - \frac{r^2}{a_0^2}\right)^{q_a+1}\right) \quad . \tag{4.17}$$

With the approximation of a currentless scrape-off layer the poloidal magnetic field outside the separatrix is given by :

$$B_\theta \approx \frac{\mu_o I_p}{2\pi r} \quad . \tag{4.18}$$

These formulae give some average values for B_θ only, because in reality there is a poloidal variation of B_θ. This poloidal dependence of the poloidal induction is determined by the condition of a constant poloidal magnetic flux between two magnetic flux surfaces. Whereas the SOLXY geometry preset a constant poloidal magnetic field along the flux surface, B2 starts from a poloidal reference position where B_θ has to be prescribed. The poloidal variation of B_θ is then computed, using the obtained magnetic equilibrium information.
Typical values for TEXTOR are $B_0 = 2$ T; $I_p = 460$ kA and, with the use of equation (4.15) $q_a = 2.63$. For these values, the poloidal variation of B_θ at the separatrix is shown in figure 4.6 and amounts to 10 % in this B2 geometry.

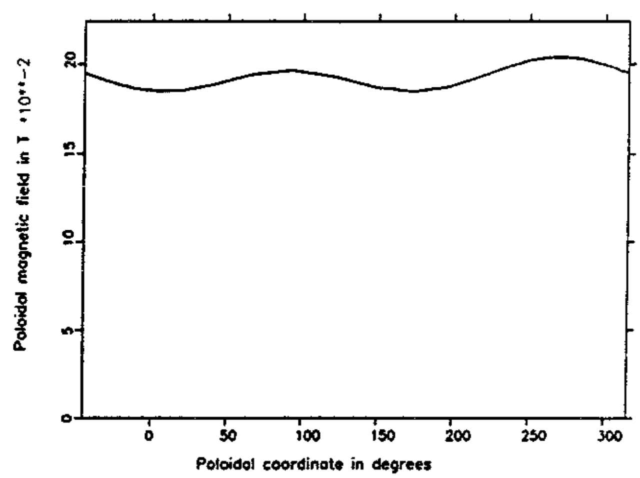

Figure 4.6: Variation of B_θ along the separatrix

4.3 Periodic boundary conditions

4.3.1 Introduction

Since a physical mesh is transformed from a rectangular grid in the numerical procedure as explained in section 3.2, the modelling of a complete poloidal cross-section of the scrape-off layer as proposed in section 4.2.1 introduces a "cut" the physical domain at the poloidal limiter position (see Fig. 4.7). Outside the separatrix boundary conditions for material interfaces can be used. On the other hand, inside the separatrix, where only plasma exists, the only boundary condition that can be applied is periodicity. As in earlier limiter calculations with the B2 code the modelled area was always reduced to a part of the scrape-off layer, the problem of periodic boundaries was first encountered in TEXTOR-applications.

Similar "cuts" are required in the case of a complete divertor scrape-off layer simulation (see figure 4.8). In this case the "cuts" are not longer at the boundaries of the numerical grid, but inside the mesh, meaning that adjacent cells in the computational domain are not necessarily adjacent in the physical domain. For divertor calculations, the internal "cuts were always prescribed as isolated areas.

The problem of periodic conditions both at boundaries and at internal "cuts" has been resolved. In the case of a limiter calculation it is straight forward to use the additional infinitesimally small boundary cells for implementation of the periodic boundary conditions. This has lead, in this work, to the development of an explicit method, which will be described in a next subsection, 4.3.3. Although at internal cuts also additional "infinitesimal" cells can be introduced, a more direct way in linking physically adjacent cells resulted in the implementation of a "semi-implicit" method. This was performed by Schneider et al. [42]. Comparison of those two methods with more usual boundary conditions, such as isolating and symmetric conditions, is performed in subsection 4.3.3.

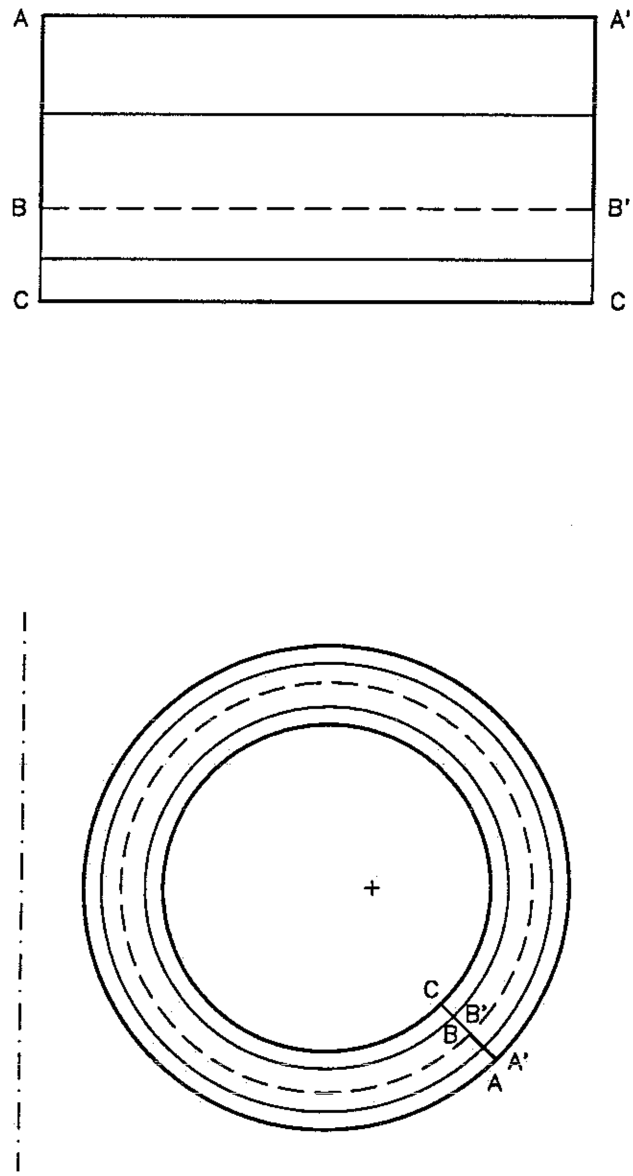

Figure 4.7: Schematic view of computational and physical mesh for TEXTOR

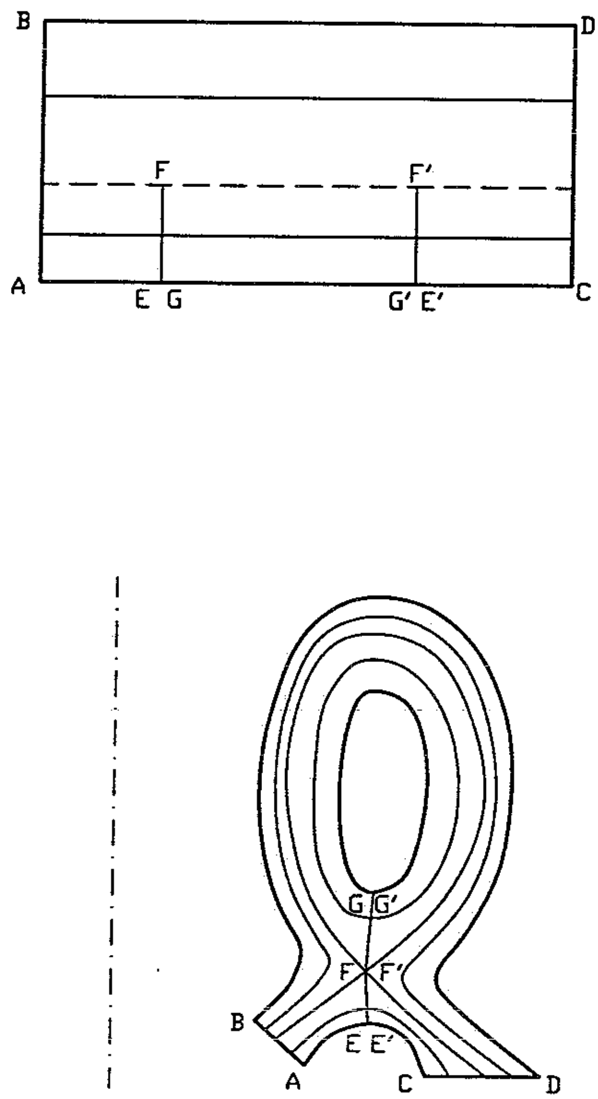

Figure 4.8: Schematic view of computational and physical mesh for a divertor

4.3.2 Explicit and implicit implementation methods of continuity at grid "cuts"

In this work, the explicit method for periodic boundaries is being employed in order to obtain a continuous profile for all plasma variables inside the separatrix of the TEXTOR geometry. The method is explicit in time, which means that fluxes and plasma parameters for periodic boundaries are determined starting from the plasma variables at an earlier time step.
Counting derivatives in the poloidal direction, two boundary conditions are necessary for the parallel momentum equation, Eq. (3.7), and for the energy equations, Eqs. (3.9) and (3.10). For the continuity equation only one condition is required. For the parallel momentum equation and the energy equations, a flux equal to the mean value of the fluxes at the left and the right boundary of the numerical mesh is imposed. An average of a parabolic extrapolation of the plasma parameters towards the centres of the boundary cells predicts a suitable value to be imposed as second boundary condition.
However, for the continuity equation, only one condition has to be imposed, i.e. the variable itself has to be continuous. Therefore, an average value (again determined from a parabolic extrapolation) is imposed on the "left" and "right" boundary of the numerical mesh. This is contradictory at first sight, but since for the discretization of this equation an "up-wind" scheme is used, only one of these two conditions will actually influence the solution (see also section 3.4.1).
This method is implemented for TEXTOR applications but could also be used inside a mesh to provide continuity over the "internal cuts" of a divertor mesh.
Only very recently the problem of "internal grid cuts" for divertor geometry has been resolved in a semi-implicit way by Schneider et al. [42]. This semi-implicit procedure is also implemented in the code for comparison with the explicit procedure. In the semi-implicit method the residuals of the equations are computed using physically adjacent plasma parameters to calculate the fluxes. This means that all fluxes are correctly and equally computed all over the mesh. Nevertheless, for the discretization, those coefficients which relate the plasma parameter corrections across the cut are omitted because they would violate the required format of the discretization matrix using Stone's "Strongly Implicit Method" [73] for matrix inversion. Thus, a change in a variable at one side of the cut will still not influence the variable correction at the physically adjacent cell. Therefore, the solution of plasma parameters is still less adequate for cells in the neighbourhood of "cuts". A fully implicit linkage method requires a different matrix solver. Such a solver is introduced and currently being tested by Schneider [75].

4.3.3 Comparison of different conditions at the periodic boundary

The semi-implicit method of [42] is implemented in the B2 code at KFA Jülich, and used for TEXTOR simulations. Both semi-implicit and explicit methods are compared now to more usual conditions, such as isolating condition and symmetric condition, but which violate the periodicity. The comparison is performed on a TEXTOR geometry with $a_{in} = 0.44$ m, $a_{out} = 0.50$ m and the position of the ALT limiter at 0.46 m, as described in section 4.2.
Taking the parallel classical transport coefficients as in SOLXY calculations (see section 4.4.2) an empirical scaling with a multiplication factor of 0.222 in comparison with

the Braginskii expressions has been used. No heat flux limiting factor was imposed for the electron heat conductivity. The radial anomalous diffusion coefficient D equals 0.6 m^2/s, and $\kappa_r^{e,i} = nD$, $\eta_r^i = mnD$.
The following boundary conditions are chosen :
On the magnetic flux surface at 44 cm :

$V_\theta = 0$ m/s, ie. zero poloidal velocity
$n_i = 4 \times 10^{18}$ m^{-3}
$T_i = T_e = 40$ eV

At the limiter, plasma sheath edge conditions are imposed. The energy transmission coefficients are computed from Eq. (3.13), with $T_i \simeq 0$ and $\gamma_e \simeq 0$:

$V_\theta = \frac{B_\theta}{B} c_s$
$Q_\theta^e = 5.1 T_e n V_\theta$
$Q_\theta^i = 2.5 T_i n V_\theta + \frac{mn}{2} V_\theta^2$

At the liner wall :

$\Gamma_r = nV_r = 0$
$\frac{\partial T_e}{h_r \partial u^r} \sim 0$
$\frac{\partial T_i}{h_r \partial u^r} \sim 0$

At the poloidal boundary, inside the separatrix, four cases have been investigated :

1) isolating boundary conditions :
$\Gamma_\theta = 0$
$V_\theta = 0$
$Q_\theta^{i,e} = 0$

2) symmetric boundary conditions :
$\frac{\partial n}{h_\theta \partial u^\theta} = 0$
$V_\theta = 0$
$\frac{\partial T_i}{h_\theta \partial u^\theta} = \frac{\partial T_e}{h_\theta \partial u^\theta} = 0$

3) explicit continuity boundary condition

4) semi-implicit continuity boundary condition

For the neutral model, the "minimal" model is used, with a recycling coefficient $R_c =$ 0.3 and the neutral particles restricted to a region near the limiter (see section 4.4.2). The recycling coefficient is defined here as the ratio between the total number of neutral particles ionized in the described region per second and the total ion particle flux to the limiter. In these limiter computations it can be expected that only a part of the neutral particles will be ionized in the described region.
A comparison of convergence rates is performed by evaluating an average over the normalized residuals for the continuity equation and the energy equations, as provided by the standard B2 code. These normalized residuals are defined by the residual R_Φ of the approximate solution for the plasma variable Φ :

$$\Sigma\overline{R} = \left(\frac{\Sigma|R_n|V}{\Sigma nV} \times \frac{\Sigma|R_{T_i}|V}{\frac{3}{2}\Sigma\left(n_iT_i + n_eT_e\right)V} \times \frac{\Sigma|R_{T_e}|V}{\frac{3}{2}\Sigma\left(n_iT_i + n_eT_e\right)V}\right)^{\frac{1}{3}} \tag{4.19}$$

with V the volume of a discretized grid cell. A geometric average is chosen in order to obtain the summation of the three decreasing residuals in a semi-logarithmic plot.
Alternatively the rate of convergence is evaluated by a different (but related) criterion proposed by Pacher et al. [76] and D'haeseleer et al. [77]. According to their experience the relative error on the total power balance has to decrease exponentially in numerical time for a converged and stable solution to be ensured.

4.3.4 Results and conclusions

In figure 4.9 the geometric average of the normalized residuals of the continuity equation and the energy equations over the grid as a function of numerical time is shown for the four different boundary conditions. Figure 4.10 represents the evolution of the relative power balance as a function of the numerical time. The time-step has been increased gradually from 5×10^{-8} s to 5×10^{-5} s as is desirable for the implicit method in order to ensure decreasing residuals, but after 1500 iterations (i.e. at $t = 2.8 \times 10^{-3}$ s) is the numerical time-step kept at this constant value of 5×10^{-5} s.

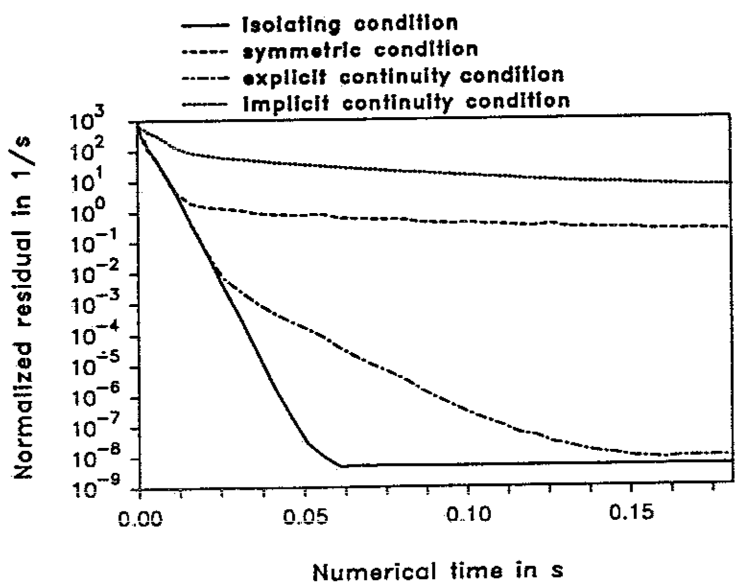

Figure 4.9: Averaged residuals for different cut treatments

Both figures show the good convergence of both the isolating and the explicit continuity condition. In contrast, the symmetric and semi-implicit continuity conditions result in almost unacceptably slow convergence behaviour. **These results demonstrate a dramatic impact of boundary conditions on convergence behaviour.** Since the isolating condition has a better convergence behaviour, replacing the symmetric condition by the isolating condition for part of the iteration could be considered in order to reduce computing time.

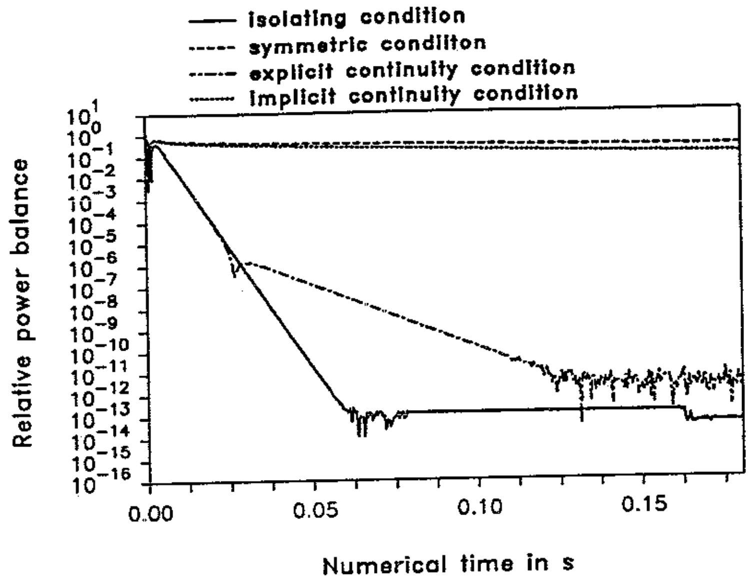

Figure 4.10: Relative power balance for different cut treatments

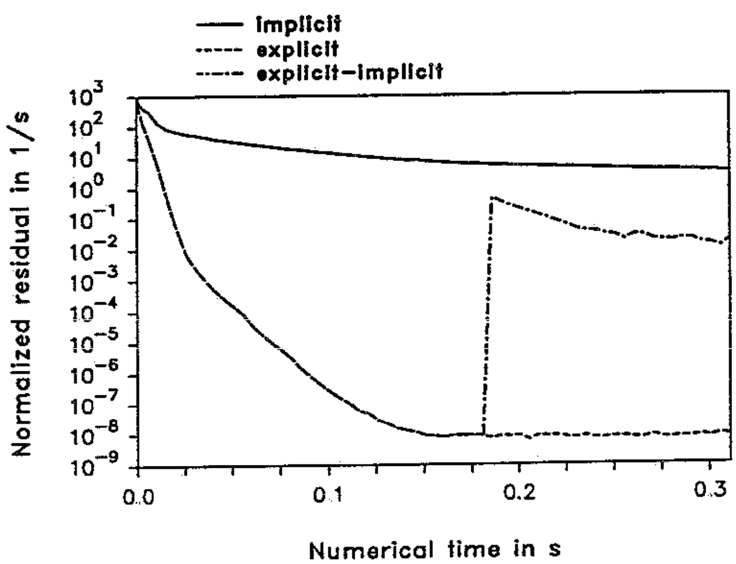

Figure 4.11: Improvement of convergence using the implicit after the explicit method

Another feature which can enhance convergence is illustrated in figure 4.11. A restart with the semi-implicit method from a solution converged with the aid of the explicit boundary method results in a better converged solution than obtained by using the semi-implicit method from the beginning.

4.4 Comparison with SOLXY results

In this section the standard B2 code is compared with the edge plasma transport code, SOLXY of Gerhauser and Claaßen [15], [53] and [16]. The latter is more complete with regard to the number of terms kept in the fluid equations, such as electric and pressure gradient drifts and electric currents. This is discussed in a first subsection, 4.4.1. On the other hand, SOLXY is restricted to TEXTOR-like dimensions and limiter configurations, to a fixed set of boundary conditions, and to an analytic neutral model, but yet much more sophisticated than the "minimal" B2 model. All these limitations make it unsuitable for simulations of future tokamak devices. The comparison is performed in order to investigate the importance and influence of the additional physics in SOLXY. For comparison the geometry, the transport coefficients and the boundary conditions of the B2 code are adapted so as to be identical to those used in SOLXY calculations (see subsection 4.4.2). Also the "minimal" B2 model for neutral particle interaction with the plasma is adapted to approximate the analytic neutral model of SOLXY. In a last subsection, 4.4.3, interpretation of the results identifies the most important terms dealing with currents and drifts, which are missing in the equations of the "standard" B2 code. This results in an adapted version of B2, the so-called B2-vdp version.

4.4.1 Comparison of the B2 basic equations with SOLXY physics content

The major advantage of the SOLXY code is that it incorporates current densities ($j_{||}$, $j_{\perp}$ and j_r) and a perpendicular drift ($V_{\perp}$). With the first results on a poloidal limiter configuration published in 1987 [15], this seems to be the first approach including such physics in a 2-dimensional edge code. Later, the code was modified to investigate the edge plasma of TEXTOR with a toroidal ALT limiter [53] to [18].
The code is based on the following assumptions :

A. Configurational aspects :

1) The metric coefficients are preset according to TEXTOR configurations with $h_\theta = r$, $h_\phi = R$, $h_r = \frac{R_0}{R}$.

2) For derivation of the basic two-fluid equations, $\frac{1}{r}$ is neglected compared to $\frac{\partial}{\partial r}$, and r is finally replaced by a_0.

Similar to the assumptions in B2, SOLXY assumes :

B. Transport :

3) The classical cross-field transport terms are replaced by anomalous expressions in the radial direction. The radial momentum equation is replaced by a diffusive transport

relation of the Fick type. Radial transport coefficients are determined by diffusion coefficients : $\eta_r = mnD_\eta$ and $\kappa_r = nD_\kappa$ with $D = D_\eta = D_\kappa$.

4) The viscosity tensor is simplified ; cross-field derivative terms are neglected.

5) Terms due to curvature of $\vec{B}$ and gradients of B are only partially retained.

In the B2-88 code all terms resulting from currents are neglected ($\vec{j} = 0$). This assumption can be justified, only partly, for typical tokamak plasma edge conditions. The influence of currents on the convective terms and of the ohmic heating term in the electron energy equation, Eq. (2.106), is negligible in comparison with the large amount of radial energy transport into the scrape-off layer. For the radial current the contribution in the convective term is small compared to the large anomalous diffusive radial transport. For the poloidal component of the current, this is a consequence of the nearly uniform plasma profiles along the magnetic flux surfaces inside the separatrix and a low induced toroidal current near the last closed flux surface. A shielding effect of the electrostatic potential reduces the poloidal component of the electric current outside the separatrix, as will be explained in subsection 5.5.3.
In contrast, the assumption of local ambipolarity applied to the third term of the right hand side of the electron energy equations, Eq. (2.106), and to the first term of the ion energy equation, Eq. (2.104), can not be justified so easily. The classical energy equations include a contribution to heat transfer from ions to electrons $\vec{j} \cdot (\vec{V}_i \times \vec{B}) = \vec{V}_i \cdot (-\vec{j} \times \vec{B})$. Neglecting radial currents, only the normal contribution $V_{i,r}(-\vec{j} \times \vec{B})_r$ remains to be considered. Keeping only the dominant terms, the radial component of the ion momentum equation reduces to the equilibrium equation $(\vec{j} \times \vec{B})_r = (\vec{\nabla} p)_r$. So, in addition to the $(\vec{V}_i \cdot \vec{\nabla} p_e)_r$ term already present in equation, Eq. (2.106), we have found an additional term

$$- V_r \frac{\partial p}{h_r \partial u^r} = -V_r \left(\frac{\partial p_i}{h_r \partial u^r} + \frac{\partial p_e}{h_r \partial u^r} \right) \tag{4.20}$$

originating from the equilibrium current heating contribution. Therefore, this ion-electron heat transfer term in the B2 equations, Eqs. (3.9) and (3.10), transform from $V_r . \frac{\partial p_e}{h_r \partial u^r}$ to $-V_r . \frac{\partial p_i}{h_r \partial u^r}$. This term can play a significant role in the energy equations, because it is, due to the assumption of anomalous radial transport, of the same order of magnitude as the radial component of the divergence of the heat flux. However, the term should be handled with care, as is discussed in appendix B.
In this case the energy equations become :

$$\begin{aligned} \frac{\partial}{\partial t}\left(\frac{3}{2} n T_e\right) + \frac{1}{\sqrt{g}} \frac{\partial}{\partial u^\theta} \left(\frac{\sqrt{g}}{h_\theta} \frac{5}{2} n V_\theta T_e - \frac{\sqrt{g}}{h_\theta^2} \kappa_\theta^e \frac{\partial T_e}{\partial u^\theta} \right) + \\ \frac{1}{\sqrt{g}} \frac{\partial}{\partial u^r} \left(\frac{\sqrt{g}}{h_r} \frac{5}{2} n V_r T_e - \frac{\sqrt{g}}{h_r^2} \kappa_r^e \frac{\partial T_e}{\partial u^r} \right) = \\ S_E^e - k\,(T_e - T_i) + \frac{V_\theta}{h_\theta} \frac{\partial p_e}{\partial u^\theta} - \frac{V_r}{h_r} \frac{\partial p_i}{\partial u^r} \end{aligned} \tag{4.21}$$

$$\frac{\partial}{\partial t}\left(\frac{3}{2}nT_i + \frac{1}{2}\rho V_{\parallel}^2\right) +$$
$$\frac{1}{\sqrt{g}}\frac{\partial}{\partial u^\theta}\left[\frac{\sqrt{g}}{h_\theta}\left(\frac{5}{2}nV_\theta T_i + \frac{1}{2}\rho V_\theta V_{\parallel}^2\right) - \frac{\sqrt{g}}{h_\theta^2}\left(\kappa_\theta^i\frac{\partial T_i}{\partial u^\theta} + \frac{1}{2}\eta_\theta^i\frac{\partial V_{\parallel}^2}{\partial u^\theta}\right)\right] +$$
$$\frac{1}{\sqrt{g}}\frac{\partial}{\partial u^r}\left[\frac{\sqrt{g}}{h_r}\left(\frac{5}{2}nV_r T_i + \frac{1}{2}\rho V_r V_{\parallel}^2\right) - \frac{\sqrt{g}}{h_r^2}\left(\kappa_r^i\frac{\partial T_i}{\partial u^r} + \frac{1}{2}\eta_r^i\frac{\partial V_{\parallel}^2}{\partial u^r}\right)\right] =$$
$$S_E^i + k\left(T_e - T_i\right) - \frac{V_\theta}{h_\theta}\frac{\partial p_e}{\partial u^\theta} + \frac{V_r}{h_r}\frac{\partial p_i}{\partial u^r} \tag{4.22}$$

Therefore, in addition to the standard B2-code, a new version of the code is written replacing equations, Eqs. (3.9) and (3.10), by equations, Eqs. (4.21) and (4.22). This version henceforth is referred to as the B2-vdp code.

4.4.2 Transport coefficients, boundary values and neutral modelling

In this subsection the transport coefficients, boundary conditions and neutral model implemented in the B2 code according to the SOLXY prescriptions are described.

Transport coefficients

The physical parameters for comparison of B2 with SOLXY have been chosen as in the SOLXY model : the classical parallel transport coefficients have been empirically scaled with a multiplication factor of 0.222. The radial anomalous diffusion coefficient D equals 0.6 m^2/s, and $\kappa_r^{e,i} = nD$, $\eta_r^i = mnD$.

Boundary conditions

On the magnetic flux surface at 44 cm :
$V_\theta = 0$ m/s, ie. zero poloidal velocity.

All other plasma variables are assumed to be constant on this flux surface and, instead of the value of these constants, the following total fluxes across that surface are prescribed :
$\Gamma_r^{total} = 1.88 \times 10^{21}\ s^{-1}$
and rather low heat fluxes are taken :
$Q_r^e = 26.6$ kW
$Q_r^i = 27.2$ kW

At the limiter, plasma sheath edge conditions are imposed on both sides :
$V_\theta = \frac{B_\theta}{B}c_s$
$Q_\theta^e = 5.5T_e n V_\theta$
$Q_\theta^i = 3.5T_i n V_\theta$

At the liner wall (coincident with the flux surface at 50 cm in this model) :
$n_i = \frac{1}{16}n_{separatrix}$

$\frac{1}{h_r}\frac{\partial T_e}{\partial u^r} \sim 0$
$\frac{1}{h_r}\frac{\partial T_i}{\partial u^r} \sim 0$

Continuity is enforced at a poloidal angle 45 ° below the outermost midplane (i.e. at the limiter position), radially inside the separatrix for :

the density,

the parallel velocity and the gradients in the poloidal direction of the parallel velocity

the electron and ion temperature and the electron and ion heat flux in the poloidal direction.

Neutral modelling

The neutral model which is used in SOLXY is much more sophisticated than the simple default analytic model of B2 (further referred to as the "minimal" model and described in section 3.5), but the motion of neutral particles is still strongly influenced by the presence of a magnetic field (see section 3.5, Refs. [15] and [78]), because neutral particle trajectories are described on the numerical rectangular grid instead of on the physical mesh. The source of neutral particles at the limiter plate comprises 5 eV atoms, which are launched towards the plasma with a maximum polar angle of 27 ° measured from the normal on the material boundary, in order to approximate Monte Carlo calculations. These atoms can interact with the plasma by ionization and charge exchange. After a charge exchange event the neutralized ion is assumed to be lost from the plasma, so that the possibility for these neutrals to subsequently ionize in the scrape-off layer is neglected. The results obtained by both codes are influenced by their neutral model, as I showed in Ref. [52], and thus can produce different profiles. Therefore, we have tuned the analytic "minimal" B2 model by appropriate choices for the free model parameters foreseen in B2-88 in order to obtain an ion density of 4.128×10^{18} m^{-3} at the core boundary and a neutral density profile similar as SOLXY results [53].
First results with the B2 code using the "minimal" model results in a neutral density (see figure 4.12) which is spread through-out the modelled volume. With this model neutral particles are even launched from the plate to the poloidal location opposite to the limiter This is mainly due to the absence of charge exchange which would reduce the mean-free-path for neutrals (cfr. Monte Carlo calculations for TEXTOR, section 4.5). Another typical but rather unrealistic feature of the "minimal" B2 model is the increasing neutral density profile in the poloidal direction away from the limiter.
In order to obtain more realistic neutral profiles similar to those of SOLXY calculations (see Fig. 4.13), the plasma particle source due to neutrals is limited to a region near the limiter (about 50 cm from the limiter according to the results of [53]). In addition, the neutrals that have migrated inside the separatrix cannot be ionized (see Fig. 4.14). After these adaptations the neutral particle model of B2 will only roughly approximate the SOLXY model, because charge exchange processes between neutrals and ions are still not incorporated. Nevertheless, the neutral particle interaction with the plasma now is at least near the limiter. Furthermore, the neutral density at the limiter tip have values of the same order of magnitude.

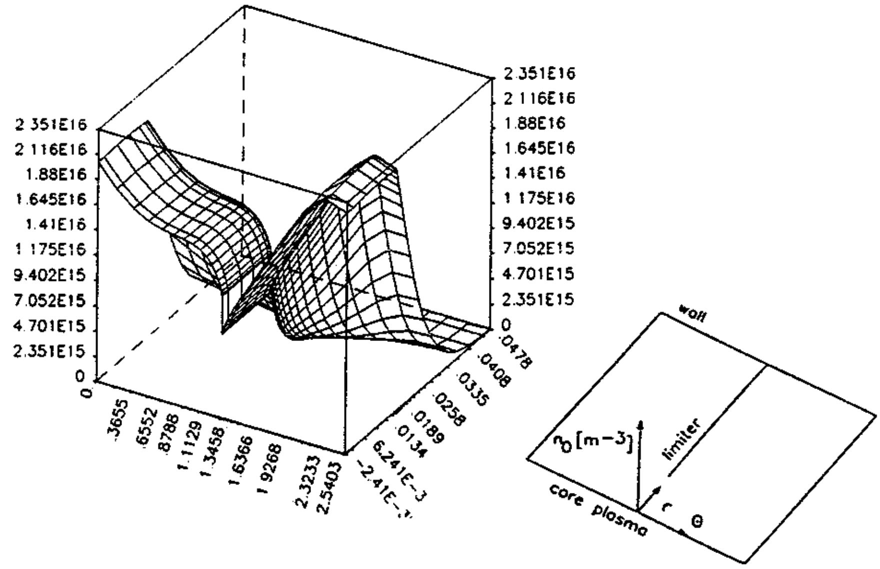

Figure 4.12: Neutral density profile obtained with the standard "minimal" model

4.4.3 Results and conclusions

Results of the B2-88 code

Even when the results of the neutral density looks like the one in SOLXY, there is not even a qualitative agreement of all other plasma parameters.
A first comparison between results of the B2-88 code with those of SOLXY is performed by looking at the plasma variables at the core boundary. It should be mentioned that in the B2 code the free parameters of the "minimal" model are chosen such that the density at the core boundary equals the value as obtained with SOLXY calculations. Therefore, the comparison of the ion and electron temperature give a relevant measure for agreement between the B2 and the SOLXY code. In table 4.1, we can see that the electron temperature at the core boundary is significantly lower and the ion temperature is significantly higher for B2. This means that in B2-88 the electrons are loosing more energy in the scrape-off layer than in the SOLXY calculations, and vice versa for the ions.

	B2	SOLXY
n_i[m^{-3}]	4.128×10^{18}	4.128×10^{18}
T_e[eV]	28.73	33.87
T_i[eV]	37.48	30.56

Table 4.1: Comparison of core boundary values, B2-88 model

By means of Figs. 4.13-4.20 plasma profiles can be compared. While the ion density represents similar results, except near the limiter tip, as is shown in figures 4.15-4.16, the electron temperature and most of all the ion temperature profiles are completely different (see figures 4.17-4.18 and 4.19-4.20 respectively). The results obtained with the B2 code lead to a weakly radially outward increasing ion temperature profile inside the separatrix. This is in sharp contrast with the SOLXY results which show an opposite behaviour. These results might be caused by differences in physics content between B2 and SOLXY. Therefore, we will introduce the additional heat exchange term (Eq. (4.20)) as was suggested in subsection 4.4.1. The code with this modification is called B2-vdp.

Results obtained with B2-vdp

The core boundary values for electron and ion temperature obtained with the B2-vdp version of the code are compared in table 4.2. This table shows that the ion temperature is reduced below the electron temperature. The neutral density (Fig. 4.21) and the ion density profiles (Fig. 4.22) do not change much. The ion temperature profile (Fig. 4.24) is now decreasing radially outward. And the shape of both the ion and electron temperature profiles (Fig. 4.22 and Fig. 4.23 respectively) are qualitatively in good agreement with the SOLXY results. Quantitative results between the B2-vdp and SOLXY code actually differ only by about 6 %.

	B2-vdp	SOLXY
$n_i[\mathrm{m}^{-3}]$	4.128×10^{18}	4.128×10^{18}
T_e[eV]	36.08	33.87
T_i[eV]	30.33	30.56

Table 4.2: Comparison of core boundary values, B2-vdp model

Conclusions

Comparison with the SOLXY code thus shows that the assumption of local ambipolarity in B2 may lead in some circumstances to unphysical ion temperature profiles which increase radially outwards. Indeed, introducing the additional heat exchange term, Eq. (4.20), in the B2-vdp version, which occurs if currents in the diamagnetic direction are partly taken into account, gives qualitatively good agreement with the original SOLXY results. Moreover, quantitative results between the B2-vdp and SOLXY code differ only by about 6 %. Nevertheless, it should be noted that this particular correspondence between the results of the two codes is not a sufficient justification for using the additional heat exchange term in the B2 code as is discussed in appendix B.

4.5 Impact of improved neutral modelling for TEXTOR applications

As was already indicated in section 4.4, B2 does not necessarily correctly describe the interaction of neutral particles with the plasma. Neither does the neutral gas model in SOLXY. Results from both codes, however, should strongly depend on such model assumptions. In order to eliminate this major uncertainty and to be able to obtain the required information concerning neutral particle interaction with the plasma in a more reliable way, the B2 code has been coupled to a Monte Carlo code, EIRENE. The coupling of these two codes was performed, as an important part of this work, in collaboration with D. Reiter (Forschungszentrum Jülich, Germany). The EIRENE code has been developed

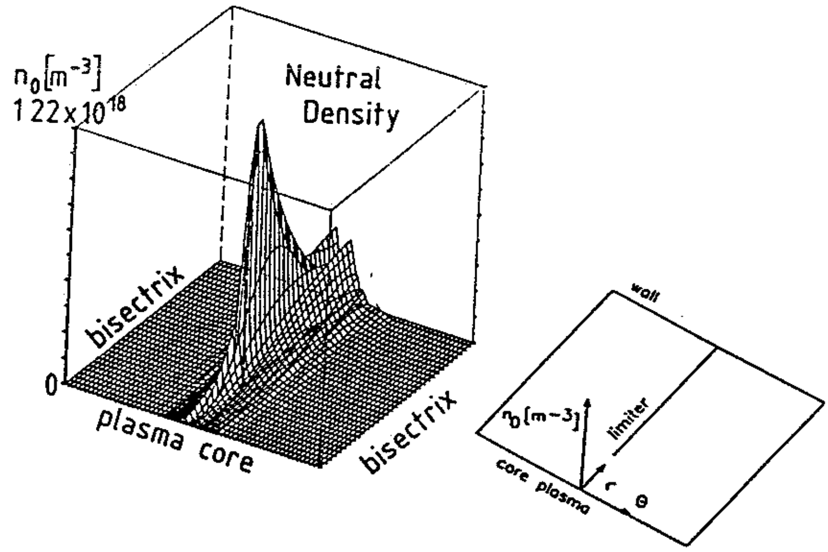

Figure 4.13: Neutral density obtained with SOLXY taken from Ref. [53]

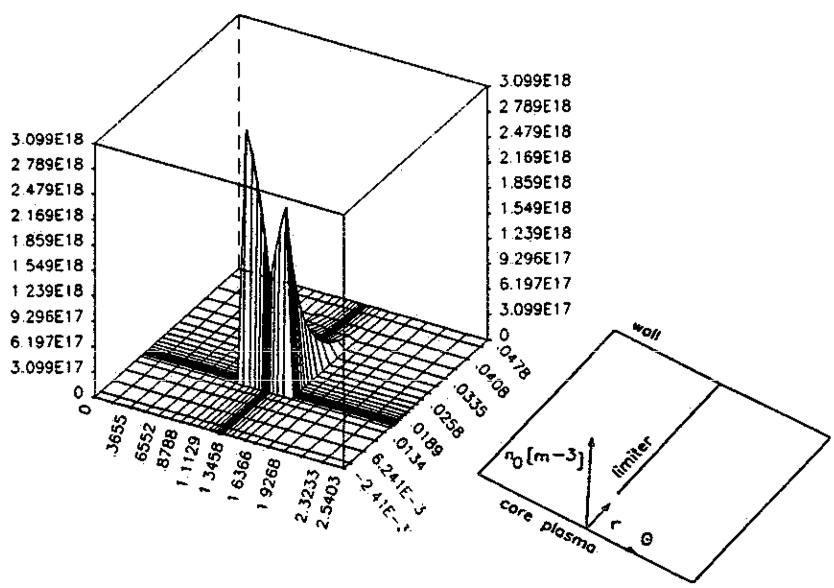

Figure 4.14: Neutral density obtained with B2

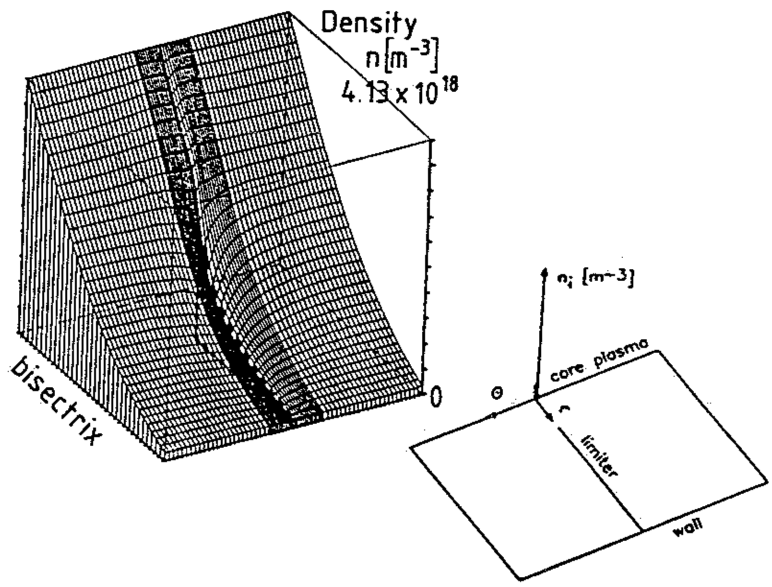

Figure 4.15: Ion density obtained with SOLXY taken from Ref. [53]

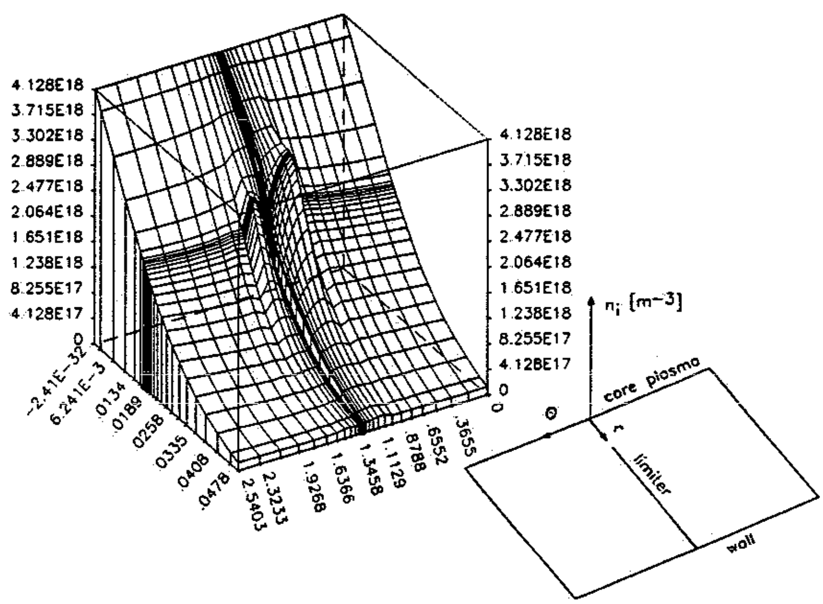

Figure 4.16: Ion density obtained with B2

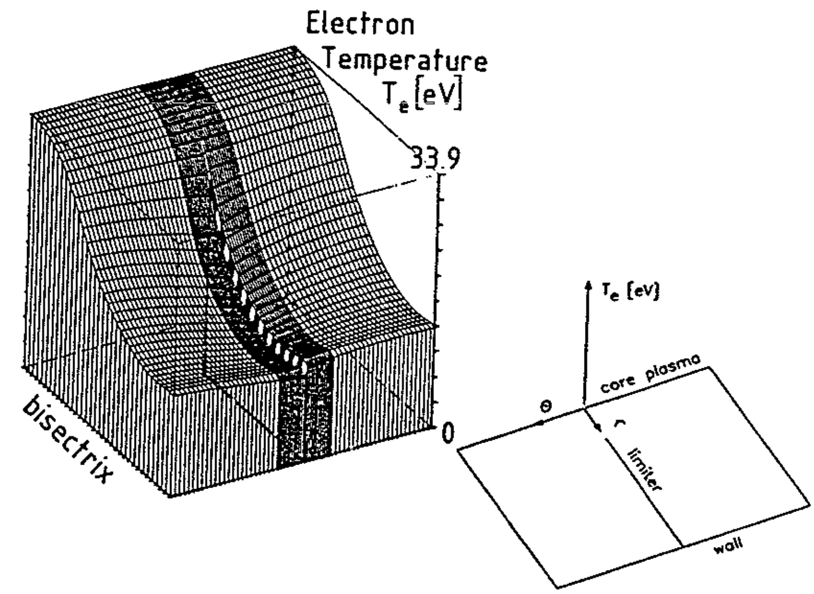

Figure 4.17: Electron temperature obtained with SOLXY taken from Ref. [53]

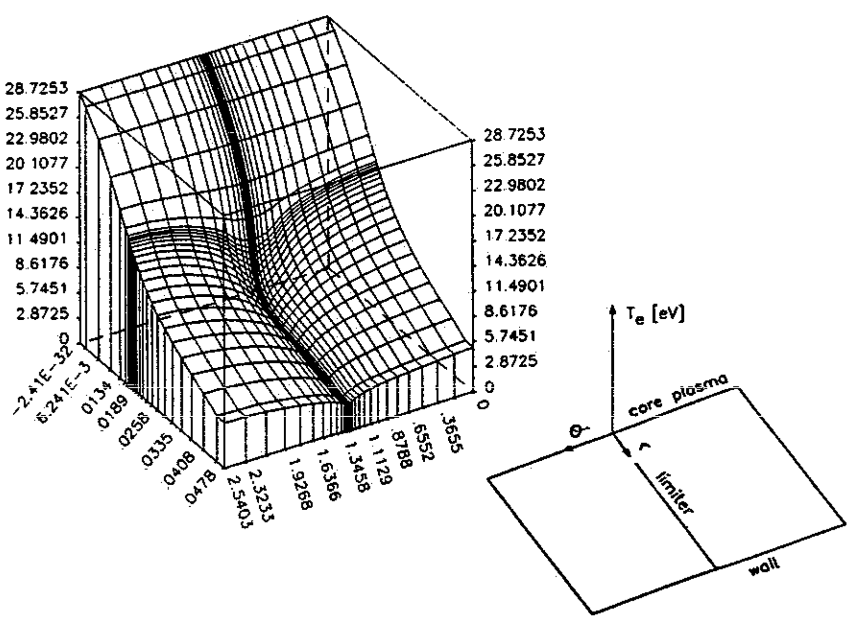

Figure 4.18: Electron temperature obtained with B2

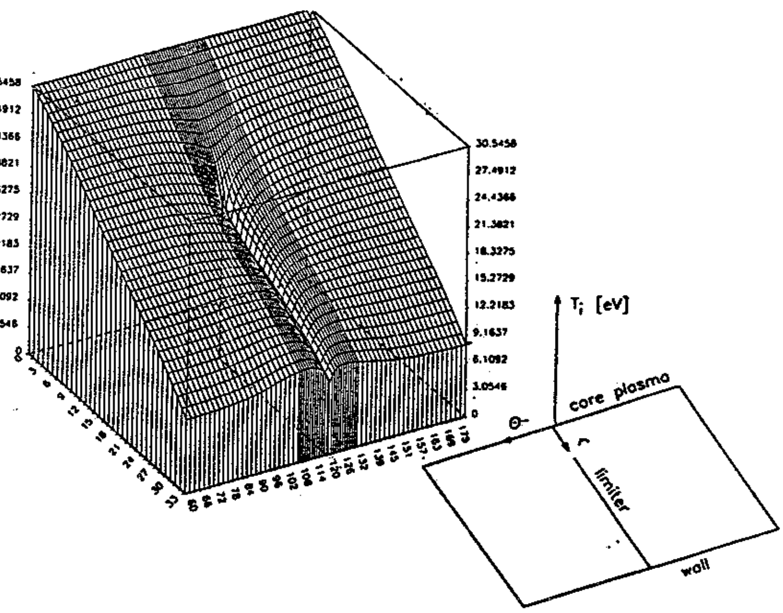

Figure 4.19: Ion temperature obtained with SOLXY

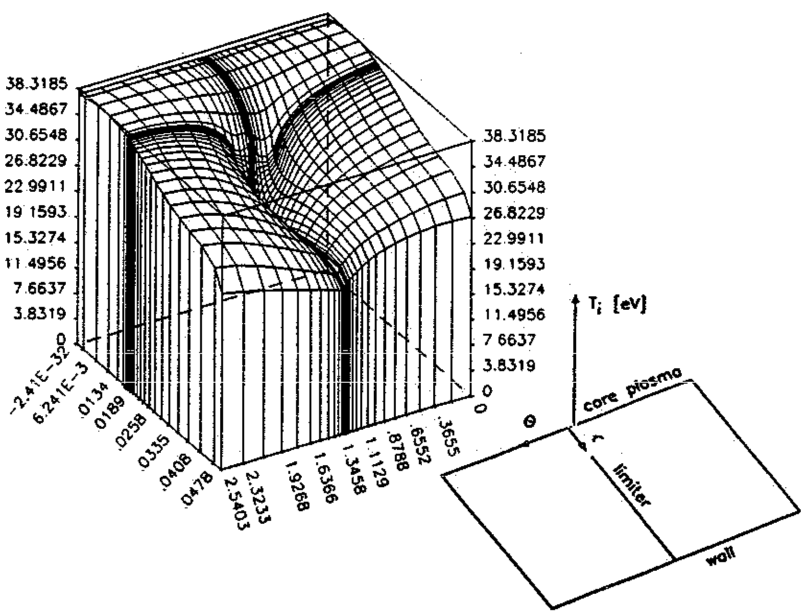

Figure 4.20: Ion temperature obtained with B2

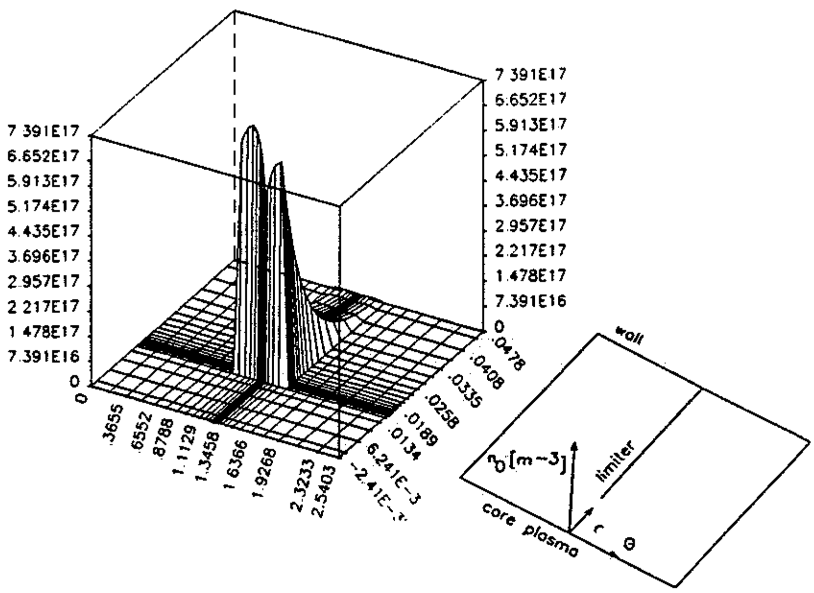

Figure 4.21: Neutral density obtained with B2-vdp

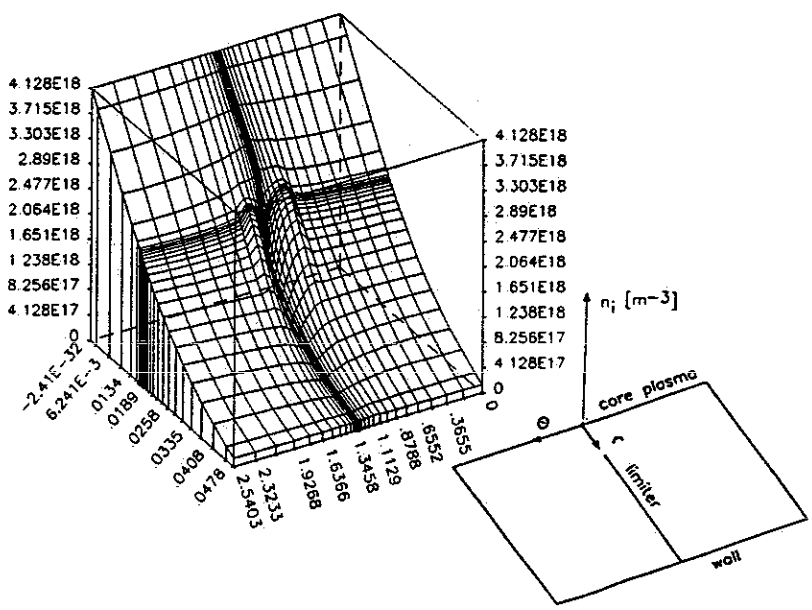

Figure 4.22: Ion density obtained with B2-vdp

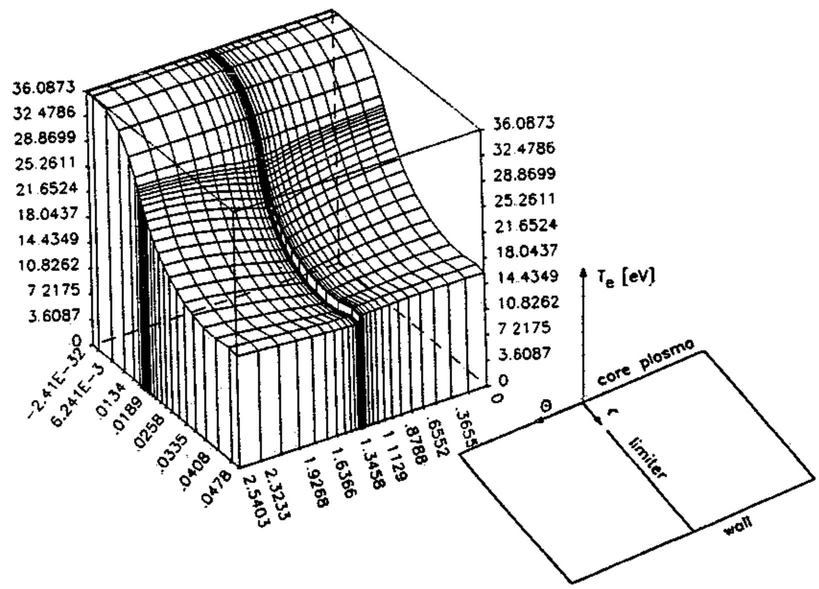

Figure 4.23: Electron temperature obtained with B2-vdp

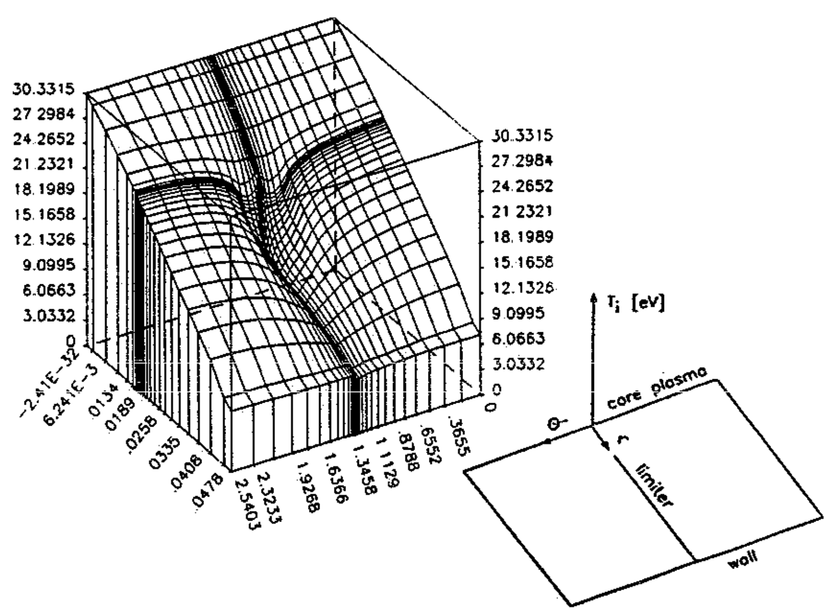

Figure 4.24: Ion temperature obtained with B2-vdp

by Reiter (see Refs. [20] and [74]) to describe neutral gas transport in tokamak plasmas, and can handle a large variety of problems. Therefore, the combination of these two codes is very useful to investigate present experimental fusion devices and to explore features of next generation tokamaks. In this section we show the importance of a relevant neutral model in edge transport calculations. In a first subsection, 4.5.1, the coupling between these two codes is described and compared with a simple iterative procedure. In a second subsection, 4.5.2, results obtained with the "minimal" model are compared to those of a coupled B2-EIRENE calculation.

4.5.1 Convergence of B2-EIRENE calculations

The B2-EIRENE coupling

The B2 code needs additional information concerning magnetic configuration and neutral particle interactions with the plasma in order to calculate plasma profiles. This is done by iteratively solving the governing fluid equations with the appropriate boundary conditions on a mesh which structure is governed by the magnetic geometry, and where these neutral particle interactions appear as sources and sinks. Conversely, the EIRENE code starts from plasma profiles, a prescription of surrounding material boundaries and atomic and molecular data ($A+M$ data) to perform 3-D Monte Carlo transport calculations of neutral particles.

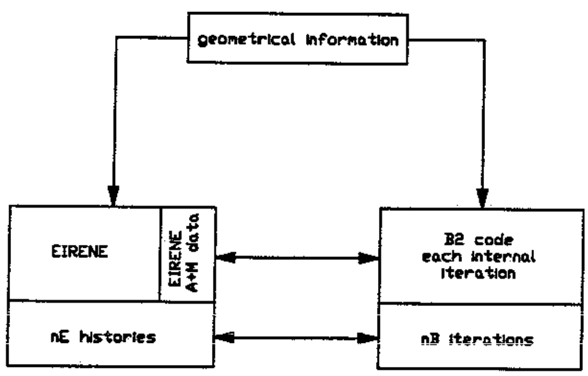

Figure 4.25: B2-EIRENE coupling

Because the numerical treatment of these two codes is totally different, the most straightforward way to couple them seems to be an iterative procedure, in which each code successively provides the necessary information for the other one. This coupling procedure is referred to as "external iteration" (see figure 4.25). In such an iterative procedure, the B2 code will run a prescribed number of iterations nB, and in the EIRENE code a certain number nE of test particles will be followed. These "stand alone" computations are interrupted regularly to permit exchange of information : the B2 plasma state is transferred to EIRENE, the plasma sources arising from interactions with neutrals are forwarded from EIRENE to B2. During a B2 calculation, the sources are adjusted proportionally to the particle flow to the targets (limiter/divertor plate) at every iteration, keeping the recycling coefficient at the material boundary constant (used to simulate pumping).

This simple procedure turned out to be insufficient to guarantee convergence in cases where the neutral model significantly influences or even dominates the plasma profiles near material boundaries, such as e.g. under high recycling divertor conditions. For example, this external iteration method provided satisfactory solutions for TEXTOR applications with a prescription of constant plasma parameters at the core boundary. But numerical problems arose when total particle and energy fluxes from the core are prescribed instead (as was done in section 4.4.2), since then e.g. the absolute value of scrape-off layer density is much more sensitive to neutral gas transport details. Furthermore, for divertor applications an improved coupling is necessary.

An improvement of the coupling is realized by introducing the so-called "short-cycle". In this case, neutral sources in B2 are not only proportional to the plasma fluxes to the targets during the iterations. In addition, influences on source terms from changes in plasma profiles are anticipated by algebraic expressions based on the atomic data and new source terms are calculated at each time-step in the B2-iteration. A B2 run is now interrupted as soon as relative changes in plasma profiles exceed a prescribed limit and an EIRENE run is started.

Results and conclusions

Figure 4.26 shows the convergence behaviour for both the external coupling with only the internal flux scaling for the neutral source-terms in B2 and the intrinsic coupling procedure, which uses the "short-cycle", for a TEXTOR case as calculated in section 4.4, but with prescribed plasma parameters at the core boundary :

$V_\theta = 0$ m/s, ie. zero poloidal velocity

$n_i = 4.128 \times 10^{18}$ s^{-1}

$T_i = 29$ eV

$T_e = 38$ eV

For this particular case, which was chosen in order to obtain an EIRENE-B2 solution without using the "short-cycle" coupling procedure, there is not enough influence from the neutral particles for the more advanced coupling to improve convergence behaviour. Nevertheless, the intrinsic coupling is needed whenever neutral particle behaviour influences plasma parameters more strongly. For example the simple external coupling, without "short-cycle" is already insufficient for TEXTOR simulations with a constant, but unknown, ion density and a total ion particle flux prescribed at the core boundary (as was used in section 4.4.2).

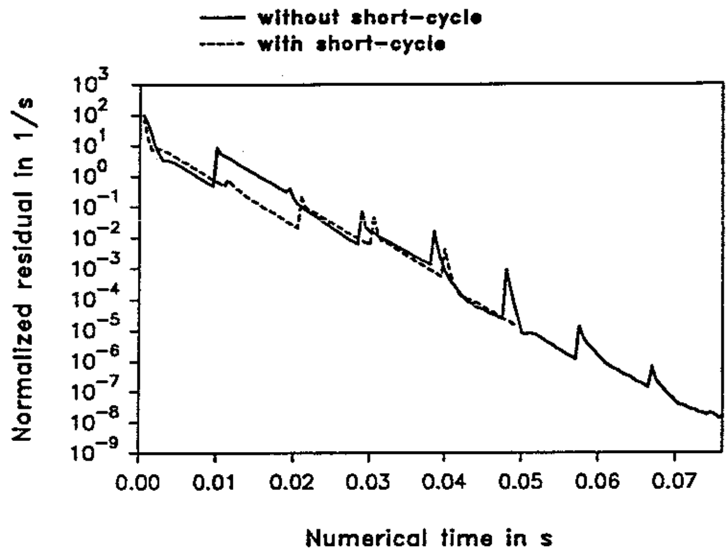

Figure 4.26: Convergence behaviour for different coupling procedures

4.5.2 Coupled B2-EIRENE calculations

Results compared with the standard "minimal" model

Figures 4.27 to 4.30 show, respectively, the results for the neutral particle density, the ion density and the electron and ion temperatures of a converged coupled B2-EIRENE run as described above. They can first be compared with the results obtained with the adapted "minimal" model (see figures 4.14, 4.16, 4.18 and 4.20 respectively).
The core boundary value for the density is now determined by the Monte Carlo recycling model, and somewhat lower than the one obtained with SOLXY, and thus with B2 calculations using the minimal model. The plasma profiles outside the separatrix are not very sensitive to the different neutral models, because for the open geometry, in which the major part of neutrals is ionized inside the separatrix, the parallel transport towards the limiter dominates over the neutral particle interactions. In contrast, the ion density and the ion temperature profiles close to but inside the separatrix are strongly influenced. For the density profile, a maximum near the limiter tip is obtained (see figure 4.28), due to the neutral particle source inside the separatrix. At the same location, a local minimum for the ion temperature profile can be observed. This shows the strong dependence of the ion temperature profile on the ion density profile as was already investigated in Ref. [52], in which I showed the need of a realistic neutral particle model in edge modelling.

Influence of the additional heat exchange term

Implementation of the additional heat transfer term in the energy equations in combination with the Monte Carlo neutral model leads to the qualitatively similar effect as with the minimal model : i.e. lowering the ion temperature (see figure 4.32) and increasing the electron temperature (see figure 4.31). Core boundary values for ion and electron temperature are respectively 10 and 6 % lower than those obtained with SOLXY.

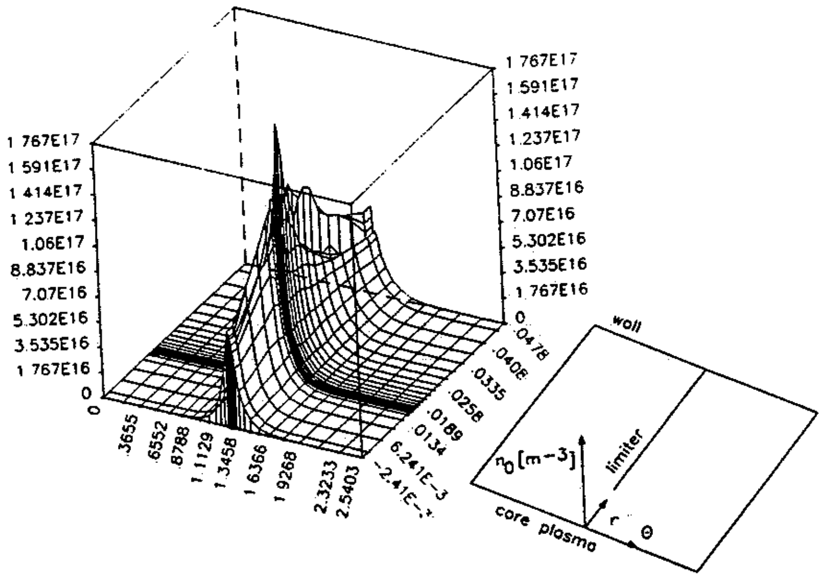

Figure 4.27: Neutral density obtained with B2-EIRENE

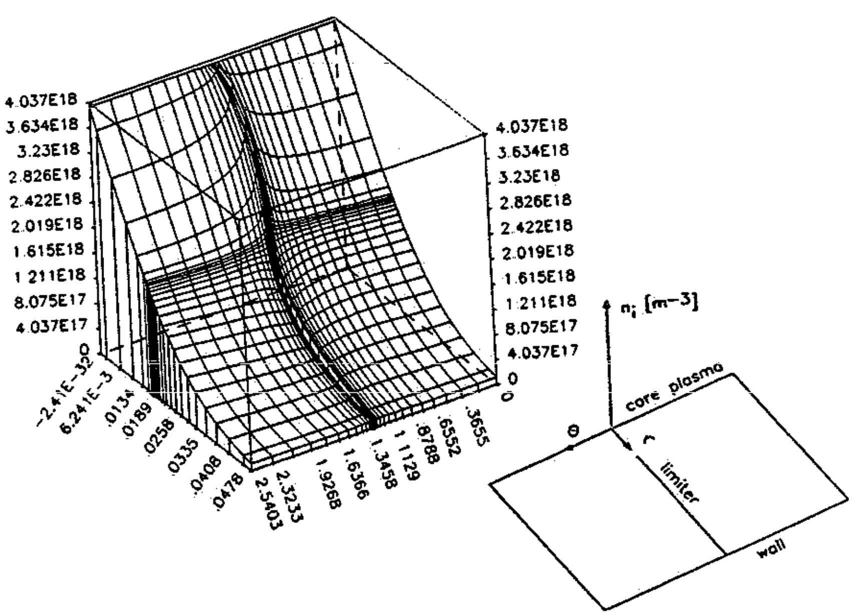

Figure 4.28: Ion density obtained with B2-EIRENE

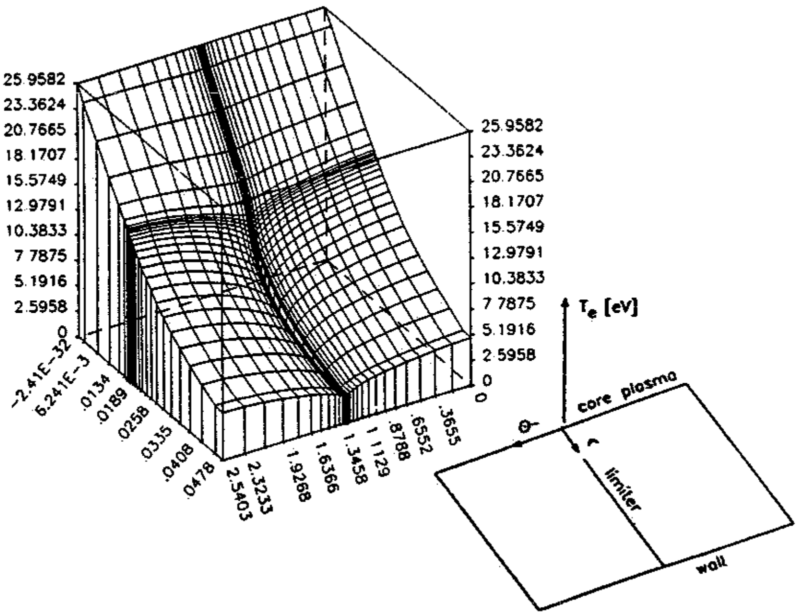

Figure 4.29: Electron temperature obtained with B2-EIRENE

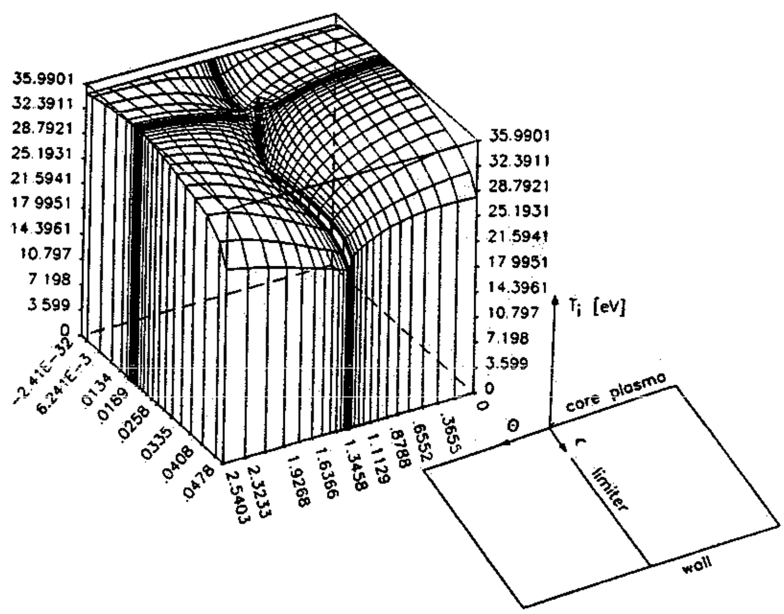

Figure 4.30: Ion temperature obtained with B2-EIRENE

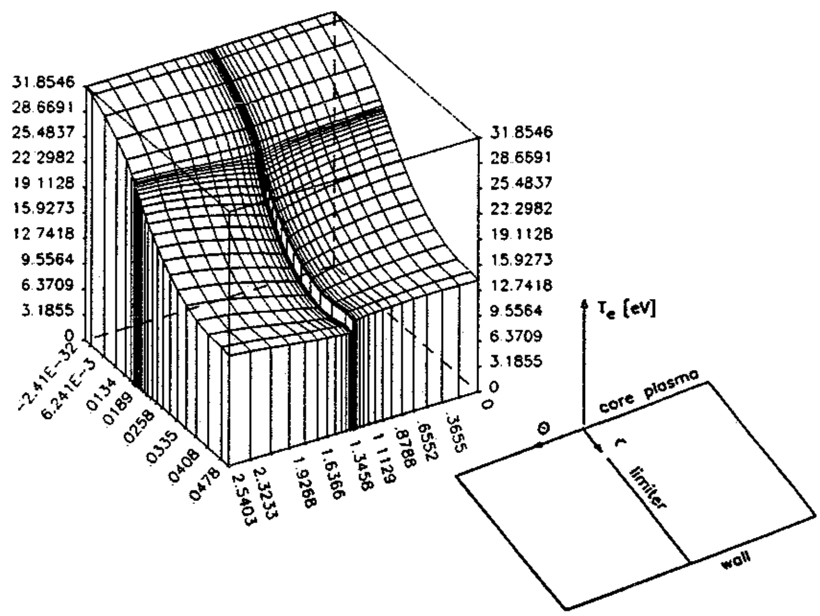

Figure 4.31: Electron temperature obtained with B2-vdp-EIRENE

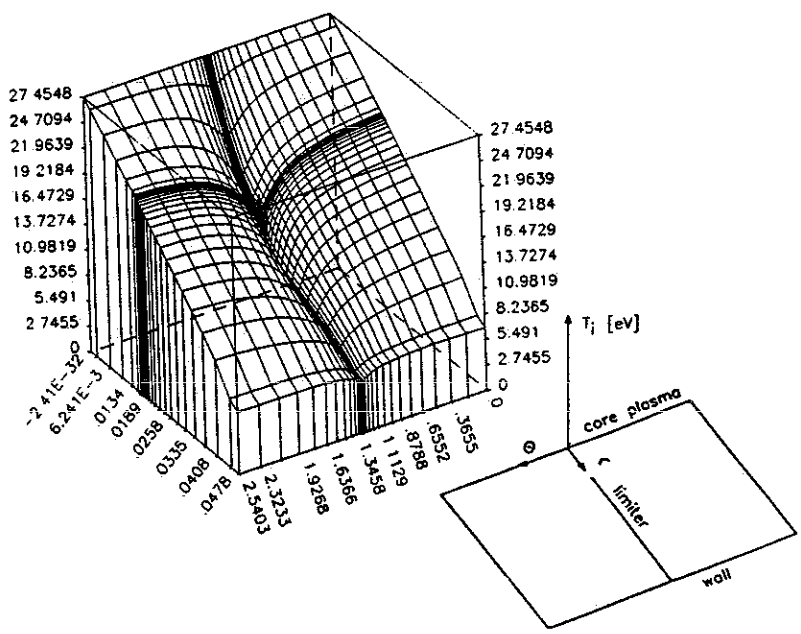

Figure 4.32: Ion temperature obtained with B2-vdp-EIRENE

Although implementation of the additional heat exchange term, at least for the calculations with the simplified analytic neutral model, gives rise to more monotonically radially decreasing profiles, the complete Monte Carlo recycling model without this additional heat transfer term already results in an ion temperature above the electron temperature. This result is close to experimental trends observed in TEXTOR [79].

Conclusions

Since the "minimal" neutral particle model of B2 is too naive to handle a variety of magnetic configurations and plasma conditions, as was already shown in section 4.4.2, the B2-EIRENE coupling provide a useful modelling tool which at least eliminates a major unknown in the fluid equations. For the TEXTOR case, it can be seen that the neutral particle model mainly influences the ion density and ion temperature profile inside the separatrix. In order to obtain similar results as with the SOLXY code, again the introduction of an additional heat exchange term between ions and electrons (*vdp* or Eq. (4.20)) is required. In this case, introduction of the detailed Monte Carlo description for neutral particles reduces the ion and electron temperature at the core boundary with 10 and 6 % respectively in comparison with the SOLXY results.

4.6 Poloidal electron density asymmetries

Poloidal asymmetries in plasma parameters in the scrape-off layer can be caused by several phenomena. For TEXTOR, already the position of the ALT-limiter will induce certain asymmetries, henceforth this will be called the geometrical effects on asymmetries. Further, poloidal plasma rotation (or drift) originated from radial pressure gradients and radial electric fields (cfr. $\frac{1}{h_r}\frac{\partial}{\partial u^r}p_i$ and $Z_i e n_i \frac{1}{h_r}\frac{\partial \phi}{\partial u^r}$ of Eq. (2.97)) can have some influence ([80], [81],[19]). Since in this equation the magnitude of the magnetic field occurs in the term of the diamagnetic component of the ion velocity, the latter will depend on the direction of $\vec{B}$.
For TEXTOR, poloidal asymmetries have already been measured by Samm et al. [19] and compared with results of the edge plasma code SOLXY. A short description of their work, together with new experimental results, is given in a first subsection. These results are compared with poloidal asymmetry effects as obtained with B2-vdp-EIRENE calculations in subsection 4.6.2.

4.6.1 Experimental results

Recently, the electron density was measured in TEXTOR with two thermal lithium beams located at the bottom and the horizontal midplane (see figure 4.33), for standard and reversed directions of the toroidal magnetic field [19]. The standard direction is antiparallel to the plasma current (see figure 4.33). The change in direction of the toroidal magnetic field in these experiments modifies the asymmetries (see figure 4.34). Taking into account the change in direction of ion and electron drift flows, Samm et al. conclude that a higher electron density was measured at the electron side in comparison to the electron density at the ion side (electron and ion drift side are defined in section 6.2.1 and depend

on the direction of both the toroidal magnetic field and of the main plasma current). These results can be explained by the influence of particle flows in the diamagnetic direction [19]. In December 1992, similar experiments were conducted, with three lithium diagnostic beams positioned at the top, the horizontal midplane and the bottom. Reversing the magnetic field did not result in large qualitative changes of the electron density profiles. Profiles for these experiments are given in figure 4.35. Because the horizontal position of the plasma during these experiments could not be checked adequately, the data obtained with the beam at midplane position will not be interpreted for these experiments.
From the experimental results, we can conclude that, with exception for the measurement with standard toroidal magnetic field in Ref. [19], asymmetries in density profiles are rather small.

4.6.2 Comparison with B2-vdp-EIRENE calculations

The purely geometrical effects on asymmetries can easily be checked with B2-vdp-EIRENE calculations, because the standard version of the code does not take into account any drift terms,
Figure 4.36 shows the density profiles calculated with the B2-vdp-EIRENE code, which includes the additional heat exchange term (see section 4.4.1), at horizontal midplane and bottom locations. These can be compared with the results given in figure 4.34. These results show profiles which correspond qualitatively to an average of the profiles obtained by Samm et al. [19] (see figure 4.34). In contrast, the SOLXY calculations, which did include the drift terms, can qualitatively simulate the measured profiles, but fail to explain the large asymmetries, as obtained with the standard direction for the toroidal magnetic field. This might be due to a change in plasma position or to the presence of material objects, which disturb the toroidal symmetry, in the vicinity of the lithium beams. In order to avoid a change in magnetic field line configuration, and thus in intersection with local material objects, it would be better to reverse both the toroidal and the poloidal magnetic field. Material objects will then at least intersect with the magnetic field lines in the same way.
In the more recent experiments (see figure 4.35), the asymmetries in electron density at top and bottom location were not influenced by the direction of the toroidal magnetic field. This indicates a purely geometrical cause of the measured asymmetries. Asymmetries in the calculated electron density profiles at top and bottom locations (see figure 4.37) correspond well with recent experimental data (see figure 4.35). It should be mentioned that since the calculated profiles are obtained with this version of the B2 code, these asymmetries in numerical results are caused exclusively by geometrical effects. In both experimental and computational results the density profiles at the bottom position are lower than those at the top position. However, the position where the two profiles intersect is slightly different (at a minor radius of 47 cm for the experimental results and at a minor radius of 46 cm for the computational results).

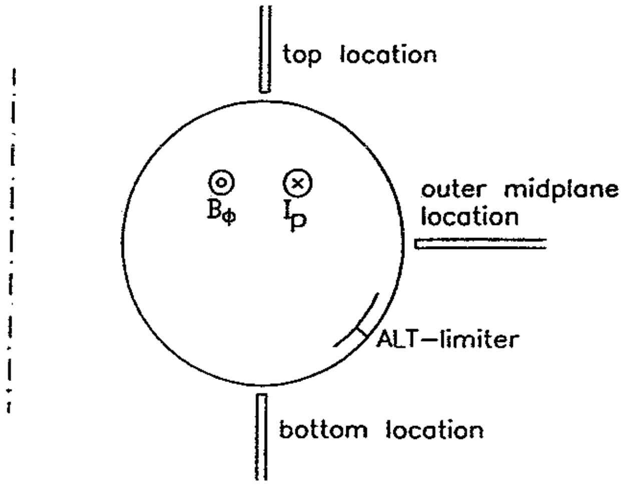

Figure 4.33: Schematic view of beam positions and magnetic field direction

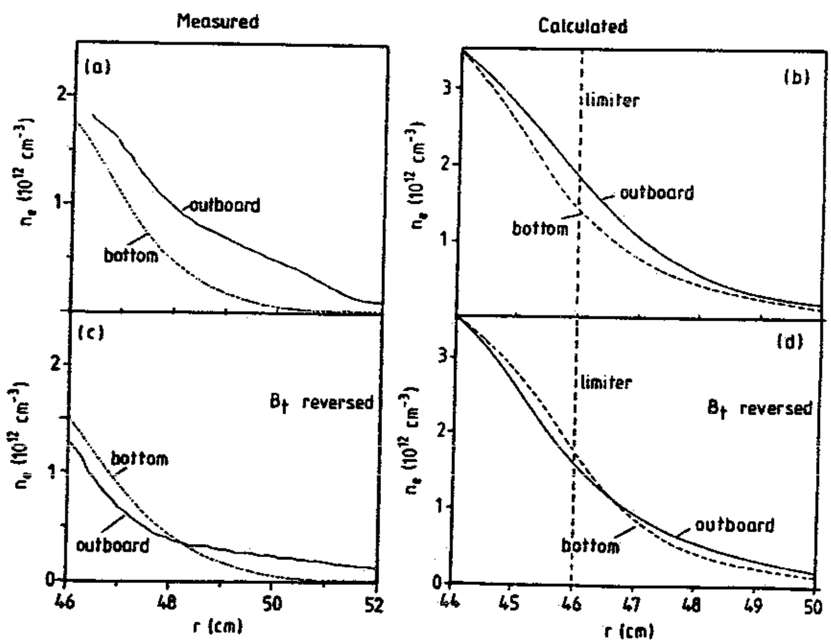

Figure 4.34: Experimental and calculated SOLXY results taken from Ref. [19]

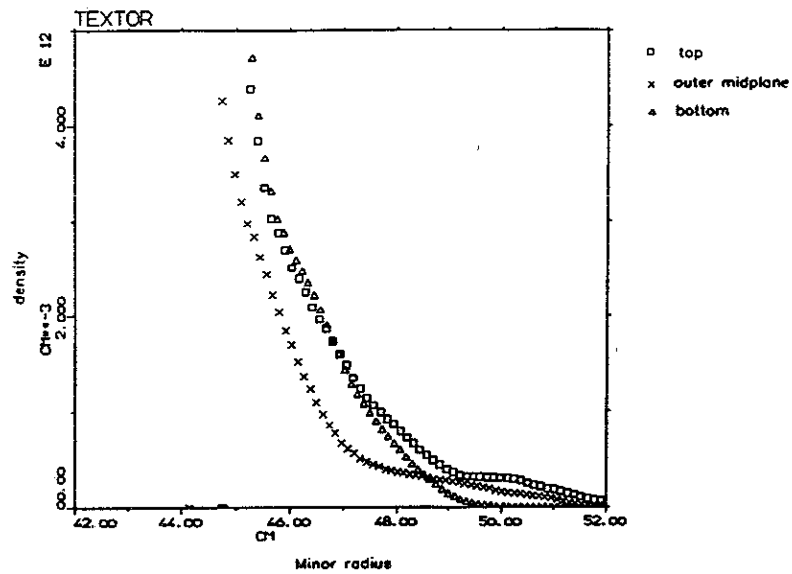

Figure 4.35: Recent experimental data

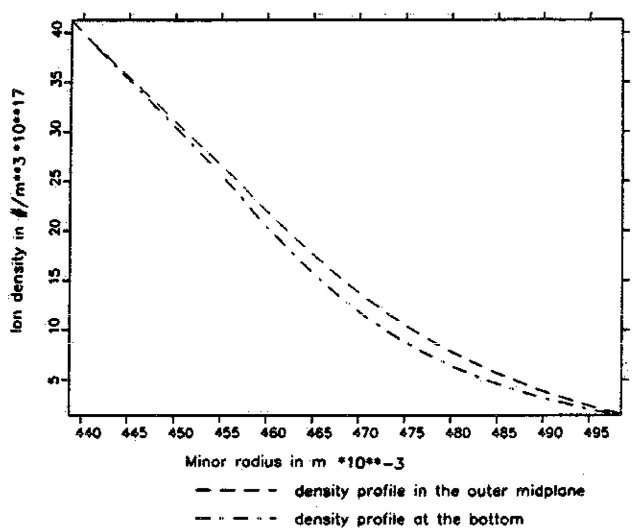

Figure 4.36: Electron density profiles at horizontal midplane and bottom locations calculated with B2-vdp-EIRENE

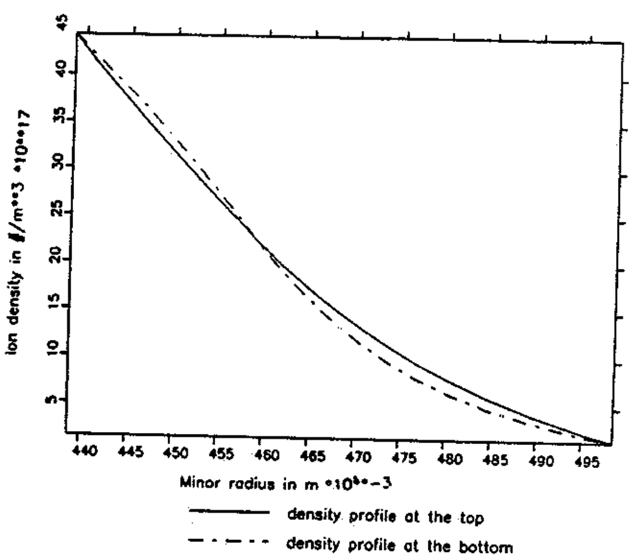

Figure 4.37: Electron density profiles at top and bottom locations calculated with B2-vdp-EIRENE

Chapter 5

Extension of the B2 code incorporating electric fields

5.1 Introduction

As was already indicated in section 2.4 two-dimensional edge plasma codes have become widespread. More recently the need to develop a data-base on edge plasma transport coefficients for the ITER divertor design has provided motivation for serious attempts at modelling edge plasma conditions in the existing Tokamaks. Although agreement between calculated and measured profiles can be achieved by altering the transport coefficients or by introducing an ad hoc constant radial inward pinch velocity, a more reliable tool for predictive calculations should be based on appropriate physics theories and therefore on local plasma conditions. In this sense more significant improvements in successful modelling of experiments can be expected from the inclusion of self-consistent plasma drifts and electric currents.

Already in 1982, Singer and Langer [65] pointed out that both influences from currents in the diamagnetic direction and from heat flow due to parallel electric currents are important for edge plasma modelling. But only very recently the implementation of these effects was the subject of considerable development efforts for edge plasma codes written for general toroidal geometries. The results obtained with the B2 code in chapter 4 confirm more particularly the major impact of the diamagnetic component of the electric current on the heat exchange term between electrons and ions.

Furthermore, in recent experimental efforts changes in plasma behaviour in general and in density control, target heat flux and target plate erosion in particular turned out to be influenced by the application of electrostatic fields in both divertor and limiter configurations [82]. This increased importance of edge control by electric fields again requires the improvement of edge plasma modelling towards a more complete description. In addition, the computation of the electric potential provides an adequate measure for comparison with reliable experimental data.

In section 5.2 the different possibilities for code extension concerning flow in the diamagnetic direction and electric fields are reviewed, a detailed survey on developed codes is given. A next section summarizes the physics content as implemented in the B2 code, henceforth referred to as extended B2. The required boundary conditions are described in section 5.4. Subsequently, the numerical treatment is given in some more detail.

5.2 Survey of 2-d edge codes incorporating flows in the diamagnetic direction or electric currents

Flows in the diamagnetic direction or electric currents can be implemented in codes with a varying degree of sophistication. In a first subsection possible extensions to standard edge modelling are described. Subsequently, a survey concerning these implementations in 2-dimensional plasma edge codes is given.

5.2.1 Possible extensions of the physics content

Different codes can be distinguished by the number of additional variables and equations, by the simplifications made in the basic equations, especially whether the additional variables are incorporated or not, and by the simplifications made in the additional equations. Starting from all possible additional variables : the diamagnetic component of the ion velocity $V_\perp$, the three components of the electric current density $j_{||}$, $j_\perp$ and j_r, and the electric potential Φ or the two components of the electric field $E_\theta = -\frac{1}{h_\theta}\frac{\partial\Phi}{\partial u^\theta}$ and $E_r = -\frac{1}{h_r}\frac{\partial\Phi}{\partial u^r}$, a logical stepwise implementation can be considered :

1) The influence of $j_{||}$ and E_θ can be introduced without knowledge of the other variables, taking the electron momentum equation in the parallel direction, Eq. (2.96), and the total continuity equation into account. Appropriate boundary conditions for boundaries at material surfaces can be derived from probe theory as described in subsection 5.4.1.

2) The inclusion of the diamagnetic component of the electric current density calculated from the radial total momentum equation is preferentially combined with the introduction of the diamagnetic component of the ion velocity, because the radial pressure gradient drives electrons and ions in opposite diamagnetic directions. As the equilibrium current density $j_\perp$ is not necessarily divergence free, at least the additional calculation of $j_{||}$ and E_θ is required.

3) For the computation of the diamagnetic component of the ion velocity knowledge of the radial electric field is required. This can easily be obtained outside the separatrix by appropriate solving of the potential equation in combination with the boundary conditions at material surfaces. On the other hand, the boundary condition inside the separatrix is a periodic condition and thus determines the electric potential up to an unknown constant value only. Therefore, inside the separatrix either the radial electric potential has to be prescribed or a correlation between radial electric current density and radial electric field has to be implemented. Based on the neoclassical equations as derived in chapter 2, this correlation is indirectly given over the diamagnetic component of the ion velocity by $j_r = f(V_\perp)$, Eqs. (2.103) or (5.7), and by $V_\perp = g(E_r)$, Eqs. (2.97) or (5.5).

4) An additional effect concerning flows in the diamagnetic direction arises in the energy equations in which a heat flow in the diamagnetic direction is originated by a radial

temperature gradient due to the so-called $\vec{B} \times \vec{\nabla} T$ drift term. The relative importance of this term is still questionable. Both Gerhauser [15] and Vold [34] neglect this term because the diamagnetic heat conduction $\kappa_\wedge$ is smaller than the parallel heat conduction $\kappa_\|$ by the classical expansion factor $(\omega \cdot \tau)^{-1} = (\rho_L/\lambda)$ (where the gyrofrequency times the collision time equals the Larmor radius over the collision mean-free path). On the other hand this term is thought to introduce asymmetries in heat power load on divertor targets [83].

5.2.2 Survey of existing codes

Only a few codes did incorporate electric currents, electric fields or particle flows in the diamagnetic direction :

1) The physics content of the EDGE-2D code [54] written by Simonini et al. only includes the parallel component of the electric current as described in item 1 of subsection 5.2.1.

2) The first 2-dimensional edge plasma code including drift terms was implemented by Gerhauser and Claaßen for a limiter Tokamak with poloidal limiter in Ref. [15]. Later on the code was adapted for a geometry with toroidal limiter in Ref. [53]. This code includes the additional plasma variables $V_\perp$, $j_\|$,$j_\perp$,j_r and Φ. The linkage between j_r and Φ is indirectly implemented by the equations using the total momentum equation in the diamagnetic direction with viscous terms omitted. Nevertheless, inside the separatrix a radial potential profile is described, which results in a discontinuity in poloidal current at the periodic boundary. Furthermore, the thermal drift flow as described in item 4 of subsection 5.2.1 is omitted. In more recent calculations [18] some additional terms resulting from $grad\vec{B}$ effects and curvature drifts are added.

3) The EPIC code [36] written in orthogonal curvilinear co-ordinates by Vold provides information about $V_\perp$ and Φ, with the electric potential calculated as described in item 2 of subsection 5.2.1. A major deficiency in these calculations is the absence of terms with the additional variables $V_\perp$ and Φ in the basic equations, which results in unphysical zero poloidal velocities in the neighbourhood of the limiter.

4) Knoll and Prinja also did some investigations on this topic in Ref. [58] implementing the same physics as in the EPIC code but including terms in $V_\perp$ and Φ in the basic equations. From their results the significance of flows in the diamagnetic direction was shown and they recommended to include both inner and outer divertor targets in the computational domain in order to avoid symmetry conditions on an intermediate poloidal boundary.

5) Only very recently Rognlien et al. [62] developed the LEDGE code, which includes cross-field drifts and electric currents in an orthogonal curvilinear co-ordinate system. In this code $\vec{B} \times \vec{\nabla} T$ was implemented, and an anomalous-like expression for the radial current density was used :

$$j_r = \sigma_{\perp,an} \left(\frac{1}{neh_r} \frac{\partial p_e}{\partial r} - \frac{1}{h_r} \frac{\partial \Phi}{\partial r} \right) \tag{5.1}$$

This code was successfully applied on a single-null divertor DIII-D [62] and a biassing experiment was simulated [84].

5.3 Basic equations of the extended B2 code

5.3.1 Assumptions

As was already mentioned in section 2.3.5, the drift velocity ($V_\perp$), which is directed perpendicular to $\vec{B}$ in a magnetic flux surface, and the three components of the electric current density ($j_{||}, j_\perp, j_r$), can be obtained by evaluating the ion and total momentum equations in the three principal transport directions (i.e. parallel to $\vec{B}$, perpendicular to $\vec{B}$ in the magnetic flux surface or diamagnetic and radial) assuming toroidal symmetry.
In the present extension of the B2 code, which I developed, and which will henceforth referred to as the extended B2 code, the neoclassical expressions are explored to link the radial current with the radial electric field. In a first approach the $\vec{B} \times \vec{\nabla} T$ drifts are omitted. More detailed description of the extended code is subject of the following section.
The extended B2 code is still based on certain simplifying assumptions to reduce the number and complexity of the equations :

1) Local charge neutrality is assumed. Therefore Poisson's law is omitted.
2) The link between j_r and E_r is completely neoclassical, so neglecting e.g. influences from anomalous transport in the additional equations (see 5.3.2).
3) The viscosity tensor is simplified ; only the parallel viscosity is taken into account and friction due to gradients of radial velocity is neglected.
4) In the friction force terms with mixed derivatives are omitted.
5) In the divergence of the heat flux terms with mixed derivatives are neglected, thus also $\vec{B} \times \vec{\nabla} T_e$.
6) The time dependence of the additional variables is not taken into account.
7) The code is presently restricted to a single ion fluid only.
8) Some terms due to curvature of $\vec{B}$ and gradients of $\vec{B}$ are neglected.

5.3.2 Additional equations

For a pure hydrogenic plasma ($Z_i = 1$; $n \equiv n_i = n_e$), these assumptions lead for the extended B2 code to the following additional equations. In order to determine the electric potential, the total current continuity equation, Eq. (2.51), is taken into account :

$$\frac{1}{\sqrt{g}}\left[\frac{\partial}{\partial u^\theta}\frac{\sqrt{g}}{h_\theta}j_\theta + \frac{\partial}{\partial u^r}\frac{\sqrt{g}}{h_r}j_r\right] = 0 \quad . \tag{5.2}$$

The electron momentum equation in the parallel direction, Eq. (2.96), is used to define the parallel electric current density :

$$j_{\|} = \frac{\sigma_{\|}}{en}\frac{B_\theta}{B}\frac{1}{h_\theta}\left(\frac{\partial p_e}{\partial u^\theta} - en\frac{\partial \Phi}{\partial u^\theta} + 0.71n\frac{\partial T_e}{\partial u^\theta}\right) \quad . \tag{5.3}$$

These two equations give rise to a second-order partial differential equation in θ for Φ :

$$\begin{aligned} -\frac{\partial}{\partial u^\theta}\frac{\sqrt{g}}{h_\theta^2}\sigma_{\|}\frac{B_\theta^2}{B^2}\frac{\partial \Phi}{\partial u^\theta} \quad &= \quad \frac{\partial}{\partial u^\theta}\frac{\sqrt{g}}{h_\theta}\left(-\frac{\sigma_{\|}}{en}\frac{B_\theta^2}{B^2}\frac{1}{h_\theta}\left(\frac{\partial p_e}{\partial u^\theta} + 0.71n\frac{\partial}{\partial u^\theta}T_e\right)\right. \\ &\left. + \frac{B_\phi}{B}j_\perp\right) + \frac{\partial}{\partial u^r}\left(\frac{\sqrt{g}}{h_r}j_r\right) \quad . \end{aligned} \tag{5.4}$$

The radial ion momentum equation, Eq. (2.97), is used to obtain the diamagnetic component of the ion velocity $V_\perp$, neglecting inertial, viscous and perpendicular conductivity effects in comparison with the radial pressure and electric potential gradients. Radial momentum sources due to interactions with neutral particles are not yet provided by the neutral model. Thus :

$$V_\perp = -\frac{1}{B}\left(\frac{1}{enh_r}\frac{\partial p_i}{\partial u^r} + \frac{1}{h_r}\frac{\partial \Phi}{\partial u^r}\right) \quad . \tag{5.5}$$

The radial component of the total momentum equation, Eq. (2.99), is similarly reduced to the equilibrium equation :

$$j_\perp = -\frac{1}{B}\frac{1}{h_r}\frac{\partial p}{\partial u^r} \quad . \tag{5.6}$$

The radial current density is obtained by evaluating the total momentum equation in the diamagnetic direction, Eq. (2.103) :

$$\begin{aligned} j_r = & \\ & \frac{1}{B}\left\{\frac{1}{\sqrt{g}}\left[\frac{\partial}{\partial u^\theta}\left(\frac{\sqrt{g}}{h_\theta}mnV_\theta V_\perp\right) - \frac{\partial}{\partial u^r}\left(\frac{\sqrt{g}}{h_r}mnV_r V_\perp\right)\right]\right. \\ & \left. + \frac{1}{\sqrt{g}}\frac{\partial}{\partial u^\theta}\left[\frac{\sqrt{g}}{h_\theta^2}\eta_0\left(\frac{2}{3}\frac{B_\theta B_\phi}{B^2}\frac{\partial}{\partial u^\theta}V_{\|} - \frac{1}{3}\frac{B_\phi^2}{B^2}\frac{\partial}{\partial u^\theta}V_\perp\right)\right] - S_{m,\perp}\right\} \quad . \end{aligned} \tag{5.7}$$

5.3.3 Changes in basic equations

Introduction of these additional variables leads to a modification of the original B2 plasma equations :

1) The poloidal ion velocity is calculated as a combination of components of the ion velocity in the parallel and the diamagnetic direction : $V_\theta = \frac{B_\theta}{B}V_{\|} + \frac{B_\phi}{B}V_\perp$.

2) The viscous term in the parallel ion momentum equation now takes into account the contribution of $V_\perp$.

3) The energy equations are supplemented with additional heat exchange terms.

4) The electron energy equation takes into account the ohmic heating.

5) The electron energy flux is modified by the existence of a poloidal current.

Therefore the basic equations, replacing Eqs. (3.6)-(3.10), can now be written as :

$$\frac{\partial}{\partial t}n + \frac{1}{\sqrt{g}}\frac{\partial}{\partial u^\theta}\left(\frac{\sqrt{g}}{h_\theta}nV_\theta\right) + \frac{1}{\sqrt{g}}\frac{\partial}{\partial u^r}\left(\frac{\sqrt{g}}{h_r}nV_r\right) = S_n \tag{5.8}$$

$$\begin{aligned}\frac{\partial}{\partial t}(\rho V_\parallel) &+ \frac{1}{\sqrt{g}}\frac{\partial}{\partial u^\theta}\left[\frac{\sqrt{g}}{h_\theta}\rho V_\theta V_\parallel - \frac{\sqrt{g}}{h_\theta^2}\eta_\theta^i\left(\frac{2}{3}\frac{\partial V_\parallel}{\partial u^\theta} - \frac{1}{3}\frac{B_\phi}{B_\theta}\frac{\partial V_\perp}{\partial u^\theta}\right)\right] \\ &+ \frac{1}{\sqrt{g}}\frac{\partial}{\partial u^r}\left(\frac{\sqrt{g}}{h_r}\rho V_r V_\parallel - \frac{\sqrt{g}}{h_r^2}\eta_r^i\frac{\partial V_\parallel}{\partial u^r}\right) = \\ &\qquad S_{mV_\parallel} - \frac{B_\theta}{B}\frac{1}{h_\theta}\frac{\partial p}{\partial u^\theta}\end{aligned} \tag{5.9}$$

$$V_r = -\frac{D}{h_r}\frac{\partial}{\partial u^r}\ln(n) \tag{5.10}$$

$$\begin{aligned}&\frac{\partial}{\partial t}\left(\frac{3}{2}nT_e\right) + \\ &\frac{1}{\sqrt{g}}\frac{\partial}{\partial u^\theta}\left[\frac{\sqrt{g}}{h_\theta}\frac{5}{2}\left(nV_\theta - \frac{j_\theta}{e}\right)T_e - \frac{\sqrt{g}}{h_\theta^2}\kappa_\theta^e\frac{\partial T_e}{\partial u^\theta} - 0.71\frac{T_e}{e}\frac{B_\theta}{B}\frac{\sqrt{g}}{h_\theta}j_\parallel\right] + \\ &\frac{1}{\sqrt{g}}\frac{\partial}{\partial u^r}\left[\frac{\sqrt{g}}{h_r}\frac{5}{2}\left(nV_r - \frac{j_r}{e}\right)T_e - \frac{\sqrt{g}}{h_r^2}\kappa_r^e\frac{\partial T_e}{\partial u^r}\right] = \\ &\qquad S_E^e - k(T_e - T_i) + \frac{V_\theta}{h_\theta}\frac{\partial p_e}{\partial u^\theta} + \frac{V_r}{h_r}\frac{\partial p_e}{\partial u^r} \\ &\qquad -j_\theta\frac{1}{h_\theta}\frac{\partial \Phi}{\partial u^\theta} - j_r\frac{1}{h_r}\frac{\partial \Phi}{\partial u^r} + j_\perp V_r B - j_r V_\perp B\end{aligned} \tag{5.11}$$

$$\begin{aligned}&\frac{\partial}{\partial t}\left(\frac{3}{2}nT_i + \frac{1}{2}\rho V_\parallel^2\right) + \\ &\frac{1}{\sqrt{g}}\frac{\partial}{\partial u^\theta}\left[\frac{\sqrt{g}}{h_\theta}\left(\frac{5}{2}nV_\theta T_i + \frac{1}{2}\rho V_\theta V_\parallel^2\right) - \frac{\sqrt{g}}{h_\theta^2}\left(\kappa_\theta^i\frac{\partial T_i}{\partial u^\theta} + \frac{1}{2}\eta_\theta^i\frac{\partial V_\parallel^2}{\partial u^\theta}\right)\right] + \\ &\frac{1}{\sqrt{g}}\frac{\partial}{\partial u^r}\left[\frac{\sqrt{g}}{h_r}\left(\frac{5}{2}nV_\theta T_i + \frac{1}{2}\rho V_\theta V_\parallel^2\right) - \frac{\sqrt{g}}{h_r^2}\left(\kappa_r^i\frac{\partial T_i}{\partial u^r} + \frac{1}{2}\eta_r^i\frac{\partial V_\parallel^2}{\partial u^r}\right)\right] = \\ &\qquad S_E^i + k(T_e - T_i) - \frac{V_\theta}{h_\theta}\frac{\partial p_e}{\partial u^\theta} - \frac{V_r}{h_r}\frac{\partial p_e}{\partial u^r} \\ &\qquad -j_\perp V_r B + j_r V_\perp B\end{aligned} \tag{5.12}$$

in which $V_\perp, j_\parallel, j_\perp, j_r$ and Φ can be substituted from the additional equations, Eqs. (5.3)-(5.7).

5.4 Boundary conditions

5.4.1 Additional boundary conditions

All additional equations, Eqs. (5.3),(5.5), (5.6) and (5.7), except the electric potential equation (5.4), are analytic expressions, meaning that the plasma parameters $j_{||}$,$V_{\perp}$, $j_{\perp}$ and j_r can be calculated directly if all other plasma parameters are known. Therefore, additional boundary conditions are only required for the electric potential, or a dependent variable. In order to determine the number of boundary conditions which is required physically, these analytic expressions are substituted in the potential equation. This leads to second order in the θ direction and third order in the r direction. The conditions for the radial direction have to be chosen according to the modelled case. The periodic boundaries in the θ direction require two continuity conditions. Outside the separatrix, the equation should be solved between two material boundaries, on which sheath conditions are imposed. Following again Stangeby's fluid approach [23], but allowing an electric current density j_θ to the material boundary one obtains :

$$\begin{aligned}\Phi_s - \Phi_w = \\ -\frac{T_e}{e} \cdot \ln \left[\sqrt{\frac{2\pi m_e}{m_i}\left(\frac{T_e+T_i}{T_e}\right)} \left(\frac{1}{1-\gamma_e}\right) \left(1 - \frac{j_\theta}{en\frac{B_\theta}{B}c_s}\right)\right]\end{aligned} \tag{5.13}$$

where γ_e is the secondary electron yield per incident ion-electron pair, and Φ_w and Φ_s are respectively the electric potential at the wall or material boundary and at the sheath entrance.
For deuterium with $T_i = 0$, $\gamma_e = 0$ and $j_\theta = 0$ this condition reduces to the formula derived for probes by Tonks and Langmuir [85] :

$$\Phi_s - \Phi_w = 3.1\frac{T_e}{e} \quad . \tag{5.14}$$

For deuterium with $T_i \approx T_e$, $\gamma_e = 0$ and $j_\theta = 0$, Eq: (5.13) leads to :

$$\Phi_s - \Phi_w \approx 2.8\frac{T_e}{e} \quad . \tag{5.15}$$

Taking an expression for the sheath boundary condition, such as Eq. (5.14) or Eq. (5.15), will simplify the numerical procedure for solving the potential equation, Eq. (5.4). However, a little difference in temperature between the places where a magnetic flux surface intersects the two targets (i.e. at the "left" and the "right" boundary of the numerical mesh), can lead to large electric currents, because of the relative high conductivity of a plasma. During modelling it turned out that for typical boundary plasmas as present in TEXTOR and ASDEX-Upgrade, the use of simplified boundary conditions results in unphysical solutions in which j_θ became larger than the electric current density carried by the ions. In this case electrons would be extracted out of the limiter or target plate. In order to avoid unphysical solutions, the full expression is needed. Indeed, with the boundary condition as proposed in Eq. (5.13) the potential will strongly increase and thus reduce the electric current density j_θ, whenever j_θ reaches the current density carried by ions as will be discussed in subsection 5.5.3.

5.4.2 Boundary conditions for primary plasma variables at the sheath

To date, kinetic calculations for the sheath region have been solely one-dimensional. Hence the influence of a diamagnetic component of the ion velocity on the Bohm criterion at the plasma sheath is not yet available. In order to ensure that no ion fluxes are drawn out of the target, the poloidal ion velocity component V_θ is still simply presumed to satisfy the Bohm condition :

$$V_\theta = \frac{B_\theta}{B} c_s \tag{5.16}$$

with c_s the isothermal ion sound velocity (see figure 5.1).

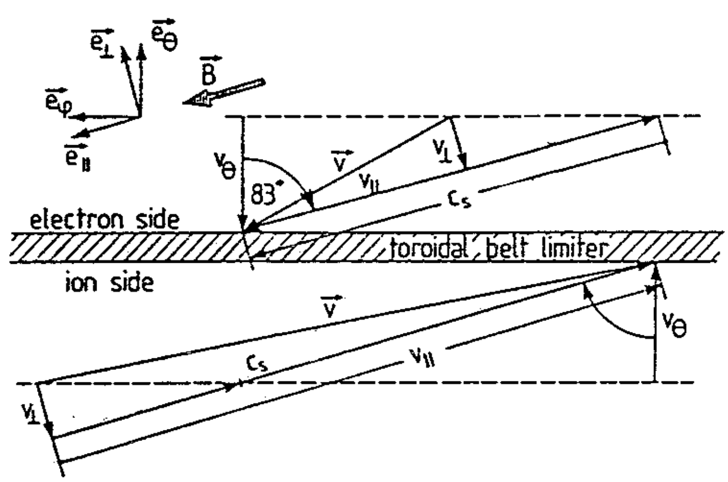

Figure 5.1: Schematic view of boundary conditions at both sides of a limiter

Indeed, the assumption that at the target plate, the parallel velocity reaches the sound velocity, could again result in unphysical solutions with a poloidal ion velocity and thus a poloidal ion particle flux directed away from the target.
Also for the electron heat flux to the target, Chodura's one-dimensional calculations [69] are not longer appropriate. Since no better information from kinetic calculations is available, the simple fluid approach of Stangeby [23] is again applied here :

$$Q_e = \delta_e T_e \Gamma_e \tag{5.17}$$

with

$$\delta_e = \frac{2}{1-\gamma_e} + \frac{e\,(\Phi_s - \Phi_w)}{T_e} \quad . \tag{5.18}$$

5.5 Numerical treatment

The additional variables ($V_\perp$,$j_\|$,$j_\perp$,j_r and Φ) are solved with the set of additional equations, Eqs.(5.3)-(5.7), at each iteration time-step. They are computed before the standard B2 equations are relaxed. In order to avoid a complex differential equation for the electric potential, which is third order in the radial co-ordinate and contains cross derivatives, this equation is solved iteratively by calculating the algebraic expressions for $V_\perp$, $j_\perp$ and j_r, Eqs. (5.5),(5.6) and (5.7) respectively, and solving the potential equation, Eq. (5.4), in the θ-direction only.
Two numerical problems arise immediately :

1) Outside the separatrix, Φ is determined by the sheath potential at the limiters, which is a non-linear expression in j_θ (and thus via Eq. (5.3) a non-linear expression in $\frac{1}{h_\theta}\frac{\partial\Phi}{\partial u^\theta}$).

2) Inside the separatrix, periodic boundary conditions apply for Φ. Therefore, the radial dependence of the potential should be brought in via the radial derivatives in the equation.

5.5.1 Potential differential equation

Similar to the method used for the basic B2 differential equations, the solution of the one-dimensional potential equation is based on the finite-volume approach. Since this equation is of a pure conduction form, both the computation of the residuals and the discretization of the potential equation are based on a central differencing scheme. Because there are no convective contributions in the potential equation, the discretization gives rise to a symmetrical, banded matrix, which can be solved directly without the aid of an iterative procedure. The calculation of $j_\|$ requires the same formulation for the gradient of Φ as implicitly used in the foregoing discretization, in order to ensure a divergence-free current from the potential equation.

5.5.2 Solution of the potential equation outside the separatrix

As was already mentioned above, the complete boundary expression, Eq. (5.13), at the targets should be implemented. Therefore, the potential equation is solved twice. First the equation is solved with boundary conditions assuming a currentless plasma :

$$\Phi_0 = \Phi_{w,0} - \frac{T_{e,0}}{e}\cdot\ln\left[\sqrt{\frac{2\pi m_e}{m_i}\left(\frac{T_{e,0}+T_{i,0}}{T_{e,0}}\right)}\left(\frac{1}{1-\gamma_e}\right)\right] \tag{5.19}$$

and

$$\Phi_N = \Phi_{w,N} - \frac{T_{e,N}}{e}\cdot\ln\left[\sqrt{\frac{2\pi m_e}{m_i}\left(\frac{T_{e,N}+T_{i,N}}{T_{e,N}}\right)}\left(\frac{1}{1-\gamma_e}\right)\right] \quad , \tag{5.20}$$

where Φ_0 and Φ_N are the sheath potentials and the indices 0 and N refer to variables at the "left" respectively the "right" side of the mesh. The solution of the potential equation will lead, in this case, to poloidal current densities at the material boundaries, $j_{\theta,0}$ and $j_{\theta,N}$.

Since the boundary conditions, in a first step, were calculated with the assumption of a currentless plasma, a correction has to be made. Therefore, a divergence-free compensation current density $j_{c\theta}$ is introduced, which means that the total poloidal current $j_{c\theta}S_\theta$ is kept constant in a flux tube. Here S_θ is the cross-section of the flux tube perpendicular to the poloidal direction.

The compensation current density $j_{c\theta}$, which is originated by a change in electric potential at the boundaries ($\Delta\Phi_0$ and $\Delta\Phi_N$), will in turn influence the sheath potential as given by Eq. (5.13). Using Eq.(5.3) and keeping all plasma variables constant except $j_{\|}$ and Φ, we can see that a change in electric potential introduces a poloidal compensation current density :

$$j_{c\theta} = \frac{B_\theta}{B} j_{c\|} = -\sigma_{\|} \left(\frac{B_\theta}{B}\right)^2 \frac{1}{h_\theta} \frac{d(\Delta\Phi)}{du^\theta} \tag{5.21}$$

Poloidally integrating this equation leads to :

$$\int_{\theta_0}^{\theta_N} \frac{j_{c\theta} S_\theta h_\theta}{\sigma_{\|} \left(\frac{B_\theta}{B}\right)^2 S_\theta} du^\theta = \Delta\Phi_0 - \Delta\Phi_N \tag{5.22}$$

Keeping in mind that this compensation current must be divergence-free and thus $j_{c\theta}S_\theta =$ *constant* one becomes :

$$j_{c\theta,0} = j_{c\theta,N} \frac{S_N}{S_0} = -\frac{(\Delta\Phi_N - \Delta\Phi_0)}{R_{tot}} \tag{5.23}$$

with

$$R_{tot} = S_0 \int_{\theta_0}^{\theta_N} \frac{h_\theta}{\sigma_{\|} (B_\theta/B)^2 S_\theta} du^\theta \quad . \tag{5.24}$$

On the other hand, the use of the expression for the boundary condition, Eq. (5.13), leads to a change in electric potential at the sheaths :

$$\Delta\Phi_N = -\frac{T_{e,N}}{e} \ln\left(1 - \frac{j_{\theta,N} + j_{c\theta,N}}{en\frac{B_{\theta,N}}{B_N} c_{s,N}}\right) \tag{5.25}$$

and

$$\Delta\Phi_0 = -\frac{T_{e,0}}{e} \ln\left(1 + \frac{j_{\theta,0} + j_{c\theta,0}}{en\frac{B_{\theta,0}}{B_0} c_{s,0}}\right) \quad . \tag{5.26}$$

with

$$j_{c\theta,N} = j_{c\theta,0} \frac{S_0}{S_N} \quad . \tag{5.27}$$

Thus, substitution of Eqs. (5.24)-(5.27), results in an equation in $j_{c\theta,0}$:

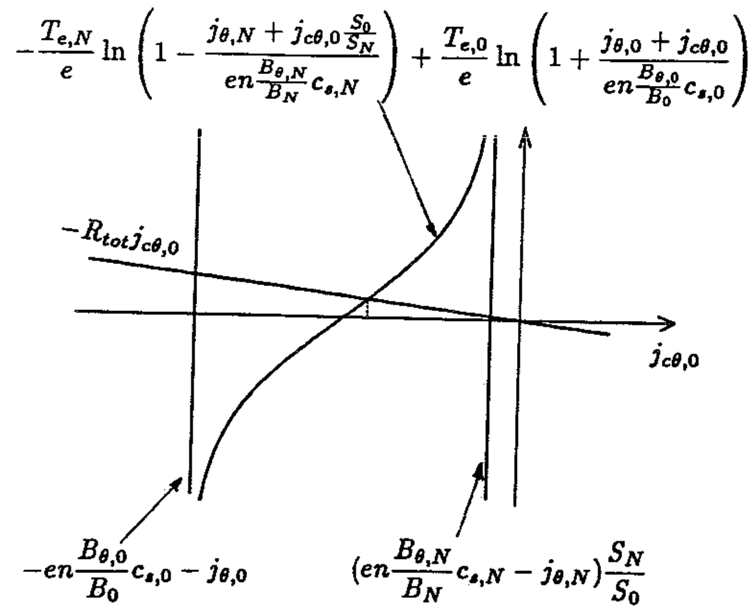

Figure 5.2: Condition to determine the magnitude of the compensation current.

$$-\frac{T_{e,N}}{e}\ln\left(1-\frac{j_{\theta,N}+j_{c\theta,0}\frac{S_0}{S_N}}{en\frac{B_{\theta,N}}{B_N}c_{s,N}}\right)+\frac{T_{e,0}}{e}\ln\left(1+\frac{j_{\theta,0}+j_{c\theta,0}}{en\frac{B_{\theta,0}}{B_0}c_{s,0}}\right)= -R_{tot}j_{c\theta,0} \quad . \tag{5.28}$$

The solution of this equation will determine the necessary compensation current to fulfil the boundary conditions. For conditions of the boundary plasma, as present in experimental Tokamaks, the value of R_{tot} is relatively small, so that $j_{c\theta}$ will strongly reduce the parallel current. This effect is referred to in this thesis as the "shielding effect".
As can be seen from figure (5.2), this equation provides a solution if

$$(-en\frac{B_{\theta,0}}{B_0}c_{s,0}-j_{\theta,0})\leq(en\frac{B_{\theta,N}}{B_N}c_{s,N}-j_{\theta,N})\frac{S_N}{S_0} \quad . \tag{5.29}$$

This is the case if the net radial incoming current $-\Delta I_r$ in a flux tube is lower than the physically maximum possible current to the targets (see fig. 5.3) :

$$-\Delta I_r = j_{\theta,N}S_N - j_{\theta,0}S_0 \leq en\frac{B_{\theta,N}}{B_N}c_{s,N}S_N + en\frac{B_{\theta,0}}{B_0}c_{s,0}S_0 \quad . \tag{5.30}$$

Finally, the potential equation is solved once again, with $j_\theta = -(j_{\theta,0}+j_{c\theta,0})$ and $j_\theta = j_\theta, N + j_{c\theta,N}$ in the equation for the boundary condition of the electric potential, Eq. (5.13). In this way the potential equation is solved taking into account the strongly non-linear boundary conditions.

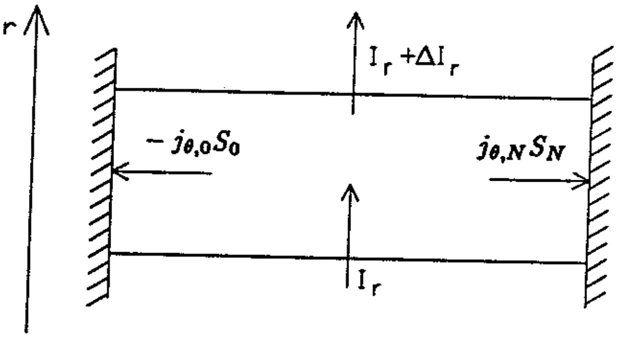

Figure 5.3: Current flow in a flux tube

It should be recognized that this procedure can only be used when the region in between two sheath boundaries is solved as a continuous region, i.e. no artificially introduced cuts may be used. Furthermore, the full poloidal cross-section has to be modelled. For divertor geometries it is therefore necessary to use one of the methods as described in section 4.3.2, which allow a continuous calculation in the private flux region. Although, these methods turned out to be useful for most standard B2 calculations, none of them are adequate for handling the strong dependence of parallel electric currents on temperature gradients. Therefore, a new solver, which solves the equations in the cells in the neighbourhood of the "cuts" as adequate as in other cells, and which is implemented by Schneider (IPP-Garching,Germany), is used in the extended B2.

5.5.3 Solution of the potential equation inside the separatrix

In this case the radial dependence of the electric potential is obtained explicitly, by imposing a radially constant total radial current across the closed flux surfaces. Because the current is ensured to be divergence-free, the gradient of Φ will be continuous over the periodic boundary. Setting an arbitrary value Φ_0 on both sides will therefore fulfil the periodic boundary condition. Furthermore, the solution of the one-dimensional equation remains valid after adding an arbitrary poloidally constant value Φ_c. This poloidally constant value $\Phi_c(r)$ is determined by deriving its influence on the ion velocity in the diamagnetic direction $V_\perp$ and on the radial electric current density j_r. This leads to a correlation between a change in total radial current I_r over a closed flux surface and a corresponding change in potential Φ_c. A constant, prescribed total radial current over the closed flux surfaces, which is generally equal to zero except for polarization experiments, determines the profile of $\Phi_c(r)$, and therefore the radial potential profile.

Chapter 6

Applications of the extended B2 code

6.1 Introduction

In this chapter applications of the extended model are elaborated. In an attempt to distinguish causes of different effects the model is applied with increasing degree of sophistication. This will allow a user of the extended B2 code to determine the necessary terms for a specific simulation with respect to the modelled experiment. In section 6.2 experimental results concerning electric currents and flows in the diamagnetic direction are described. As a first step in extending the code, the influences from implementing a parallel current density $j_{\|}$ and a poloidal electric field E_θ are investigated and compared to experimental results from divertor magnetic configurations in section 6.3. Before completely extending the B2 code, the relative importance of particle flow in the diamagnetic direction in comparison with poloidal flow for convective poloidal transport at the material boundary is estimated both numerically and analytically for the TEXTOR limiter configuration and the divertor configuration of ASDEX-Upgrade. Since applications of the completely extended B2 model for a limiter geometry turned out to be much more computer time consuming, due to the large effects of including drift flows for this case, the extended B2 model is applied to a single-null divertor geometry instead; results are discussed in section 6.5.

6.2 Qualitative experimental results concerning drift flows and/or electric currents

6.2.1 Electric currents in the scrape-off layer

Electron and ion drift side

One might expect that in the scrape-off layer electric currents can flow in the direction of the main plasma current, induced by the loop voltage. In this sense it is always possible, for a particular geometry, to define an ion and an electron side. The ion side is reached by following a magnetic field line in the direction such that its toroidal component is in the direction of the plasma current. The other side is called the electron side (see figure

6.1). Please note that a reversal of the toroidal electric field will therefore change an ion side in an electron side and vice versa. Not too much attention should be paid to this way of definition. The ion (electron) **drift side** should clearly be distinguished from the ion (electron) **strike side**, i.e. the place where the ion (electron) particle flow mainly strikes the target. Moreover, in the scrape-off layer where $(\vec{\nabla}p)$ is mainly directed radially inward, the diamagnetic flow $(\frac{\vec{B}\times\vec{\nabla}p}{enB^2})$ is directed to the electron side.

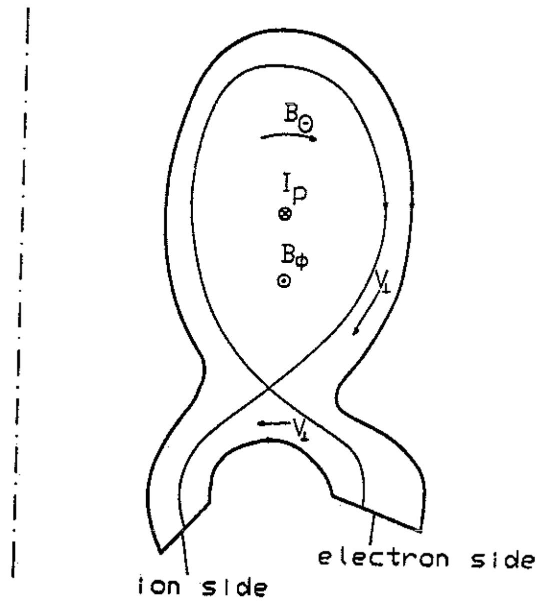

Figure 6.1: Schematic view to determine electron and ion drift side

In most experiments ([86], [87], [88],[89]), the measured currents are indeed found to flow in the direction of the main plasma current, but the magnitude of these edge currents are much greater than estimated from Spitzer resistivity and loop voltage (up to 5 A/cm^2 [90] in ASDEX-Upgrade experiments). Therefore, an alternative driving mechanism for this scrape-off layer current has to be found.

Influences from electron temperature and electron pressure asymmetries on the currents

A theory was initialized by Harbour [91], extended by Staebler and Hinton [92] and reviewed by Stangeby [93]. In this theory the thermoelectric current, which is caused by differences in sheaths at the two sides of an open magnetic field line due to asymmetries in electron temperature, is thought to be one of the major contributors to the edge current. Especially, for discharges with strong asymmetry in electron temperatures between the strike zones, this theory is confirmed by experimental results in JET [86], and in DIII-D [88], [87], where measurements of both temperature and electric currents are performed. However, for these discharges where the electron temperatures at the two sides were comparable, but with a substantial difference in plasma density, the density difference has been found to be a possible candidate for an additional driving force for the current [89]. Data on electron pressure asymmetries obtained in JET, TEXTOR [94], PLT [95], PDX [95],

[96], T-10 [97], [98], DITE [99], without specifically measuring the current, all suggest that the electron pressure rises at the ion drift side. This asymmetry in electron pressure and thus in plasma density, can therefore counteract the thermoelectric force and can explain the measured reversal of the current as discussed in Ref. [89].

From these results it is clear that the parallel electric current strongly depends on the plasma parameters at the target. In some experiments asymmetries in these parameters depend on the direction of the drift flows.

6.2.2 Effects of divertor and limiter biassing on plasma flow

Motivation for biassing experiments

Two major problems in future fusion reactors can be considered. First, the removal of ash and contaminants requires sufficient high neutral pressure at the pump entrance. This problem is even more pronounced in the high confinement regime (so-called "H-mode") where the particle confinement time is several times the energy confinement time and therefore the neutral pressure at the pumping aperture is even lower. Secondly, the spatially peaked thermal loads on the targets make design for future Tokamaks difficult. Because of these peaked profiles present technological limits will easily be reached.

Although the first problem can be reduced by optimizing geometrical aspects of the pump aperture, this optimization strongly depends on the specific magnetic configuration. On the other hand the heat load at the peak of the profiles are so high that the profile should be flattened. Therefore it might be necessary to "sweep" the separatrix strike point position up and down across the target to reduce the time-averaged heat load. However, the variable divertor geometry will then preclude optimization for high exhaust pressure.

With creating electric fields in so-called biassing experiments, it is possible to change the scrape-off layer profiles, which determine the power densities on the targets as well as the pumping efficiency. Furthermore, it is hoped that control will be possible over impurity behaviour and over access to improved confinement regimes. In addition, biassing experiments are expected to provide information about underlying mechanisms such as fluctuation stabilisation, H-mode transition physics, etc.

Experimental results

In biassing experiments, electric fields are created by applying a voltage difference between different material boundaries (e.g. between two divertor plates, between limiter and vessel wall, etc.) or by introducing an electrode inside the last closed flux surface, the so-called polarization experiment or electrode biassing. In biassing experiments both a radial or a poloidal electric field can be intended. A recent review is given by Weynants and Van Oost [12].

Radial electric fields are e.g. created during limiter or electrode biassing in **limiter Tokamaks**, such as TEXTOR [100], [11], TEXT [101], ATF [102] and influence edge plasma parameters. In these experiments, events of L-H transition signature are reported, in which, independent from the sign of the applied voltage, the particle confinement time τ_p increases and the energy confinement time τ_E increases marginally. In some machines, fluctuations in ion density are measured and show a decreasing effect in the case of positive polarization in ATF [102] and in the case of negative polarization in TEXTOR [100] and TEXT [101].

In **divertor biassing** experiments, various schemes are in use, which can provide both radial and poloidal electric fields. Recent biassing experiments on the Doublet single-null poloidal divertor (DIII-D) [103] and on the Tokamak de Varennes double-null magnetic divertor (TdeV) [104] indicate possibilities to improve control on both particle exhaust and heat power load at the targets. Furthermore, in biassing experiments with additional heating the input power threshold for L-H transition is significantly reduced. This result again provides motivation for further research on biassing experiments.

On both DIII-D and TdeV [104] experimental devices the neutral pressure could be enhanced by applying a voltage between one divertor plate and the wall (see figures 6.2 and 6.3). As the enhancement of neutral pressure depends on both the sign of applied voltage and the direction of the toroidal magnetic field, according to the direction of the diamagnetic drift flow, there is experimental evidence that $E_r \times B_\phi$ drift flows cause this effect.

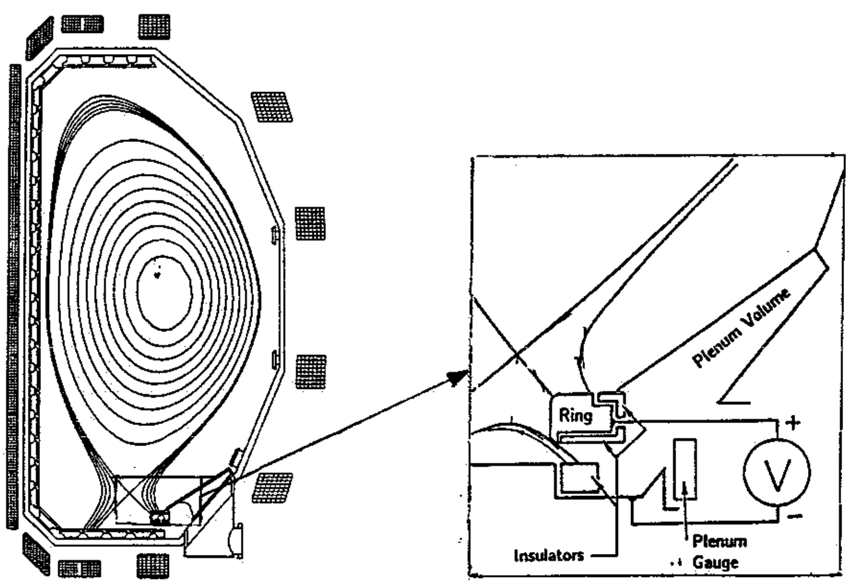

Figure 6.2: Schematic view of the biassing experiments on DIII-D taken from [88]

On the other hand in DIII-D [103], the heat power load on the two targets is influenced by the sign of applied voltage only. Therefore, this effect has been attributed to a current induced convective heat flow. For all combinations of electrode polarity and toroidal magnetic field direction, a shift of power from cathode to anode is observed (see figure 6.4). Furthermore, it should be mentioned that the total heat flux to the targets increases with increasing applied voltage, but this increase does not equal the total bias input power. There are not enough experimental indications yet to conclude that the other part of bias input power is lost by radiation in the scrape-off layer. Therefore, more experimental data is required to evaluate the total power balance correctly.

Changes in electric potential have been measured during biassing experiments and show an increase of the separatrix potential with approximately the applied voltage [105], [116], [117].

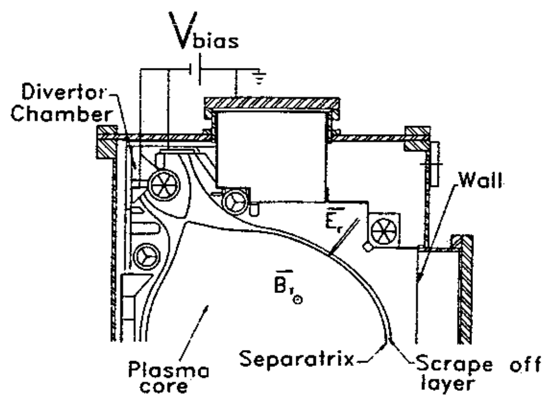

Figure 6.3: Schematic view of the biassing experiments on TdeV taken from [104]

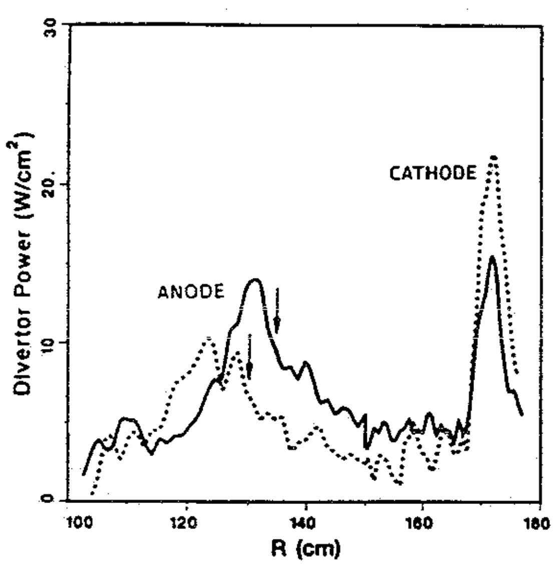

Figure 6.4: Changes in heat power load due to biassing taken from [88]

From these experiments one can conclude that divertor bias has potentially important applications to Tokamak reactor divertors. In a divertor with an oscillating strike position, a high pressure at the pump entrance could be maintained by appropriately biassing the divertor plates, despite the variable strike position. Furthermore, it might be possible to oscillate the heat flux position by an alternating or modulated bias. Such a modulation in biassing might eliminate the need for large oscillating currents in magnetic coils.

Edge modelling for biassing experiments

Among others, the effect of reduced fluctuations, as they occur in limiter biassing experiments and which can change anomalous transport, is one of the possible explanation for the observed L- to H-mode transition [106]. Another explanation is based on the change in viscous damping of the induced poloidal rotation layer inside the last closed flux surface. This change can only be explained by non collisionally dominated neoclassical transport [32], [80]. Since both anomalous and kinetically determined neoclassical transport are beyond the scope of this thesis, no computations are performed for limiter configurations with respect to these experiments. Furthermore, for the simulation of large potential differences between a limiter, divertor plate or electrode and the wall more investigation is required with respect to the plasma condition near the vessel wall. Therefore, in this thesis we will concentrate on the modelling of divertor biassing experiments involving poloidal electric fields. In section 6.3experimental data is compared with computational results based on an edge model incorporating the poloidal electric field E_θ and the parallel electric current density $j_{||}$. The influence from radial electric fields, as they occur in non-biassing experiments, on the other plasma parameters will be discussed in section 6.5, using the extended B2 code, which calculates profiles of $V_\perp$,$j_\perp$,$j_{||}$,j_r and Φ.

6.3 Modelling parallel currents and poloidal electric fields

6.3.1 Introduction

In this section a first extension of the physics content implemented in the B2 code is investigated. This extension consists of step 1 of section 5.2.1, namely the introduction of the parallel current density $j_{||}$ and the poloidal electric field $E_\theta = -\frac{\partial\Phi}{h_\theta \partial u^\theta}$. Furthermore, because j_θ not longer equals zero, strongly non-linear boundary conditions are imposed for Φ at limiter targets or target plates as described in section 5.5.3.

Inside the separatrix, in the core, the absolute value of the electric potential cannot be determined as long as a relation between the radial current density j_r and the radial electric field E_r is not incorporated. Since in this first extension of the code the additional equations (5.3) and (5.4) are solved, information is provided about E_θ and $j_{||}$, but not about E_r. Outside the separatrix, in the scrape-off layer and the private flux region, the electric potential, and thus the radial electric field, will be determined by the boundary condition at the sheath.

In order to compare with available experimental results on poloidal electric currents, attention is paid to divertor configurations. For these devices there are different installations with conducting target plates possible : the plates can either be grounded or floated. Whereas a floating condition requires that no total current flows to the plate with equipotential

surface, this electric potential at the target will be determined by the plasma behaviour. Although most edge plasma codes assume **local** ambipolarity at the sheath, it should be mentioned here that this is not a required condition for grounded nor for floating divertor targets.
As the parallel current density $j_{\|}$ is not influenced by the direction of the magnetic field, such effects as obtained from reversing the magnetic field, cannot be simulated. On the other hand, influences on power heat load at material boundaries, which do not depend on the direction of $\vec{B}$, will be compared with the information obtained from standard B2 calculations. In subsection 6.3.2 the influence from introducing a parallel electric current for grounded divertor plates is investigated.
Another possibility for the electric installation of divertor plates exists in applying a voltage between two targets. As this will induce an electric current in the plasma, plasma parameters will be affected by this method. Comparison will be made with experimental results of biassing experiments in the experimental divertor Tokamaks DIII-D and TdeV, as discussed in subsection 6.3.3. In this last subsection qualitative changes in biassing experiments introduced by the parallel current are considered.

6.3.2 Calculations for a divertor with grounded plates

Introduction

In this subsection qualitative effects of currents in the scrape-off layer are investigated. For all simulations the ASDEX-Upgrade geometry is used. Therefore, the magnetic configuration, transport coefficients, boundary conditions and neutral model are described. Subsequently, the direction of the poloidal electric current is compared with the calculated temperature asymmetry between inner and outer targets. Furthermore, the changes in heat power load on the targets are discussed.

ASDEX-Upgrade simulations

Computational studies with the first extension of B2, including $j_{\|}$ and E_θ are performed for ASDEX-Upgrade, an axisymmetric poloidal divertor Tokamak situated at the Max-Planck Institut für Plasmaphysik, Garching bei München, Germany.

Magnetic configuration Information about the magnetic configuration of this experiment is provided with a grid generator code SONNET developed by Schneider et al. [42], which allows a fast, flexible and simple implementation of MHD-equilibria (DIVA equilibrium code). The physical mesh for ASDEX-Upgrade is shown in figure 6.5.
As discussed in section 3.4.1, the mapping procedure in B2 requires topological "cuts" (EFG and E'F'G' on figure 4.8), which in the standard version introduce an artificial isolating barrier across the X-point region. Starting these calculations with isolating cuts and proceeding with the semi-implicit cut-linkage (see section 4.3) relatively good convergence is reached (total residual of 10^{-3}).

Transport coefficients The physical parameters in these B2 calculations for ASDEX-Upgrade have been chosen according to realistic parameters used in validation modelling [75]. For the parallel transport coefficients the Braginskii expressions are used. Using

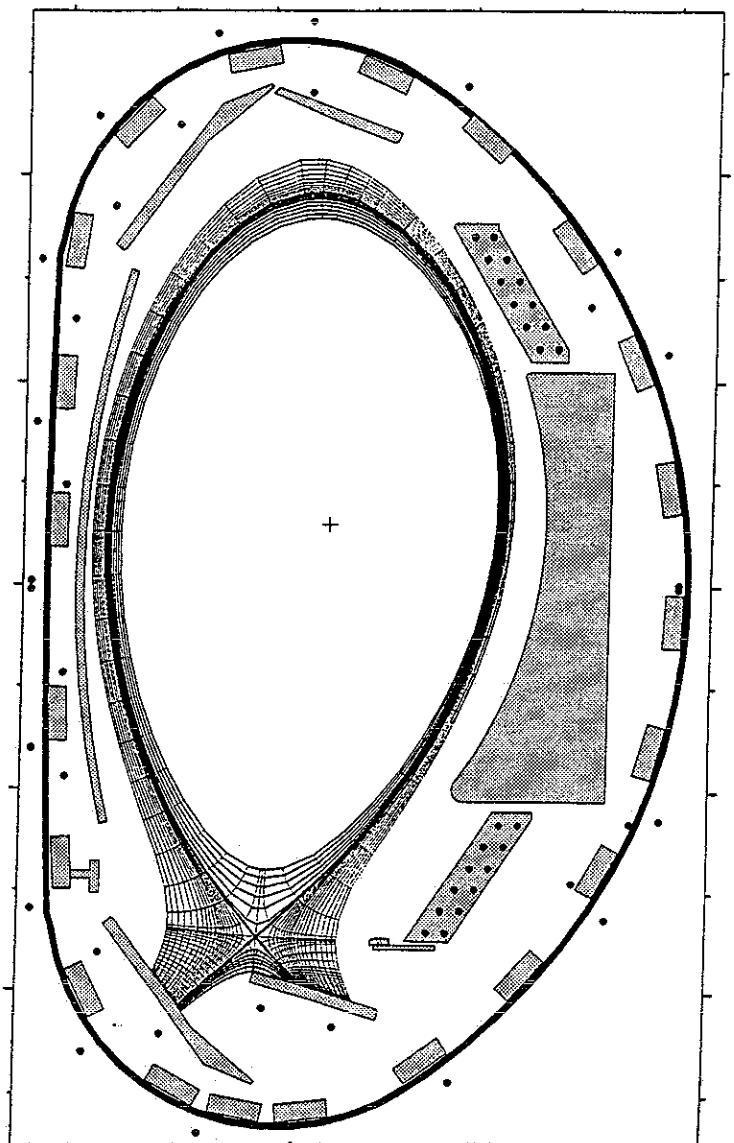

Figure 6.5: Physical mesh for ASDEX-Upgrade

a heat of 1000, no flux limiting was imposed for the electron heat conductivity. The radial anomalous diffusion coefficient D equals 2 m^2/s, $\kappa_r^e = nD_{\kappa,e}$ with $D_{\kappa,e} = 4m^2/s$, $\kappa_r^i = nD_{\kappa,i}$ with $D_{\kappa,e} = 1m^2/s$ and $\eta_r^i = mnD_\eta$ with $D_\eta = 0.2m^2/s$.

Boundary conditions On the magnetic flux surface at the core plasma interface :

$V_\theta = 0$ m/s, ie. zero poloidal velocity.

For the density a so-called "weak" boundary condition is imposed :

$\Gamma_r = nV_r = (n - 1.1 \times 10^{20}) \times 100 \ \mathrm{m^{-2}s^{-1}}$

which means

$n \approx 1.1 \times 10^{20} \ \mathrm{m^{-3}}$.

For the energy equations a constant radial heat flux is prescribed :

$Q_r^e = 0.66 \times 10^5 \ \mathrm{W/m^2}$,

$Q_r^i = 0.33 \times 10^5 \ \mathrm{W/m^2}$.

This leads to a total radial heat flow from the core into the scrape-off layer of 4 MW.

At the targets, plasma sheath edge conditions are imposed on both sides :

$V_\theta = \frac{B_\theta}{B} c_s$

$Q_\theta^e = 4.8 T_e n V_\theta$

$Q_\theta^i = 2.5 T_i n V_\theta + \frac{1}{2} m n V_\parallel^2$

At the wall in the scrape-off layer :

$V_r = 100$ m/s

$\frac{1}{h_r}\frac{\partial V_\parallel}{\partial u^r} = 0$

$T_e = T_i = 2$ eV

At the wall in the private flux region the same boundary conditions are applied except for the parallel velocity. Limited shear is prescribed here :

$\frac{1}{h_r}\frac{\partial V_\parallel \sqrt{T_i}}{\partial u^r} = 0$ or $\frac{1}{h_r V_\parallel}\frac{\partial V_\parallel}{\partial u^r} = -\frac{1}{2 h_r T_i}\frac{\partial T_i}{\partial u^r}$.

Neutral modelling Although the "minimal" neutral model is rather naive and limited in the prediction of some features in scrape-off layer profiles, we will concentrate in this section on qualitative effects caused by the additional physics in the code and we hope that these effects are not too much influenced by the neutral model. Therefore, in order to reduce computing time the standard "minimal" model is used, with neutral particles restricted to the divertor legs (i.e. they cannot penetrate further than the topological cuts). The global recycling coefficient for edge modelling at the plates is set equal to 0.7 so that the local recycling factor in a flux tube is always less than one.

Currents in the scrape-off layer

The implementation of the parallel electric current density $j_\parallel$ and the poloidal electric field E_θ in the physics model gives rise to a poloidal current in the scrape-off layer. Because the averaged electron temperature at the outer target is higher than the averaged electron temperature at the inner target, the sheath potential, which is roughly proportional to the

electron temperature, is expected to have a similar behaviour. Therefore, a poloidal current is induced from the outer to the inner divertor target and amounts to 2.851 kA. This value is in agreement with experimental results from DIII-D presented in Ref. [88]. For DIII-D, which is a single-null divertor with comparable dimensions as ASDEX-Upgrade, poloidal currents in the scrape-off layer typically amount to 1-2 kA in ohmic shots with about 1 MW ohmic heating. In this context it should be mentioned that similar computations including $j_{||}$ were performed on the DIII-D geometry by Rognlien et al. [62]. With their computations a poloidal electric current, also directed to the inner target, of 0.5 kA was obtained. The difference between these values can be caused by differences in magnetic configuration, in transport coefficients or in boundary conditions.
For the particular choice of a clockwise toroidal magnetic field B_ϕ clockwise and a counter clockwise main plasma current I_p, viewed from above, (as in both ASDEX-Upgrade and DIII-D), the direction of the induced SOL-current corresponds to the direction of the main plasma current (see figure 6.6). It should be mentioned that the correspondence in direction of main plasma current and scrape-off layer current is completely accidentally because changing the direction of the main plasma current I_p would not alter the induced parallel scrape-off layer current for this model.

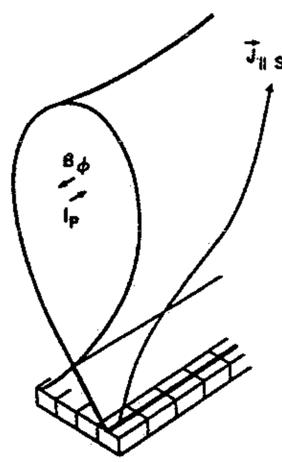

Figure 6.6: Direction of currents and magnetic fields in standard configurations for ASDEX-Upgrade and DIII-D taken from [88]

In figure 6.8, both the computed electron temperature asymmetry, which is defined as the difference between electron temperatures at outer and in target on the same magnetic flux surface ($T_{out} - T_{in}$), and the poloidal electric current density j_θ from the outer target are shown. From this figure one can conclude that the poloidal current density is indeed directed from the higher to the lower electron temperature side. This corresponds to the expected direction from both experimental results and the theory as described by Staebler and Hinton [92] (see section 6.2.1).
Data obtained by Pitcher et al. [90] on poloidal electric current density profiles in ASDEX-

Upgrade show radial profiles which change sign in the neighbourhood of the separatrix (see figure 6.7). The calculated poloidal electric current density profile for ASDEX-Upgrade geometry demonstrates a similar behaviour (see figure 6.8). This geometrical effect is induced by electron temperature asymmetries, which can be explained by looking at the radial electron heat fluxes $q_{e,r}$ through the separatrix :

$$\begin{aligned} q_{e,r} &= \frac{5}{2} n V_r T_e - \kappa_r \frac{1}{h_r} \frac{\partial T_e}{\partial u^r} \\ &= -\frac{5}{2} D T_e \frac{1}{h_r} \frac{\partial n}{\partial u^r} - D n \frac{1}{h_r} \frac{\partial T_e}{\partial u^r} \quad . \end{aligned} \tag{6.1}$$

Assuming an almost constant plasma density and electron temperature on a flux surface, one can conclude that :

$$q_{e,r} \propto \frac{1}{\Delta_{SOL}} \tag{6.2}$$

with Δ_{SOL} the scrape-off layer width. It can be seen from the magnetic configuration in figure 6.5, that this scrape-off layer width at the outside is about the half of the width at the inside. Therefore, if one assumes that the radial electric heat flux is "scraped off" towards the nearest target, the heat flux at the sheath entrance of the outer target is expected to be about twice the one of the inner target. The toroidal effect on surfaces ($\propto Ra$, with R the major radius and a the minor radius) can even enhance this factor. From this estimation one can expect larger electron temperatures at the sheath entrance of the outer target than at the one of the inner target.
Further one can see from figures 6.7 and 6.8, that measured and calculated profiles quantitatively do not well agree : the measured profile is much more flattened in the scrape-off layer and the absolute value of the maximum current density differ by about a factor of 3. These differences between measurements and computational results can be caused by two effects :

1) The induced poloidal current strongly depends on electron temperature asymmetries. However, differences in asymmetries can not be compared, because there is no experimental data available.

2) The experimental results as shown in figure 6.7 are obtained with the "in-vessel probe" [90]. They are inferred from the current density entering the probe when the voltage of the probe with respect to the probe arm is zero. These net currents are probably related to currents in the plasma in the absence of the probe, but it is not evident that they are exactly the same.

A comparison can also be made between experimental and computational results on the plasma potential (see figures 6.9 and 6.10 respectively). Qualitatively the profiles agree, but absolute values differ by about 20-30 V in the scrape-off layer. This could be caused by differences in electron temperature at the target. More detailed comparison therefore require experimental data on electron temperature at the targets.
The implementation of the parallel electric current density $j_{\parallel}$ and the poloidal electric field E_θ in the physics model gives in turn rise to an increase in temperature asymmetries

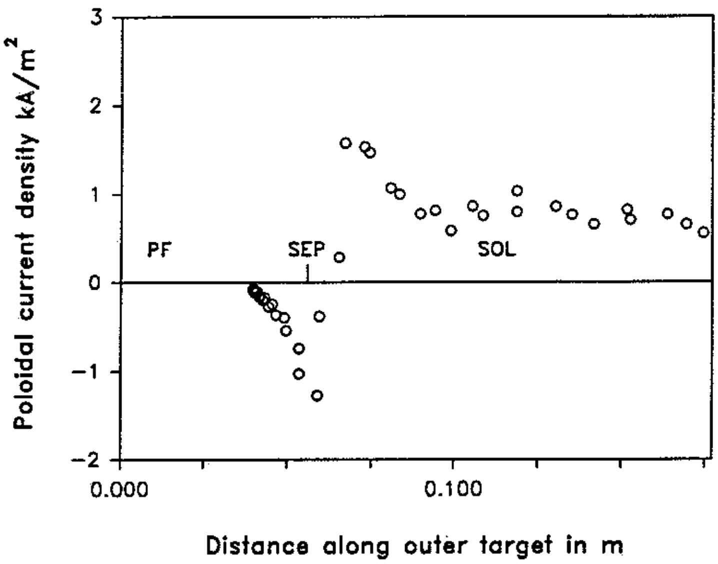

Figure 6.7: Measured poloidal electric current densities [90]

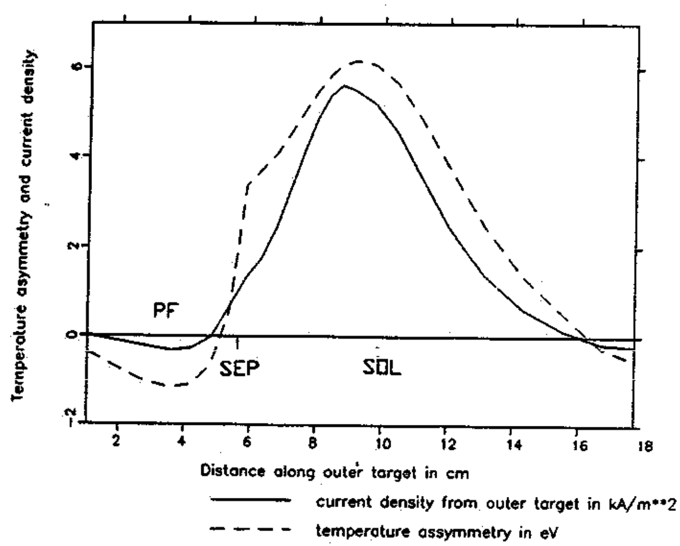

Figure 6.8: Computed electron temperature differences between outer and inner plates and computed poloidal current densities from the outer target

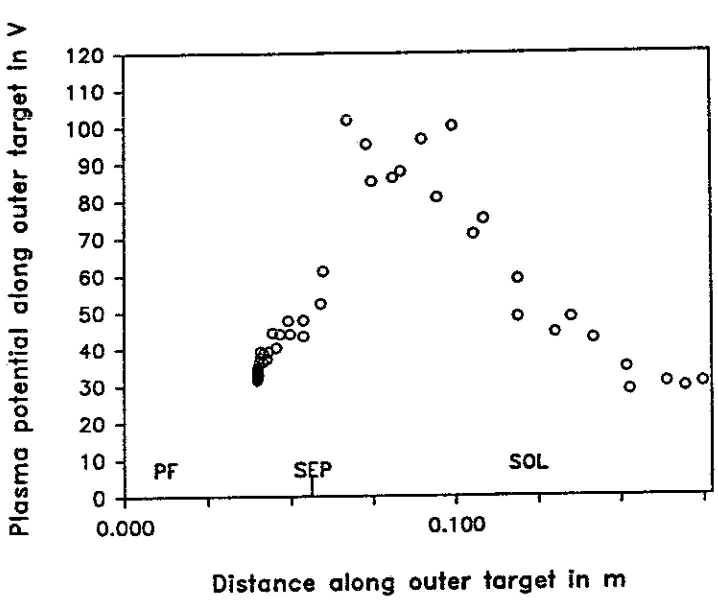

Figure 6.9: Measured plasma potential profiles at the outer target [90]

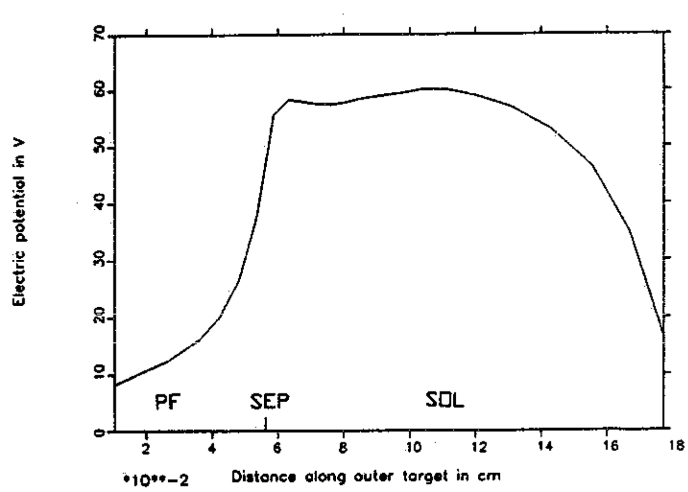

Figure 6.10: Computed plasma potential profiles at the outer target

in the scrape-off layer as is shown in figure 6.11. In this figure differences between electron temperatures at outer and inner targets, i.e. $T_{e,out} - T_{e,in}$, are compared with those of the B2-vdp code.

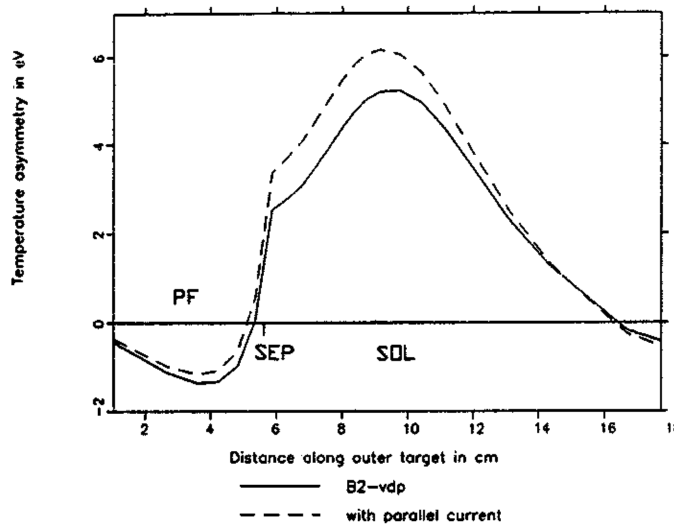

Figure 6.11: Changes in electron temperature asymmetries by implementing parallel electric currents

Changes in heat power load

Before numerical results concerning heat fluxes reaching the targets can be interpreted it should be noted that the values of the electron and ion heat fluxes ($Q_{e,s}$ and $Q_{i,s}$, respectively) given by B2 calculations are those at the sheath entrance (see figure 6.12). The heat flux impinging on the material boundaries therefore should include the change in heat flux due to acceleration of the ions and retardation of the electrons.
As the electron and ion heat fluxes ($Q_{e,s}$ and $Q_{i,s}$ respectively) at the sheath entrance are given by :

$$\begin{aligned} Q_{e,s} &= \delta_e T_e n V_{e,\theta} = \left(\delta_e^* + \frac{e(\Phi_s - \Phi_w)}{T_e}\right) T_e n V_{e,\theta} \\ Q_{i,s} &= \delta_i T_i n V_{i,\theta} \end{aligned} \tag{6.3}$$

according to the boundary conditions, the electron and ion heat fluxes arriving at the material boundaries ($Q_{e,w}$ and $Q_{i,w}$ respectively) become :

$$\begin{aligned} Q_{e,w} &= Q_{e,s} - e\,(\Phi_s - \Phi_w)\, n V_{e,\theta} = \delta_e^* T_e n V_{e,\theta} \qquad (6.4) \\ Q_{i,w} &= Q_{i,s} + e\,(\Phi_s - \Phi_w)\, n V_{i,\theta} = \left(\delta_i + \frac{e(\Phi_s - \Phi_w)}{T_i}\right) T_i n V_{i,\theta} \end{aligned}$$

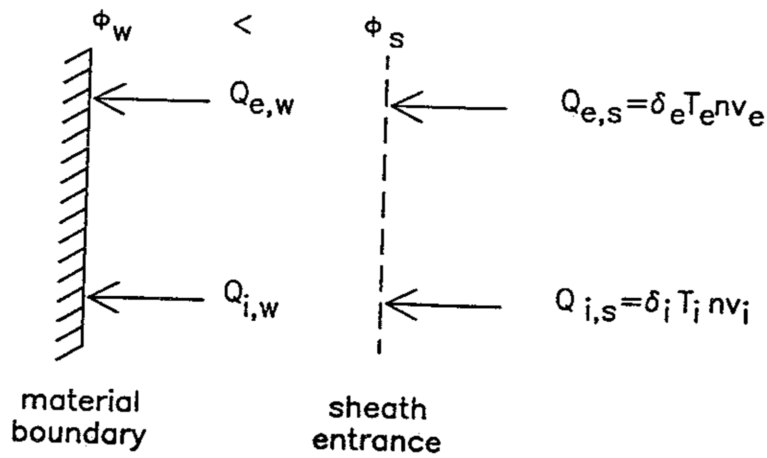

Figure 6.12: Heat fluxes to material boundaries

Therefore, the total heat flux towards a target $Q_{i+e,w}$ does not equal the total heat flux at the sheath entrance $Q_{i+e,s}$ for non-ambipolar calculations. The relation between those two fluxes can be written as :

$$Q_{i+e,w} = Q_{i+e,s} + (\Phi_s - \Phi_w) j_\theta \tag{6.5}$$

Indeed, a current towards the plate will gain energy by the potential difference between sheath entrance and wall.
Figures 6.13 and 6.14 show that the heat power load is not much affected by the implementation of parallel electric currents and poloidal electric fields. Nevertheless, the slight decrease at the inner target already confirms the observed qualitative trends during biassing experiments. Namely, at the target where a current arrives (for biassing the cathode) the heat power load decreases (see subsection 6.2.2). Furthermore, computational results indicate an in/out asymmetry in heat flow to the targets of $\frac{Q_{out}}{Q_{in}} = 1.5$. Experimentally, asymmetries in power load towards the target, for ASDEX-Upgrade, have been measured and amount to about 1.9 [83].

6.3.3 Calculations for a divertor configuration with biassed plates

Changes in heat power load

For these calculations a voltage of 10 V is applied on the inner target as shown in figure 6.15. This relatively low applied voltage already induces a SOL-current from the inner to the outer target of 3.88 kA. It should be noted that the experimental results of DIII-D [88] indicate a much lower induced current for an applied voltage of 10 V. On the other hand, similar results to those obtained with the extended B2 code are obtained with the LEDGE code [84].

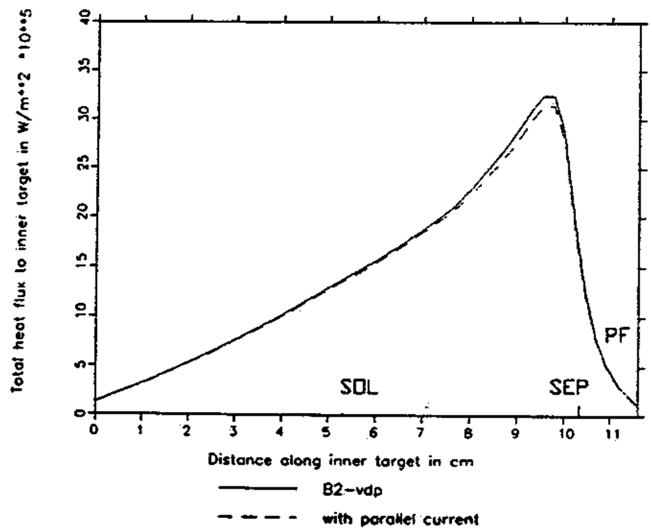

Figure 6.13: Heat flux to the inner target

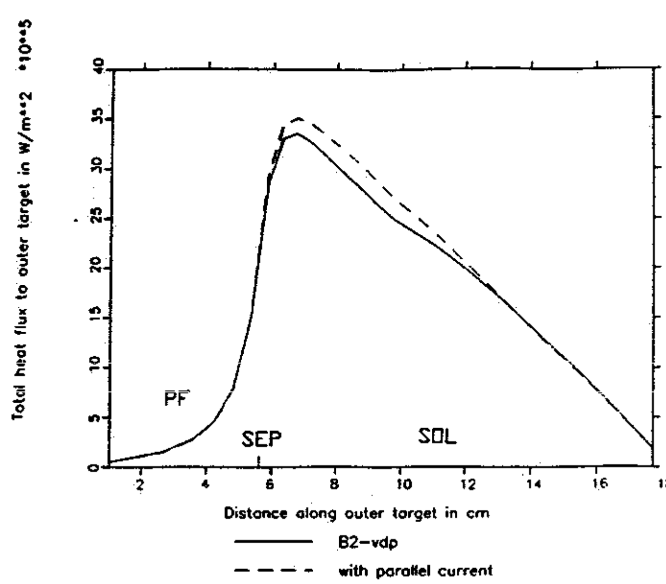

Figure 6.14: Heat flux to the outer target

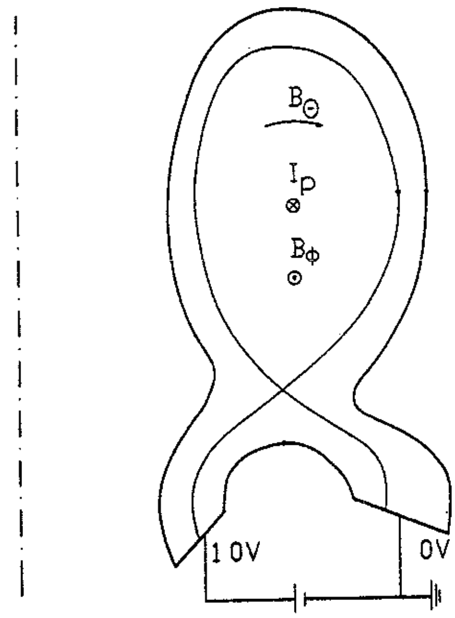

Figure 6.15: Schematic view of the simulated biassing experiment

If one looks in some more detail now at the expressions for heat fluxes to the wall, Eqs. (6.5), assuming that plasma parameters at the target are not much affected by the poloidal current, except for the sheath potential Φ_s and the electron velocity $V_{e,\theta} = V_{i,\theta} - \frac{j_\theta}{en}$, it is possible to predict the qualitative changes in heat fluxes reaching the wall. Starting from the expression for the electron heat flux, Eq. (6.5), we obtain :

$$Q_{e,w} = \delta_e^* T_e n \left(V_{i,\theta} - \frac{j_\theta}{en} \right) \quad . \tag{6.6}$$

Therefore, a variation in electric current density Δj_θ will result in a change in electron heat flux $\Delta Q_{e,w}$:

$$\Delta Q_{e,w} \approx -\delta^* \frac{T_e}{e} \Delta j_\theta \quad . \tag{6.7}$$

This is illustrated in figures 6.16 and 6.17, where indeed the electron heat flux to the target increases and the electron heat flux to the outer target decreases.
The ion heat flux is influenced by the potential difference over the sheath. The change in ion heat flux $\Delta Q_{i,w}$can be written as :

$$\Delta Q_{i,w} \approx enV_{i,\theta} \Delta \left(\Phi_s - \Phi_w \right) \tag{6.8}$$

As the potential difference changes logarithmically with the poloidal current density :

$$\Phi_s - \Phi_w = C - \frac{T_e}{e} \ln \left(1 - \frac{j_\theta}{enV_{i,\theta}} \right) \tag{6.9}$$

where C is a function of local plasma parameters, one obtains :

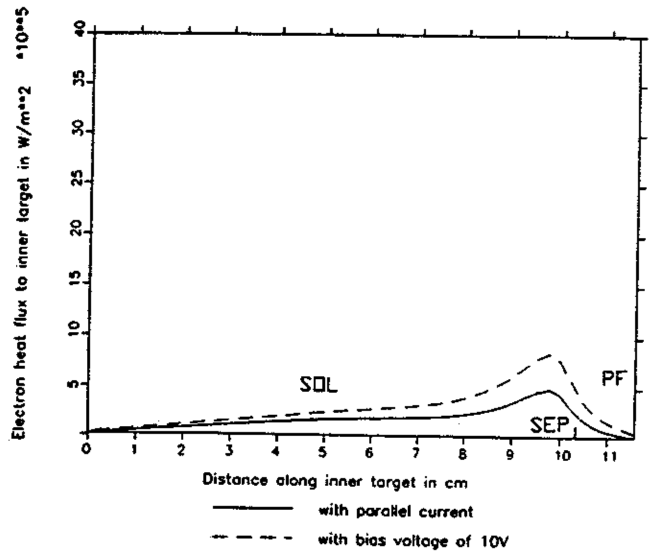

Figure 6.16: Electron heat flux to the inner target

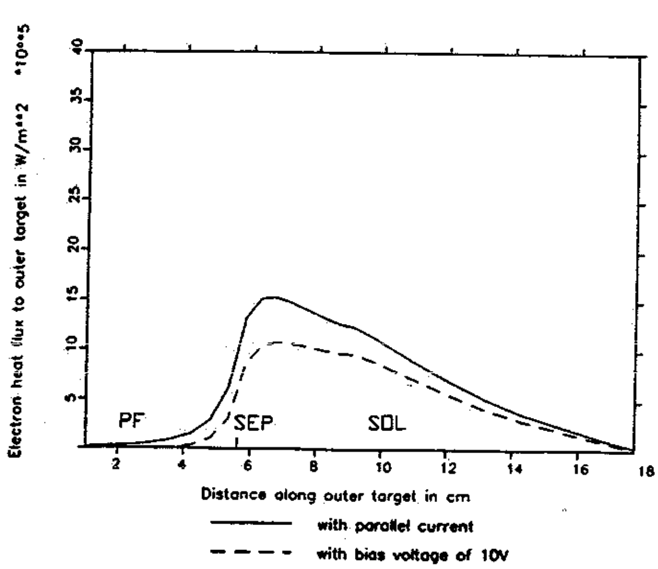

Figure 6.17: Electron heat flux to the outer target

$$\Delta\left(\Phi_s - \Phi_w\right) \approx \frac{T_e}{e}\frac{1}{1-\frac{j_\theta}{enV_{i,\theta}}}\frac{\Delta j_\theta}{enV_{i,\theta}} \quad . \tag{6.10}$$

Therefore, the change in ion heat flux reaching the wall can be expressed as :

$$\Delta Q_{i,w} \approx \frac{T_e}{e}\frac{1}{1-\frac{j_\theta}{enV_{i,\theta}}}\Delta j_\theta \quad . \tag{6.11}$$

For low current densities this expressions results in :

$$\Delta Q_{i,w} \approx \frac{T_e}{e}\Delta j_\theta \quad . \tag{6.12}$$

This is illustrated in figures 6.18 and 6.19, where indeed the ion heat flux reaching the inner target decreases and that reaching the outer target increases.
Since δ^* approximately equals 2, the total heat flux will decrease if a current strikes the target :

$$\Delta Q_{i+e,w} \approx \left(1-\delta^*\right)\frac{T_e}{e}\Delta j_\theta \quad . \tag{6.13}$$

Expression 6.10 shows that for larger poloidal current densities the ion heat flux will increase more strongly at the cathode, where a positive current arrives, and a weaker decrease at the anode. Since for higher current densities the assumption of unchanged plasma parameters at the target is questionable, numerical verification is required here.
The total heat flux, as obtained from numerical simulations, is shown in figures 6.20 and 6.21. This qualitatively confirms both the experimental results and the indicative formulae as derived above, that the heat power load is shifted from cathode to anode (see section 6.2.2 and [103]).

Electric potential

Although, the electric potential profile at the outer midplane is increased with biassing, the difference does not equal the applied voltage (see Fig. 6.22) as was measured in biassing experiments (see subsection 6.2.2). This is probably due to the relative low induced electric current. In comparison with the ion saturation current the induced current amounts only to 20%. For larger electric currents, again due to the logarithmic behaviour of the sheath potential with the poloidal current density, it can be expected that the electric plasma potential adapt to the highest voltage applied at one of the targets. In addition, it should be notated that in the PBX-M experiment, radial electric fields are created. Therefore, differences between these numerical and experimental results could be expected.

Power balances

In table 6.1 to 6.2 the electron and ion energy flows are given for grounded and biassed plates respectively. The power balance for the plasma is fulfilled when the heat flow coming from the core equals the sum of heat flows to the material boundaries (more specifically to the sheaths and the wall) and power sinks due to interactions of the plasma with neutral particles. Since for these computations the "minimal model" was used with

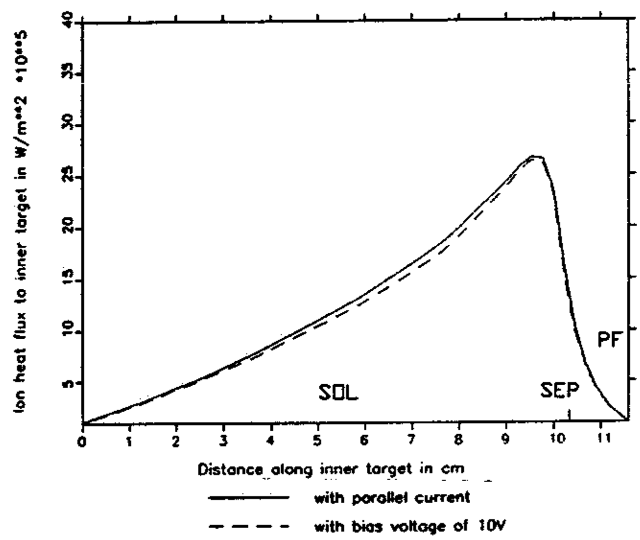

Figure 6.18: Ion heat flux to the inner target

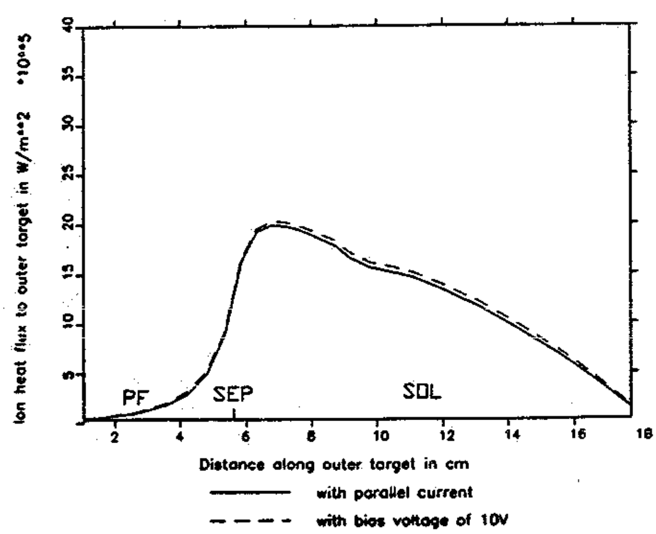

Figure 6.19: Ion heat flux to the outer target

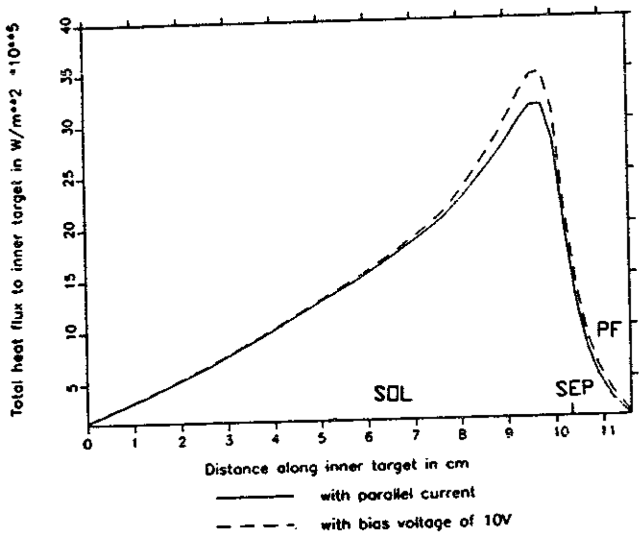

Figure 6.20: Total heat flux to the inner target

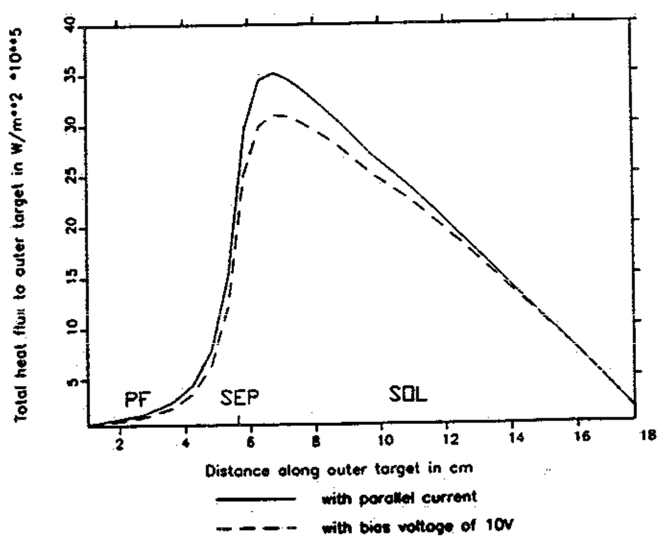

Figure 6.21: Total heat flux to the outer target

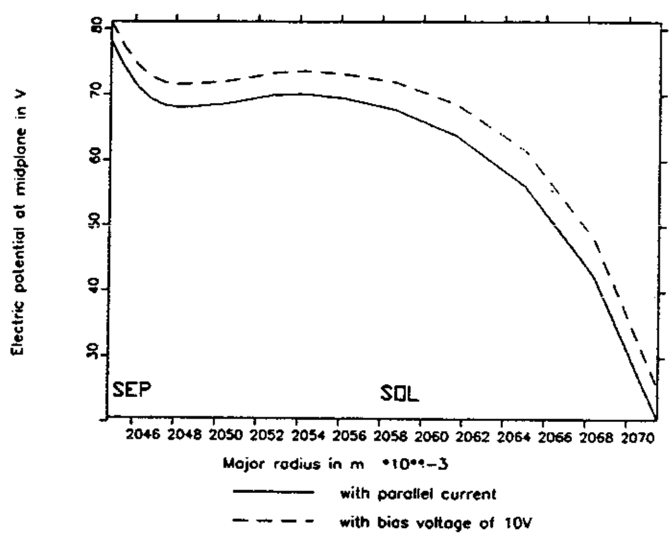

Figure 6.22: Change in electric potential at the outer midplane position

a recycling coefficient at the targets of 0.7 (see section 3.5), the latter can be computed as $0.7 \times 25\text{eV} \times \Gamma_{targets}$ for the electrons and $-0.7 \times 5\text{eV} \times \Gamma_{targets}$ (thus a source) for the ions. From these data one can conclude that the heat flow towards the targets indeed is increases with the applied biassing power.

Conclusions

It is clearly demonstrated that already the implementation of the parallel electric current density $j_{||}$ and the poloidal electric field E_θ bring out the qualitative effects of poloidal current direction and biassing effects on plasma potential and heat power load.

6.4 Relative contribution of additional flows

Since the introduction of $V_\perp$ can strongly influence the boundary value of $V_{||}$ at the targets (see section 5.4.2), difficulties can be expected if relatively large values for $V_\perp$ are involved at these targets. Therefore, in this section we will estimate the parameter α, which is defined as the ratio of absolute values of the poloidal projection of $V_\perp$ and V_θ near the material boundaries. In subsection 6.4.1 a simplified computation of the ion velocity in the diamagnetic direction brings out differences between the relative importance of these flows at the targets of limiter and divertor Tokamaks. An analytic, one-dimensional model indicates the main features of these two magnetic configurations in subsection 6.4.2.

6.4.1 Numerical studies for TEXTOR and ASDEX-Upgrade

Since the ion velocity in the diamagnetic direction $V_\perp$ depends on radial gradients of electric potential Φ and total pressure p (see Eq.(5.5)), the complete calculation of this

	Q from main plasma in MW	Q_s to inner target in MW	Q_s to outer target in MW	Q to wall in MW
Electrons	2.639	0.669	1.430	0.369
Ions	1.320	0.392	0.525	0.134
	Neutral sources in MW	**Q_w to inner target in MW**	**Q_w to outer target in MW**	**Biassing power in MW**
Electrons	-0.573	0.147	0.335	0
Ions	0.115	1.059	1.461	0

Table 6.1: Power balance for divertor calculation with grounded plates

	Q from main plasma in MW	Q_s to inner target in MW	Q_s to outer target in MW	Q to wall in MW
Electrons	2.636	0.997	1.083	0.373
Ions	1.320	0.392	0.530	0.132
	Neutral sources in MW	**Q_w to inner target in MW**	**Q_w to outer target in MW**	**Biassing power in MW**
Electrons	-0.414	0.243	0.244	0.039
Ions	0.083	1.019	1.520	

Table 6.2: Power balance for divertor calculation with biassed plates

velocity component requires the implementation of electric currents. Only such an implementation can provide adequate information about the radial electric field throughout the modelled volume. However, a first estimate of the ion velocity in the diamagnetic direction $V_\perp$ can be obtained in between two material boundaries with the assumption that the electric potential in the scrape-off layer is determined mainly by the sheath potential (Eq. (5.13)). We will approximate this equation by Eq. (5.14) :

$$\Phi_s - \Phi_w = 3.1\frac{T_e}{e} \quad . \tag{6.14}$$

This will permit us to compute $\alpha = (\frac{B_\phi}{B}V_\perp)/V_\theta$ at the limiter boundaries of TEXTOR and ASDEX-Upgrade.

TEXTOR calculations

For TEXTOR, with standard direction of the toroidal magnetic field anti-parallel to the plasma current, results of the B2-vdp-EIRENE calculation (see section 4.5.2) are investigated. For these results, with a counter clockwise plasma current, if viewed from above, the projection in a poloidal cross-section (at the right of the magnetic axis) of the ion particle flow in the diamagnetic direction is in clockwise direction (see figure 6.23).

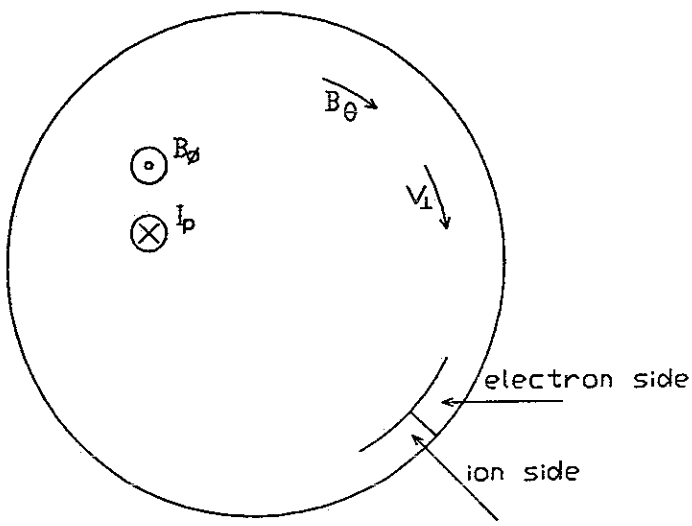

Figure 6.23: Direction of the diamagnetic flow for standard TEXTOR configuration

Taking into account the sheath boundary condition (see figure 5.1), this direction of $V_\perp$ will induce a lower parallel velocity at the upperside and a larger parallel velocity at the lowerside of the limiter. As a result of this plasma parameters at the target will slightly change. The effect of these changes on the value of α, however, is not taken into account for these estimations.
The ratio α of absolute values of the poloidal projection of $V_\perp$ and V_θ at ion and electron drift side of the limiter are shown in figure 6.24. From this figure it can be seen that α

is rather high, especially at the limiter tip where α exceeds unity. Therefore, problems in solving the equations of the extended B2 model can be expected near the separatrix.

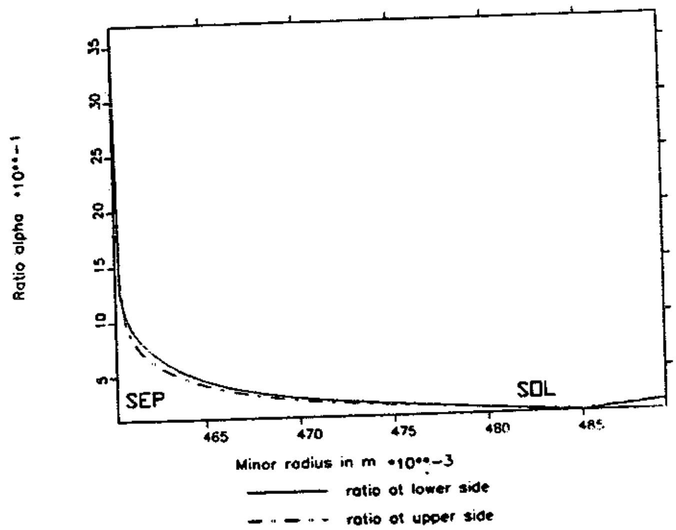

Figure 6.24: Ratio α of the poloidal projection of $V_\perp$ and V_θ for TEXTOR

ASDEX-Upgrade calculations

For ASDEX-Upgrade, an axisymmetric poloidal divertor experiment situated at the Max-Planck Institut für Plasmaphysik, Garching bei München, Germany, similar computations are performed. For these calculations , the magnetic configuration, transport coefficients, boundary conditions and neutral model are taken as described in subsection 6.3.2.
The ratio α of the poloidal projection of $V_\perp$ and V_θ at both target plates are presented in figure 6.25. In this figure 6.25, the profile peaks at the place where the separatrix strikes the target, (indicated with "SEP"). The significant difference in α between the scrape-off layer (SOL) and the private flux region (PF), can be explained by the shorter connection length of the latter, since $\alpha \propto \frac{1}{\sqrt{L_\parallel}}$ (see section 6.4.2).
It can be seen that the average value of α over the target is significantly lower for the ASDEX-Upgrade calculations than for the TEXTOR-calculations. Results of those two experimental devices differ by a factor of 10.

6.4.2 One-dimensional analytic approach

In an attempt to understand the differences in α between the limiter configuration of TEXTOR and divertor configurations of ASDEX-Upgrade, as observed in section 6.4.1, a one-dimensional model is worked out in this subsection.
In order to obtain the radial decay length for the ion density λ_n in the scrape-off layer, the continuity equation is evaluated in a flux tube with a radial width dr and a length L_θ, poloidally measured along a flux surface between the two targets (see figure 6.26). A local

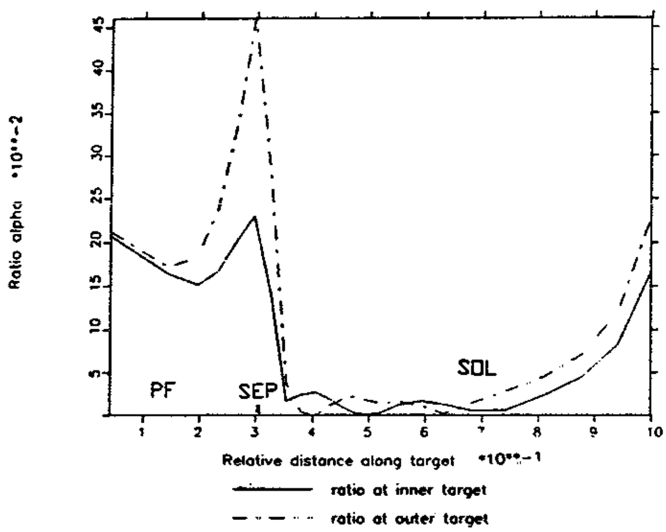

Figure 6.25: Ratio α of the poloidal projection of $V_\perp$ and V_θ for ASDEX-Upgrade

recycling coefficient R_c is defined as the ratio between ionized neutral particles in the flux tube and ion particles outflowing from the latter.
For this flux tube, the continuity equation integrated along the magnetic field from target to target becomes :

$$\frac{1}{h_r}\frac{\partial}{\partial u^r}\Gamma_r L_\theta = -2n\left(\overline{\frac{B_\theta}{B}}\right)c_s + 2R_c n\left(\overline{\frac{B_\theta}{B}}\right)c_s \tag{6.15}$$

with Γ_r the radial particle flux and c_s the isothermal sound velocity, $\left(\overline{\frac{B_\theta}{B}}\right)$ the average of the value of $\frac{B_\theta}{B}$ at the "left" and the "right" target and $\left(\overline{\frac{B_\theta}{B}}\right)c_s$ being the average poloidal ion velocity with which the particles impinge on the "left" and the "right" plate.
Assuming that n can be written as

$$n(\theta, r) = n(\theta)e^{-r/\lambda_n} \tag{6.16}$$

and

$$\Gamma_r = -D\frac{1}{h_r}\frac{\partial n}{\partial u^r} \tag{6.17}$$

substitution of these equations in equation (6.15) leads to the determination of the decay length for the plasma density λ_n :

$$\lambda_n = \sqrt{\frac{DL_\theta}{2\left(1-R_c\right)\left(\overline{\frac{B_\theta}{B}}\right)c_s}}\ . \tag{6.18}$$

If the decay lengths of the radial temperature profiles in the scrape-off layer are assumed to be constant and can approximately be written as :

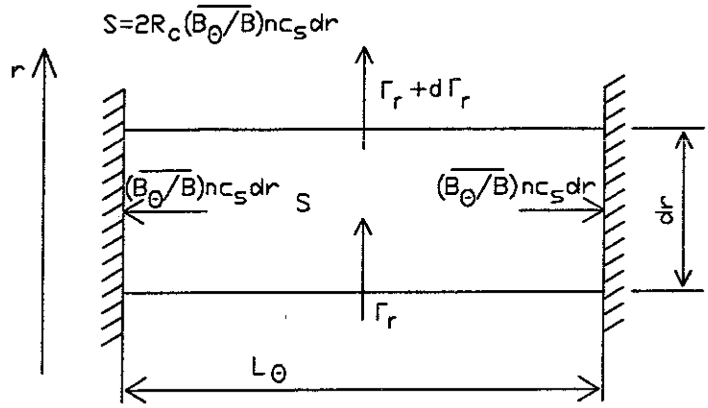

Figure 6.26: Conservation of ionized particles in a flux tube

$$\lambda_T \approx \lambda_n \approx \lambda \tag{6.19}$$

and

$$\Phi \approx 3\frac{T_e}{e} \ , \tag{6.20}$$

the diamagnetic component of the ion velocity which is determined by, Eq. (5.5) :

$$V_\perp = -\frac{1}{enB}\frac{\partial p_i}{h_r \partial u^r} - \frac{1}{B}\frac{\partial \Phi}{h_r \partial u^r} \tag{6.21}$$

becomes at the target :

$$V_\perp = -\frac{nT_i}{enB\lambda} - \frac{1}{eB}\frac{3T_e}{\lambda} \tag{6.22}$$

or with $T \approx T_i \approx T_e$:

$$|V_\perp| = \frac{4T}{eB\lambda} \quad . \tag{6.23}$$

Therefore, the proportion α of the poloidal projections of the ion velocity in the diamagnetic direction $V_\perp$ to the averaged poloidal ion velocities to the targets $V_\theta = \left(\frac{B_\theta}{B}\right) c_s$ reads :

$$\alpha = \frac{\frac{B_\phi}{B} V_\perp}{\left(\frac{B_\theta}{B}\right) c_s} \approx \sqrt{\frac{2\,(1-R_c)}{DL_\theta \left(\frac{B_\theta}{B}\right) c_s}\frac{B_\phi}{B}\frac{4T}{eB}} \tag{6.24}$$

where $c_s = \sqrt{\frac{2T}{m_i}}$.

For TEXTOR with following properties used for the simulation of a deuterium plasma in the scrape-off layer :

$L_\theta \approx 3$ m

$D \approx 0.6$ m^2/s

$T \approx 20$ eV

$R_c \approx 0.25$

$\left(\frac{B_\theta}{B}\right) \approx 0.1$

$B \approx 2$ T

the value of α becomes :

$$\alpha \approx 0.55 \quad . \tag{6.25}$$

For ASDEX-Upgrade with following properties used for the computations in the scrape-off layer :

$L_\theta \approx 5$ m

$D \approx 2$ m^2/s

$T \approx 20$ eV (at the target)

$R_c \approx 0.7$

$\frac{B_\theta}{B} \approx 0.2$

$B \approx 2.5$ T

on the other hand, the value for α is only :

$$\alpha = 0.082 \quad . \tag{6.26}$$

For the private flux region the poloidal length L_θ amounts only to 0.45 m. The ratio α in this region is thus estimated to be :

$$\alpha = 0.27 \quad . \tag{6.27}$$

These numbers are in good agreement with the numerical results of section 6.4.1.
From the derived formula, one can conclude that the relative importance of ion particle flow in the diamagnetic direction is higher the lower the local recycling coefficient and therefore one can expect generally these terms to be more important for limiter than for divertor geometries. Furthermore, it can be seen from both expression (6.24) and from figure 6.25, that the ratio α will be higher in the private flux region. This is induced by a smaller poloidal connection length L_θ. It should be notated that at the X-point also a ratio α can be defined as $\alpha = \frac{B_\phi}{B} V_\perp / \frac{B_\theta}{B} V_\|$. Since B_θ equals zero at this point, α goes to infinity, which means that there exists a major impact of the ion particle flow in the diamagnetic direction in the neighbourhood of the magnetic X-point.

6.5 Extended B2-calculations

6.5.1 Introduction

In this section the extended physics model as described in chapter 5, which is based on the additional equations Eqs. (5.3)-(5.7), is applied to the ASDEX-Upgrade single-null divertor geometry in the case of no bias. Calculations with this model, including the computation of $V_\perp$, $j_\perp$, $j_{||}$, j_r and Φ, lead to real-time oscillations originating from the X-point, as will be described in subsection 6.5.2. Nevertheless, this is a very localized problem and we will anyway be able to obtain steady state solutions. Since the electric potential is calculated in these simulations, the assumption of quasineutrality can easily be checked. This is done in subsection 6.5.3. In order to determine the electric potential profile inside the separatrix the total momentum equation in the diamagnetic direction, Eq. (5.7), is used. In this equation the influence from poloidal pressure gradients is neglected. Furthermore, the simple B2 model for neutrals does not provide any information about the momentum sources from neutrals in the diamagnetic direction, so that these effects are also excluded. Inertia terms and viscous terms of the total momentum equation in the diamagnetic direction are investigated with respect to the radial electric potential profile in subsection 6.5.4. In a next subsection the influence on power load and on asymmetries in plasma parameters is discussed.

6.5.2 Oscillations originating at the X-point

In order to obtain a well-converged solution all over the grid (total residuals of $10^{-3}s^{-1}$ for time-steps of $10^{-7}s$) with the extended B2 code with realistic time-scales, the code has to iterate internally after each numerical time-step. Therefore, it provides transient information in real time. Computational results indicate local radial oscillations in plasma density, electric potential and ion velocity in the diamagnetic direction starting from the X-point, but not affecting the electron nor the ion temperature at this location. Plasma profiles in other grid cells are only slightly changed by induced changes in parallel electric currents.

As these oscillations are independent from numerical time-step and grid-spacing, these oscillations are likely to be induced by the physics model. The cause of this phenomenon is beyond the scope of this thesis, but certainly requires more attention in further research. It should be mentioned that the presence of these oscillations is not surprising, since B_θ equals zero at the X-point. Therefore there is a major impact of $V_\perp$ in the neighbourhood of this point (see section 6.4.2). Figure 6.27 shows a typical radial ripple in the plasma density profile originated at the X-point. However, we can still work with it because these oscillations are local and steady state solutions are obtained every where else.

6.5.3 Quasineutrality

With the extended B2 code, the electric potential is computed all over the modelled area. Therefore, one of the assumptions, made in both the B2 and the extended B2 code, can easily be checked, namely the assumption of quasineutrality. This is done by calculating the electric charge density from the electric potential with the use of equation (2.54) :

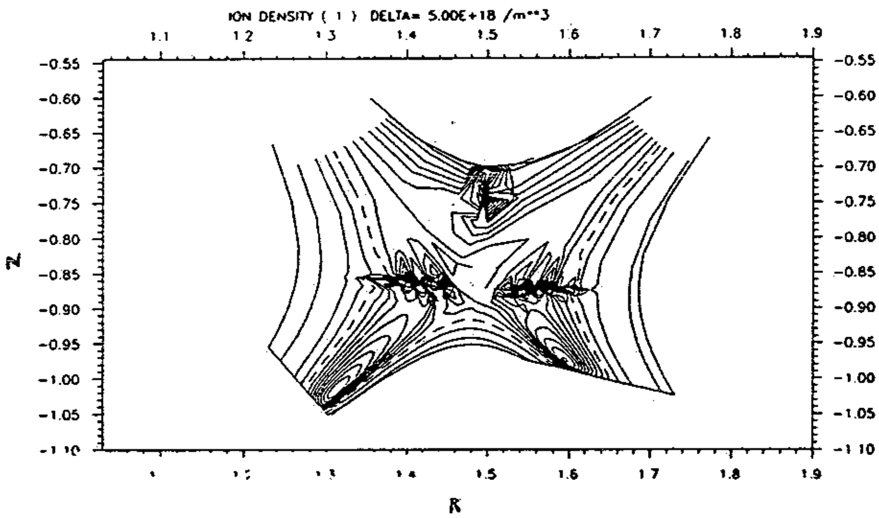

Figure 6.27: Radial ripple in plasma density profile

$$\nabla^2 \Phi = -\rho / \epsilon_0 \tag{6.28}$$

The relative charge density $\left|\frac{n_i - n_e}{n_i}\right|$ maximally amounts to 10^{-5}. One can thus conclude that the assumption of quasineutrality is well satisfied.

6.5.4 Potential profile inside the separatrix

As discussed in chapter 5, the relation between the radial current density j_r and the radial electric field E_r is obtained by a combination of two collisionally dominated neoclassical transport equations, Eqs.(5.5) and(5.7). These equations also provide information about the electric potential inside the separatrix. Therefore, calculated profiles bring already an indication of physics involved in correlating radial electric fields and radial electric current densities.

More specifically, equation (5.7), which will be used to compute j_r, contains two terms in $V_\perp$, namely an inertia and a viscous term. In an effort to distinguish the contribution of those two terms, we first will take the inertial term, and then, in a second computation, we will add the viscous term. When only the inertia term is used, one obtains the same expression for the radial current density as the one used in the SOLXY model of Gerhauser and Claaßen [15] :

$$j_r = \frac{1}{B}\frac{1}{\sqrt{g}}\left[\frac{\partial}{\partial u^\theta}\left(\frac{\sqrt{g}}{h_\theta} mnV_\theta V_\perp\right) - \frac{\partial}{\partial u^r}\frac{\sqrt{g}}{h_r}(mnV_r V_\perp)\right] \quad . \tag{6.29}$$

Adding the viscous contribution to this equation

$$j_r = \frac{1}{B}\left\{\frac{1}{\sqrt{g}}\left[\frac{\partial}{\partial u^\theta}\left(\frac{\sqrt{g}}{h_\theta} mnV_\theta V_\perp\right) - \frac{\partial}{\partial u^r}\left(\frac{\sqrt{g}}{h_r} mnV_r V_\perp\right)\right]\right.$$

$$+ \quad \frac{1}{\sqrt{g}}\frac{\partial}{\partial u^\theta}\left[\frac{\sqrt{g}}{h_\theta^2}\eta_0\left(\frac{2}{3}\frac{B_\theta B_\phi}{B^2}\frac{\partial}{\partial u^\theta}V_\parallel - \frac{1}{3}\frac{B_\phi^2}{B^2}\frac{\partial}{\partial u^\theta}V_\perp\right)\right]\Bigg\} \tag{6.30}$$

yields an electric potential profile that much better agree with experimental profiles [105],[12]. Computed radial electric potential profiles at the midplane for both cases are shown in figure 6.28. From this it can be seen that, using only the inertial terms to compute the radial current density, (Eq. 6.29), the electric potential inside the separatrix strongly increases radially inward. This might be the reason that in SOLXY [15] an ad hoc profile for $V_\perp$ inside the separatrix is assumed. However, in their work, this assumption leads to a discontinuity of poloidal electric current density inside the separatrix at the poloidal position of the limiter [53]. Therefore, it might be better to include the viscous terms, Eq.(6.30), as is done in the extended B2 code. The radial electric potential profiles inside the separatrix can then be computed based on the neoclassical equations, Eqs. (5.5) and (5.7).

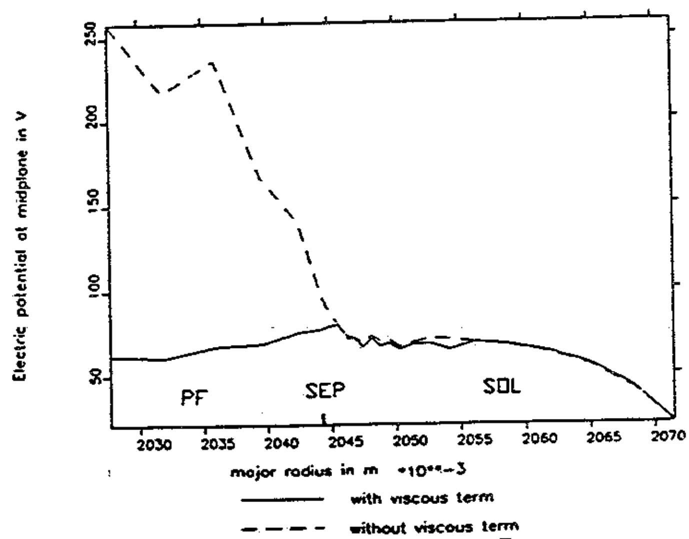

Figure 6.28: Computed radial electric potential profile with and without including the viscous term

6.5.5 Power load on the targets and plasma parameter asymmetries

In the scrape-off layer the electric current density in the diamagnetic direction, obtained with Eq. (5.5), for the standard configuration of ASDEX-Upgrade, will be directed towards the outer target (see figure 6.1). Therefore, in comparison with results obtained with the code including only $j_\parallel$ and E_θ, one might expect a decrease of the poloidal electric current to the inner target and an enhancement of the total heat flow impinging on the inner target (cfr. Eq. (6.13)). Our computational results do not agree with these estimations : in comparison with the computations as performed in subsection 6.3.2, the total poloidal current to the inner target is increased to 3.193 kA, the total heat flow reaching the outer target is not affected and the total heat flow to the inner target is slightly enhanced (see table 6.3).

Effects	Current to innner target in kA	Power load on inner target in MW	Power load on outer target in MW	T_e at inner target in eV	T_e at outer target in eV
B2-vdp	0	1.230	1.778	17.38	20.61
$j_{\parallel}$	2.851	1.206	1.796	17.44	20.79
Bias 10V	-3.880	1.262	1.763	18.01	20.91
Ext. B2	3.193	1.216	1.796	17.54	20.97

Table 6.3: Comparison for code results adding various effects

That equation (6.13) is not longer applicable is due to the fact that the plasma parameters at the targets are affected by the implementation of flows in the diamagnetic direction. Indeed, the ion particle flow in the diamagnetic direction is directed towards the outer target, the parallel ion velocity at this target has to be reduced in order to fulfil the boundary condition at the sheath (see section 6.4.1 and figure 5.1). This requires an enhancement of the pressure at the outer and a decrease in total pressure at the inner target, in order to force the parallel ion velocity to fulfil the boundary conditions. In the private flux region the ion particle flow in the diamagnetic direction is directed towards the inner target. Therefore, an opposite behaviour in total pressure is expected in this region, i.e. an increase of total pressure at the inner target and a decrease at the outer one. The effect of implementing $V_{\perp}$ and $j_{\perp}$ on the total pressure profiles at inner and outer target are shown in figures 6.29 and 6.30. Except for the scrape-off layer at the inner target it can be seen that the total pressure indeed is adapted according the expectations, as described above.

Furthermore, the experimental results on electron pressure asymmetries as described in subsection 6.2.1, can be confirmed with these calculations. The electron pressure at the inner target, or ion drift side for this configuration, has been increased by including terms which depend on the direction of the magnetic field (see figure 6.31).

Finally, the results concerning power load assymetries and scrape-off layer currents for different models are summarized in table 6.3. From this table one can see that the direction of the poloidal electric current in the edge is directed from higher to lower target temperatures. However, applying a voltage of only 10 V on the inner target, can already change this direction.

From the point of view of design studies, it can be seen that the implementation of additional physics in the code hardly affects the results on heat flow or on peak electron temperature. Therefore, one can conclude that, at least for divertors with grounded plates, the implementation of these additional physics is not required. On the other hand, for analysis of physics concerning electric currents, electric potential profiles and for simulations of biassing experiments, the extended B2 can provide helpfull information.

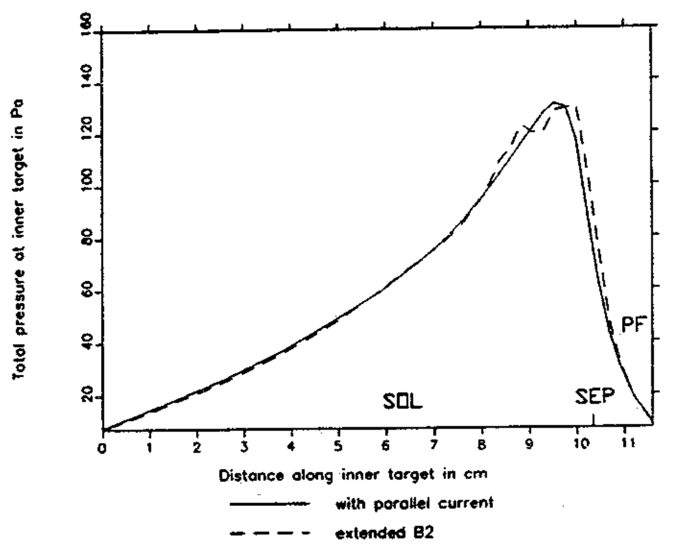

Figure 6.29: Total pressure at the inner target

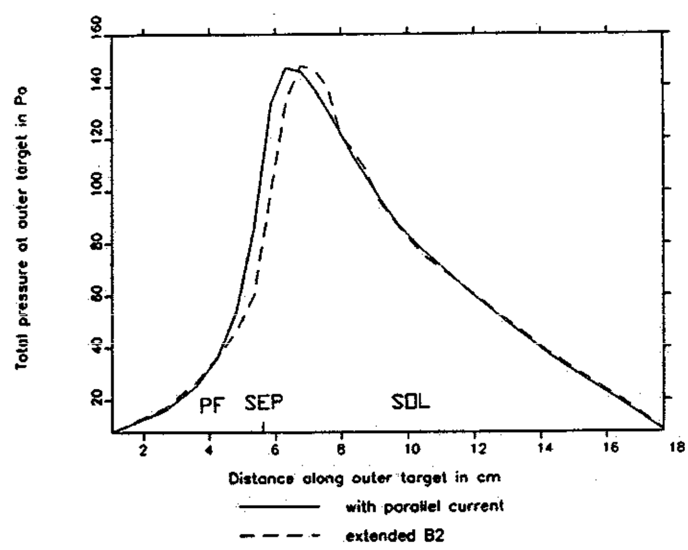

Figure 6.30: Total pressure at the outer target

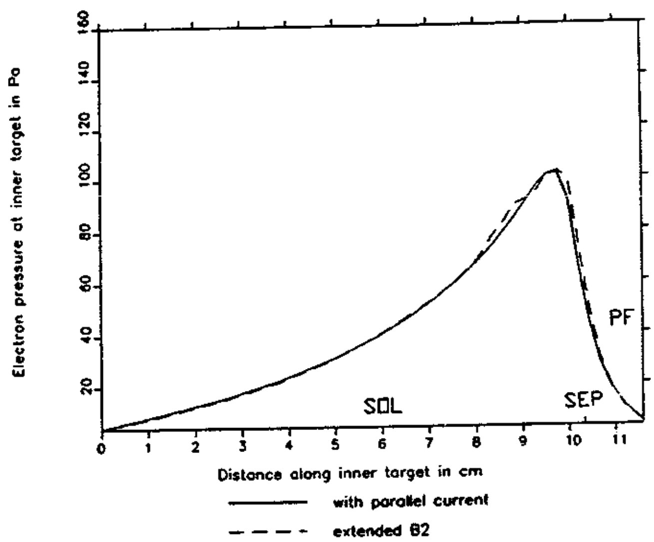

Figure 6.31: Electron pressure at the inner target

6.5.6 Conclusions

Although we have observed oscillations in ion density, electric potential and ion velocity in the diamagnetic direction near the X-point, these oscillations only locally influence the other plasma parameters. This permits us to discuss results at the targets and at the midplane. However, the singularity in the magnetic configuration will require some more investigation, in order to improve the model at this point.
In an attempt to provide the experimentally obtained electric potential profiles inside the separatrix, a neoclassical formulation of the total momentum equation in the diamagnetic direction can be used. Calculations bring out that this expression must contain the visous term.
Although the ion particle flow in the diamagnetic direction is directed towards the outer target, the scrape-off layer current towards the inner target is increased by implementing $V_{\perp}$. This can be explained by the influence of the ion particle flow in the diamagnetic direction on the plasma parameters at the targets. Furthermore, in agreement with experimental results, the electron pressure increases at the ion drift side, which is for these calculations the inner target.
Coming to the end of this thesis, it is clear that the investigation of electric currents and flows in the diamagnetic direction is not finished yet. However, this work provides usefull information for further research on this topic. Possible items for future work are manifold : the implementation of $\vec{B} \times \vec{\nabla} T$ as proposed in item 4) of subsection 5.2.1; the investigation of detailed neutral modelling using the coupling procedure with the EIRENE code; the simulation of reversed field and biassing experiments with the extended B2 code, including $V_{\perp}$, $j_{\perp}$, j_r and E_r; etc. Since the applicability of the extended B2 code, is still limited because of the low convergence rate of the code, further improvement of the numerical procedure will be desirable.

Chapter 7

General conclusions and suggestions for further research

7.1 General conclusions

The plasma edge, which determines the boundary conditions for the core plasma, plays an important role in controlling particle and energy exhaust. Furthermore, scrape-off layer profiles determine the screening efficiency of wall released particles, which can contaminate the core plasma. In order to optimize the design of future fusion Tokamaks, such as NET and ITER, it is essential to understand the physics involved in the plasma edge region. In particular, influences on plasma edge profiles from different magnetic configurations, from geometrical details of the reactor vessel and from active means for controlling the edge are important issues of present fusion research. Therefore, experimental, theoretical and modelling efforts, as are performed in this thesis, are required.
In this work a two-dimensional plasma edge code "B2", which was written by Braams [13], is used. The major advantage of this code is that it can handle different magnetic configurations. Therefore, it can both be confronted with present experimental data and contribute to the design of NET and ITER. This thesis is concerned with the evaluation, improvement and extension of this B2 code. The main contributions and results of this work are the following :

1) Starting from the Braginskii equations [14], the collisionally dominated neoclassical transport equations are derived for a two-dimensional orthogonal curvilinear coordinate system assuming toroidal symmetry in Tokamaks. This leads to a set of coupled non-linear differential equations, which permits us to determine simplifying assumptions in presently used edge plasma codes and to extend the physics content of the B2 code.

2) Applications of the B2 code to the experimental limiter Tokamak TEXTOR, brings out that the convergence behaviour of the code strongly depends on the formulation of boundary conditions. Especially, in this work, the problem of implementing a periodic condition inside the last closed flux surface is solved using an explicit method. In an attempt to treat the equations at this boundary region in the same way as for internal cells, a semi-implicit method developed by Schneider et al. [42]

is implemented. Despite the better treatment of the evaluation of the equations, the convergence behaviour of this second method is less rapid than the one of the explicit method.

3) First application of the B2 code on the TEXTOR geometry shows that the "minimal" model for neutral particle behaviour, as present in B2, is too incomplete to handle different magnetic configurations and plasma conditions. In order to get reliable information on neutral particle behaviour for all possible geometries, the B2 code is successfully coupled to a Monte Carlo code EIRENE, written by Reiter [20]. Although this leads to more computer time consuming modelling (for TEXTOR-conditions about a factor of two), this coupling provides excellent possibilities for reliable plasma edge modelling, especially on new divertor concepts.

4) Results of the B2 code are compared with those of a TEXTOR-specific edge plasma code SOLXY [15]. This second code is already confronted with experimental data and is more complete concerning terms and plasma variables kept in the model. As drifts and electric currents are incorporated in the SOLXY code, the assumption of ambipolarity in the B2 code is investigated. It is shown that in the energy equations one particular heat exchange term, called vdp-term, arising from the equilibrium current strongly influences the ion and electron temperature profiles. As this current is mainly determined by the radial pressure gradient, this heat exchange term can easily be introduced. After implementation differences in plasma profiles between SOLXY and B2 results are below 5 %.

5) As a consequence of this comparison, and due to the attention paid to biassing and polarization experiments, the code is extended to include drift terms and electric currents in a consistent way. This means that not only the heat exchange term vdp is introduced, but that the additional variables, such as electric currents, diamagnetic ion velocity and electric potential are computed. For the implementation of strongly non-linear boundary conditions for the electric potential at the target, a specific numerical treatment is invented. This leads to the so-called "extended B2".

6) The extensions are implemented with increasing degree of sophistication. The introduction of parallel electric current $j_{||}$ and poloidal electric field E_θ can already model qualitative effects such as poloidal current direction and biassing effects on plasma potential and heat power load.

7) Introduction of the diamagnetic component of the ion velocity give rise to an unacceptably low convergence rate for TEXTOR applications. In applications to the magnetic divertor of ASDEX-Upgrade, the convergence behaviour is already much better. This is because of a lower impact of the diamagnetic component of the ion velocity on the boundary condition for the parallel ion velocity. Estimation of the relative importance of the ion drift velocity for poloidal convective flow on the targets shows the differences between limiter and divertor configurations. A combined effect of recycling model, geometrical aspects and plasma properties can explain the distinction in the specific cases of TEXTOR and ASDEX-Upgrade.

8) Although application of the extended B2 code result in time-dependent oscillations in density, electric potential and diamagnetic flow near the X-point, these oscillations

only effect local radial profiles. This allows us to discuss the results of the extended model. In order to provide experimentally obtained electric potential profiles inside the separatrix, a neoclassical formulation of the diamagnetic total momentum equation can be used. It turned out that this expression has to contain at least the viscous terms. Further, the enhancement of the scrape-off layer current can be explained be the changes in plasma parameters at the target, which are induced by introducing flows in the diamagnetic direction.

9) Although little is known about fluctuations in plasma, there is consensus that phase-correlated oscillations enhance the neoclassical radial transport and even dominate transport perpendicular to the magnetic flux surfaces. Therefore, edge plasma models describe the so-called anomalous transport with an ad hoc diffusive Fick relation for the radial particle velocity, and with ad hoc radial transport coefficients for the momentum and energy equations. This description, however, can lead to inconsistencies with the other equations. Furthermore, the introduction of anomalous constants make extrapolation towards larger fusion devices questionable. In an appendix, the inconsistencies which arise by implementing such an ad hoc anomalous radial velocity are discussed.

7.2 Suggestions for further research

During the study of plasma edge phenomena it became clear that both theoretical and modelling efforts are required.
Since the radial transport for particles, momentum and energy is expected to be caused by anomalous transport, the implementation of existing anomalous theories with different degree of sophistication in the neoclassical two-dimensional fluid equations has to be elaborated further (see appendix B). Also possibilities for not collisionally dominated transport effects (plateau and banana regime) have to be investigated.
In order to reduce uncertainties in the physics model and to provide as much information as possible about anomalous transport coefficients further validation against experimental data is required. Also for the extended B2 code, quantitative comparison of biassing and reversed field effects with experimental data on different divertor devices is necessary to evaluate the existing model.
The recent experiments on the role of electric fields, in particular the radial ones, in the edge plasma, provided a lot of useful information. As the additional equations incorporated in the extended B2 code, are expected to describe adequately the involved physics, it is worth-while to simulate radial electric field experiments (see subsection 6.2.2). For these simulations it is necessary to improve the numerical treatment in order to obtain converged solutions for these cases within an acceptable computing time. The extended B2 code will then provide an excellent tool to continue the investigation of physics in biassing and polarization experiments.
The extended B2 code can be coupled with the Monte Carlo code EIRENE for neutral particle modelling. For such coupled calculations again an excessive computing time can be expected. However, only in combination with a realistic and detailed neutral particle model the physics concerning influences of charge exchange events on plasma rotation and radial electric potential profiles inside the separatrix can be explored.

Furthermore, a variety of terms in the collisionally dominated neoclassical fluid equations can be introduced. Most important terms are : $\vec{B} \times \vec{\nabla} T_e$-terms for the conductive heat flux (see subsection 5.2.1) and neoclassical expressions in addition to the anomalous terms for radial transport.

Appendix A

The dyads $\vec{\nabla}\vec{A}$ and $\vec{A}\vec{B}$

In this appendix, expressions for physical components of the dyad $\vec{\nabla}\vec{A}$ and the vector $\vec{\nabla}\cdot\vec{A}\vec{B}$ are derived for an orthogonal curvilinear co-ordinate system. These physical components, which are defined as the real length of the orthogonal projection from a vector in the direction along the co-ordinate curves, have the advantage to represent the magnitude of macroscopic properties such as the velocity, independent of the magnitude of the base vectors.

A.1 The gradient of a vector or the dyad $\vec{\nabla}\vec{A}$

The contravariant component of the dyad $\vec{\nabla}\vec{A}$ can be derived starting from its definition [33]. In following expressions, the Einstein convention is used for the indices i, j, k, l, which means that the summation over repeated symbols is understood. This convention is **not** used for the repeated symbols α, β, γ.

$$\begin{aligned}
\left(\vec{\nabla}\vec{A}\right)^{\alpha\beta} &= \vec{e}^{\alpha}\cdot\left(\vec{\nabla}\vec{A}\right)\cdot\vec{e}^{\beta} \\
&= \vec{e}^{\alpha}\cdot\left(\vec{e}^{j}\frac{\partial}{\partial u^{j}}A^{i}\vec{e}_{i}\right)\cdot\vec{e}^{\beta} \\
&= g^{\alpha j}\left(\vec{e}_{i}\frac{\partial}{\partial u^{j}}A^{i} + A^{i}\frac{\partial}{\partial u^{j}}\vec{e}_{i}\right)\cdot\vec{e}^{\beta} \\
&= g^{\alpha j}\left(\delta_{i}^{\beta}\frac{\partial}{\partial u^{j}}A^{i} + A^{i}\left\{\frac{\partial}{\partial u^{j}}\vec{e}_{i}\cdot\vec{e}^{\beta}\right\}\right) \\
&= g^{\alpha j}\left(\frac{\partial}{\partial u^{j}}A^{\beta} + A^{i}\left\{\begin{array}{c}\beta \\ ij\end{array}\right\}\right) \qquad \text{(A.1)}
\end{aligned}$$

with

$$\left\{\begin{array}{c}\beta \\ ij\end{array}\right\} = \frac{1}{2}g^{\beta k}\left[\frac{\partial g_{kj}}{\partial u^{i}} + \frac{\partial g_{ki}}{\partial u^{j}} - \frac{\partial g_{ij}}{\partial u^{k}}\right] \quad , \qquad \text{(A.2)}$$

where the symbol with curly brackets represent the Christoffel symbol of the second kind and g^{ij} and g_{ij} are respectively the contra- and covariant components of the metric tensor [33].

For orthogonal co-ordinate systems these metric coefficients g^{ij} and g_{ij} vanish for $i \neq j$, and the Christoffel symbols acquire simple values for $l \neq k \neq i$:

$$\left\{ \begin{array}{c} l \\ ki \end{array} \right\} = 0 \quad , \tag{A.3}$$

$$\left\{ \begin{array}{c} l \\ li \end{array} \right\} = \left\{ \begin{array}{c} l \\ il \end{array} \right\} = \frac{1}{h_l}\frac{\partial h_l}{\partial u^i} \quad , \tag{A.4}$$

$$\left\{ \begin{array}{c} l \\ kk \end{array} \right\} = -\frac{h_k}{h_l^2}\frac{\partial h_k}{\partial u^l} \quad , \tag{A.5}$$

$$\left\{ \begin{array}{c} l \\ ll \end{array} \right\} = \frac{1}{h_l}\frac{\partial h_l}{\partial u^l} \quad , \tag{A.6}$$

where, $h_i \equiv |\vec{e}_i|$ is the length of the tangent-basis vector and therefore equals $\sqrt{g_{ii}} = 1/\sqrt{g^{ii}}$.

Thus, for $\alpha \neq \beta$ the expression for the contravariant component of a dyad $\vec{\nabla}\vec{A}$ in an orthogonal co-ordinate system $(u^\alpha, u^\beta, u^\gamma)$ reduces to :

$$\begin{aligned} \left(\vec{\nabla}\vec{A}\right)^{\alpha\beta} &= \frac{1}{h_\alpha^2}\left(\frac{\partial}{\partial u^\alpha}\left(A^\beta\right) + A^\alpha \left\{ \begin{array}{c} \beta \\ \alpha\alpha \end{array} \right\} + A^\beta \left\{ \begin{array}{c} \beta \\ \beta\alpha \end{array} \right\}\right) \\ &= \frac{1}{h_\alpha^2}\left(\frac{\partial}{\partial u^\alpha}\left(A^\beta\right) - A^\alpha \frac{h_\alpha}{h_\beta^2}\frac{\partial h_\alpha}{\partial u^\beta} + A^\beta \frac{1}{h_\beta}\frac{\partial h_\beta}{\partial u^\alpha}\right) \quad . \end{aligned} \tag{A.7}$$

Here, no summation over the repeated symbols α, β, γ is understood.

On the other hand for $\alpha = \beta$, the contravariant component reads :

$$\begin{aligned} \left(\vec{\nabla}\vec{A}\right)^{\alpha\alpha} &= \frac{1}{h_\alpha^2}\frac{\partial}{\partial u^\alpha}(A^\alpha) + \frac{A^k}{h_\alpha^2}\left\{ \begin{array}{c} \alpha \\ k\alpha \end{array} \right\} \\ &= \frac{1}{h_\alpha^2}\frac{\partial}{\partial u^\alpha}(A^\alpha) + \frac{A^\alpha}{h_\alpha^2}\frac{1}{h_\alpha}\frac{\partial h_\alpha}{\partial u^\alpha} + \frac{A^\beta}{h_\alpha^2}\frac{1}{h_\alpha}\frac{\partial h_\alpha}{\partial u^\beta} + \frac{A^\gamma}{h_\alpha^2}\frac{1}{h_\alpha}\frac{\partial h_\alpha}{\partial u^\gamma} \quad . \end{aligned} \tag{A.8}$$

Since, a physical component $\tilde{A}_\alpha$ of a vector $\vec{A}$ is determined as the real length of the orthogonal projection from a vector in the direction along the co-ordinate curves a physical component can be written as :

$$\tilde{A}_\alpha = h_\alpha A^\alpha = \frac{A_\alpha}{h_\alpha} \quad . \tag{A.9}$$

Therefore, the physical component for the dyad $\vec{\nabla}\vec{A}$ for $\alpha \neq \beta$ reads :

$$\begin{aligned} \left(\widetilde{\vec{\nabla}\vec{A}}\right)_{\alpha\beta} &= h_\alpha h_\beta \left(\vec{\nabla}\vec{A}\right)^{\alpha\beta} \\ &= \frac{h_\beta}{h_\alpha}\left(\frac{\partial}{\partial u^\alpha}\frac{\tilde{A}_\beta}{h_\beta} - \frac{\tilde{A}_\alpha}{h_\alpha}\frac{h_\alpha}{h_\beta^2}\frac{\partial h_\alpha}{\partial u^\beta} + \frac{\tilde{A}_\beta}{h_\beta^2}\frac{\partial h_\beta}{\partial u^\alpha}\right) \end{aligned}$$

$$
\begin{aligned}
&= \frac{1}{h_\alpha}\frac{\partial}{\partial u^\alpha}\tilde{A}_\beta + \frac{h_\beta}{h_\alpha}\tilde{A}_\beta\frac{\partial}{\partial u^\alpha}\frac{1}{h_\beta} - \frac{\tilde{A}_\alpha}{h_\alpha h_\beta}\frac{\partial h_\alpha}{\partial u^\beta} + \frac{\tilde{A}_\beta}{h_\alpha h_\beta}\frac{\partial h_\beta}{\partial u^\alpha} \\
&= \frac{1}{h_\alpha}\frac{\partial}{\partial u^\alpha}\tilde{A}_\beta - \frac{\tilde{A}_\alpha}{h_\alpha h_\beta}\frac{\partial h_\alpha}{\partial u^\beta} \quad . \qquad \text{(A.10)}
\end{aligned}
$$

On the other hand one obtains :

$$
\begin{aligned}
\left(\widetilde{\vec{\nabla}\vec{A}}\right)_{\alpha\alpha} &= h_\alpha^2\left(\vec{\nabla}\vec{A}\right)^{\alpha\alpha} \\
&= \frac{\partial}{\partial u^\alpha}\frac{\tilde{A}_\alpha}{h_\alpha} + \frac{\tilde{A}_\alpha}{h_\alpha^2}\frac{\partial h_\alpha}{\partial u^\alpha} + \frac{\tilde{A}_\beta}{h_\alpha h_\beta}\frac{\partial h_\alpha}{\partial u^\beta} + \frac{\tilde{A}_\gamma}{h_\alpha h_\gamma}\frac{\partial h_\alpha}{\partial u^\gamma} \\
&= \frac{1}{h_\alpha}\frac{\partial \tilde{A}_\alpha}{\partial u^\alpha} + \tilde{A}_\alpha\frac{\partial 1/h_\alpha}{\partial u^\alpha} + \frac{\tilde{A}_\alpha}{h_\alpha^2}\frac{\partial h_\alpha}{\partial u^\alpha} + \frac{\tilde{A}_\beta}{h_\alpha h_\beta}\frac{\partial h_\alpha}{\partial u^\beta} + \frac{\tilde{A}_\gamma}{h_\alpha h_\gamma}\frac{\partial h_\alpha}{\partial u^\gamma} \\
&= \frac{1}{h_\alpha}\frac{\partial \tilde{A}_\alpha}{\partial u^\alpha} + \frac{\tilde{A}_\beta}{h_\alpha h_\beta}\frac{\partial h_\alpha}{\partial u^\beta} + \frac{\tilde{A}_\gamma}{h_\alpha h_\gamma}\frac{\partial h_\alpha}{\partial u^\gamma} \quad . \qquad \text{(A.11)}
\end{aligned}
$$

So that one can conclude

$$
\left(\widetilde{\vec{\nabla}\vec{A}}\right)_{\alpha\beta} = \frac{\partial \tilde{A}_\beta}{h_\alpha \partial u^\alpha} + \sum_k \tilde{A}_k \Gamma^\alpha_{\beta k} \quad , \qquad \text{(A.12)}
$$

with

$$
\Gamma^\alpha_{\beta\gamma} = \delta^\alpha_\beta \frac{\partial \ln h_\alpha}{h_\gamma \partial u^\gamma} - \delta^\alpha_\gamma \frac{\partial \ln h_\alpha}{h_\beta \partial u^\beta} \quad . \qquad \text{(A.13)}
$$

In this form, these formulae are used by Stacey and Sigmar [30].

A.2 The vector components of the divergence of a dyad $\vec{A}\vec{B}$

The derivation of the divergence of a dyad written in physical components leads to

$$
\begin{aligned}
\left[\vec{\nabla}\cdot\widetilde{\left(\vec{A}\vec{B}\right)}\right]_l &= h_l\left[\vec{\nabla}\cdot\left(\vec{A}\vec{B}\right)\right]^l \\
&= h_l\left[\left(\vec{A}\cdot\vec{\nabla}\vec{B}\right)^l + \left(\left(\vec{\nabla}\cdot\vec{A}\right)\cdot\vec{B}\right)^l\right] \quad . \qquad \text{(A.14)}
\end{aligned}
$$

With the use of

$$
\vec{\nabla}\cdot\left(\vec{A}\vec{B}\right) = \vec{A}\cdot\vec{\nabla}\vec{B} + \left(\vec{\nabla}\cdot\vec{A}\right)\cdot\vec{B} \quad , \qquad \text{(A.15)}
$$

one finds

$$
\left[\vec{\nabla}\cdot\widetilde{\left(\vec{A}\vec{B}\right)}\right]_l = h_l\left[A^i\vec{e}_i\cdot\vec{e}_\alpha\left(\vec{\nabla}\vec{B}\right)^{\alpha\beta}\vec{e}_\beta\cdot\vec{e}^l\right] + \left(\vec{\nabla}\cdot\vec{A}\right)\cdot\tilde{B}_l
$$

$$
\begin{aligned}
&= h_l A^i g_{ii} \left(\vec{\nabla}\vec{B}\right)^{il} + \left(\vec{\nabla}\cdot\vec{A}\right)\cdot\tilde{B}_l \\
&= \tilde{A}_i \left(\widetilde{\vec{\nabla}\vec{B}}\right)_{il} + \left(\vec{\nabla}\cdot\vec{A}\right)\cdot\tilde{B}_l \\
&= \tilde{A}_i \left(\frac{\partial\tilde{B}_l}{h_i\partial u^i} + \sum_k \tilde{B}_l\Gamma^i_{lk}\right) + \left(\frac{1}{\sqrt{g}}\frac{\partial}{\partial u^i}\frac{\sqrt{g}}{h_i}\tilde{A}_i\right)\tilde{B}_l \\
&= \sum_i \frac{1}{\sqrt{g}}\frac{\partial}{\partial u^i}\left(\frac{\sqrt{g}}{h_i}\tilde{A}_i\tilde{B}_l\right) + \sum_i\sum_k \tilde{A}_i\tilde{B}_k\Gamma^i_{lk} \\
&= \sum_i \frac{1}{\sqrt{g}}\frac{\partial}{\partial u^i}\left(\frac{\sqrt{g}}{h_i}\tilde{A}_i\tilde{B}_l\right) \\
&\quad +\tilde{B}_\beta\left(\tilde{A}_\alpha\frac{\partial\ln h_\alpha}{h_\beta\partial u^\beta} - \tilde{A}_\beta\frac{\partial\ln h_\beta}{h_\alpha\partial u^\alpha}\right) \\
&\quad +\tilde{B}_\gamma\left(\tilde{A}_\alpha\frac{\partial\ln h_\alpha}{h_\gamma\partial u^\gamma} - \tilde{A}_\gamma\frac{\partial\ln h_\gamma}{h_\alpha\partial u^\alpha}\right) \quad . \qquad \text{(A.16)}
\end{aligned}
$$

Appendix B

Anomalous radial transport

Although the introduction of anomalous transport is based on experimental data, blind implementation of it in a model suffers from consistency as long as the underlying physics is not well understood. Namely, the assumption of anomalous radial transport gives rise to problems in deriving the energy equations. Depending on whether the energy moment equation is derived from multiplication of the Boltzmann equation by $\frac{1}{2}m_\alpha\vec{v}^2$ or $\frac{1}{2}m_\alpha\left(\vec{v}^2 - \vec{V}_\alpha\right)^2$, where $\vec{v}$ is the individual particle velocity and $\vec{V}_\alpha$ is the fluid velocity, one finds, respectively,

$$\begin{aligned}&\frac{\partial}{\partial t}\left(\frac{3}{2}n_\alpha T_\alpha + \frac{m_\alpha n_\alpha}{2}\vec{V}_\alpha^2\right) + \\ &\vec{\nabla}\cdot\left[\left(\frac{5}{2}n_\alpha T_\alpha + \frac{m_\alpha n_\alpha}{2}\vec{V}_\alpha^2\right)\vec{V}_\alpha + \overleftrightarrow{\Pi}_\alpha \cdot\vec{V}_\alpha + \vec{q}_\alpha\right] = \\ &\qquad\qquad \vec{V}_\alpha\cdot\left(Z_\alpha e n_\alpha\vec{E} + \vec{R}_\alpha\right) + Q_\alpha\end{aligned} \tag{B.1}$$

and

$$\frac{3}{2}n_\alpha\frac{dT_\alpha}{dt} + p_\alpha\vec{\nabla}\cdot\vec{V}_\alpha = -\vec{\nabla}\cdot\vec{q}_\alpha - \overleftrightarrow{\Pi}_\alpha : \vec{\nabla}\vec{V}_\alpha + Q_\alpha \quad . \tag{B.2}$$

Using continuity and momentum equations one can convert one equation into the other. Substituting an anomalous expression for one of the momentum equations, however, makes these two formulations of the energy equation no longer equivalent, and therefore the plasma solution will depend on the arbitrary choice made for the energy form (based on total or internal energy).

Although Tokamak turbulence phenomena have been studied extensively, neither their source nor their role in anomalous energy transport are yet understood. Recent reviews are given by Liewer [107] and Wootton et al. [108]. This theory is very involved and not subject of this work. However, the presently understood theoretical fundamentals can already bring out some effects on the energy equations. The mechanism driving anomalous transport is often taken to be electric and magnetic field fluctuations : $\vec{E} = \bar{\vec{E}} + \delta\vec{E}$, $\vec{B} = \bar{\vec{B}} + \delta\vec{B}$. These, in turn, induce fluctuations in the macroscopic plasma parameters, which again can be written as a sum of a time averaged and a fluctuating part : $n = \bar{n} + \delta n$, $T = \bar{T} + \delta T$, etc.

To clarify effects of anomalous transport on the edge plasma model equations, we explicitly retain those perturbation terms which are caused by electric fluctuations in the ion moment equation in the diamagnetic direction. For the diamagnetic component of the ion momentum equation this leads to a radial particle flux :

$$\begin{aligned} \overline{\Gamma}_r &= \Gamma_{r,neocl.} + \overline{\Gamma}_{r,turb} & \text{(B.3)} \\ &= \overline{n}\overline{V}_r + \overline{\delta n \delta V_r} & \text{(B.4)} \end{aligned}$$

with

$$\overline{\Gamma}_{r,turb.} = -\frac{1}{B} \cdot \left(\overline{\delta n_e \delta E}\right)_{\perp} \qquad \text{(B.5)}$$

which, in linear theory, is often assumed to be driven by thermodynamic forces. In the 2-dimensional edge modelling, it is implemented as $\overline{\Gamma}_r = -D \frac{1}{h_r} \frac{\partial n}{\partial u^r}$.
Already at this point, it is obvious that the definition of the fluid velocity should be treated carefully, because there are at least two possibilities. Namely,

$$V_r^{(1)} = \overline{V_r + \delta V} = V_{r,neocl.} \qquad \text{(B.6)}$$

and

$$V_r^{(2)} = \frac{\overline{\Gamma}_r}{n} = \frac{\overline{n}\overline{V}_r + \overline{\delta n \delta V_r}}{\overline{n}} \quad . \qquad \text{(B.7)}$$

Since present edge plasma codes are not based on this anomalous theory, but only use an ad hoc expression instead of the neoclassical ion momentum equation in the diamagnetic direction, they do not distinguish between $V_{r,neocl.}$ and $V_{r,turb.}$ and therefore end up with some terms in $V_{i,r}$ which depend on the arbitrary choice for the energy formulation in terms of total or internal energy. Furthermore, ambiguity exists whenever the radial velocity occurs in the neoclassical equations.
We can also derive the energy equation including fluctuating plasma parameters

$$\frac{\partial}{\partial t}\left(\frac{3}{2}\overline{p} + \frac{1}{2} mn\overline{V^2}\right) + \vec{\nabla}.\overline{\vec{Q}} = e\overline{\vec{\Gamma}}.\overline{\vec{E}} + e\overline{\delta\vec{\Gamma}\delta\vec{E}} + \overline{\vec{R}}.\overline{\vec{V}} + \overline{\delta\vec{R}.\delta\vec{V}} + \overline{\vec{Q}_{ie}} + \overline{S_E^e} \qquad \text{(B.8)}$$

where the energy flux is given as :

$$\overline{\vec{Q}} = \frac{5}{2}\overline{p}\overline{\vec{V}} + \frac{5}{2}\overline{\delta p \delta \vec{V}} + \vec{q}_{cl} + \left(\frac{mn}{2}\overline{V^2 \vec{V}}\right) + \frac{m}{2}\overline{\delta\vec{\Gamma}\delta\vec{V^2}} + \overline{\overleftrightarrow{\Pi}}.\overline{\vec{V}} + \overline{\delta\overleftrightarrow{\Pi}.\delta\vec{V}} \quad . \qquad \text{(B.9)}$$

In order to evaluate the energy equation, further information is needed about the phase correlations between the fluctuating plasma quantities. This can either be obtained by an anomalous transport theory, or based on experimental data. The latter should be handled carefully, as was emphasized by Ross, Refs. [109] and [110]. In this work Ross discussed different formulations of the energy equations, and this has lead to a uniquely identified radial conductive heat flux. Therefore every assumption of an anomalous radial heat flux should correspond to a well-defined transport equation. Furthermore, he stated that in previous studies, either the moment equations are considered rigorously but the fluxes are

not given explicitly, or else the fluxes are derived correctly but the averaged fluid equations are not sufficiently detailed. Because in many edge codes the radial thermal conductivity is taken empirically as $\kappa_y = nD$, it is not clear what the influence of this assumption should be on the right-hand side of the energy equations.
In Ref.[111] Manheimer et al. show that the dominant effect of additional turbulence terms in the energy equations is electron-ion energy exchange, although these anomalous exchange terms are small compared to ordinary collisional temperature equilibration. Assuming that the usual radial heat fluxes that appear in edge modelling can be replaced by Manheimers expressions [111], this would mean that the right-hand side of the energy equations, Eqs. (2.105) and (2.107), reduces to the neoclassical expression :

$$e\overline{\vec{\Gamma}}.\overline{\vec{E}} + \overline{\vec{R}}.\overline{\vec{V}_{neocl.}} + \vec{Q}_{ie} + S_E^e \tag{B.10}$$

with $V_{r,neocl.} \simeq 0$.
Therefore, the neoclassical velocity has to be used in the right-hand side of the energy equations, which means that terms as $V_{i,r}\frac{\partial p_i}{h_r \partial u^r}$ in Eqs. (2.105) and (2.107) as used in B2 and $V_{i,r}\frac{\partial p_e}{h_r \partial u^r}$ in Eqs. (4.21) and (4.22) as used in B2-vdp vanish.

Appendix C

A conformal mapping for limiter simulations

In this appendix we will concentrate on the properties of the conformal mapping function $z(\zeta)$:

$$z = x + iy = R_0 + a_0 \frac{e^{-i\zeta} + \delta}{\delta e^{-i\zeta} + 1} \tag{C.1}$$

where $\zeta = 2\pi f(\xi) + \alpha_0 + ig(\eta)\frac{W}{a_0}$.
In a first section it is shown that, starting from a rectangular grid, this transformation generates a physical mesh of non-concentric circles. Therefore, it can be used for the simulation of edge plasmas in limiter configurations. In this case the transformation parameters are :

R_0 : the major radius of the reference circle

a_0 : the limiter minor radius of the reference circle

δ : parameter to characterize the Shafranov shift

W : parameter to define the radial width of the grid

α_0 : parameter to define the poloidal angle of the limiter position.

In a second section expressions to compute these transformation parameters are derived.

C.1 Properties of the conformal mapping function

It can easily be seen that the conformal mapping function, Eq. (C.1), can be written as :

$$z = x + iy = R_0 + a_0 \frac{\rho e^{-i\alpha} + \delta}{\delta \rho e^{-i\alpha} + 1} \tag{C.2}$$

where $\alpha = 2\pi f(\xi) + \alpha_0$ and $\rho = e^{g(\eta)W/a_0}$.
Substitution of $e^{-i\alpha} = \cos\alpha - i\sin\alpha$ in Eq. (C.2) leads to :

$$\begin{aligned} z &= R_0 + a_0 \frac{\rho\cos\alpha - i\rho\sin\alpha + \delta}{\delta\rho\cos\alpha - i\delta\rho\sin\alpha + 1} \\ &= R_0 + a_0 \frac{(\rho\cos\alpha + \delta - i\rho\sin\alpha)(\delta\rho\cos\alpha + 1 + i\rho\delta\sin\alpha)}{(\delta\rho\cos\alpha + 1)^2 + \rho^2\delta^2\sin\alpha} \quad . \end{aligned} \tag{C.3}$$

Therefore, the complex number z can be written as :

$$z = x + iy \tag{C.4}$$

with

$$\begin{aligned} x &= R_0 + a_0 \frac{X^*}{N^*} \\ y &= a_0 \frac{Y^*}{N^*} \quad . \end{aligned} \tag{C.5}$$

In these expressions $X^* = \rho^2\delta + \delta + (\delta^2\rho + \rho)\cos\alpha$, $Y^* = \rho(\delta^2 - 1)\sin\alpha$ and $N^* = \rho^2\delta^2 + 1 + 2\rho\delta\cos\alpha$.
Starting from the assumption that this conformal mapping indeed provide a circle with centre on the x-axis if $g(\eta) = constant$ and thus if $\rho = constant$, the position of the centre can be derived.
For $\alpha = 0$ the circle intersects the x-axis at the point $z_1 = x_1 + iy_1$:

$$\begin{aligned} x_1 &= R_0 + a_0 \left(\frac{\rho^2\delta + \delta + \delta^2\rho + \rho}{(\rho\delta + 1)^2} \right) \quad ; \\ y_1 &= 0 \quad , \end{aligned} \tag{C.6}$$

and for $\alpha = \pi$ at the point $z_2 = x_2 + iy_2$:

$$\begin{aligned} x_2 &= R_0 + a_0 \left(\frac{\rho^2\delta + \delta - \delta^2\rho - \rho}{(\rho\delta - 1)^2} \right) \quad ; \\ y_2 &= 0 \quad . \end{aligned} \tag{C.7}$$

Therefore, the position of the centre $z_c = x_c + iy_c$ can now be computed :

$$\begin{aligned} x_c &= \frac{x_1 + x_2}{2} \\ &= R_0 + a_0 \frac{\delta(\rho^2 - 1)}{\rho^2\delta^2 - 1} \\ y_c &= 0 \quad . \end{aligned} \tag{C.8}$$

The radius of a circle with centre z_c equals the modulus of $z - z_c$:

$$
\begin{aligned}
|z - z_c| &= \left| R_0 + a_0 \frac{X^*}{N^*} - R_0 - a_0 \frac{\delta\left(\rho^2 - 1\right)}{\rho^2 \delta^2 - 1} + i a_0 \frac{Y^*}{N^*} \right| \\
&= a_0 \left| \frac{\rho\left(\delta^2 - 1\right)\left[\cos\alpha\left(\delta^2\rho^2 + 1\right) + 2\delta\rho\right]}{\left[2\delta\rho\cos\alpha + \left(\rho^2\delta^2 + 1\right)\right]\left(\delta^2\rho^2 - 1\right)} \right. \\
&\quad \left. + i \frac{\left[\rho\left(\delta^2 - 1\right)\sin\alpha\left(\delta^2\rho^2 - 1\right)\right]}{\left[2\delta\rho\cos\alpha + \left(\rho^2\delta^2 + 1\right)\right]\left(\delta^2\rho^2 - 1\right)} \right| \\
&= \frac{\rho\left(\delta^2 - 1\right)}{\delta^2\rho^2 - 1} a_0
\end{aligned}
\tag{C.9}
$$

Since, for $\rho = constant$ the modulus of $z - z_c$ is also a constant value, one can conclude that this transformation provide a mesh of non-concentric circles with the following properties :

at $g(\eta) = \text{constant}$, the centre of the circle is located at $R_0 + a_0 \frac{(\rho^2-1)\delta}{\delta^2\rho^2-1}$ and its radius equals $a_0\rho\frac{\delta^2-1}{\delta^2\rho^2-1}$, with $\rho = e^{Wg(\eta)/a_0}$;

at $g(\eta) = 0$, $\rho = 1$ and the centre of the circle is located at R_0 and its radius is a_0.

Different choices of the parameters R_0, a_0, δ, W, α_0 and of the scale functions f and g allow a wide range of limiter configurations to be modelled.

C.2 Determination of transformation parameters

In order to set up a mesh for simulations of a limiter Tokamak with non-concentric circular magnetic flux surfaces, information about geometrical aspects and the magnetic equilibrium is required. More specifically, for the conformal mapping as described above values are needed for the major radius R_0, minor radius a_0, Shafranov shift $\Delta(0)$, minor radii of inner and outer circles of the described region, a_{in} and a_{out} respectively, and the limiter position. With this information the transformation parameters δ, W, α_0 and $g(0)$ can be computed.

C.2.1 The reference circle

For simulations, the reference circle is usually chosen to correspond with the last closed flux surface. Information about centre and radius of this magnetic flux surface immediately determines the values of R_0 and a_0 respectively.

C.2.2 The Shafranov shift

The Shafranov shift $\Delta(0)$ is defined as the displacement between the centre of the reference circle with minor radius a_0 and the magnetic axis. For a mesh generated by the conformal mapping as described above, the centre of the reference circle with minor radius a_0 is located at R_0. The magnetic axis, which is defined by the location of a circle with a radius equal to zero (and thus $\rho = 0$), is located at $R_0 + a_0\delta$.

Therefore,

$$\Delta(0) = a_0\delta \quad . \tag{C.10}$$

This expression provides a value for $\delta = \frac{\Delta(0)}{a_0}$.

C.2.3 The outer circle of the described region

At $g(1) = 1$ the radius of the corresponding circle in the physical mesh should equal a_{out}. This means that :

$$\frac{\rho a_0 \left(\delta^2 - 1\right)}{\delta^2\rho^2 - 1} = a_{out} \tag{C.11}$$

For the outer circle ρ can be obtained by :

$$\rho = \frac{a_0 \left(\delta^2 - 1\right) \pm \sqrt{a_0^2 \left(\delta^2 - 1\right)^2 + 4a_{out}^2\delta^2}}{2a_{out}\delta^2} \quad . \tag{C.12}$$

Since $\rho = e^{g(\eta)W/a_0} = e^{W/a_0}$, the transformation parameter W is determined by :

$$W = a_0 \ln \rho \tag{C.13}$$

Because the minus sign of expression (C.12) results in negative values for ρ, the latter must be computed as :

$$\rho = \frac{a_0 \left(\delta^2 - 1\right) + \sqrt{a_0^2 \left(\delta^2 - 1\right)^2 + 4a_{out}^2\delta^2}}{2a_{out}\delta^2} \quad . \tag{C.14}$$

C.2.4 The inner circle

The inner boundary is provided by the choice of $g(0)$ for which the radius of the corresponding circle in the physical mesh equals a_{in}. A similar derivation as in subsection C.2.3 leads to :

$$g(0) = \frac{a_0}{W} \ln \rho \tag{C.15}$$

with

$$\rho = \frac{a_0 \left(\delta^2 - 1\right) + \sqrt{a_0^2 \left(\delta^2 - 1\right)^2 + 4a_{in}^2\delta^2}}{2a_{in}\delta^2} \quad . \tag{C.16}$$

C.2.5 The limiter position

The position of the limiter tip in the physical mesh must correspond to the boundary of the numerical mesh in the ξ-direction. This leads for the specific case of TEXTOR with its limiter positioned at 45 $^\circ$ beneath the outer midplane to a condition for the complex number z which is transformed from the point where $f(0) = 0$ and $g(\eta) = 0$:

$$\Re(z) - R_0 = -\Im(z)$$

where $\Re(z)$ is the real part and $\Im(z)$ is the imaginary part of z.
Or making use of Eqs. (C.5) :

$$X^* = -Y^*$$

With $f(0) = 0$ and $\rho = 1$, this leads to :

$$2\delta + \left(\delta^2 + 1\right) \cos \alpha_0 = -\left(\delta^2 - 1\right) \sin \alpha_0 \tag{C.17}$$

Based on goniometric relations, the expression can be written as :

$$\sin\left(\alpha_0 + \phi\right) = \frac{-2\delta}{\sqrt{(\delta^2+1)^2 + (\delta^2-1)^2}} \tag{C.18}$$

with $\phi = \arctan\left(\frac{\delta^2+1}{\delta^2-1}\right)$ and $\frac{\pi}{2} < \phi < \pi$
This goniometric expression leads to two series of possible solutions :

$$\begin{aligned} \alpha_{0,1} &= \arcsin\left(\frac{-2\delta}{\sqrt{(1+\delta^2)^2 + (\delta^2-1)^2}}\right) + k2\pi - \phi \\ \alpha_{0,2} &= \pi - \arcsin\left(\frac{-2\delta}{\sqrt{(1+\delta^2)^2 + (\delta^2-1)^2}}\right) + k2\pi - \phi \end{aligned} \tag{C.19}$$

with k an integer.
Since it is necessary that $0 < \alpha_0 < \frac{\pi}{2}$, the second solution has to be taken :

$$\alpha_0 = -\arcsin\left(\frac{-2\delta}{\sqrt{(1+\delta^2)^2 + (\delta^2-1)^2}}\right) - \phi \tag{C.20}$$

with $\phi = \arctan\left(\frac{\delta^2+1}{\delta^2-1}\right)$ and $-\frac{\pi}{2} < \phi < 0$.
The expressions as derived above can now be used to determine the parameters for a limiter configuration with non-concentric circular flux surfaces. This is done for the experimental Tokamak TEXTOR in subsection 4.2.3.

Bibliography

[1] R.A. Gross, "Fusion Energy", Wiley and Sons, New York (1984).

[2] J. Wesson, "Tokamaks", Clarendon Press, Oxford (1987).

[3] M. Stacey, Jr., "Fusion Plasma Analysis", Wiley and Sons, New York (1981).

[4] "Report of the Senior Committee on Environmental, Safety and Economic Aspects of Magnetic Fusion Energy", Report UCRL-53766, University of Californie, Livermore (1987).

[5] H.-S. Bosch, "Review of Data and Formulas for Fusion Cross-sections", IPP-Report I/252, Max Planck Institut, Garching bei München, Germany (1990).

[6] J. Eidens, G.H. Wolf, "Kontrollierte Kernfusion : Stand, Probleme, Entwicklungsschritte", VDI-berichte, Nr.984, p.283 (1992).

[7] P.C. Stangeby and G.M. McCracken, "Plasma Boundary Phenomena in Tokamaks", Nucl. Fus., Vol.30, p.1225 (1990).

[8] J. Winter, "Wall Conditioning of Fusion Devices by Reactive Plasmas", J. Nucl. Mat., Vol.161, p.265 (1989).

[9] J. Winter, H.G. Esser, L. Könen et al., "Boronization in TEXTOR", J. Nucl. Mat., Vol.162-164, p.713 (1989).

[10] J. Winter, H.G. Esser, G. Jackson et al., "TEXTOR Operation with Si Covered Walls", Proc. 20th Eur. Conf. on Contr. Fus. and Plasma Phys., Vol.17C, p.279, Lisboa (1993).

[11] R.R. Weynants, G. Van Oost, G. Bertschinger et al., "Confinement and Profile Changes induced by the Presence of Positive and Negative Radial Electric Fields in the Edge of the TEXTOR Tokamak", Nucl. Fus., Vol.32, p.837 (1992).

[12] R.R. Weynants and G. Van Oost, "Edge Biassing in Tokamaks", 20th EPS Conference on Contr. Fus. and Plasma Phys., Lisboa (1993), to be published in Plasma Phys. and Contr. Fus.

[13] B.J. Braams, "Computational Studies in Tokamak Equilibrium and Transport", Ph.D. Thesis, Rijksuniversiteit Utrecht (1986).

[14] S.I. Braginskii, "Transport Processes in a Plasma", in Reviews of Plasma Physics, Vol.1, M. Leontovich, Ed., Consultants Bureau, New York, p.205 (1965).

[15] H. Gerhauser, H.A. Claaßen, "Calculation of Poloidal Rotation in the Edge Plasma of Limiter Tokamaks", KFA-Report JÜL-2125, Forschungszentrum Jülich, Germany (1987).

[16] H. Gerhauser, H.A. Claaßen, "Boundary Layer Calculations for Tokamaks with Toroidal Limiter", J. Nucl. Mat., Vol.176-177, p.721 (1990).

[17] H. Gerhauser, H.A. Claaßen, "Boundary Layer Calculations for Tokamaks with Toroidal Limiter", 9th Int. Conf. in Contr. Fus. Devices, Paper R:06, Bournemouth, U.K. (1990).

[18] H. Gerhauser, H.A. Claaßen, "Boundary Layer Calculations for Tokamaks with Toroidal Limiter", Contrib. Plasma Phys., Vol.30, p.89-99 (1990).

[19] U. Samm, et al., "Evidence for the Influence of Radial and Poloidal Drift Velocities on the Scrape-off Layer of a Toroidal Limiter", Nucl. Fus., Vol.31, p.1386 (1991).

[20] D. Reiter, "Randschicht-Konfiguration von Tokamaks : Entwicklung und Anwendung stochastischer Modelle zur Beschreibung des Neutralgastransports", KFA-Report, JÜL-1947, Forschungszentrum Jülich, Germany (1984).

[21] R. Chodura, "Basic Problems in Edge Plasma Modelling", Contrib. Plasma Phys., Vol.28, p.303 (1988).

[22] NRL Plasma Formulary, NRL Publication 0084-4040, Naval Research Laboratory, Washington D.C., USA (1987).

[23] P.C. Stangeby, "The Plasma Sheath", in "Physics of Plasma-Wall Interaction in Controlled Fusion Devices", D.E. Post and R. Behrisch editors, Plenum Press, New York, p.41 (1986).

[24] J.F. Luciani, P. Mora and J. Virmont, "Nonlocal Heat Transport Due to Steep Temperature Gradients", Phys. Rev. Lett., Vol.51, pp. 1664-1667 (1983).

[25] Yu. L. Igitkhanov, A.S. Kukushkin, A. Yu. Pigarov et al., "Advanced Two-Dimensional Simulation of Edge Plasma in a Poloidal Divertor". Proc. of the 10th Int. Conf. on Plasma Phys. and Contr. Nucl. Fus. Research, London (IAEA, Vienna) Vol.2, p.113 (1984).

[26] Proc. 3rd Int. Workshop on Plasma Edge Theory in Fusion Devices, Bad Honnef 1992, Contrib. Plasma Phys., Vol.32, p.171 (1992).

[27] D.E. Post and K. Lackner, "Plasma Models for Impurity Control Experiments", in "Physics of Plasma-Wall Interaction in Controlled Fusion Devices", D.E. Post and R. Behrisch editors, Plenum Press, New York, p.627 (1986).

[28] F.L. Hinton, "Collisional Transport in Plasmas", in "Handbook of Plasma Physics", M.N. Rosenbluth and R.Z. Sagdeev, Eds., North-Holland Publ. Company, New York, Vol.1, p.147 (1983).

[29] A.B. Mikhailovskii and V.S. Tsypin, "Viscosity of a Collisional Plasma in Curvilinear Magnetic Field and Drift Equilibrium (Rotation) of a Plasma", Sov. J. Plasma Phys., Vol.10, p.51 (1984).

[30] W.M. Stacey, Jr., "Viscous Effects in a Collisional Tokamak Plasma with Strong Rotation", Phys. Fluids, Vol.28, p.2800 (1985).

[31] F.L. Hinton and R.D. Hazeltine, "Theory of Plasma Transport in Toroidal Confinement Systems", Rev. of Mod. Phys., Vol.48, p.240 (1976).

[32] S.P. Hirshman and D.J. Sigmar, "Neoclassical Transport of Impurities in Tokamak Plasmas", Nucl. Fus., Vol.21, p1079 (1981).

[33] W.D. D'haeseleer, W.N.G. Hitchon, J.D. Callen, J.L. Shohet, "Flux Coordinates and Magnetic Field Structure", Springer-Verlag, Berlin, New York, (1991).

[34] E.L. Vold, F.Najmabadi and R.W. Conn, "Fluid Model Equations for the Tokamak Plasma Edge", Phys. Fluids B, Vol.3, p.3132 (1991).

[35] D. Reiter, "Progress in 2-Dimensional Plasma Edge Modelling", J. Nucl. Mat., Vol.196-198, p.241 (1992).

[36] E.L. Vold, "Multidimensional and Multifluid Plasma Edge Modelling : Status and New Directions", Contrib. Plasma Phys., Vol. 32, p.404 (1992).

[37] Yu. L. Igitkhanov, A. Yu. Pigarov, "Non-local Transport Effects on the Tokamak SOL Plasma Parameters", J. Nucl. Mat., Vol.176-177, p. 557 (1990).

[38] A. Taroni, G. Corrigan, G. Radford et al., "The Multi-Fluid Codes EDGE1D and EDGE2D : Models and Results", Contr. Plasma Phys., Vol. 32, p.438 (1992).

[39] S.V. Patankar, "Numerical Heat Transfer and Fluid Flow", Hemisphere, New York (1980).

[40] E.L. Vold, "Transport in the Tokamak Plasma Edge", Ph.D. Thesis, University of Californie, Los Angeles, U.S.A. (1989).

[41] N. Ueda, M. Kasai, M. Tanaka et al., "Development of a Two-Dimensional Fluid Code and its Applications to the Doublet III Divertor Experiment", Nucl. Fus., Vol.28, p.1183 (1988).

[42] R. Schneider, D. Reiter, H.P. Zehrfeld et al., "B2-EIRENE Simulation of ASDEX and ASDEX-Upgrade Scrape-off Layer Plasmas", J. Nucl. Mat., Vol.196-198, p.810 (1992).

[43] R. Zanino and W. Schneider, "1-D 1-Fluid SOL Modelling with Finite Elements", Contrib. Plasma Phys., Vol.30, p.127 (1990).

[44] R. Zanino, "Finite Element Fluid Modelling of Axisymmetric Magnetized Boundary Plasma with Recycling Neutrals", J. Nucl. Mat., Vol.196-198, p.326-331 (1992).

[45] Th. Pütz, "Entwicklung eines Finite Elemente Verfahrens zur Modellierung der Plasmaströmung in der Randschicht von Tokamaks", Ph.D. Thesis, Univ. Düsseldorf, Germany, to be published.

[46] D.A. Knoll and P.R. McHugh, "A 2-D Fully Implicit Edge Plasma Fluid Code for Advanced Physics and Complex Geometries", J. Nucl. Mat., Vol.196-198, p.352 (1992).

[47] T.D. Rognlien, J.L. Milovich, M.E. Rensink and G.D. Porter, "A Fully Implicit, Time Dependent 2-D Fluid Code for Modelling Tokamak Edge Plasmas", J. Nucl. Mat., Vol.196-198, p.347 (1992).

[48] G.P. Maddison, E.S. Hotston, D. Reiter et al. "Towards Fully Authentic Modelling of ITER Divertor Plasma's", Proc. 18th Eur. Conf. on Contr. Fus. and Plasma Phys., Berlin, Vol.15C, p.197 (1991).

[49] B.J. Braams, "Numerical Studies of the Two-Dimensional Scrape-off Layer", Proc. 11th Eur. Conf. on Contr. Fus. and Plasma Phys., Aachen, Vol.7D, p.431 (1983).

[50] B.J. Braams, M.F.A. Harrison, E.S. Hotston and J.G. Morgan, "Application of Two-Dimensional Modelling to the Scrape-off and the Single-null Poloidal Divertor Plasma of INTOR", Proc. 10th Int. Conf. Plasma Phys. and Contr. Nucl. Fus., London (IAEA, Vienna), Vol.2, p.125 (1985).

[51] B.J. Braams, "A Multi-fluid Code for Simulation of the Edge Plasma in Tokamaks", NET-Report, EUR-FU/XII-80/87/68, Comm. of the EC, Brussels, (1987).

[52] M. Baelmans, D. Reiter, H. Kever et al., "Assessment of Critical Physical Assumptions in Consistent 2D Plasma Edge Modelling", J. Nucl. Mat., Vol.196-198, pp.466 (1992).

[53] H. Gerhauser, H.A. Claaßen, "Boundary Layer Calculations for Tokamaks with Toroidal Limiter", Proc. 16th Eur. Conf. on Contr. Fus. and Plasma Phys., Venice, Vol.3, p.931 (1989).

[54] R. Simonini, W. Feneberg, A. Taroni, "Two-Dimensional Analytic and Numerical Models of the Scrape-Off layer of Toroidal Limiters", Proc. 12th Eur. Conf. on Contr. Fus. and Plasma Phys., Budapest, p.484 (1986).

[55] R. Simonini, A. Taroni, M. Keilhacker et al., "Modelling Impurity Control at JET", J. Nucl. Mat., Vol.196-198, p.369 (1992).

[56] Yu.L. Igitkhanov, A.S. Kukushkin, A.Yu. Pigarov and V.I. Pistunovich, "Two-Dimensional Calculations of Near-Wall Plasma Dynamics for a Tokamak with a Poloidal Divertor", Proc. 11th Eur. Conf. on Contr. Fus. and Plasma Phys., Aachen, Part II, p.397 (1983).

[57] Yu. L. Igitkhanov, V.A. Pozharov, I.V. Kurchatov, "2-D Modelling of the Edge Plasma with Arbitrary High Level of Impurity Concentration", Proc. 18th Eur. Conf. on Contr. Fus. and Plasma Phys., Berlin, p.29 (1991).

[58] D.A. Knoll and A.K. Prinja, "Self-Consistent grad P and ExB Drifts in a Two-Dimensional One-Fluid Edge Plasma Model, J. Nucl. Mat., Vol.176-177, p.562 (1990).

[59] A.K. Prinja and C. Koesoemodiprodjo, "A First Flight Corrected Neutral Diffusion Model for Edge Plasma Simulation", J. Nucl. Mat., Vol.196-198, p.340 (1992).

[60] M. Petravic, D. Heifetz, G. Kuo-Petravic and D. Post, "INTOR Divertor in a Realistic 2-D Geometry", J. Nucl. Mat., Vol.128-129, p.111 (1984).

[61] M. Petravic, "A Code for Studying Plasmas in Contact with Solids", J. Nucl. Mat., Vol.196-198, p.883 (1984).

[62] T.D. Rognlien, J.L. Milovich, M.E. Rensink and T.B. Kaiser, "Simulation of Tokamak Divertor Plasmas Including Cross-field Drifts", Contrib. Plasma Phys., Vol.32, p.495, (1992).

[63] R. Zanino, M. Paolini and A. Russo, "Towards Finite Element Modelling of the Tokamak Scrape-Off Layer", Contrib. Plasma Phys., Vol.32, p.432 (1992).

[64] M. Petravic, D.E. Post, D. Heifetz and J. Schmidt, "Cool, High Density Regime for Poloidal Divertors", Phys. Rev. Letters, Vol.48, p.326 (1982).

[65] C.E. Singer and W.D. Langer, "Axisymmetric Tokamak Scrape-off Transport", Report PPPL-20, Princeton Plasma Physics Laboratory (1982) and in Phys. Rev. A, Vol.28, p.994 (1983).

[66] G.P. Maddison, "The LINDA Magnetic Geometry Interpolator", NET-Report, EUR-FU/XII-80/87/72, Comm. of the EC, Brussels, Belgium (1987).

[67] J. Neuhauser, W. Schneider, R. Wunderlich, "Impurity Flow in the Tokamak Scrape-off Layer", Proc. 11th Eur. Conf. on Contr. Fus. and Plasma Phys., Aachen, Vol. 29C, p. 475 (1983).

[68] K. Behringer, "Description of the Impurity Transport Code STRAHL", JET-Report, JET-R(87)08, JET Joint Undertaking, Abingdon, U.K. (1987).

[69] R. Chodura, "Plasma Flow in the Sheath and Pre-sheath of a Scrape-off Layer", in "Physics of Plasma-Wall Interaction in Controlled Fusion Devices", D.E. Post and R. Behrisch editors, Plenum Press, New York, p.99 (1986).

[70] R.C. Bissell, P.C. Johnson and P.C. Stangeby, "A Review of Models for Collisionless One-dimensional Plasma Flow to a Boundary", Phys. Fluids B 1, Vol.5, p.1133 (1989).

[71] R.K. Janev et al., D.E. Post, W.D. Langer, K. Evans et al., "Survey of Atomic Processes in Edge Plasmas", J. Nucl. Mat., Vol.121, p.10 (1984).

[72] M.F.Harrison, E.S. Hotston, J.G. Morgan and G.P. Maddison, "Plasma Edge Physics for NET/INTOR" , Report CLM-P761, UKAEA, Culham Laboratory, Abingdon, U.K. (1985).

[73] H.J. Stone, "Iterative Solution of Implicit Approximations of Multi-dimensional Partial Differential Equations", SIAM, J. Numer. Anal., Vol.5, p.530 (1968).

[74] D. Reiter, "The EIRENE Code, Version : Jan.92, Users Manual", KFA-Report, JÜL-2599, Forschungszentrum Jülich, Germany (1992).

[75] R. Schneider, private communication, Max Planck Institut, Garching bei München, Germany.

[76] H.D. Pacher, W.D. D'haeseleer and G.W. Pacher, "2-D Edge Modelling : Convergence and Results for Next Step Devices in the High Recycling Regime", Proc. Intern. Conf. on Plasma Phys., Innsbruck, Vol.16C, p.775 (1992).

[77] W. D'haeseleer, H.D. Pacher and G.W. Pacher, "Sensitivity of Divertor Operating Conditions on Plasma Parameters in a Next Step Device", Contrib. Plasma Phys., Vol.32, p.444 (1992).

[78] H. Gerhauser, H.A. Claaßen, private communication, Forschungszentrum Jülich, Germany.

[79] J. Boedo, private communication, University of California, Los Angeles, U.S.A.

[80] K.C. Shaing and E.C. Crume, Jr., "Bifurcation Theory of Poloidal Rotation in Tokamaks : A Model for the L-H Transition", Phys. Rev. Lett., Vol.63, p.2369 (1989).

[81] M. Tendler, V. Rozhansky, "Poloidal Rotation, Asymmetry and Electric Field Effects at the Edge of a Divertor Tokamak", Report TRITA-PFU-89-02, Royal Institute of Technology, Stockholm, Sweden.

[82] Proc. IAEA Technical Conference Meeting on Tokamak Plasma Biassing, Montréal, (IAEA Vienna) (1992).

[83] J. Neuhauser, private communication, Max Planck Institut, Garching bei München, Germany.

[84] M.E. Rensink, J. Milovich and T. Rognlien, "Simulation of DIII-D D Divertor Biassing with the LEDGE code", Proc. IAEA Technical Conference Meeting on Tokamak Plasma Biassing, Montréal, (IAEA Vienna), p.375 (1992).

[85] L. Tonk and I. Langmuir, "A General Theory of the Plasma of an Arc", Phys. Rev., Vol.34, p.876 (1929).

[86] P.J. Harbour, D.D.R. Summers, S. Clement et al., "The X-Point Scrape-off Plasma in JET with L- and H-Modes, J. Nucl. Mat., Vol.162-164, p.236 (1988).

[87] D. Buchenauer, W.L. Hsu, D.N. Hill, M.A. Mahdavi, "Divertor Plasma Characterization using Langmuir Probes in DIII-D", J. Nucl. Mat., Vol.176-177, p.528 (1990).

[88] M.J. Schaffer and B.J. Leikind, "Observation of Electric Currents in Diverted Tokamak Scrape-off Layers", Nucl. Fus., Vol.30, p.1750 (1991).

[89] A.V. Chankin, S. Clement, L. de Kock al. "Parallel Currents in the Scrape-off Layer of JET Diverted Discharges", J. Nucl. Mat., Vol.196-198, p.739 (1992).

[90] C. Pitcher, "First Results with the In-Vessel Probe on ASDEX-Upgrade", Proc. 20th Eur. Conf. on Contr. Fus. and Plasma Phys., Vol.17C, Lisboa (1993).

[91] P.J. Harbour, "Current Flow Parallel to the Field in a Scrape-off Layer", Contrib. Plasma Phys., Vol.28, p.417 (1988).

[92] G.M. Staebler and F.L. Hinton, "Currents in the Scrape-off Layer of Diverted Tokamaks", Nucl. Fus., Vol.29, p.1820 (1989).

[93] P.C. Stangeby, "Currents in the Scrape-off Layer of Diverted Tokamaks : Power to the Divertor Plates", Nucl. Fus., Vol.30, p.1153 (1990).

[94] D.M. Goebel, G.A. Campbell, R.W. Conn et al., "Langmuir Probe Measurements in the TEXTOR Tokamak During ALT-I Pump Limiter Experiments", Plasma Phys. and Contr. Fus., Vol.29, p.473 (1987).

[95] D.M. Manos, R. Budny, T. Satake and S.A. Cohen, "Calorimeter Probe Studies of PDX and PLT", J. Nucl. Mat., Vol.111-112, p.130 (1984).

[96] R. Budny, M.G. Bell, K. Bol et al., "Initial Results from the Scoop Limiter Experiment in PDX", J. Nucl.Mat., Vol.121, p.294 (1984).

[97] V.A. Vershkov, S.A. Grashin and A.V. Chankin, "Experimental Study of Plasma Fluxes in the Shadow of a Scoop Limiter on T-10", J. Nucl. Mat., Vol.145-147, p.611 (1988).

[98] V.A. Vershkov, the T-10 Group and the CIEP Group, "Edge Plasma Investigation on T-10" J. Nucl. Mat., Vol.162-164, p.195 (1988).

[99] R.A. Pitts, G. Vayakis, G.F. Mathews and V.A. Vershkov, "Poloidal SOL Asymmetries and Toroidal Flow in Dite", J. Nucl. Mat., Vol.176-177, p.893 (1990).

[100] G.R. Tynan, J.A. Boedo, D.S. Gray et al., "Effects of Radial Electric Fields on the Turbulence and Transport in the TEXTOR Edge and SOL Plasma", J. Nucl. Mat., Vol.196-198, p.771 (1992).

[101] P.E. Philips, A.J. Wootton, W.L. Rowan et al., "Biassed Limiter Experiments on TEXT", J. Nucl. Mat., Vol. 145-147, p.807 (1987).

[102] T. Uckan, S.C. Aceto, L.R. Baylor et al., "Effects of Limiter Biassing on the ATF Torsatron" J. Nucl. Mat., Vol.196-198, p.308 (1992).

[103] M.G. Schaffer, M. ali Mahdavi, C.C. Klepper et al., "Effect of Divertor Bias on Plasma Flow in the DIII-D Scrape-off Layer", Nucl. Fus., Vol.32, p.855 (1992).

[104] D. Michaud, G.G. Ross, B.L. Stansfield et al. "Modification of the Plasma Edge Properties during Divertor Plate Biassing Experiments on TdeV", J. Nucl. Mat., Vol.196-198, p.316 (1992).

[105] L. Schmitz, H. Kugel, R. Bell et al., "M=1 Divertor Biassing Experiments in PBX-M", Proc. IAEA Technical Conference Meeting on Tokamak Plasma Biassing, Montréal, (IAEA Vienna), p.285 (1992).

[106] H. Biglari, P.H. Diamond and P.W. Terry, "Influence of Sheared Poloidal Rotation on Edge Turbulence", Physics of Fluids B2, p.1 (1990).

[107] P.C. Liewer, "Measurements of Microturbulence in Tokamaks and Comparisons with Theories of Turbulence and Anomalous Transport", Nucl. Fus., Vol.25, p.543 (1985).

[108] A.J.Wootton, B.A. Carreras, H. Matsumoto et al., "Fluctuations and Anomalous Transport in Tokamaks", Phys. Fluids, Vol.B-2, p.2879 (1990).

[109] D.W. Ross, "On Standard Forms for Transport Equations and Quasilinear Fluxes", Comments on Plasma Phys. and Contr. Fus., Vol.12, p.155 (1989).

[110] D.W. Ross, "On Standard Forms for Transport Equations and Quasilinear Fluxes-Part II", Plasma Phys. and Contr. Fus., Vol.34, p.137 (1992).

[111] W.M. Manheimer, E. Ott and W.M. Tang, "Anomalous Electron-Ion Energy Exchange from the Trapped Electron Mode", Phys. of Fluids, Vol.20, p.806 (1977).

[112] D. Reiter, H. Kever, G.H. Wolf et al., "Helium Removal from Tokamks", Plasma Phys. and Contr. Fus., Vol.33, p.1579 (1991).

[113] R. Schneider, B.J. Braams, D. Reiter et al., "Extensions of B2 for the Simulation of ASDEX-Upgrade Scrape-off Layer Plasmas", Contrib. to Plasma Phys., Vol.32, p.450 (1992).

[114] H.-S. Bosch, R. Schneider, D. Reiter, "Modelling of the ASDEX-Upgrade Scrape-off Layer Plasma", Proc. of Int. Conf. on Plasma Phys., Innsbruck, Austria (1992)

[115] R. Schneider, D. Reiter, J. Neuhauser et al., "Analysis of Cold Divertor Concepts by 2-D simulations" Proc. 20th Eur. Conference on Contr. Fus. and Plasma Phys., Lisboa (1993).

[116] T. Shoji, H. Aikawa, B.M. Annaratone et al., "Divertor Bias Experiment on JFT-2M", Plasma Phys. and Contr. Nucl. Fus. Research 1992, Vol.1 (IAEA, Vienna), p.323 (1993).

[117] J.-L. Lachambre, P. Couture, A. Boileau et al., "Current Injection and Plasma Biassing in TdeV", Proc. IAEA Technical Conference Meeting on Tokamak Plasma Biassing, Montréal, (IAEA Vienna), p.268 (1992).

Bij het afsluiten van dit onderzoek, wil ik een dankwoord richten tot iedereen die mij steun heeft verleend bij dit doktoraatswerk.

Bijzonder erkentelijk ben ik Roger Weynants, die op een vriendschappelijke en begeesterende wijze dit doktoraat in goede banen leidde. De kansen op succes werden aanzienlijk verhoogd door prof. Dutré die mij onvoorwaardelijk de materiële en immateriële mogelijkheden heeft geboden om gedegen wetenschappelijk werk te verrichten.

Ook dank ik prof. Vandenplas die mij steeds gesteund heeft in dit onderzoek en daarbij de nodige financiële middelen ter beschikking stelde om de verplaatsingen naar Jülich mogelijk te maken.

Verder gaat mijn gemeende waardering uit naar alle leden van het "Laboratorium voor Plasmafysica" voor de talrijke en interessante wetenschappelijke discussies. Ik dank ook mijn vrienden en collega's van de "Afdeling Toegepaste Mechanica en Energieconversie", met wie ik in een aangename sfeer heb mogen samenwerken en die zo een al dan niet tastbare bijdrage hebben geleverd tot het welslagen van dit werk.

This work would not have been possible without the support of the "Institut für Plasmaphysik", for which I thank in particular prof. Wolf.

The excellent collaboration with and the guidance from Detlev Reiter and Petra Börner have contributed greatly to a successful completion of this thesis. I am grateful to Geoff Maddison, Eric Hotston and Mike Harrison for sharing with me their insight into the physics of the edge plasma and their experience with the B2 code.

I am particularly indebted to prof. Engelmann, Bas Braams, Ralf Schneider, Jozef Neuhauser and William D'haeseleer for their continuous and generous interest in this work. I also thank dr. Gerhauser, dr. Claaßen and dr. Pitcher for the helpful discussions and comments on their results. I feel very grateful to all the members of the "Institut für Plasmaphysik" for the pleasant atmosphere they created and for sharing their knowledge with me.

Ook dank ik mijn ouders, schoonouders en familieleden voor hun steun en aanmoediging.

Tenslotte dank ik Lieven, en onze kinderen Maarten, Pieter en Jeroen, om hun flexibiliteit die mij in staat stelde naast moeder ook onderzoeker te zijn.

Tine Baelmans
oktober 1993

FORSCHUNGSZENTRUM JÜLICH GmbH

KFA

Jül-2891
März 1994
ISSN 0944-2952
LPP-ERM / KMS-Rep. N° 100

ÉCOLE ROYALE MILITAIRE-KONINKLIJKE MILITAIRE SCHOOL